TEMPERATURE DEPENDENT FRETTING DAMAGE MODELING OF AISI 301 STAINLESS STEEL

A Dissertation
Presented to
The Academic Faculty

by

Michael Robert Hirsch

In Partial Fulfillment
of the Requirements for the Degree
Doctor of Philosophy in the
Woodruff School of Mechanical Engineering

Georgia Institute of Technology
December 2013

TEMPERATURE DEPENDENT FRETTING DAMAGE MODELING OF AISI 301 STAINLESS STEEL

Approved by:

Dr. Richard W. Neu, Advisor
School of Mechanical Engineering
School of Materials Science and Engineering
Georgia Institute of Technology

Dr. Stephen D. Antolovich
School of Materials Science and Engineering
School of Mechanical Engineering
Georgia Institute of Technology

Dr. David L. McDowell
School of Mechanical Engineering
School of Materials Science and Engineering
Georgia Institute of Technology

Dr. Preet M. Singh
School of School of Materials Science and Engineering
Georgia Institute of Technology

Dr. Suresh K. Sitaraman
School of Mechanical Engineering
Georgia Institute of Technology

Date Approved: November 4, 2013

TABLE OF CONTENTS

Page

CHAPTER

LIST OF TABLES

LIST OF FIGURES

LIST OF SYMBOLS AND ABBREVIATIONS

a	New fretting damage parameter detrimental effects constant
AFM	Atomic Force Microscopy
b	New fretting damage parameter detrimental effects exponent
BCC	Body Centered Cubic
c	New fretting damage parameter beneficial effects constant
CG	Course Grained
COF	Coefficient of Friction
CTE	Coefficient of Thermal Expansion
d	New fretting damage parameter beneficial effects exponent
D	New fretting damage parameter fatigue damage modification factor
eFFDP	Enhanced Fretting Fatigue Damage Parameter
EL	Elongation to failure
FCC	Face Centered Cubic
FDP	Fretting Damage Parameter
FF	Fretting Fatigue
FFDP	Fretting Fatigue Damage Parameter
FG	Fine Grained
FS	Fatemi-Socie
GMR	Giant Magneto-Resistance sensor
GSR	Gross Slip Regime
HCF	High Cycle Fatigue

HCP	Hexagonal Close Packed
k_{dam}	Fraction of total frictional energy causing material damage
M_d	Upper limit temperature for martensite formation
M_f	Lower limit temperature for presence of austenite
MFM	Magnetic Force Microscopy
MMPDS	Metallic Material Properties Data Sheet
MRFM	Material Response Fretting Map
M_s	Upper limit temperature for thermally induced martensite transformation
MSR	Mixed Slip Regime
mSWT	Modified Smith-Watson-Topper
N_f	Cycles to failure
P	Normal Force
p_0	Hertz peak normal pressure
PF	Plain Fatigue
PSR	Partial Slip Regime
Q	Global tangential force
q(x)	Shear traction distribution
R	Force ratio
RCFM	Running Condition Fretting Map
S-N	Stress-life
SQUID	Superconducting Quantum Interference Device
TEM	Transmission Electron Microcopy
TRIP	Transformation Induced Plasticity

TS	Tensile Strength
VSM	Vibrating Sample Magnetometer
$V\alpha$	Volume fraction of α' martensite
W_{eff}	Effective work
XRD	X-Ray Diffraction
YS	Yield Strength
α'	BCC martensite phase
α_{cp}	Ratio of energy going toward the contacting body to energy going toward the body of interest
γ	FCC austenite phase
δ	Displacement
Δ	Displacement Amplitude
$\Delta\varepsilon d$	Cyclic strain amplitude
ε	HCP martensite phase
μ	Coefficient of Friction
σ	Maximum Normal Stress Parallel to the Surface
τ	Shear stress

SUMMARY

Prediction of fatigue damage due to fretting is complex due to the number of influential factors and the competitive interaction between wear and fatigue. The majority of current fretting damage modeling approaches are limited to narrow ranges of conditions where little competition between damage mechanisms occurs. Recent models which account for damage interaction are largely phenomenological in nature and are still limited to a narrow range of applicability. A method to characterize and model the level of fatigue damage due to fretting was developed in this work to address the shortcomings of the current methods available by extending the range of conditions captured and enhancing the physical basis of the damage model.

Baseline material properties for thin sheets of AISI 301 stainless steel in the full hard condition were determined as a function of temperature through tensile tests, fatigue tests, and metallography. Fretting experiments were performed for contact between 301 stainless steel and each ANSI A356 aluminum and AISI 52100 steel. Fretting experiments were performed over a range of material combinations, normal forces, displacement amplitudes, atmospheres, and temperatures. Subsequent characterization of the damage due to fretting was performed to determine the level of wear and fatigue damage incurred for each condition tested.

A finite element model of the experiment was created to determine the cyclic stress-strain behavior and local frictional energy dissipation for each condition. Fatigue damage metrics were evaluated to determine the effects of the contact conditions on the driver for fatigue damage. A new model for fatigue damage due to fretting was developed

which incorporates the wear behavior to describe the effect of wear on the level of fatigue damage caused by fretting. The level of fatigue damage is influenced using a function of frictional energy dissipation and wear rate to account for differences in wear mechanisms and changes in the severity of wear caused by changes in oxidation behavior and mechanical properties which result from changes in temperature or contacting materials.

CHAPTER 1

INTRODUCTION

Fretting is a low amplitude oscillatory motion between two bodies that results in wear and fatigue damage. Components subjected to fretting can exhibit a drastic reduction in fatigue performance due to the acceleration of fatigue crack formation. It has been suggested that there are as many as 50 parameters that affect the type and extent of fretting damage [1], making design against fretting damage difficult. The main influential parameters include the contact pressure, slip amplitude, coefficient of friction (COF), and the properties of the contacting materials [2]. It is important to understand how each of these parameters affects the severity of fretting damage so that components can be designed for minimal fretting damage.

There have been many studies seeking to model material damage (both fatigue and wear) that occurs through a variety of different processes. Material damage due to fretting is a complex process to model since both fatigue damage and wear occur simultaneously and have competing effects. Fatigue processes and wear processes are challenging to model individually without consideration of their interaction. Therefore, most current fatigue damage parameters for fretting are focused on conditions where only one of the damage mechanisms is dominant, thus limiting the range of applicability. More recent work has addressed modeling the effects of combining these two damage mechanisms; however these methods are largely empirical and are not able to account for wide range of conditions.

Studying fretting damage of thin sheets of austenitic stainless steel offers additional challenges over other materials and geometries. The effect of fretting specimen thickness has received some attention in the literature [3-6], however, the common fretting experimental methods are not well suited for testing thin sheets [7]. Therefore, the minimum specimen thickness in an experimental study reported in the literature is 1 mm [8]. The properties of the 300 series austenitic stainless steels are strongly influenced by the transformation of austenite to martensite, which is highly temperature sensitive. This causes changes in the oxidation, wear, and fatigue behavior with relatively small changes in temperature, and therefore has a significant effect on the fretting response.

This work addresses the challenges associated with designing against fretting damage through a combination of fretting experiments with fretting damage characterization and finite element modeling of the imposed conditions. An experimental method was developed to perform experiments on thin sheets of austenitic stainless steel over a range of displacement amplitudes, normal forces, contacting material properties, atmospheres, and temperatures. These tests constitute the thinnest material used for fretting experiments reported in open literature. These experiments also constitute the first fretting experiments performed on 301 stainless steel in the fully cold rolled condition available in the open literature. Material damage was characterized to determine the extent of wear and fatigue damage resulting from each fretting condition. The oxidation characteristics and the sensitivity of the mechanical properties on the austenite stability was determined as a function of temperature. A finite element model was created to determine the cyclic stress-strain response and local frictional energy dissipation. These investigations help to separate the influence of the various physical processes on the damage mechanisms that occur during fretting, and facilitate establishment of a link between material properties and sensitivity to fretting degradation.

A fatigue damage metric was developed based on the observed damage and the relationship with the behavior identified by finite element modeling. The fatigue damage metric serves as a measure of fatigue damage due to fretting that can be evaluated via FEM to serve as a design evaluation tool to increase component reliability by mitigation of fatigue damage due to fretting in complex systems.

CHAPTER 2

BACKGROUND

2.1 Fretting

2.1.1 Damage Mechanisms and Characteristics

Fretting is a low amplitude oscillatory motion between two bodies in contact which can result in fatigue damage, wear, or both. Fretting is experienced across many industries, with failures occurring in aircraft, trains, automobiles, ships, and electrical contacts [9-11]. Depending on the materials, environment, and contact conditions, three forms of fretting can occur: fretting corrosion, fretting wear, and fretting fatigue.

The first reported study on fretting was performed in 1927 in regard to fretting corrosion by Tomlinson [12]. Fretting corrosion is the process of particle removal by contact and subsequent formation of oxides [13]. Materials such as stainless steel are resistant to corrosion because of the formation of a passivation layer. In the case of stainless steel, this passivation layer is composed of Cr_2O_3 [14]. When this passivation layer is removed by fretting, the exposed surface is susceptible to corrosion. Fretting corrosion is more severe when the frequency of motion is low, which allows more time for environmental interaction [13].

Fretting wear is characterized by the removal of surface material. In a 1985 survey, Sato [15] reported that the occurrence of fretting wear in machinery had not declined over previous decades, unlike other forms of wear. Wear can take place by abrasion, adhesion, or delamination. Abrasive wear is characterized by the formation of hard granular wear debris, often referred to as third body particles. These third body particles can accelerate the removal of material when they have high hardness and irregular shape. Wear debris can also be smaller spherical particles. These fine third body particles can act as a solid lubricant, lowering the COF (the ratio of tangential force to normal force during gross slip) and decreasing the wear rate [16]. Adhesive wear takes place when local welding occurs between the two contacting bodies and the welds are broken during cycling. This removes large particles from the surface and results in large tangential forces. Tangential forces are higher for hard material pairs because of the increased force required to break welds. Adhesion is common between like materials because similar chemistry promotes welding. Adhesion is also more dominant in noble metals and in inert environments because surface oxides interfere with the local welding. High temperatures and forces promote adhesive wear because of the increased likelihood of welding [17]. Some materials that have been shown to exhibit adhesion include copper, austenitic stainless steel, and mild steel [18].

Delamination is caused when cracks are formed near the surface and run parallel to the surface. The cracking leads to removal of material which has a plate-like appearance. Suh's delamination theory [19] states that the subsurface microcracks are caused by the cyclic shear stresses caused by asperity contact on the surface. Cracks are not generated at the surface because of the high triaxiality of the stress state at the surface [20]. The depth of the microcracks is less when the COF is lower causing the plate-like debris to be thinner [21]. Titanium alloys have been found to wear primarily by delamination during fretting [17]. The appearance of wear caused by delamination on Ti-6Al-4V is shown in Figure 2.1.

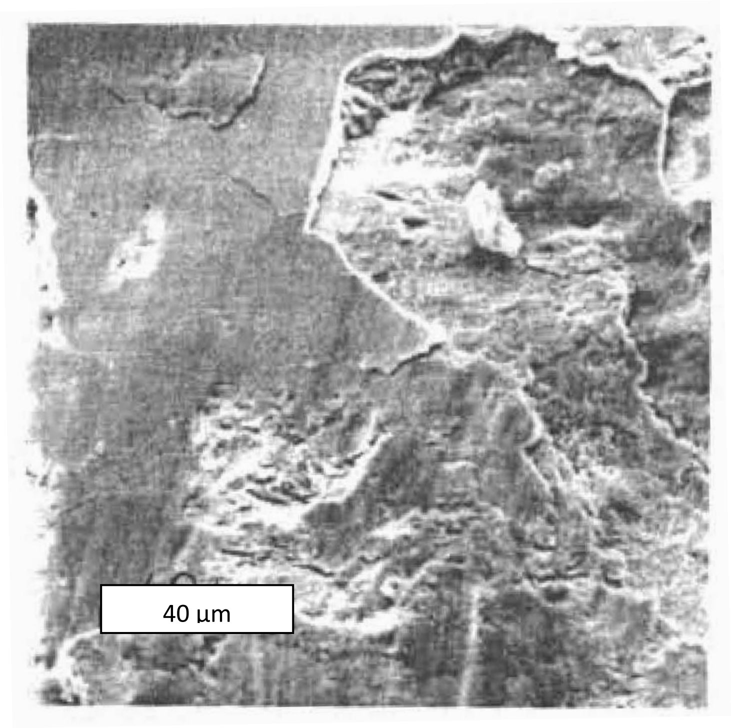

Figure 2.1: The plate-like appearance of wear of Ti-6Al-4V by delamination [17].

The term fretting fatigue is used to describe the simultaneous occurrence of fretting and an externally applied fatigue loading, and is also used to describe the damage due to fretting when fatigue is the primary damage mechanism.. The fatigue process can be divided into crack nucleation and crack propagation. When a component subjected to fatigue loading also experiences fretting, the crack nucleation process is accelerated due to the cyclic stresses at contact. Cracks have been found to form due to fretting in the absence of bulk cyclic loading [22]. Therefore, several authors have proposed separating the fretting fatigue life of the component where initiation is controlled by fretting and subsequent long crack propagation or arrest is controlled solely by bulk stresses in thick specimens [23-27]. The initial growth of initiated cracks is determined by the stresses at contact. Cracks initially form at an angle between 35 and 55 degrees from the surface and propagate under shear (mode II) conditions due to shear from friction forces at contact. Once the crack has grown out of the influence of the contact stresses, cracks turn to 90 degrees from the surface and growth is controlled by tensile (mode I) conditions due to bulk stresses [16].

The term knockdown refers to the decrease in fatigue performance due to fretting. A knockdown in fatigue life refers to the difference between the number of cycles to failure due to plain fatigue and the number of cycles to failure due to fretting fatigue for the same cyclic stress conditions divided by the plain fatigue life. A knockdown in fatigue strength refers to the difference between the cyclic stress level that results in a certain life of a component during plain fatigue and the cyclic stress level that results in the same life during fretting fatigue divided by the plain fatigue limit. The fatigue life reduction factor is the fretting fatigue life divided by the plain fatigue life. Similarly, the fatigue limit reduction factor is defined as the fretting fatigue limit divided by the plain fatigue limit.

The knockdown in the fatigue life due to fretting has been reported to be as high as 74% [28]. Cracks initiated during fretting are especially problematic because they are hidden by the contact itself, making visual inspection of components ineffective. In 1999, Nicholas [29] reported that “Fretting fatigue in dovetail joints is one of the most difficult and costliest problems in the US Air Force related to HCF”.

2.1.2 Influential Parameters

Fretting damage is a complex combination of damage mechanisms with competitive effects. The type and extent of damage resulting from fretting has been suggested to be influenced by as many as 50 parameters [1]. The primary parameters include the COF, contact pressure, and magnitude of slip, which are interrelated and affected by many aspects of the interaction. Fatigue damage due to fretting is caused by cyclic contact stresses, which are multiaxial, non-proportional, and have strong gradients that can occur on the scale of the microstructure. The contact stress field is sensitive to the contact geometry, which evolves as wear occurs. Therefore, the cyclic contact stresses also evolve with time under conditions where wear is significant. Fatigue damage is more severe when the COF is high due to an increase in the tensile stress at the trailing edge of contact [30].

Oxygen content and humidity of the atmosphere affect the oxidation behavior of the surface. The composition and quantity of oxides have a strong effect on the fretting behavior. High oxygen content and humidity increase oxidation. Fine oxides can act as lubrication which helps prevent adhesion, lowering stress due to friction. Alternatively, oxides can cause abrasive wear. Low oxygen and humidity decrease oxidation. The absence of oxides may result in adhesion, which increases friction and therefore the driving force for crack nucleation [2]. Temperature affects the material properties and the oxidation behavior. High temperatures can degrade material strength which can accelerate damage. However, a thicker glaze oxide can form at high temperatures which lowers the COF and increases the fretting fatigue life [31]. These effects vary greatly depending on material combination.

The contact condition during fretting is described by hysteresis loops; tangential force Q plotted versus displacement δ. The area inside the loop describes the amount of energy dissipated by frictional work. The two different types of contact conditions with their corresponding characteristic hysteresis loops are shown in Figure 2.2. Partial slip is the contact condition where a portion of the body is stuck and the edges of contact are experiencing slip. This is characterized by a narrow elliptical hysteresis loop. The amount of slip at the edge of contact increases as the tangential force increases and the hysteresis loop widens. When the ratio of tangential force to normal force rises above the COF, the entire interface experiences slip. This is known as gross slip, and is characterized by a wide hysteresis loop having a slope of nearly zero along the top and bottom portions of the loop. Reciprocating sliding occurs when the displacement amplitude is larger than the contact half-width, so that the contact area at the peak displacement in one direction does not overlap the contact area at the peak displacement in the reverse direction.

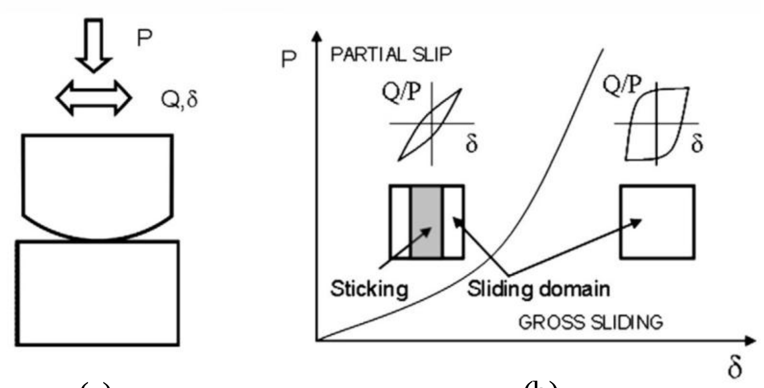

(a) (b)

Figure 2.2: (a) Contact schematic and (b) contact conditions with corresponding hysteresis loops [32].

During fretting, the contact condition can change. A three dimensional plot of friction force versus displacement as a function of cycles, called a friction log, describes the change in contact condition as a function of cycles [33]. The running condition is divided into three different regimes: the Partial Slip Regime (PSR), Mixed Slip Regime

(MSR), and Gross Slip Regime (GSR) [34]. These regimes make up the running condition fretting map shown in Figure 2.3 with the corresponding characteristic friction logs. The partial slip regime is distinguished by a partial slip contact condition for all cycles. The friction log for partial slip shows hysteresis loops that stay closed for all cycles. The mixed slip regime (also known as the mixed fretting regime) is characterized by gross slip initially and a transition to partial slip as cycling continues. This can be seen in the friction log as open loops that transition to closed loops over the duration of cycling, typically because friction is increasing with cycles as fretting damage is generated at the interface. The gross slip regime is defined by gross slip conditions for all cycles.

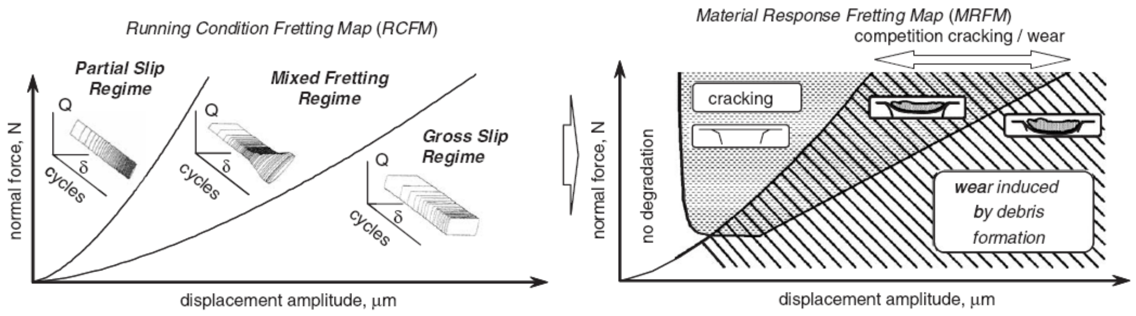

(a) (b)

Figure 2.3: (a) Running condition fretting map and (b) material response fretting map [35].

The relationship of the running condition fretting map to the material response, as shown in Figure 2.3, was first shown by Blanchard et al. in 1991 [36]. When the displacement amplitude is small, there is no damage. This is a very small value however, as damage has been observed at displacement amplitudes as low as 0.5 μm [37]. For larger displacement amplitudes in the partial slip regime, cracking is the dominant damage mechanism, with little or no wear. The mixed slip regime demonstrates a combination of wear and cracking. In the gross slip regime wear is the prevailing damage process.

The general relationship between fatigue life and wear for different running conditions as a function of displacement amplitude and constant normal force between similar materials is shown in Figure 2.4 [34]. This is the expected behavior for a specimen that is thick relative to the wear depth. The largest knockdown in fatigue life due to fretting occurs near the transition between mixed slip and gross slip where both cracking and wear occur. At higher displacement amplitudes the increasing wear rate is responsible for reducing the knockdown in fatigue life. The wear rate becomes greater than the crack growth rate. Cracks are worn away, and therefore do not decrease the fatigue life [38-41]. In addition, the wearing of the surface changes the pressure distribution in a way that decreases the shear traction at the interface by spreading the pressure over a larger area [40, 42-43].

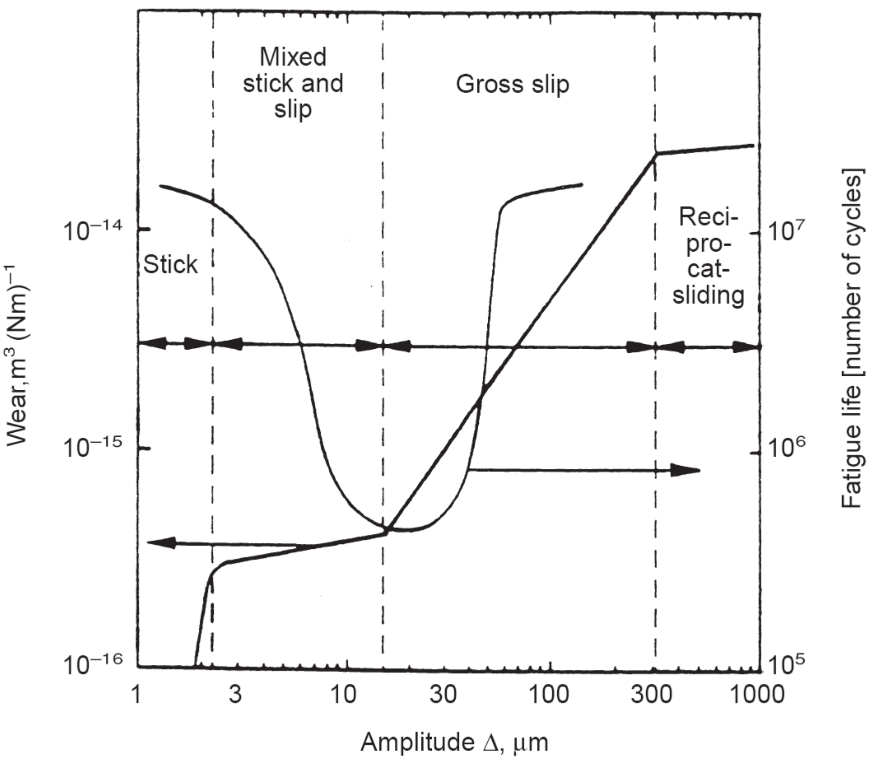

Figure 2.4: Typical relationship between fatigue life and wear for different running conditions as a function of displacement amplitude for contact of similar materials and a constant normal force [34].

The classical solution of the shear tractions for perfectly smooth elastic cylinders in contact, derived by Mindlin [44] and Cattaneo [45], is shown in Figure 2.5. The global normal force P, the global friction force Q, and the COF μ determine the size of the stick region (-c to c) within the contact region (-a to a). Figure 2.5(b) shows how the shear traction within contact (q(x) normalized by the product of the COF μ and the Hertz peak normal pressure p_0) changes as a function of Q/μP. When Q is equal to μP (Q/μP = 1) the entire contact will be in slip and the shear traction has a parabolic shape, which is the same as the Hertz normal pressure distribution since q(x) = μp(x) where p(x) is the normal pressure distribution. When the interface remains in partial slip, |Q| is less than μP, and a region of stick occurs in the center of contact. The shear traction in the slip region remains the same but decreases in the stick region. Therefore, the peak shear traction occurs at the boundary between stick and slip. As the tangential force decreases further, the boundary between stick and slip, and therefore the maximum shear traction, shifts closer to the edge of contact.

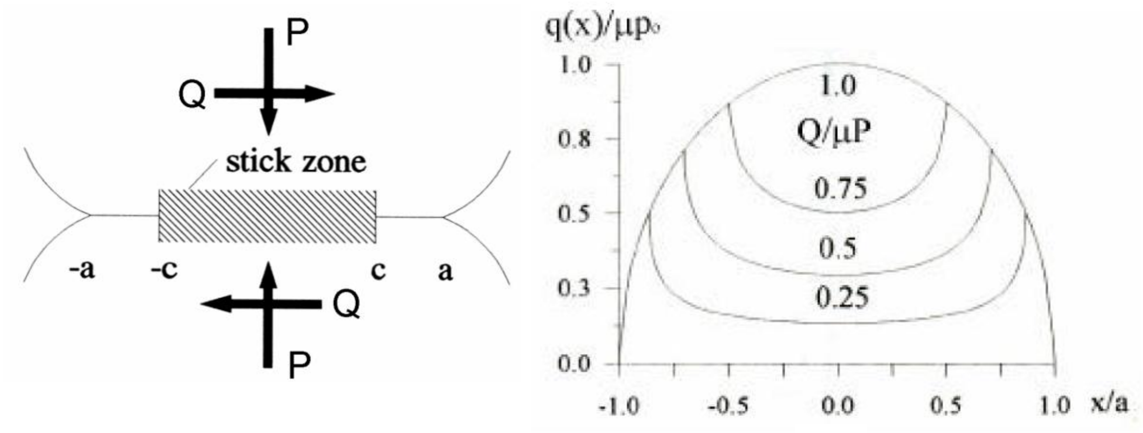

(a) (b)

Figure 2.5: (a) Schematic of the stick and slip regions during partial slip, and (b) shear stress distribution for partial slip conditions [46].

During fretting the friction force varies sinusoidally as shown in Figure 2.6(a). Here, the shear tractions along the interface also vary with time as shown in Figure 2.6(b). The hash marks indicate the region experiencing stick. At the peak tangential force, at point A in the cycle, the traction is as described above. Upon instantaneous unloading (point B), the shear reduces infinitesimally and the stick region expands to cover the entire contact. As Q is reduced (point C), reverse slip occurs near the edges of contact. This is because the normal pressure at the edge of contact is too low to prevent slip. At point D, the global friction force is zero and so the local tractions over the contact area must sum to zero to maintain equilibrium. Reversing Q to -Q_{max} (point E) results in a shear state equal to that at point A but in the reverse direction.

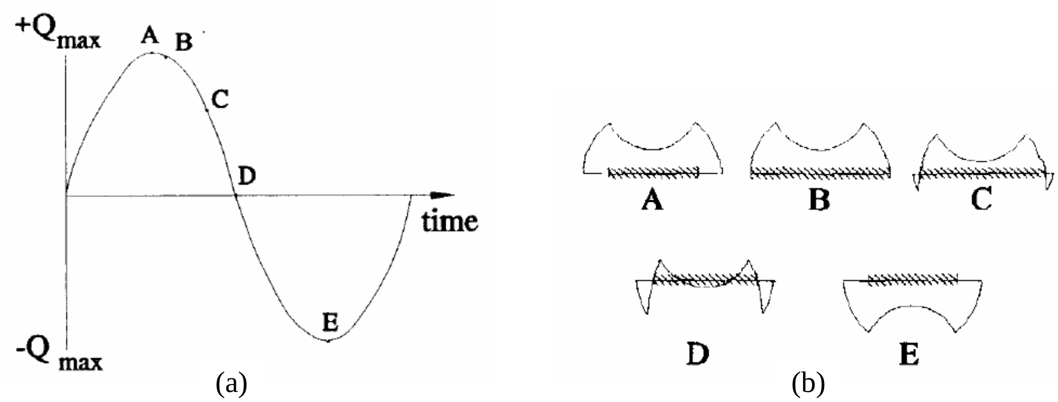

(a) (b)

Figure 2.6: (a) Friction force history and (b) corresponding local shear tractions during fretting [46].

The location of crack formation from fretting during gross slip running conditions can occur anywhere in the scar from the interactions of asperities or microstructural inhomogeneities. The location of crack formation in partial slip often occurs in the microslip region near the boundary of stick and slip [16] because of the peak in shear stress at that location. The tangential stress distribution during fretting fatigue has been shown by Nowell and Hills [47]. The peak value of the FFDP has been found to correlate well with the location of fretting fatigue crack initiation and its magnitude can correlate to the number of cycles to crack formation [48-52].

2.2 Austenitic Stainless Steel

Bermo Strauss and Edward Maurer developed the austenitic Fe-Cr-Ni alloys in Krupp Laboratories in Germany from 1909 to 1912. Strauss et al. later developed steels which led to the 18-8 series of stainless steels (the 300 series) [53].

Austenitic stainless steels are the most used metallic materials in applications requiring corrosion resistance because of their high strength and ductility [54]. In the cold worked condition they have been used as clamps and springs including head gaskets in automobiles [55]. They are relatively soft in the annealed condition where the composition is fully austenitic, but can be hardened substantially through cold work due to a transformation from austenite to martensite [56]. The yield strength of AISI 301 in the annealed condition is 275 MPa, but ultimate strengths as high as 1900 MPa can be obtained by cold work [57]. Ductility is very high in the annealed condition, with a minimum elongation to failure for 301 specified by ASTM A 666-03 of 40%. Intermediate amounts of cold work can alter the material properties to suit a variety of applications.

Austenitic stainless steels belong to the category of steels known as Transformation Induced Plasticity (TRIP) steels [58]. Austenitic stainless steels belong to one of two categories called H-TRIP steels, which are classified by high Ni and Cr contents that results in a structure consisting of metastable austenite at room temperature. The other category, L-TRIP steels, contains less alloying and consists of a ferritic-bainitic matrix with 10-15% retained austenite [59-61]. The austenite in TRIP steels undergoes a deformation induced transformation to martensite [62]. The transformation in H-TRIP steels is strain-induced while the transformation in L-TRIP steels is stress-assisted at room temperature. The TRIP effect provides a considerable enhancement of ductility and toughness [63].

Austenitic stainless steels have excellent resistance to corrosion because of the formation of a passivation layer. This passivation layer is composed of a chemically resistant chromium oxide film that protects the substrate from chemical attack. Type 301 has on oxide film composed of as much as 90% Cr_2O_3 [14]. This film is very thin, with a typical thickness of between 1 and 10 nm in air at room temperature [64-65]. This layer can be removed easily by abrasion, and readily reforms until the local Cr content is depleted.

The compositions of the austenitic stainless steels as specified by ASTM A 666-03 are shown in Table 2.1. Types with an L designation have lower carbon content and types with an LN designation have reduced carbon and nitrogen content for better weldability. The 200 series have lower nickel content than the 300 series, making them less temperature resistant and less expensive. Manganese is added to maintain the austenite stability lost by removing nickel. Type 301 is the least alloyed of the 300 series, resulting in the lowest austenite stability and stacking fault energy [66].

Table 2.1: Composition of austenitic stainless steels specified by ASTM A 666-03.

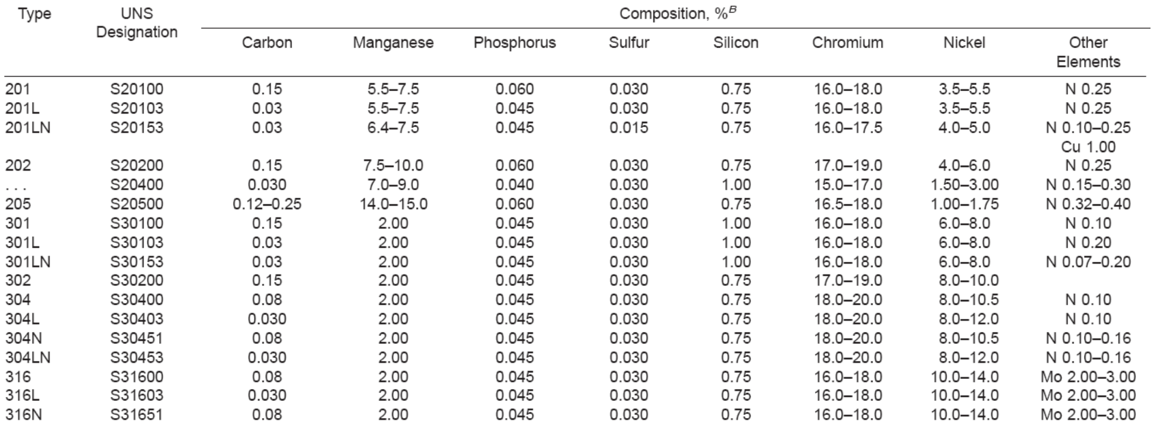

Type	UNS Designation	Composition, %^{B}							
		Carbon	Manganese	Phosphorus	Sulfur	Silicon	Chromium	Nickel	Other Elements
201	S20100	0.15	5.5–7.5	0.060	0.030	0.75	16.0–18.0	3.5–5.5	N 0.25
201L	S20103	0.03	5.5–7.5	0.045	0.030	0.75	16.0–18.0	3.5–5.5	N 0.25
201LN	S20153	0.03	6.4–7.5	0.045	0.015	0.75	16.0–17.5	4.0–5.0	N 0.10–0.25 Cu 1.00
202	S20200	0.15	7.5–10.0	0.060	0.030	0.75	17.0–19.0	4.0–6.0	N 0.25
. . .	S20400	0.030	7.0–9.0	0.040	0.030	1.00	15.0–17.0	1.50–3.00	N 0.15–0.30
205	S20500	0.12–0.25	14.0–15.0	0.060	0.030	0.75	16.5–18.0	1.00–1.75	N 0.32–0.40
301	S30100	0.15	2.00	0.045	0.030	1.00	16.0–18.0	6.0–8.0	N 0.10
301L	S30103	0.03	2.00	0.045	0.030	1.00	16.0–18.0	6.0–8.0	N 0.20
301LN	S30153	0.03	2.00	0.045	0.030	1.00	16.0–18.0	6.0–8.0	N 0.07–0.20
302	S30200	0.15	2.00	0.045	0.030	0.75	17.0–19.0	8.0–10.0	
304	S30400	0.08	2.00	0.045	0.030	0.75	18.0–20.0	8.0–10.5	N 0.10
304L	S30403	0.030	2.00	0.045	0.030	0.75	18.0–20.0	8.0–12.0	N 0.10
304N	S30451	0.08	2.00	0.045	0.030	0.75	18.0–20.0	8.0–10.5	N 0.10–0.16
304LN	S30453	0.030	2.00	0.045	0.030	0.75	18.0–20.0	8.0–12.0	N 0.10–0.16
316	S31600	0.08	2.00	0.045	0.030	0.75	16.0–18.0	10.0–14.0	Mo 2.00–3.00
316L	S31603	0.030	2.00	0.045	0.030	0.75	16.0–18.0	10.0–14.0	Mo 2.00–3.00
316N	S31651	0.08	2.00	0.045	0.030	0.75	16.0–18.0	10.0–14.0	Mo 2.00–3.00

The phase of 300 series stainless steel depends on the temperature. Three temperatures define the possible composition and transformation mechanisms: $M_f < M_s < M_d$. The values of M_s and M_d for 301 are approximately -100^{o}C and 100^{o}C [67]. Above M_s (including room temperature), austenitic stainless steels are composed of a Face Centered Cubic (FCC) γ austenite phase. Below M_s, austenite begins to spontaneously transform to martensite by thermally assisted transformation. Below M_f, all austenite has transformed to martensite. Between M_s and M_d, austenite is metastable and can transform to martensite by a strain-induced transformation mechanism Between M_s and M_f, a stress-assisted transformation to martensite can take place.

There are two common second-phase constituents found in austenitic stainless steels. The most commonly observed carbides have the composition $M_{23}C_6$ shown in Figure 2.7(a) [66, 68]. $M_{23}C_6$ has reported compositions of $(Cr_{16}Fe_5Mo_2)C_6$, $(Cr_{17}Fe_{4.5}Mo_{1.5})C_6$, and $(Fe,Cr)_{23}C_6$ [68]. Fewer carbides are present in the L and LN grades because of the reduced carbon content. However, the L and LN grades are more likely to contain the other common constituent, δ-ferrite. δ-ferrite is brittle, and often forms stringers as shown in Figure 2.7(b) [68].

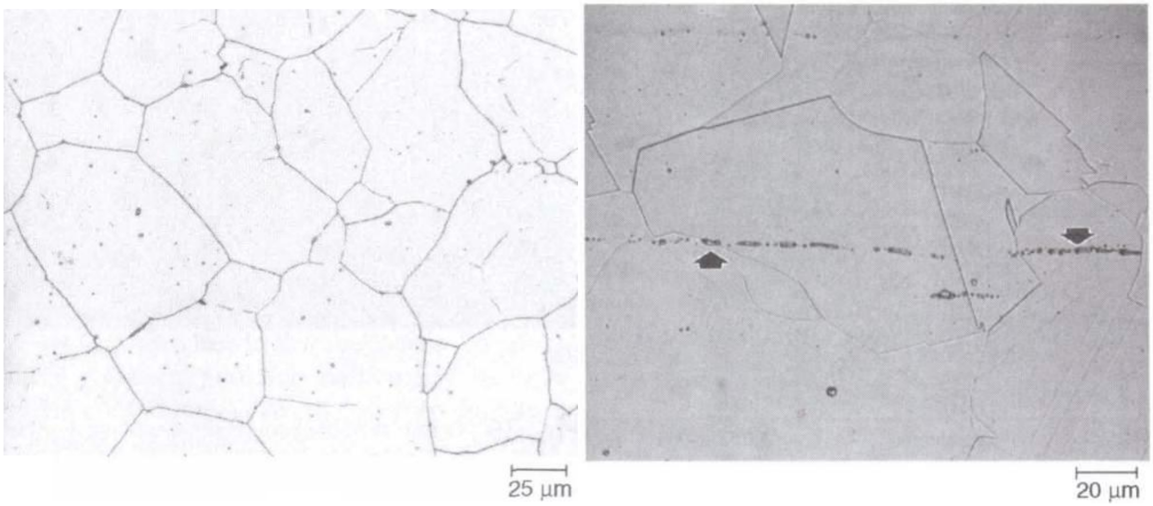

(a) (b)

Figure 2.7: (a) $M_{23}C_6$ carbides in annealed 304 and (b) δ-ferrite stringer in annealed 302 stainless steel [68].

Austenite undergoes a deformation-induced transformation to either a Body Centered Cubic (BCC) α' plate martensite, or a fine, lathlike Hexagonal Close Packed (HCP) ε martensite [56]. The deformation induced transformation can be either stress-assisted or strain-induced. Stress-assisted transformation occurs when an increase in stress is the only additional driving force required for the transformation and generally occurs at the M_s temperature and below. This results in formation of BCC martensite. Strain-induced martensite forms as a result of development of nucleation sites for transformation from cold work when between the M_s and M_d temperatures [69]. An example of the appearance of martensite due to cold work in type 303 is shown in Figure 2.8.

Figure 2.8: Martensite formed by cold rolling (arrows) in type 303 etched with waterless Kalling's reagent [68].

The extent of the transformation depends on the stability of the austenite. The stability is dependent on the composition and temperature. Increasing the amount of alloying increases the stability of the austenite [70]. Type 301 is the lowest alloyed member of the 300 series, and therefore has the lowest stability [71]. Stability also increases with increasing temperature.

Austenite is paramagnetic, and BCC martensite is ferromagnetic. Ferromagnetic materials respond to a magnetic field, and retain their own field once removed from the externally applied field. Paramagnetic materials also respond to a magnetic field, but do not sustain their own. Therefore, the amount of BCC martensite present can be detected by magnetic testing equipment such as a ferrite scope, Vibrating Sample Magnetometer (VSM), Giant Magneto-Resistance sensor (GMR), or Superconducting Quantum Interference Device (SQUID) [72]. Magnetic Force Microscopy (MFM), which is a variant of Atomic Force Microscopy (AFM) where a magnetic tip is used to measure forces, is another option for detection of martensite with high special resolution (better than 50 nm) [73]. The HCP martensite phase is not magnetic, and is therefore requires Transmission Electron Microscopy (TEM) and X-ray diffraction (XRD) to detect.

Because the transformation takes place during deformation, cold worked materials can contain a substantial amount of martensite. BCC martensite content and mechanical properties as a function of percent cold work for type 301 are shown in Figure 2.9. Elongation to failure is enhanced by the transformation due to reduction of local plastic instability, and there is an optimal stability to result in maximum elongation [56, 74-76]. The extent of transformation of austenite to martensite is decreased as the austenite content decreases, thus increasing martensite increases strength but reduces ductility.

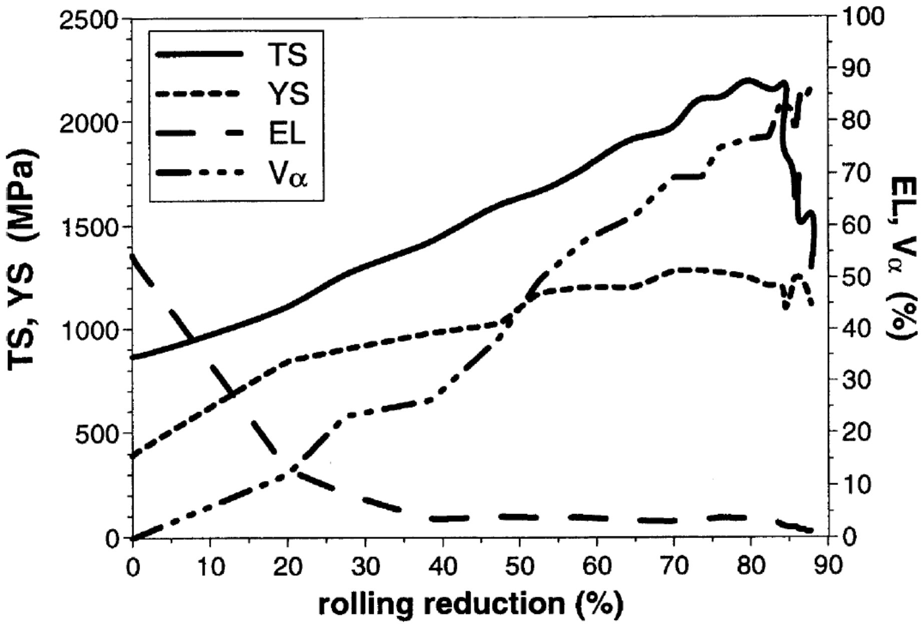

Figure 2.9: Mechanical properties and BCC martensite content as a function of the rolling reduction for 301 stainless steel [77].

The sensitivity of martensite stability to temperature is shown in Figure 2.10. Talyan et al. [78] conducted tensile tests on type 301 while measuring temperature rise of the sample due to deformation as well as martensite content for three strain rates. At low strain rates, the deformation induced heating was low and a large amount of martensite formed. At higher strain rates, deformation induced heating caused a more significant temperature rise which inhibited transformation. As a result, the ultimate strength fell from 980 MPa to 720 MPa. The effect was proven to be temperature driven by performing high strain rate tests in room temperature water. The increased convection reduced the temperature increase due to deformation and the influence of strain rate was reduced.

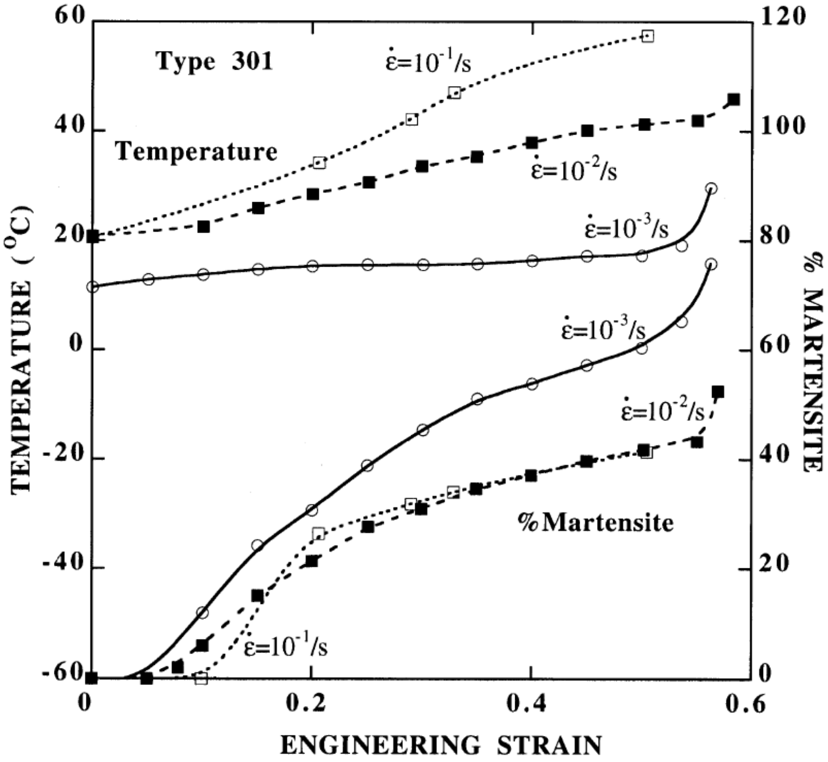

Figure 2.10: Effect of strain rate on the temperature rise and martensite transformation in 301 stainless steel [78].

The extent of cyclic hardening resulting from cyclic stress-strain at four temperatures within the M_s to M_d range is shown in Figure 2.11 [79]. At lower temperatures, much more cyclic hardening takes place due to the lower stability of austenite. As temperature increases, the cyclic hardening decreases because less transformation to martensite occurs. This demonstrates the sensitivity of behavior on temperature relating to the effect of phase transformation.

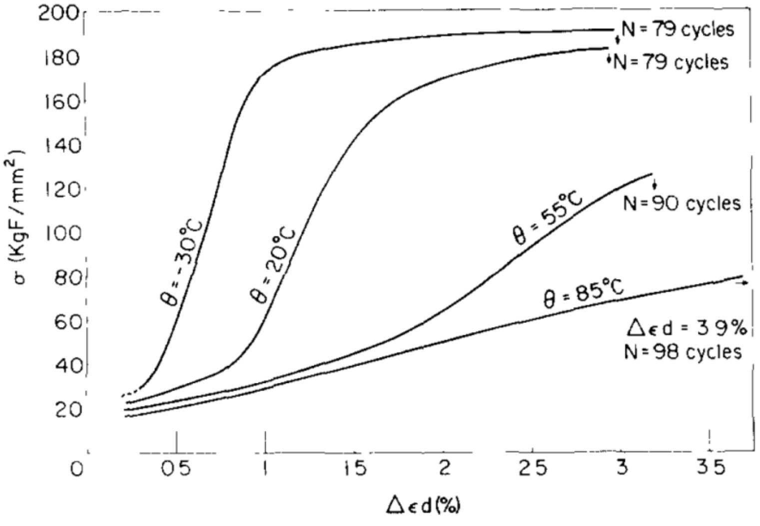

Figure 2.11: Cyclic stress-strain curves for type 301 at four temperatures between M_s and M_d indicating cycles to failure, N [79].

Barclay et al. [80] examined the deformation mechanisms austenitic stainless steel by TEM and XRD. The following six mechanisms were found to taking place during tensile deformation: (1) dislocation motion in austenite, (2) dislocation tangles, cell formation, and formation of stacking faults in austenite, (3) deformation twins in austenite, (4) martensite formation, (5) dislocation motion in martensite, and (6) deformation twins in martensite. These mechanisms were observed to take place in this order, with overlap by as many as three mechanisms.

The low alloyed austenitic stainless steels have low stacking fault energies. Values range from less than 15 mJ/m^2 for type 301 to 90 mJ/m^2 for type 316. Therefore, lower alloyed austenitic stainless steels primarily deform by planar dislocation glide. Cross slip of dislocations is impeded and therefore the dislocation motion is restricted to the corresponding slip plane. This limits the formation of 3D dislocation arrangements such as cell structures [81].

An optimal austenite stability exists where the transformation to martensite occurs at an intermediate level of plastic strain to maximize strength and elongation. If the transformation occurs to readily, the material becomes brittle [56, 78, 82]. If the austenite is too stable, excessive dislocation generation and twinning in the austenite occurs causing fracture in the austenite prior to transformation to martensite [80]. It is difficult to obtain the optimal stability because of the high sensitivity to composition and temperature [56], however type 301 with 7% Ni is said to be close to optimum at room temperature [80].

The transformation to martensite has a significant effect on the fatigue crack growth behavior. At low mean stresses in annealed material, unstable austenite has a lower fatigue crack growth rate than stable austenite. This is due to a positive volume change associated with the transformation. The lower density of martensite causes the introduction of compressive stresses from transformation when the volume is constrained. Compressive stresses are introduced in the plastic zone surrounding the crack tip where transformation occurs. This lowers the mean stress and therefore reduces the driving force for crack growth [71]. However, the high hardening due to the transformation tends to increase the crack growth rate because of reduction in the resistance to crack growth due to the brittle nature of the martensite phase. This effect offsets the beneficial reduction in mean stress when tests are conducted with high mean stress [83]. Stress amplitude has been found to increase due to the secondary cyclic hardening when tests are conducted in strain control [79, 84-85]. Hardening increases at decreased temperature because of the decreased austenite stability. In highly cold worked material the fatigue crack growth resistance is higher than in the annealed condition by a factor of 2 to 3 and is not dependent on the stability of the austenite [71]. Separate work has reported the fatigue crack growth resistance is lower for highly cold worked material when ΔK is less than 44 MPa √m [67].

Formation of fretting cracks occurs in a volume of material experiencing a multiaxial state of cyclic stress and strain [52]. Hence, the crack formation under multiaxial loading is relevant. The cracking behavior exhibited by annealed type 304 when tested in tension or torsion is shown in Figure 2.12. The life of the material is divided into three regions. Region A is a failure mode dominated by shear crack growth. Region B is shear crack nucleation followed by crack growth on planes of maximum principal strain (stage II growth planes). Region C is life dominated by crack nucleation. In torsion, region A behavior was observed for short lives while region B behavior was exhibited for long lives. Region C was only observed for the longest lives. When tested in tension, the fracture surface was dominated by stage II growth [86]. At low strain amplitudes up to 90% of the life is taken up by nucleation, while at high strain amplitudes 90% may be stage II growth [87]. Fretting cyclic stresses cracks early in the life, which suggests that shear crack growth might be important. Thin specimens, which have less constraint, will tend to be shear cracking.

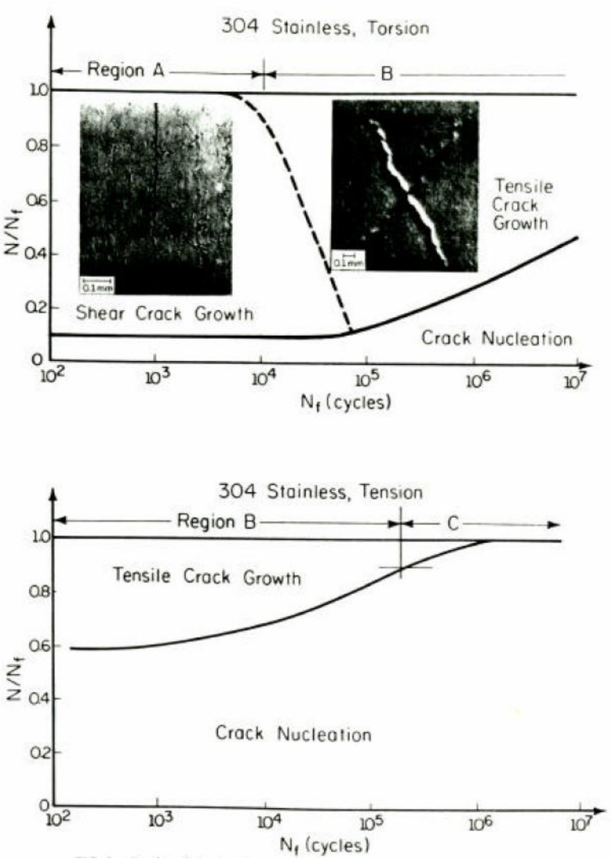

Figure 2.12: Cracking behavior of annealed type 304 in torsion and in tension [86].

During high cycle fatigue of annealed types 301, 304, and 310 cracks were found to initiate in a slip band near a grain or twin boundary [88]. Cracking at inclusions was not found. Cracks that caused failure were typically microcracks that coalesced to form the catastrophic flaw. Typical microcracks were measured to be approximately 25 μm after slow growth before linking with other cracks by fracture of the intermediate material. In cold worked material, cracks were initiated at cracked inclusions and microcrack linking did not play a role [88].

It is well known that austenitic stainless steels have poor wear and galling resistance. Macro welding can occur, which increases surface damage [18]. Materials with low stacking fault energies typically have lower crack nucleation rates, which can decrease the tendency for delamination [89]. The transformation to martensite also occurs during wear and alters the contact behavior, however whether the effect is beneficial depends on the conditions of the interaction. The transformation hardens the surface layer, which is then supported by a softer layer. This can lead to cracking of the surface layer at the interface between the hard and soft layer where subsequent deformation tends to be more intense and can lead to an increased wear rate [90]. The oxidation behavior is influenced by the transformation because the grain boundaries between austenite and martensite grains have very high diffusion rates of Cr and Fe [91] which strongly affects the wear behavior. There are many competing mechanisms which make the wear behavior complex.

2.3 Fretting of Austenitic Stainless Steel

Many fretting studies have been carried out on austenitic stainless steel because of its widespread use and the severe damage which can be caused by fretting. Fretting tests have been conducted in a variety of environments including H_2 [92], CO_2 [31], vacuum [93-94], and simulated body fluids [95-98]. Tests have been performed at temperatures up to 650^{o}C. However, no reported research was found on austenitic stainless steel in the cold-rolled condition.

Austenitic stainless steels have excellent resistance to corrosion because of the formation of a chemically resistant chromium oxide passivation layer that protects the substrate from chemical attack. Type 301 has on oxide film composed of as much as 90%

Cr_2O_3 [14], which has a thickness typically between 1 and 10 nm in air at room temperature [64-65]. This layer can be removed easily by fretting, and has a high hardness resulting in a high wear rate when trapped in the contact [31]. Reformation of the protective oxide eventually results in depletion of Cr in the near surface region. The removal of the protective Cr_2O_3 by fretting results in formation of chromium spinel oxide ($FeCr_2O_4$), which is not suitable for wear prevention [99]. Fretting between 304 stainless steel and itself has been reported to produce Fe_2O_3 at room temperature. The composition of the iron oxide transitions to Fe_3O_4 at 300^oC and then to FeO at temperatures above 650^oC [100]. The presence of Fe_2O_3 has been shown to result in higher wear rates compared to Fe_3O_4 [100].

Hsu et al. [90] studied the effect of the martensitic transformation on the fretting wear behavior. They reported an increase in the wear rate as the stability of the austenite decreased because of the composition of the oxide. Type 304 produced a fine BCC α' martensite wear debris, whereas type 316 (higher stability) had a larger plate like α' debris that had a more damaging effect on the surface. Using TEM, it was observed that the subsurface composition of 304 transformed to the structure shown in Figure 2.13.

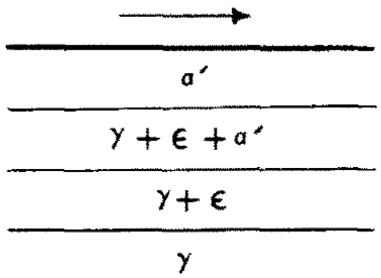

Figure 2.13: Surface composition as a function of depth resulting from sliding wear of 304 with an arrow indicating the direction of sliding [90].

The effect of grain size on the fretting fatigue behavior of 304 was studied by Raman and Jayaprakash [82]. For the two grain sizes studied (47 μm and 277 μm) the COF was found to be higher for the fine grained material by approximately 20%. The presence of martensite in the fretting scars was documented for the two grain sizes studied and was found to have a very inhomogeneous distribution. More martensite was found in the course grained material as shown in Figure 2.14. This is a result of the higher quantity of annealing twins. The martensite was measured with a ferrite scope, and so the quantity of martensite was reported in terms of ferrite number. More martensite was found in fretting scars due to the increased stresses from contact. Less martensite was found in the bulk of the specimens when subjected to fretting fatigue compared to plain fatigue because of the shorter life in fretting fatigue. The fretting fatigue life of the fine grained material was found to be 50% lower than the plain fatigue life, whereas the coarse grained material showed almost no reduction. This is due to the higher COF for the fine grained material and the increased crack growth resistance from the higher martensite content in the coarse grained material.

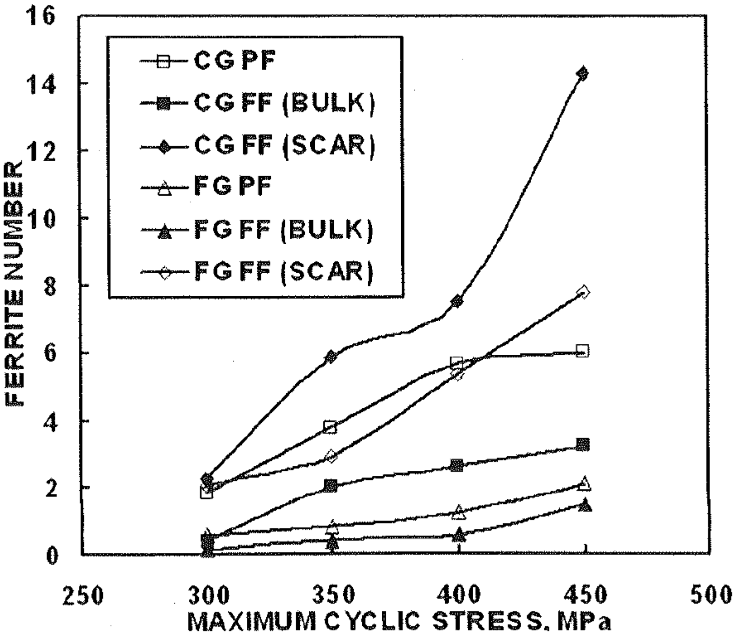

Figure 2.14: Presence of martensite in course grained (CG) and Fine Grained (FG) 304 resulting from Fretting Fatigue (FF) or Plain Fatigue (PF) [82].

Nakazawa et al. [101] investigated the effect of contact pressure on the fretting fatigue life of 316L. At a stress amplitudes of 150 MPa, the fretting fatigue life using a 60 MPa contact pressure was one third of the fretting fatigue life using a 30 MPa contact pressure, as shown in Figure 2.15. However, the stress amplitude resulting in infinite life was the same for both pressures. The reduction in fatigue strength due to fretting was found to be 30% with a 30 or 60 MPa contact pressure. Increasing pressure caused the catastrophic crack to form more toward the edge of the scar due to the increased stick region. Hence, cracks initiated at the boundary between stick and slip.

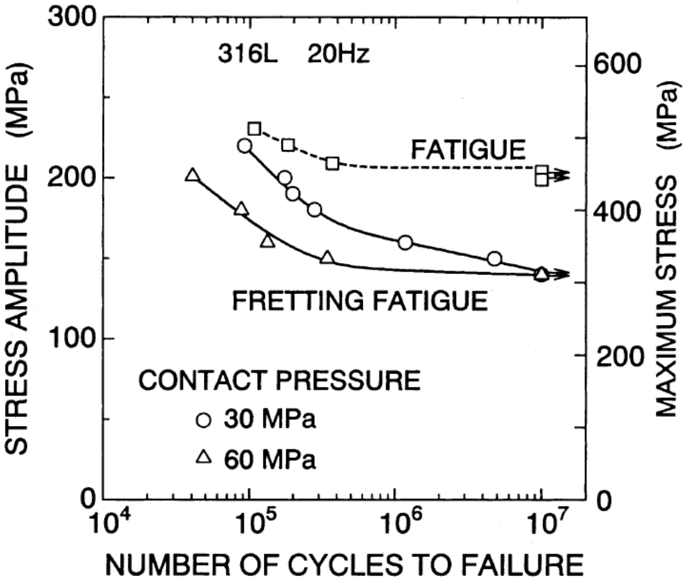

Figure 2.15: Influence of contact pressure on the fretting fatigue life of 316L [101].

In an investigation of the fretting wear of type 304 in a vacuum, Iwabuchi et al. [94] found the formation of cracks in the high slip portion of the mixed slip regime and at the lower slip portion of the gross slip regime. In the mixed slip regime a high number of small cracks were found to form. In the gross slip regime the cracks had linked so that fewer but larger cracks were present. Cracks were not created during tests in air with the same contact conditions. This was due to the oxide formation and the resulting increase in wear. The oxides formed during testing in air were removed easily from the surface, increasing the wear rate. This increased the contact conformity, which lowered the contact stress. The oxides also decreased the stress due to friction by acting as a lubricant. The beneficial effect of the oxide was also found in other studies [100, 102].

The composition of the iron oxide formed by type 304 during fretting has been found to be Fe_2O_3 at temperatures from 20°C to 300°C. Increasing temperature resulted in the formation of Fe_3O_4 as the dominant iron oxide. Temperatures above 700°C resulted in the formation of FeO as the dominant iron oxide. At higher temperatures, adhesion was promoted causing transfer of material between the contacting bodies.

The extent of material transfer between bodies in contact has been reported to be dependent on the frequency [100]. A chance in frequency from 1.2 Hz to 16.6 Hz was found to cause an increase in the material transfer by a factor of two. This may be a result of the temperature rise of the material due to frictional dissipation which can cause an increase in adhesion due to decreased hardness. Increasing temperature has also been found to cause the formation of a glaze oxide for type 304, which reduces friction and wear [31, 92, 102].

Several studies have been performed in corrosive fluids, including fretting of type 316 in pseudo body fluid [95-97] and type 304 in NaCl [98]. It was found that the NaCl reduced the wear rate of 304 as a result of lubrication and convective heat transfer. The cooling promoted transformation to hard martensite, which therefore reduced wear. The increased oxidation in NaCl reduced the COF by eliminating adhesion that was observed during sliding in air [98]. At lower loads, delamination was found to be the dominant wear mechanism.

The frequency of the fretting test also has an effect on the response. Increasing the frequency leaves less time for dissipation of heat generated from friction which raises the temperature at the contact. This is especially important for stainless steel because of its relatively low thermal conductivity (16.3 W/m-K) and the sensitivity of temperature on martensitic transformation. The frequency of fretting also affects the extent of oxidation during each cycle, thus affecting the friction and wear response.

Because the fatigue crack growth and wear behavior are quite sensitive to the hardness of the material, the fretting behavior is expected to be much different for the cold rolled condition compared to the annealed condition. Increased hardness typically improves the wear and high cycle fatigue properties but can be detrimental to low cycle fatigue behavior, which has been related to fretting crack formation [52].

2.4 Modeling Fretting Damage

There have been many studies seeking to model material damage that occurs through a variety processes. Material damage due to fretting is a complex process since both fatigue damage and wear occur simultaneously and have competing effects. The stress-strain response due to fretting is complex in that it is multiaxial, non-proportional, and has strong gradients that occur on the scale of the microstructure. Also, surface morphology due to wear alters the stress-strain response so that the cyclic response evolves with further cycling and causes the location of maximum fatigue damage to shift. Wear also can remove a volume of material which has accumulated fatigue damage, making wear an important aspect of a successful fretting fatigue damage metric. While most material damage parameters focus on either the fatigue or wear aspects that occur due to fretting, more recent work has addressed modeling the effects of combining these two damage mechanisms.

Different damage metrics are best suited for different conditions based on the dominant damage driver for a particular material (e.g. shear versus tensile crack formation, adhesive versus abrasive wear) and the damage mechanism active in the different fretting running conditions (e.g. wear is dominant in the gross slip regime). The following sections discuss the various parameters that are currently used for fretting damage analysis with respect to the conditions for which they are best suited.

2.4.1 Fatigue Modeling Methods

Multiaxial fatigue damage parameters can be categorized into five main types: modifications of the Coffin-Manson equation, application of stress or strain invariants, use of the space averages of stress or strain, critical plane approaches, and energy approaches [103-106]. Critical plane based multiaxial fatigue damage parameters, which are based on identification of the plane on which the maximum value of a certain combination of stress and strain occurs, have been used successfully as a metric of the extent and location of fatigue damage due to fretting in many studies, especially in partial slip conditions where the amount of wear is low [107-115]. It has been reported that the use of critical plane methods for evaluation of fatigue damage due to fretting tends to yield overly-conservative life predictions for rapidly varying contact stresses [106, 116-119], however this does not affect the ability of these parameters to be used as relative fatigue damage measures.

The parameter that provides the best prediction of the extent of fatigue damage is dependent on the dominant damage mechanism for the material of interest, e.g. annealed AISI 304 stainless steel has been reported to demonstrate shear crack formation and subsequent growth for lives less than 10^4 cycles when tested in torsion [86] annealed AISI 304 stainless steel has been reported to demonstrate shear crack formation and subsequent growth for lives less than 10^4 cycles when tested in torsion [86] thus indicating that a fatigue damage parameter based on shear driven formation would be most promising.

The Fatemi-Socie (FS) [120] and Smith-Watson-Topper (SWT) [121] parameters are two of the most commonly used fatigue indicator parameters due to their long history of use and ease of implementation. The FS parameter is based on the principle that fatigue damage is driven by the combination of the shear strain range and the maximum normal stress on the same plane during a cycle so that the fatigue life is related to the maximum value of that combination for all planes,

$$\left(\frac{\Delta\gamma}{2}\left[1+k\frac{\sigma_n^{\max}}{\sigma_y}\right]\right)_{\max} = f\left(N_f\right) \tag{2.1}$$

where $\Delta\gamma$ is the shear strain range, $\sigma_n^{\max}$ is the maximum normal stress on the same plane during a cycle, σ_y is the yield strength, k is a constant that approaches unity for long lives [122], and $f(N)$ is a function of life which is inversely related to the magnitude of the parameter. Thus, the parameter serves as a relative measure of the severity of fatigue damage and indicates the orientation of the plane on which crack formation and growth is most likely to occur.

The SWT parameter is evaluated similarly, but is based on fatigue damage being driven by the normal strain amplitude and maximum stress on the same plane over a cycle so that the fatigue life is related to the maximum value of their product for all orientations,

$$\left(\frac{\Delta\varepsilon}{2}\sigma_{\max}\right)_{\max} = f\left(N_f\right) \tag{2.2}$$

where $\Delta\varepsilon$ is the normal strain range and $\sigma_{\max}$ is the maximum stress normal to the same plane. The SWT parameter has been used extensively for fretting of Ti-6Al-4V analysis with success [107-110, 114, 119, 123-124]. It has been reported to provide reasonably accurate crack formation life predictions for relatively mild stress gradients [125]. The exact expression for $f(N_f)$ has not been established for AISI 301 stainless steel in the full hard condition, thus these parameters can provide only a relative indication of fatigue damage.

The McDiarmid parameter is another popular critical plane multiaxial fatigue parameter [126-129]. The McDiarmid parameter is based only on the local cyclic stress state in the material rather than a combination of stress and strain as for the SWT and FS parameters. It operates on the premise that crack formation is controlled by the shear stress, and is given by

$$\left(\tau_a\left(1-\frac{\sigma_{\max}}{2\sigma_u}\right)^{-1}\right)_{\max} = f\left(N_f\right) \tag{2.3}$$

where τ_a is the shear stress amplitude on a plane, $\sigma_{\max}$ is the maximum normal stress perpendicular to the same plane, and σ_u is the ultimate strength of the material. The McDiarmid parameter has been used successfully for analysis of fretting fatigue in several studies [113, 119], however it has also been found to correlate poorly with uniaxial fatigue of Ti-6Al-4V, and was found to correlate well with moderate scatter to biaxial fatigue in the same study [130].

The Findley parameter [131] is similar to the McDiarmid parameter in that it is based on fatigue crack formation being governed by the shear stress and does not contain a dependence on the cyclic strain response. The Findley parameter is given by

$$\left(\tau_a + k\sigma_{\max}\right)_{\max} = f\left(N_f\right) \tag{2.4}$$

where τ_a is the shear stress amplitude on a plane, $\sigma_{\max}$ is the maximum normal stress perpendicular to the same plane, and k is a material constant. The Findley parameter has been found to correlate well with both uniaxial and biaxial fatigue of Ti-6Al-4V [130], and has been used successfully for high cycle multiaxial fatigue analysis of Nickel base superalloys [128].

The Dang Van parameter [132-133] is a mesoscopic approach to multiaxial fatigue analysis [106]. Modifications to this parameter have been made by Papadopoulos [134-136]. This parameter is based on an average measure of the accumulated plastic strain within crystals experiencing slip within a critical volume of material, or equivalently the average resolved shear stress amplitude, combined with a measure of the hydrostatic stress which would act to grow embryo cracks present within the critical volume [127]. The parameter is given by

$$\sqrt{\left\langle \tau_a^2 \right\rangle} + \alpha\sigma_{H,\max} = f\left(N_f\right) \tag{2.5}$$

where the first term represents the volumetric root mean square of the resolved shear stress amplitude, given by

$$\sqrt{\frac{5}{8\pi^2}\int_{\varphi=0}^{2\pi}\int_{\theta=0}^{\pi}\int_{\chi=0}^{2\pi}\left(\tau_a\left(\varphi,\theta,\chi\right)\right)^2 d\chi \sin\theta d\theta d\varphi} \quad (2.6)$$

where $\sigma_{H,\max}$ is the maximum hydrostatic stress, α is a material constant, and χ describes the gliding direction on the plane described by θ and φ within the critical volume.

The Dang Van parameter has been used successfully for analysis of fatigue damage due to fretting [106, 117, 119, 137-139]. The Dang Van parameter is based on the cyclic deviatoric stress and the hydrostatic stress state over a critical volume. Volume averaging is necessary when using the Dang Van parameter, however the appropriate volume size is not necessarily intuitive [106], and essentially becomes a fitting parameter based on the microstructure [117]. The Dang Van parameter is less practical to evaluate than the other fatigue damage parameters discussed here due to the material dependent parameters and the need for volume averaging.

The Crossland parameter [140] is similar to the Dang Van parameter in that it is also a stress-invariant mesoscopic multiaxial fatigue damage metric that is based on the cyclic deviatoric stress and hydrostatic stress state. The Crossland parameter has been the preferred multiaxial fatigue crack nucleation criterion in several recent important studies involving AISI 1034 steel [141-142]. However, the Crossland parameter also has shortcomings similar to the Dang Van parameter since it also requires the added complexity of material dependent volume averaging.

2.4.2 Wear Modeling Methods

The wear behavior during fretting has a large effect on the extent of fatigue damage that occurs [34, 36, 38-43, 143-145]. It is therefore important to account for the effect of wear in simulations of fatigue damage due to fretting when the amount of wear is significant, i.e. in cases involving soft materials, corrosive environments, and large slip amplitudes combined with high normal forces.

Ideally, wear would be modeled explicitly so that the effect of altering the contact profile on the cyclic stress-strain behavior is captured. The most commonly used method for explicit fretting wear modeling involves using an Archard Wear Law [146] to relate the dissipated energy to the wear rate, and incrementally modify the contact geometry with the necessary mesh modification. Implementation is complex and the wear model for fretting has yet to be proposed, since the Archard Wear Law does not account for the wear effects specific to fretting such as debris entrapment [147]. This limits the applicability of explicit fretting wear modeling while being computationally expensive.

Due to the impracticality of the current methods for explicit fretting modeling, fretting wear parameters have been proposed which account for the effects of wear using contact parameters without modeling wear directly. The extent of wear for a particular environment and contact pair is related to the amount of energy dissipated due to friction [146]. Many fatigue damage models are also driven by dissipated energy since cyclic plasticity results in energy dissipation [148-154]. Fretting fatigue damage metrics specific to fretting therefore incorporate a measure of the energy dissipated by friction in the contact to account for wear or as a fatigue damage mechanism.

The Fretting Damage Parameter (FDP) was developed by Ruiz et al. [50] and bases the extent of fretting damage on the amount of frictional energy dissipation. The FDP is given by

$$\tau_{fric} \cdot \delta = f\left(N_f\right) \tag{2.7}$$

where τ_{fric} is the contact shear stress at the interface, and δ is the relative slip during a cycle. This parameter is overly simplified since it is a path-independent average over the whole contact interface and does not account for fatigue damage due to cyclic stresses or strains. It was recognized that a more accurate local representation of the energy dissipated due to fretting is the integral over a cycle of the product of the local shear stress and local infinitesimal slip, therefore being a path-dependent local measure [155]. Represented in numerical form, the Ruiz parameter is therefore more appropriately given by

$$\left(\sum_{i=1}^{n} \tau_i \delta_i\right)_{\max} = f\left(N_f\right) \tag{2.8}$$

where τ_i is the average shear stress on a node during increment *i*, and δ_i is the slip magnitude at the same node during the same increment. The node that experiences the maximum value of this combination will experience the most fretting damage, with the value of the parameter being inversely related to the fatigue life or proportionally related to the extent of wear. The FDP has been used successfully in a number of studies, with the most success occurring in situations where there are no stresses in the body other than those generated by contact [49-50, 110]. However, the FDP as a fretting fatigue damage metric predicts a higher level of fatigue damage as the displacement amplitude increases, which is inconsistent with the expected result of decreasing fatigue damage as the running condition becomes gross slip [34]. The FDP is therefore best suited as a fretting wear metric.

2.4.3 Combined Fretting Damage Modeling Methods

It was recognized that the amount of fatigue damage that occurs in a specimen subjected to fretting increased due to an externally applied cyclic load and that the FDP did not account for this observation. Ruiz and Chen therefore proposed the Fretting Fatigue Damage Parameter (FFDP) [51], which is given by

$$\sigma_{\tan} \cdot \tau_{fric} \cdot \delta = f\left(N_f\right) \tag{2.9}$$

where $\sigma_{\tan}$ is the maximum tensile stress in the direction of fretting motion, τ_{fric} is the shear stress due to friction at the interface, and δ is the relative slip during a cycle. Similar to the FDP, the FFDP is also often used in a modified form that more accurately reflects the amount of energy dissipated [111, 155], represented numerically as

$$\left(\sigma_T^{\max} \sum_{i=1}^{n} \tau_i \delta_i\right)_{\max} = f\left(N_f\right) \tag{2.10}$$

where τ_i is the average shear stress on a node during increment i, and δ_i is the slip displacement at the same node during the same increment, and $\sigma_T{}^{\max}$ is the maximum normal stress parallel to the surface that occurs during a cycle at the same node. The addition of the maximum normal stress parallel to the contact surface helps to account for the effect of the plain fatigue load during a fretting fatigue test. The Ruiz FFDP has been found to indicate the location of fatigue crack formation well in many studies [48, 51-52, 110, 112, 156], however not all studies found the parameter to be accurate for determination of fatigue life. The simplicity of the FFDP is its main strength since it can be more readily computed compared to other parameters which combine energy dissipation with consideration of additional fatigue loading.

Ding et al. [110, 157] recently proposed a modified SWT parameter that considers the combined effects of frictional energy dissipation and the cyclic stress state to determine the level of fatigue damage. The modified SWT parameter accounts for the cyclic stress state more thoroughly than the FFDP by using the SWT critical plane based multiaxial fatigue damage parameter in conjunction with a dissipated energy measure rather than simply the tangential tensile stress. The parameter is based on crack formation being driven by energy dissipation to account for cyclic plastic energy dissipation such as plastic ratcheting or plastic shakedown in the near surface region [158] and subsequent crack growth being driven by the combination of stress and strain. However, high energy dissipation results in a high wear rate which tends to increase the fatigue life of a component by increasing contact conformity which lowers contact stresses due to the increased contact area [40, 42-43] and due to the wearing away of the surface material which was subjected to the highest level of fatigue damage [38-41]. Therefore, the modified SWT parameter incorporates a threshold energy dissipation term, where the extent of fatigue damage incurred increases with dissipated energy and then decreases as the dissipated energy approaches the threshold value. In the case where the dissipated energy is greater than or equal to the threshold value the parameter indicates zero fatigue damage. The FFDP does not make this distinction, and therefore provides an inaccurate indication of the level of fatigue damage as the dissipated energy becomes large. The modified SWT parameter is given by

$$\left(\sigma_{\max}\varepsilon_a D_{fret2}\right)_{\max} = f\left(N_f\right) \tag{2.11}$$

where $\sigma_{\max}$ is the maximum normal stress on a plane, ε_a is the strain amplitude normal to the same plane, τ is the shear stress from friction, δ is the slip amplitude, and D_{fret2} is given by

$$D_{fret2} = \left(1 + C\tau\delta\right)\left\langle 1 - \frac{\tau\delta}{\left(\tau\delta\right)_{th}} \right\rangle^{n} \tag{2.12}$$

where C and n are empirical constants that are dependent on the wear and fatigue properties of the material, $\tau\delta$ is the dissipated energy, and $(\tau\delta)_{th}$ is the empirical threshold dissipated energy that defines the transition to infinite life at high energy dissipation levels.

The modified SWT parameter has been used for analysis of three sets of experiments, and was found to be successful in each: a CrMoV spline coupling [110, 158], a Ti-6Al-4V half cylinder on flat fretting fatigue arrangement [159], and a Al4%Cu (HE15-TF) half cylinder on flat fretting fatigue arrangement [116]. The three empirical constants in the modified SWT enhance the ability of the modified SWT to provide successful predictions in a variety of conditions, but determination of the values of the constants adds complexity to the evaluation of the parameter. Computation of the modified SWT is only slightly more difficult than the FFDP once the constants are determined, but the modified SWT is significantly more accurate for all running conditions since indication of fatigue damage is based on the use of the SWT parameter rather than merely the axial stress in the direction of fretting motion and since a very high dissipated energy does not falsely indicate a high level of fatigue damage as would the FFDP. These traits suggest that the modified SWT parameter is a good candidate for evaluation to determine the extent of fatigue damage due to fretting for all running conditions.

Vidner and Leidich recently proposed another energy based fretting fatigue damage parameter that incorporates a critical-plane based fatigue damage metric which is referred to as the enhanced Fatigue-Fretting Damage Parameter (eFFDP) [111]. The eFFDP accounts for the modes of energy dissipation in a more physically based manner than the empirical method used for the modified SWT parameter. The measured dissipation is divided into categories based on the method of dissipation [160]: a mechanical component (deformation and wear), a thermal component (heat), a chemical component (tribo-oxidation [161]), and other tribo-physical components (e.g. sound [162]). Only a portion of the total frictional energy causes fretting damage to the specimen, which is referred to as the effective frictional energy. The effective frictional energy is divided between the two bodies in contact. The effective damaging energy for the body of interest is therefore given by

$$W_{eff}^{*} = \frac{k_{dam}}{1+\alpha_{CP}} W_{fric}^{*} \tag{2.13}$$

where k_{dam} is the fraction of the total frictional energy that goes toward material damage, α_{CP} is the ratio of the frictional energy that goes toward the contacting body to the frictional energy that goes toward the body of interest, and W^{*}_{fric} is the total frictional work. The eFFDP is given by

$$\frac{W^{*}_{eff}}{T_{LC}} SWT = f\left(N_f\right) \qquad \text{or} \qquad \frac{W^{*}_{eff}}{T_{LC}} FS = f\left(N_f\right) \tag{2.14}$$

where T_{LC} is the period of the load cycle. The damage is therefore rate dependent, which is important to account for in corrosive environments, and the parameters $\mathrm{k}_{\mathrm{dam}}$ and α_{CP} are dependent on the materials and geometry.

The eFFDP is an improvement on the FFDP because of the addition of the multiaxial fatigue parameter, however it does not capture the breakdown of the proportionality between the frictional dissipated energy and the fatigue damage for gross slip running conditions. The modified SWT parameter therefore more accurately captures the fatigue damage behavior with a similar level of implementation difficulty, and will therefore provide the more robust fatigue damage prediction.

2.4.4 Summary and Conclusion

Of the currently available methods for analysis of fretting fatigue damage, the modified SWT parameter is the only method capable of producing a result which is consistent with the classic result of Vingsbo and Soderberg where the minimum fretting fatigue life occurs at intermediate displacement amplitudes. The critical plane based methods do not account for wear, thus they do not capture the beneficial effects of wear observed in high wear cases. The wear based methods do not capture the effects of a superimposed fatigue load. The eFFDP combines the effects of fatigue and wear through the combination of a critical plane based fatigue damage metric and an energy dissipation measure, however it also does not capture the observed result of minimum fretting fatigue life at intermediate levels of wear. The strong point of the eFFDP is the physical basis of the wear metric, which accounts for the various means of energy dissipation as whether there is a contribution to damage for each dissipation method. The lack of physical basis is the weakness of the mSWT parameter. The mSWT parameter is narrow in its range of applicability because of this. Therefore, the goal of this work is to develop a parameter which is capable of capturing a wide range of observed fretting fatigue damage responses by representing effects of the physical processes occurring in the interaction.

CHAPTER 3

STRUCTURE AND PROPERTIES OF 301 STAINLESS STEEL

The structure and mechanical properties of the materials in contact influence the damage response and are important to consider during analysis of the fretting behavior. Identification of aspects of the material behavior such as change in ductility with changing temperature provides insight into the causes of changes in the fretting damage response. The temperature sensitivity of austenitic stainless steel increases the importance of including the change in mechanical properties with temperature. Data on the tensile and fatigue behavior of thin sheets of 301 stainless steel in the full hard condition is not available in the open literature despite being a commonly used material.

Tensile tests were performed using 301 stainless steel as a function of temperature and strain rate to determine the changes in deformation behavior with changing temperature. The modulus of 52100 steel and 304 stainless steel was determined for use in finite element modeling. Fatigue tests were performed using 301 stainless steel at room temperature and 250^{o}C to determine the change in fatigue response with changing temperature. Samples of 301 stainless steel were etched after exposure to various temperatures to reveal the phase composition.

3.1 Tensile Testing

The mechanical properties of the materials in contact influence the damage response and need to be accounted for during analysis of the fretting behavior. The temperature and strain rate sensitivity of austenitic stainless steel increases the importance of including the change in mechanical properties with temperature in analysis of the fretting damage response. Therefore, tensile tests were performed on 301 stainless steel as a function of temperature and strain rate, and the modulii of 52100 steel and 304 steel were determined as a function of temperature for use in FEA.

3.1.1 Procedure

Specimens of 301 stainless steel in the full hard condition were fabricated to have the dimensions shown in Figure 3.1. The faces of the specimens were left in the as-rolled condition, with values of the average and maximum roughness of 0.10 µm and 0.78 µm respectively. Specimens were machined using conventional milling with the final 0.1 mm removed from each edge with material removal rates of no more than 0.02 mm per pass.and the final polished longitudinally with SiC paper to a maximum surface roughness R_y of 0.2 µm.

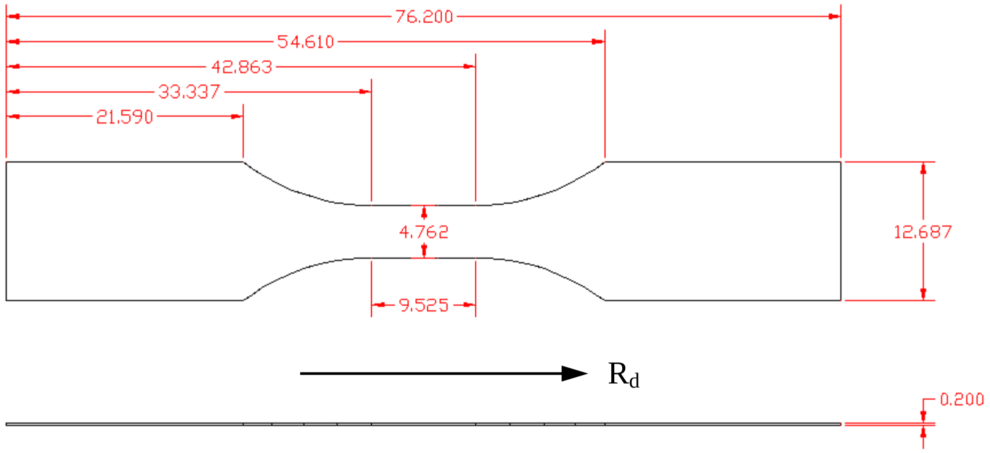

Figure 3.1: Dog-bone specimen with an arrow indicating the rolling direction, R_d, with dimensions in millimeters.

Tests were performed using a 44.5 KN (10 kip) axial servo-hydraulic MTS test machine with water cooled collet grips (MTS model 646). A 9 KN force calibration was used and was found to provide sufficient resolution for the forces used. The system uses a dual channel TestStar II controller with Testware SX 4.0D software. A flow chart of system signals is shown in Figure 3.2.

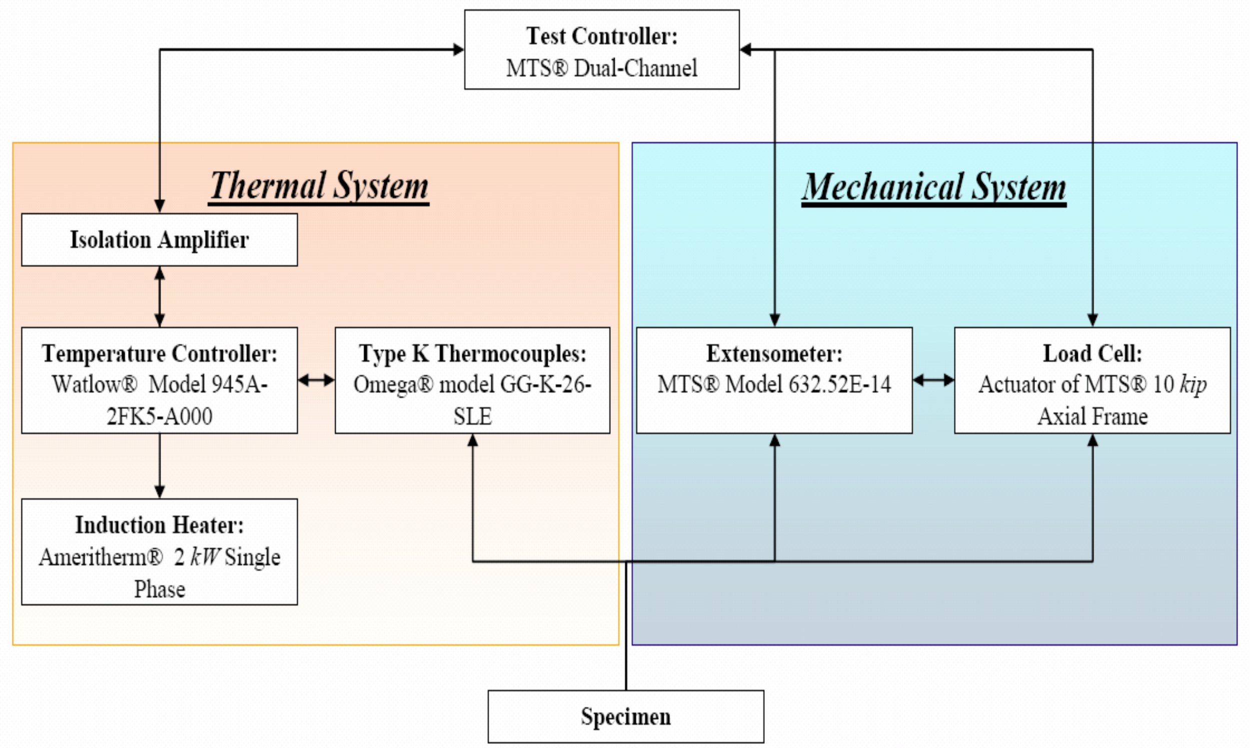

Figure 3.2: Signal flow diagram of test system [163].

Induction heating was used to heat the dog-bone specimens during testing. An Ameritherm 2 kW single-phase radio-frequency induction heater was used, with temperature continuously controlled using a Watlow closed-loop PID controller with feedback from a K type thermocouple attached to the specimen. The temperature control setpoint was specified from MTS Testware SX 4.0D software, which also recorded the temperature, force, strain, and displacement throughout the tests.

An induction coil was fabricated using copper tubing with an outer diameter of 3.2 mm (1/8 inch). The coil consists of two windings with clearance for extensometer rods. Water was circulated through the coil to prevent the coil from overheating. The large surface area to volume ratio of the thin specimens resulted in a low induced power relative to the rate of cooling of the specimen. Susceptors were used to increase the power transferred from the heater to the specimen. The susceptors were heated by the induction coil, and their proximity to the specimen heated the specimen by radiant and convective heat transfer. The susceptors were fabricated from Inconel 625 and were designed with clearance for thermocouples and to accommodate extensometer rods with V chisel tips as well as to be integral with the gripping method. The assembly of the grip adapters, susceptors, and specimen is shown in Figure 3.3a. The heated assembly with the extensometer attached after a tensile test was completed is shown in Figure 3.3b.

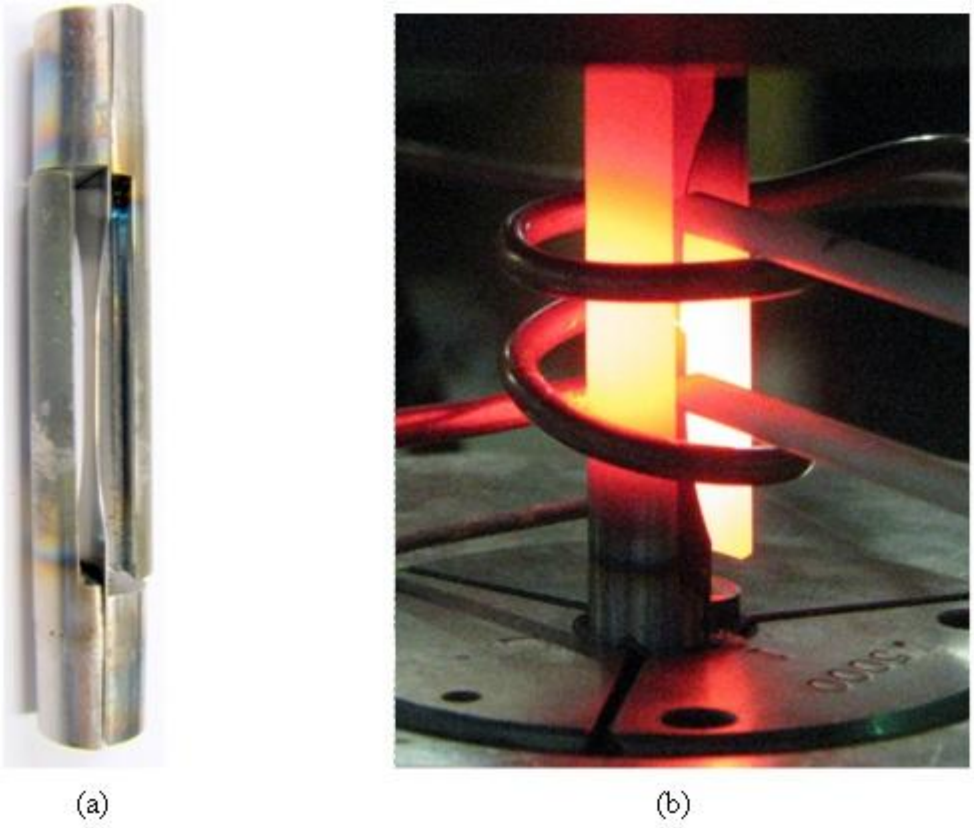

Figure 3.3: (a) Specimen, susceptor, grip adapter assembly, and (b) the assembly being tested.

The temperature distribution was determined by welding four thermocouples along the length of the specimen in the locations shown in Figure 3.4a. The resulting temperature distribution in terms of deviation from the target temperature in degrees Celsius is shown in Figure 3.4b. The temperature differences are within 2% degrees Kelvin of the target temperature except for the cases of 200^{o}C and 250^{o}C, which had maximum deviations of 2.3% and 3.4%, respectively. The same procedure was repeated for temperatures of 700^{o}C and 800^{o}C. The maximum temperature deviation was less than 2% in degrees Kelvin, which corresponds to 21.5^{o}C for 800^{o}C. The measured modulus is a representation of the average response between the extensometer rod contact points, thus providing an accurate measurement at the average temperature which is nearly equal to the target temperature. The elongation to failure measured here represents a lower bound value since deformation will be localized at the location of maximum temperature. This is not expected to be a significant effect, and the trends determined are accurate which is the more critical result for subsequent analysis.

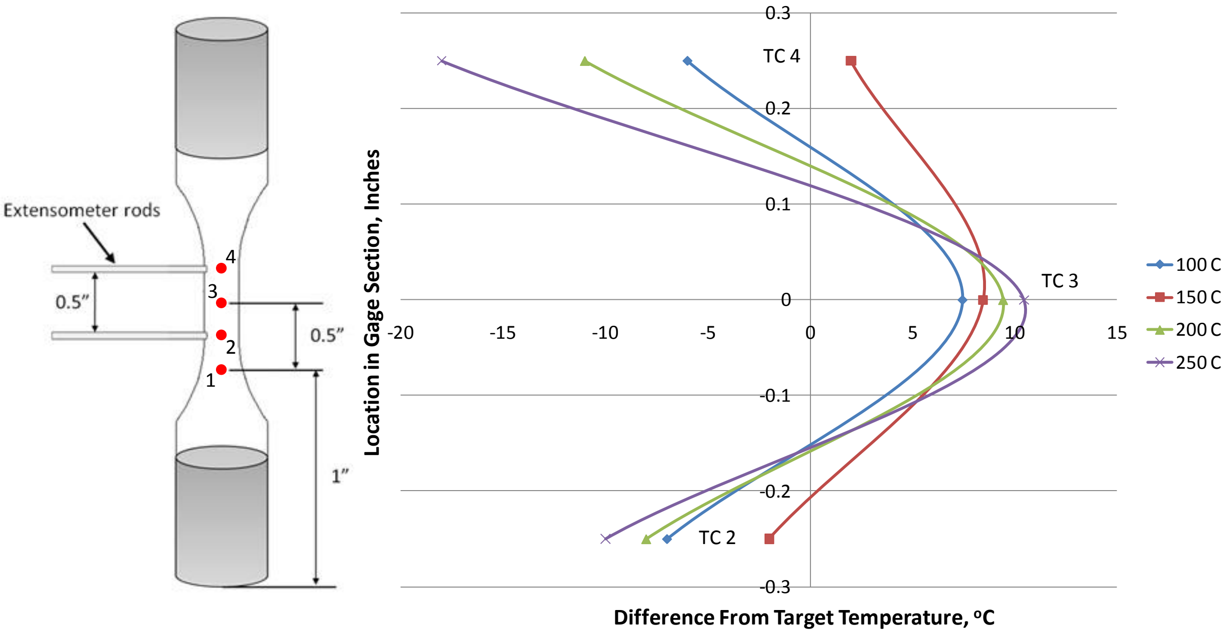

(a) (b)

Figure 3.4: (a) Thermocouple placement during temperature profile determination and (b) resulting temperature distribution in terms of degrees Celsius deviation from the target temperature for each target temperature.

Previous tensile tests performed with specimens having thermocouples welded in the center of the specimen failed at the thermocouple location with significantly fewer visible Luders bands than were present in the absence of thermocouples, thus showing that the thermocouple had a significant effect on the behavior. Therefore, tests were performed with one thermocouple at location one shown in Figure 3.4a. The additional cross-sectional area at location one ensured that specimen failure would not take place at the thermocouple. The temperature was controlled at that location and was set to the temperature measured at that location during the temperature distribution measurements for each target temperature. Using this relationship ensured that the proper gage section temperature was maintained without influencing the deformation behavior by having a thermocouple within the gage section.

Specimens tested at elevated temperature were heated to test temperature using a two minute ramp followed by a two minute hold to allow the temperature to stabilize. The axial force during heating and stabilization was maintained at zero to allow for free expansion.

Tests were performed in displacement control with constant displacement rates. The three displacement rates used resulted in plastic strain rates approximately equal to 10^{-4}, $10^{-2.5}$, and 10^{-1} s^{-1}. The plastic strain rates were approximately constant since the material response was very nearly elastic-perfectly plastic, thus the deformation in the test system was approximately zero during plastic deformation of the sample. The conditions tested are shown in Table 3.1.

Table 3.1: Tensile test conditions.

	Temperature, ^{o}C									
Strain Rate, s^{-1}	20	100	150	200	250	400	450	550	700	800
10^{-1}	X	X	X	X	X					
$10^{-2.5}$	X				X	X	X	X	X	X
10^{-4}	X	X	X	X	X					

The effects of aging on the tensile properties of 301 stainless steel were investigated to determine the sensitivity to thermal history. Specimens were aged in a tube furnace in laboratory air at the temperatures and durations shown in Table 3.2. Tensile tests were then performed on the aged specimens at room temperature to evaluate their tensile properties.

Table 3.2: Exposure times and temperatures imposed prior to room temperature tensile testing.

Exposure Time	**Exposure Temperature, °C**				
	250	400	550	700	1100
1 min					X
1 h			X	X	
10 h	X		X	X	
100 h	X	X	X	X	
1000 h	X				

Two tensile tests were performed at 250°C in order to verify repeatability of the results. The resulting stress-strain curves are shown in Figure 3.5. The two tests demonstrated nearly identical modulii, yield strengths, and strains to failure, with a difference in ultimate strength of 3%. Duplicates of other tests were not performed due to the low variability of the results.

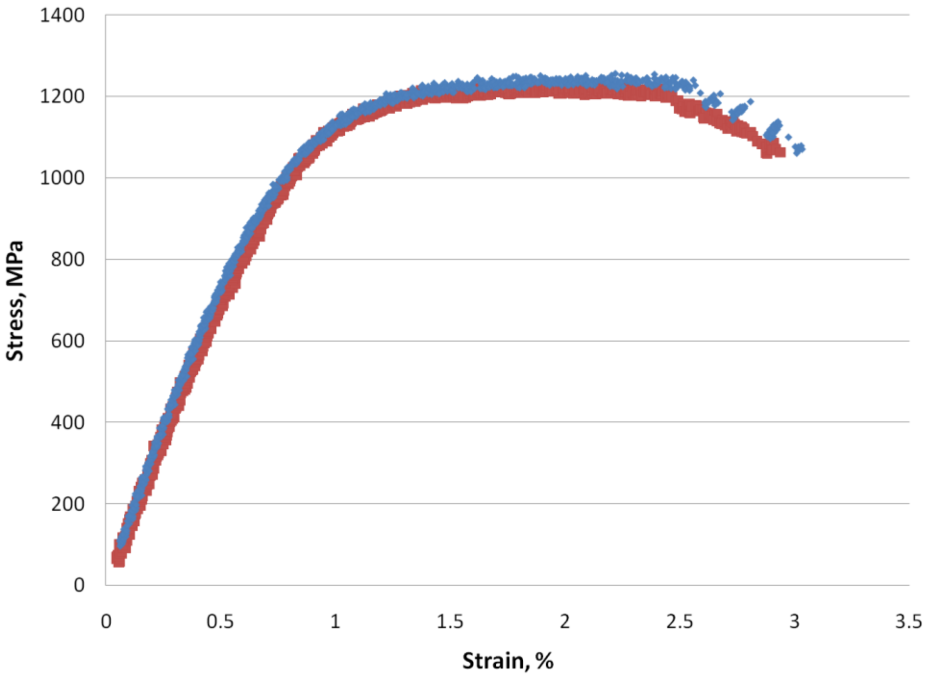

Figure 3.5: Monotonic stress-strain response repeatability comparison for 301 stainless steel at 250°C.

The modulus of 304 stainless steel and 52100 steel were determined as a function of temperature for use in finite element analysis. Samples were cylindrical dog-bone specimens with a gage section length of 13.2 mm and a diameter of 6.35 mm (0.25 inches). The temperature distribution was determined using five thermocouples along the gage section length, and was found to be within 2% of the target temperature in degrees Kelvin. Tests were conducted using a single thermocouple welded to the center of the gage section as the control thermocouple. The modulus was determined by imposing three fully reversed cycles in force control with a force of approximately half of the force to cause yielding. This was performed at several temperatures using a single specimen starting at room temperature and increasing to a maximum temperature of 550°C.

3.1.2 Low Temperature Strain-Rate Sensitivity

The material properties measured for each condition tested are shown in Table 3.3. Yield strengths were determined using the 0.2% offset method. The stress-strain response at room temperature shown in Figure 3.6. The elongation to failure decreased by 50% when increasing the strain rate from $10^{-2.5}$ to10^{-1} s^{-1}. There was no effect on the modulus, and the yield strength increased by only a nearly negligible amount of 2.3% from 10^{-4} to $10^{-2.5}$ s^{-1} and by another 2.3% from $10^{-2.5}$ to 10^{-1} s^{-1}. The UTS for the three rates was similar, but with the UTS occurring at a low strain for the high rate case since most of the hardening that occurred in the lower rate tests occurred above the failure strain of the high rate case. The reduced ductility at the higher rate is attributed to the reduced time for heat generated by plastic deformation to dissipate, which causes the temperature of the specimen to increase since the process approaches an adiabatic condition as the strain rate approaches infinity [78, 164]. The increase in temperature decreases the likelihood of the martensite formation which is the primary hardening mechanism of austenitic stainless steel [165]. The high ductility of austenitic stainless steel is due to the hardening by martensite formation which reduces strain localization and thus ductility is reduced when martensite formation is reduced [83].

Table 3.3: Conditions of tensile tests conducted and resulting properties.

Strain Rate s^{-1}	Temp ^{o}C	Modulus Gpa	Yield Strength Mpa	Ultimate Strength Mpa	Elongation %
10^{-4}	20	169	1300	1500	27.0
10^{-4}	100	166	1200	1380	7.4
10^{-4}	150	157	1125	1300	3.4
10^{-4}	200	139	1130	1270	3.6
10^{-4}	250	138	1070	1220	4.6
10^{-4}	20	151	1380	1485	22.1
10^{-4}	100	155	1330	1400	5.0
10^{-4}	250	135	1070	1240	2.9
$10^{-2.5}$	20	162	1330	1450	30.7
10^{-1}	20	167	1360	1480	15.0
10^{-1}	100	159	1250	1400	5.4
10^{-1}	150	168	1170	1340	3.2
10^{-1}	200	154	1100	1270	2.9
10^{-1}	250	142	1100	1230	2.8

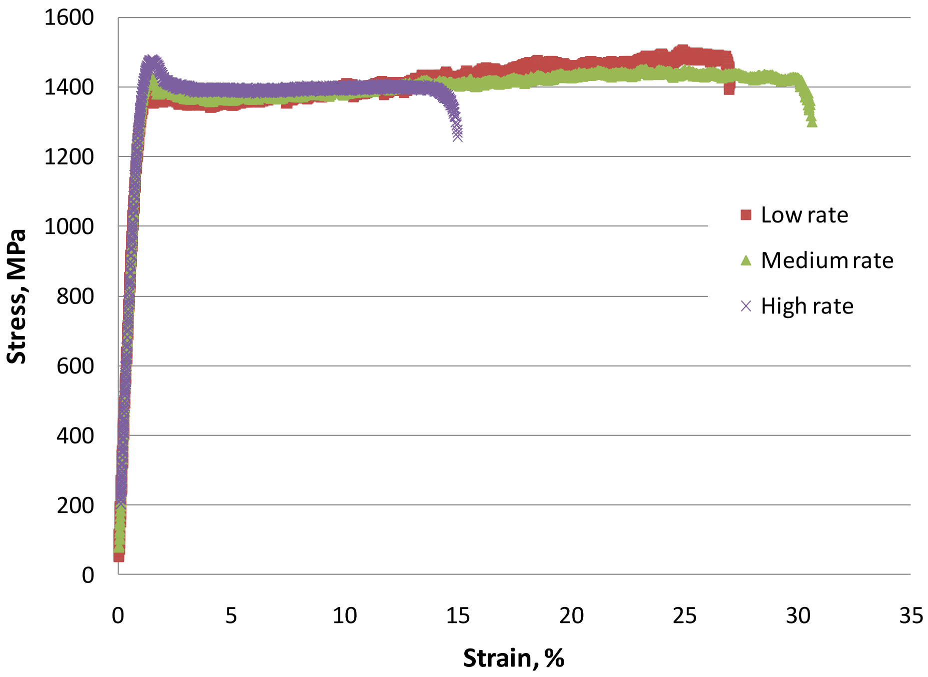

Figure 3.6: Stress-strain response at room temperature and strain rates of 10^{-4}, $10^{-2.5}$, and 10^{-1} s^{-1}.

A summary of the effect of strain rate on the tensile properties as a function of temperature is shown in Figure 3.7. The values shown are the properties at a strain rate of 10^{-1} s^{-1} as a percent of the values at a 10^{-4} s^{-1} strain rate. Little variation was found in any of the properties other than elongation to failure. The variation of yield strength and ultimate strength are within 5% and is considered negligible. The variation in modulus is inherently larger due to the added error associated with the calculation being a derived quantity involving measurements from two sensors which have individual error, and so this variation is also considered negligible. The elongation to failure showed a drastic decrease at most temperatures with a maximum reduction of 45% at room temperature. The maximum reduction in elongation occurring at the lowest temperature investigated is attributed to the temperature rise due to plastic deformation being more significant relative to the ambient temperature since the rate of heat transfer from the specimen was lowest. The increase in relative reduction of elongation as the temperature is increased beyond 150°C is more sensitive to noise since the elongation decreased drastically in both cases relative to room temperature.

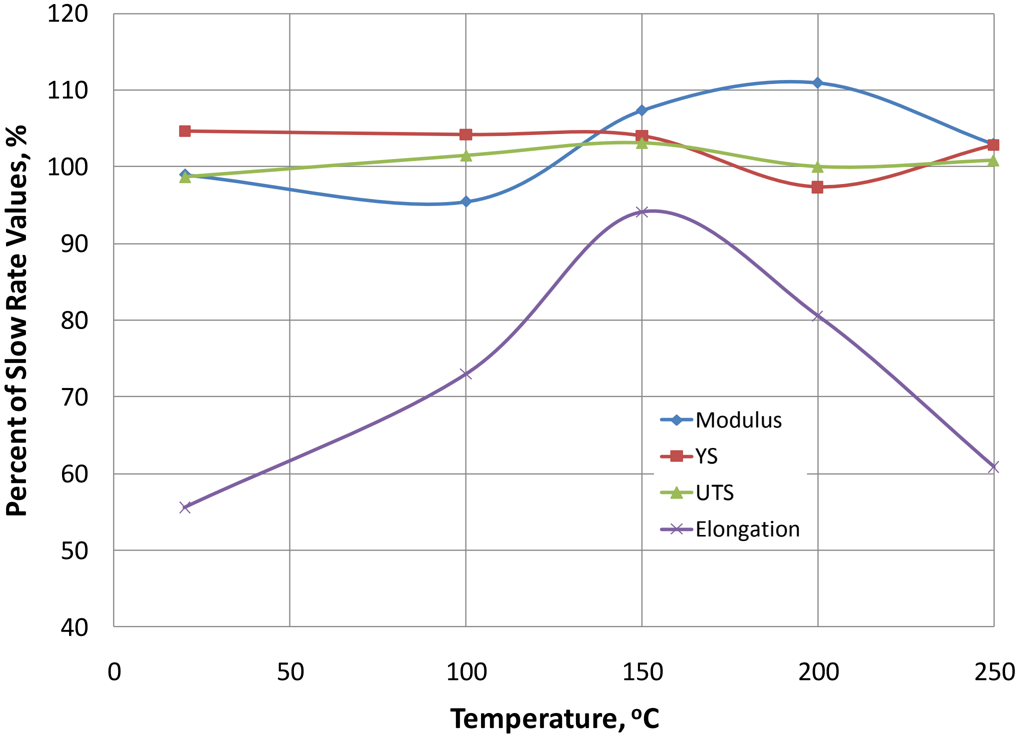

Figure 3.7: Properties obtained from tests conducted at a strain rate of 10^{-1} s^{-1} as a percent of the properties obtained at the slow rate of 10^{-4} s^{-1} as a function of temperature.

The influence of temperature on the stress-strain response for a strain rate of 10^{-4} s^{-1} is shown in Figure 3.8. A summary of the tensile properties as a function of temperature in terms of percent of the room temperature values for the tests using a strain rate of 10^{-4} s^{-1} is shown in Figure 3.9. There is a steady decrease in elastic modulus, yield strength, and ultimate strength as the temperature is increased to 250°C at which point all three values are approximately 82% of their room temperature values. The elongation to failure was reduced drastically at all temperatures above room temperature. The maximum reduction in elongation was 87% at a temperature of 150°C. The reduction in elongation remained similar to that of at 150°C as temperature increased to 250°C. Similar to the reduction of elongation due to increased strain rate, the decrease in elongation to failure with increasing temperature is attributed to the increase in austenite stability, which reduces the extent of material hardening due to transformation to martensite and therefore increases strain localization. Strain localization is also promoted by the temperature gradient in the specimen, however this effect is expected to be low relative to the effect of austenite stability.

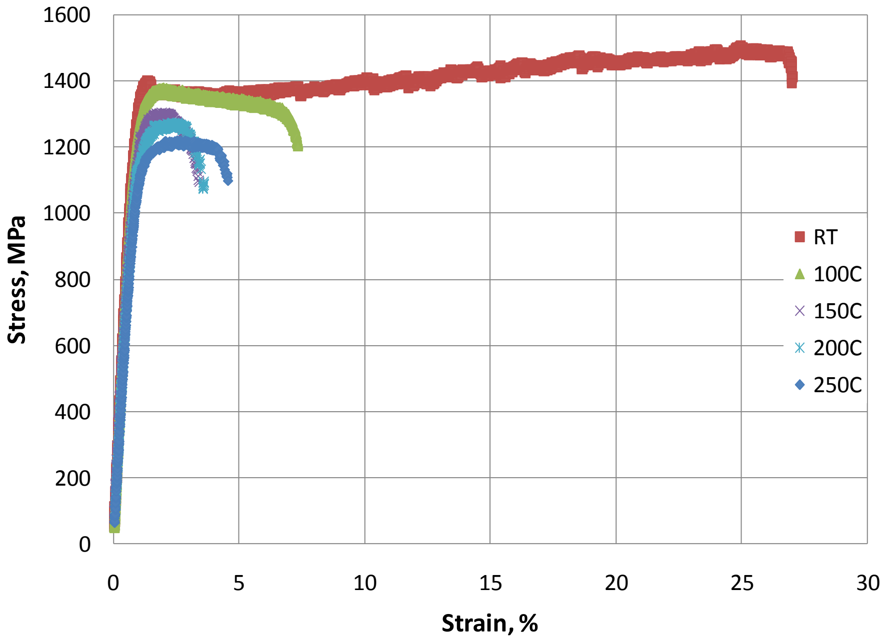

Figure 3.8: Stress-strain response for tests conducted at a strain rate of 10^{-4} s^{-1}.

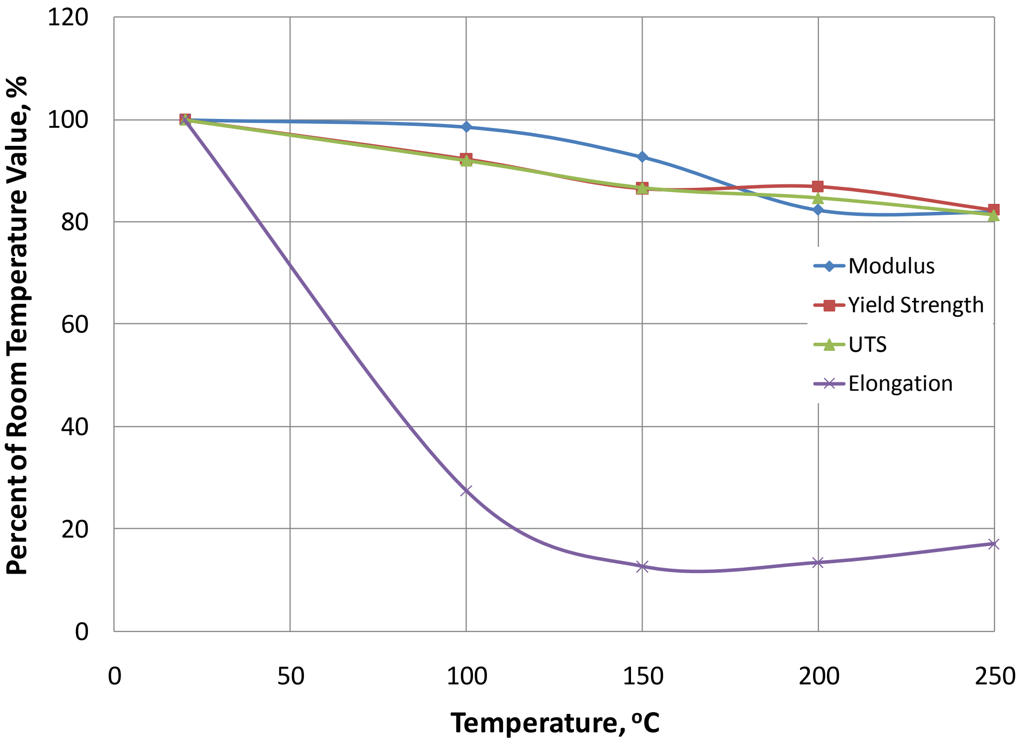

Figure 3.9: Tensile properties for tests conducted at a strain rate of 10^{-4} s^{-1} in terms of percent of room temperature values as a function of temperature.

The influence of temperature on the stress-strain response for a strain rate of 10^{-1} s^{-1} is shown in Figure 3.10. A summary of the tensile properties for tests conducted using a strain rate of 10^{-1} s^{-1} in terms of percent of the room temperature values as a function of temperature is shown in Figure 3.11. As with the tests completed at the low strain rate, there was a decrease in elastic modulus, yield strength, and ultimate strength as the temperature was increased to 250^{o}C at which point all three values were approximately 83% of their room temperature values. The elongation to failure was again reduced drastically at all temperatures above room temperature. The maximum reduction in elongation relative to room temperature was 81% at 250^{o}C.

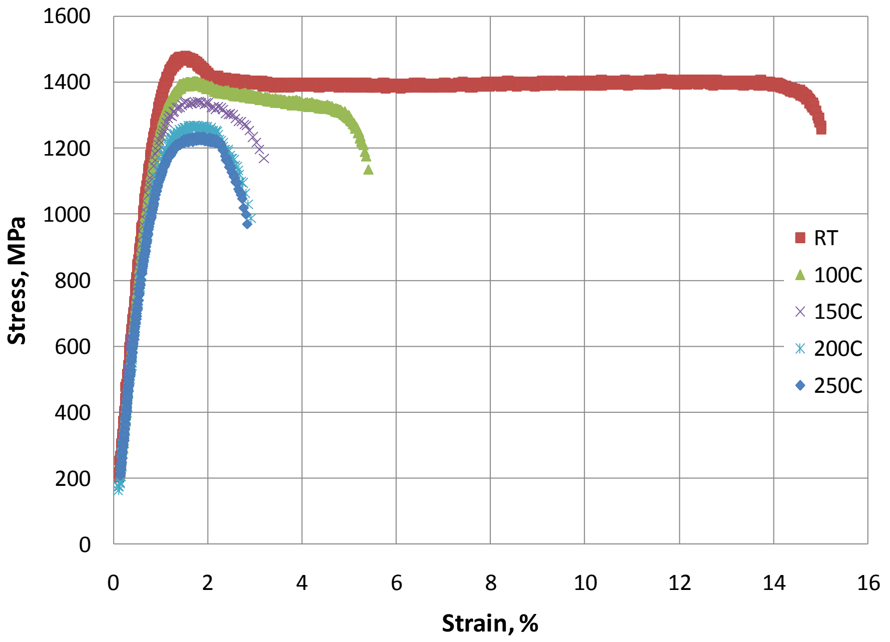

Figure 3.10: Stress-strain response for tests conducted at a strain rate of 10^{-1} s^{-1}.

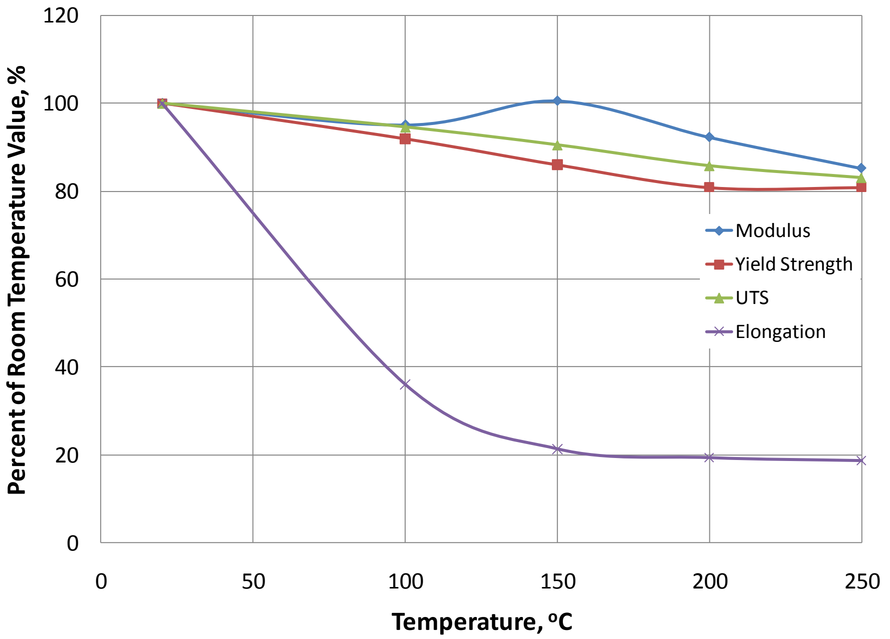

Figure 3.11: Tensile properties for tests conducted at a strain rate of 10^{-1} s^{-1} in terms of percent of room temperature values as a function of temperature.

Formation of concentrated deformation (Lüders) bands was observed for all strain rates tested at 250°C and below. Lüders bands started to become visible on the surface of the specimen just past yielding and expanded with further deformation as shown in Figure 3.12. The high visibility of these Lüders bands is due to the low stacking fault energy of type 301, which promotes deformation bands and twins. Band formation correlated proportionally with ductility and therefore inversely with strain rate and temperature, with increasing strain rate causing a decrease in band formation and increasing temperature causing a decrease in band formation. This observation coincides with the explanation of the increase in temperature (both from external heating and heating by deformation) causing reduced martensite formation which increases strain localization by reducing strain hardening [78], as well as the increase in temperature causing a rise in the stacking fault energy, thus reducing the propensity for planar slip.

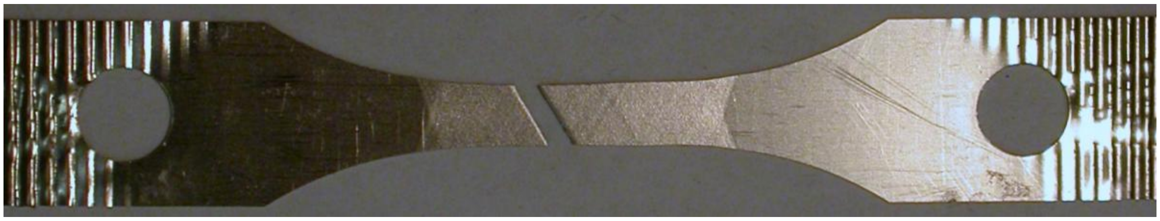

Figure 3.12: A tensile specimen showing the formation of Lüders bands in the gage section.

3.1.3 High Temperature Tensile Properties

The monotonic stress-strain curves for 301 stainless steel for temperatures from 20°C to 800°C are shown in Figure 3.13. There is a significant reduction in ductility from room temperature to 250°C. The ductility increases with temperature above 250°C with the exception of a slightly lower value at 550^{o}C. This reduction in ductility above room temperature is due to the reduced likelihood for formation of martensite at elevated temperatures [56]. The reduction in transformation decreases local strain hardening which limits the amount of material that undergoes plastic deformation before failure occurs, thus reducing the total strain to failure.

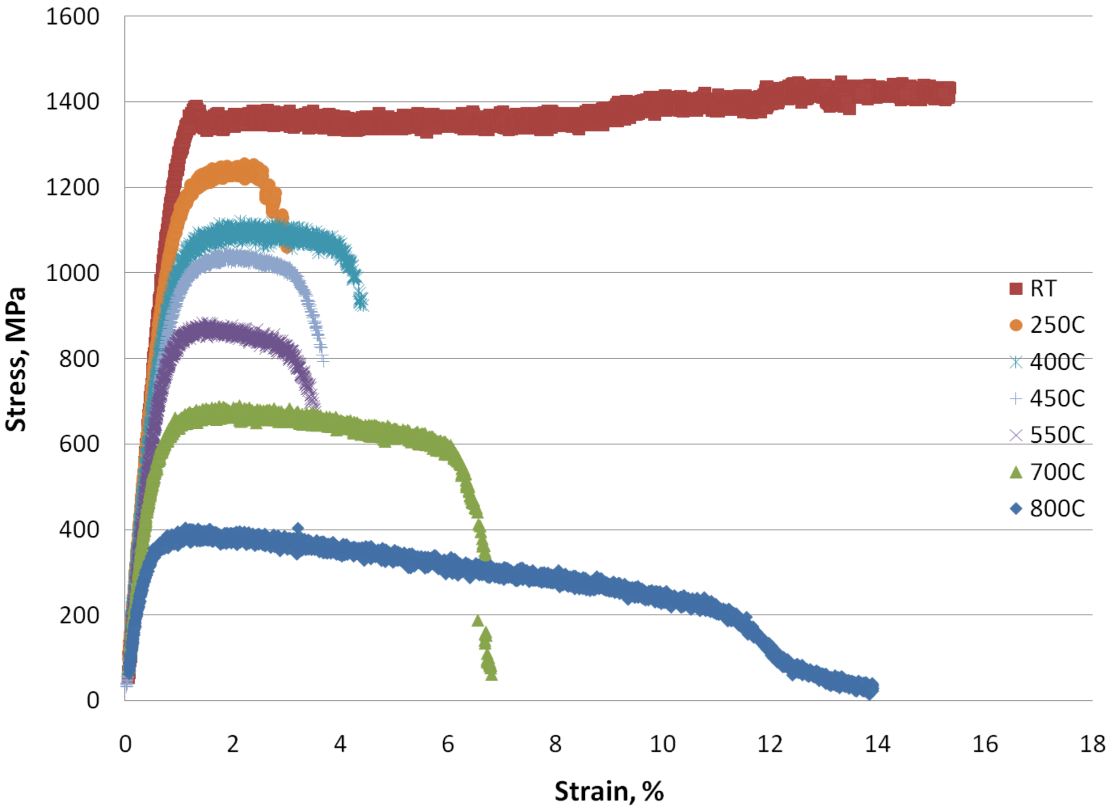

Figure 3.13: Elevated temperature tensile test results for 301 stainless steel.

The room temperature values for the tensile properties determined for 301 are shown in Table 3.4. The modulus determined is approximately 9% below the reported modulus for full hard sheet in the longitudinal direction of 179 GPa [166]. There was a 10% lower modulus reported for the full hard condition than the annealed condition which suggests that the difference in modulus between the material tested here and the full hard material tested in the literature may be due to a higher rolling reduction in this material. Yield strength, ultimate strength, and modulus consistently decreased with increasing temperature. The values determined in this study are compared to results from the literature for full hard 301 sheet [167] in terms of percent of the room temperature values in Figure 3.14. The material tested here shows a similar level of property degradation for the range of temperatures reported. The rate of modulus and strength degradation with temperature is fairly constant at temperatures below 550^{o}C and increases as the temperature increases further.

Table 3.4: Room temperature tensile properties of 301 stainless steel.

Modulus, GPa	Yield Strength, MPa	Ultimate Strength, Mpa	Elongation, %
163	1250	1430	15.3

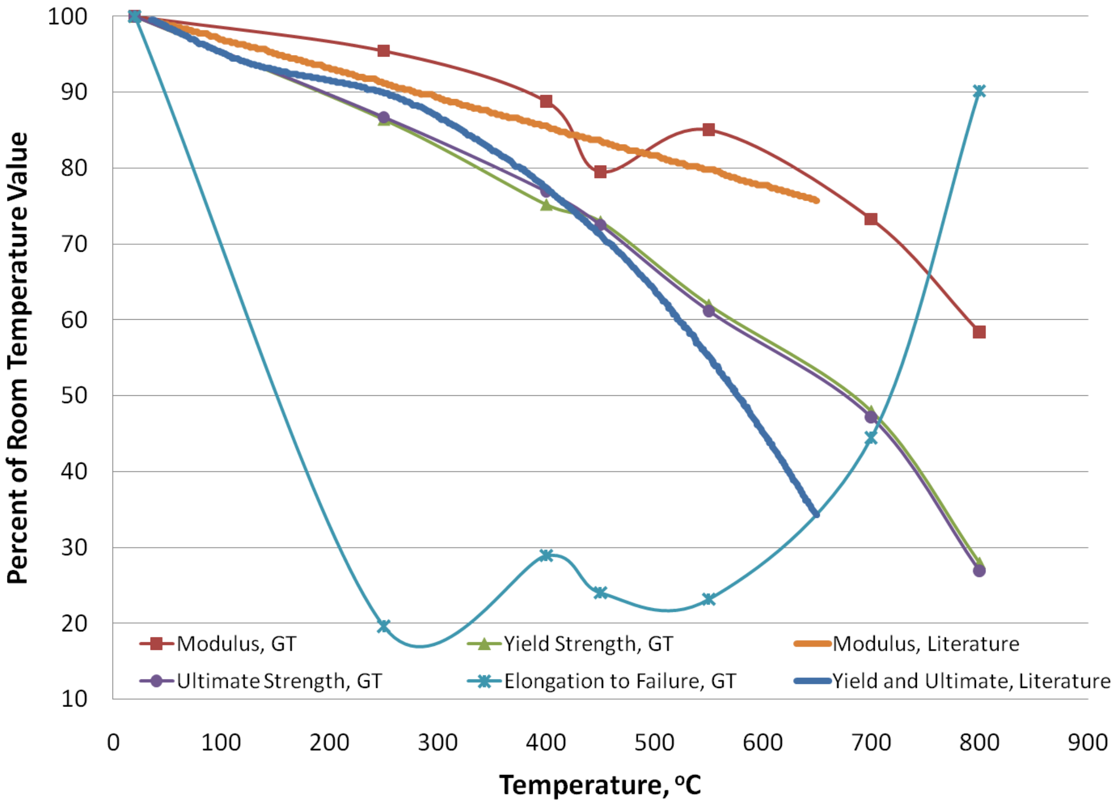

Figure 3.14: Tensile properties of 301 stainless steel relative to room temperature values with a comparison to values in the literature for full hard sheet [167].

Images of 301 stainless steel specimens after testing are shown in Figure 3.15. Luders bands were not prominent at temperatures above 250°C. The angle of fracture ranged from 60 to 64 degrees from the normal for tests at temperatures other than 800°C, consistent with the orientation of the Luders bands. The 800°C test specimen showed considerable necking and the angle of failure was perpendicular to the loading direction.

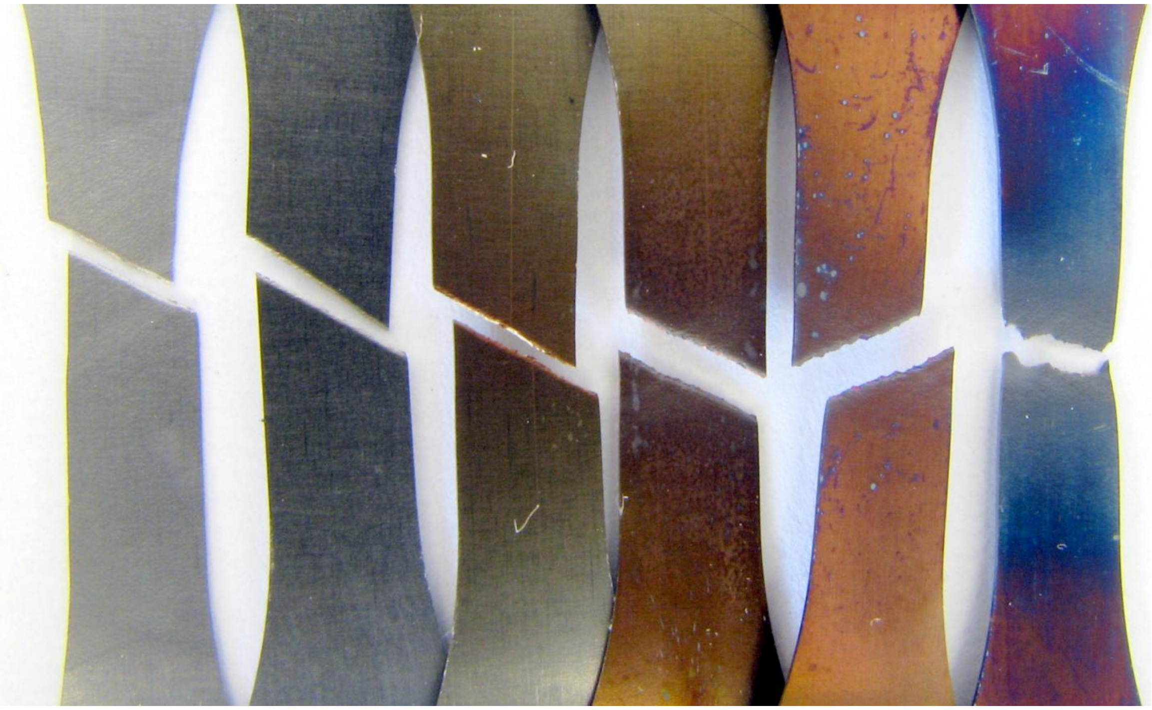

Figure 3.15: 301 stainless steel specimens after testing at temperatures from left to right of 20^{o}C, 250^{o}C, 400^{o}C, 550^{o}C, 700^{o}C, and 800^{o}C.

3.1.4 Aged Tensile Property Results

The monotonic stress-strain response from tensile tests conducted at room temperature on the aged samples are shown in Appendix A. A summary of the elongation to failure, yield strength, and ultimate strength are shown in Figures A6 to A8 respectively. Ductility and strength were higher for longer exposures at temperatures of 400^{o}C and bellow. This could be due to recovery taking place in the higher energy regions of the material that serve as the defects that localize deformation and cause decreased ductility. Exposure to 550^{o}C caused a reduction in strength and ductility which was more pronounced for longer exposure times. Specimens exposed to 700^{o}C showed large decreases in strength as time increased but with less ductility decrease than was seen at 550^{o}C. The hardening that occurred at higher strains at temperatures of 550^{o}C and

700^{o}C indicate that recrystallization took place during exposure, which resulted in the decreased strength.

3.1.5 Tensile Property Summary and Conclusions

The deformation behavior of AISI 301 stainless steel is dominated by the austenite-martensite phase transformation behavior which is highly strain-rate and temperature dependent due to the thermodynamics of the transformation. It is important to understand how temperature and strain-rate affect the tensile response for more accurate analysis of gasket deformation behavior. Tensile tests were performed on 301 stainless steel at three strain rates from 10^{-1} to 10^{-4} s^{-1} and five temperatures from room temperature to 250^{o}C to determine the influence of these factors on the tensile properties. Elongation to failure decreased at elevated temperature, with a reduction of 68% at just 100^{o}C and a maximum reduction of 82% at 250^{o}C relative to room temperature. Elongation to failure was found to decrease by 50% as strain rate increased from $10^{-2.5}$ s^{-1} to 10^{-1} s^{-1} at room temperature.

The elastic modulus was found to decrease as the temperature increases. This will cause an increase the contact size and thus lower the peak stresses during fretting. The change in modulus between room temperature and 250^{o}C is approximately 5%. This change is small relative to the change in the other tensile properties since the modulus is not significantly dependent on the transformation behavior. The yield strength of the material decreased by 15% between room temperature and 250^{o}C. The relatively small change occurs because transformation does not occur below the yield point and therefore does not influence the yield strength. The ductility was found to decrease drastically for only a small temperature increase. Austenite is stable above 100^{o}C [67] and will not transform to martensite through plastic deformation. The lack of transformation causes a decrease in the resistance to premature plastic instability and therefore decrease elongation to failure [168]. This is expected to reduce the fatigue resistance based on the concept of ductility exhaustion and therefore increase the amount of fatigue damage caused by fretting.

3.2 Microstructural Characterization

3.2.1 Procedure

The microstructure of 301 stainless steel was examined by mechanically polishing and etching to reveal various aspects of the structure. These etched samples were examined using optical microscopy to determine grain size, inclusion size and abundance, and phase distribution.

Samples were mounted using Struers Epoes cold mount epoxy. Epoes has a cure time of approximately 12 hours and has better adhesion and lower shrinkage than faster curing acrylics and epoxies. Mounted samples were polished with a Struers RotoPol-15 automatic polisher and Struesrs abrasives using the procedure in Table 3.5. Samples were cleaned using ethanol in an ultrasonic cleaner between steps to remove abrasive particles that could cause scratching in subsequent steps. Ethanol was used for cleaning rather than water to limit oxidation.

Table 3.5: Polishing procedure.

Disc	Solution	RPM	Force (N)	Time (min)
P800 SiC paper	Water	300	20	variable
MD-Allegro	DiaPro Allegro - Largo (9 µm diamond)	150	15	8
MD-Dac	DiaPro Dac (3 µm diamond)	150	15	4
MD-Chem	OP-A (0.02 µm alumina)	150	10	2

Polished samples were etched using three solutions commonly used for 300 series stainless steel. The solutions were chosen from ASTM E 407-99: Standard Practice for Microetching Metals and Alloys. The three solutions selected are shown in Table 3.6. These etchants were chosen based on availability and relative safety (absence of perchloric and hydrofluoric acids). Kalling's No. 2 exposes carbides, attacks austenite slightly, and darkens martensitic phases. Glyceregia also exposes carbides, with less ability to expose other phases. The electrolytic etching in 10% oxalic acid solution exposes grain boundaries and attacks austenite more rapidly, therefore also exposing martensite phases [68]. Exposure time was varied to expose different features, while chemistry and voltage were kept constant.

Table 3.6: Etchants used from ASTM E 407-99.

Etchant name	Solution	Procedure
Kalling's No. 2	5 g CuCl2, 100 mL HCl 100 mL ethanol	Swab 1 minute
Glyceregia	3 parts HCI, 2 parts glycerol 1 part HNO3	Swab 30 seconds
!0% oxalic acid	10 g oxalic acid 100 ml water	Electrolytic at 6 V 15-30 s for carbides 1 minute for grain boundaries and martensite

3.2.2 Results

Poor results were obtained when etching with Kalling's No. 2 and with Glyceregia. Kalling's No. 2 darkened the entire surface and did not expose any distinguishable features, even for very short exposure times. Glyceregia also did not expose any distinguishable features.

The surface resulting from electrolytic etching of the face of a sheet of 301 with a 10% oxalic acid solution with 6 volts for 1 minute is shown in Figure 3.16. Arrows point to martensite and several inclusions are circled. Martensite appears as short dark lines while austenite remains light [68]. The grain size was measured to be approximately 30 μm. Inclusions are approximately 10 μm in diameter and are expected to be $M_{23}C_6$ [66].

Figure 3.16: Face of a 301 sheet etched with a 10% oxalic acid solution at 6 volts for 1 minute showing martensite (arrows) and inclusions (circled).

The edge of a sheet electrolytically etched with 10% oxalic acid with 6 volts for 1 minute is shown in Figure 3.17. The vertical rolling direction is evident by the elongated structure. Several δ-ferrite stringers were observed on the edges of the sheets. These δ-ferrite stringers are brittle [68] and are a likely location for crack formation.

Figure 3.17: The edge of a 301 sheet etched with 10% oxalic acid with 6 volts for 1 minute showing longitudinal structure and a δ-ferrite stringer (arrow).

The microstructure of 301 stainless steel after exposure to elevated temperature is shown in Figure 3.18. The rolling direction is normal to the page. The as-received condition has an elongated structure and a considerable martensite volume fraction. The annealed material has a nearly equiaxed structure. Exposure to 550°C and 700°C resulted in a darker appearance for the same etching conditions. This suggests the occurrence of sensitization, where diffusion of carbon to the grain boundaries causes precipitation of chromium rich carbides (type $M_{23}C_6$) and reduces the local concentration of chromium available to form passive chromium oxide, therefore reducing the corrosion resistance of the material. This has been reported to take place during exposure to temperatures between 550°C and 850°C in 304 stainless steel [169] and would be more prominent in 301 stainless steel due to the reduced chromium content.

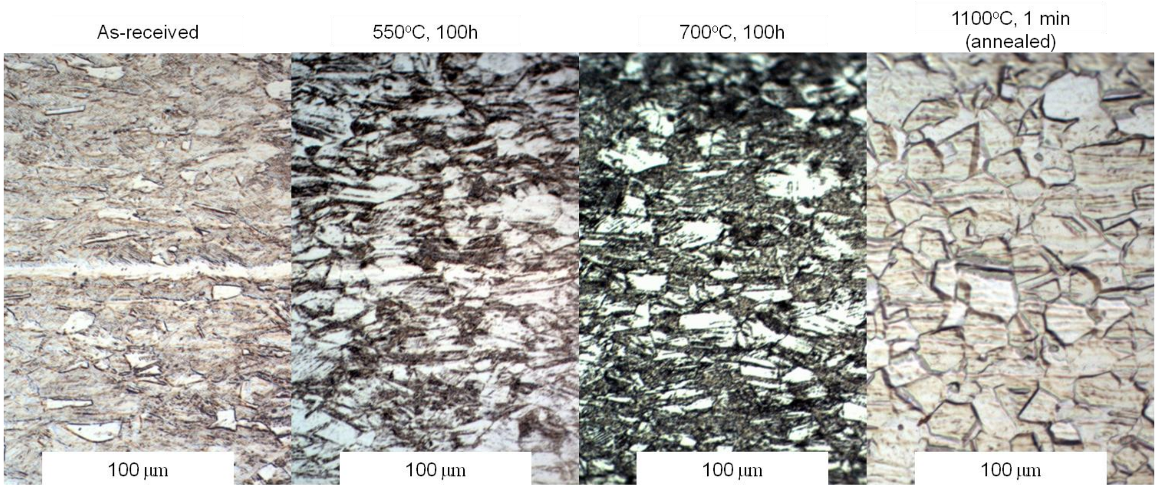

Figure 3.18: Microstructure of 301 stainless steel in the as-received condition compared to after high temperature exposure with the rolling direction normal to the page.

The surface appearance of 301 stainless steel after exposure to high temperatures for various times and temperatures is shown macroscopically in Figure 3.19 and microscopically in Figure 3.20. The color of the surface continued to change after exposure of up to 100 h in all cases. The oxidation thickness was less than 5 µm in all cases, and did not obscure surface features except for the case of exposure to 700°C for 100 h.

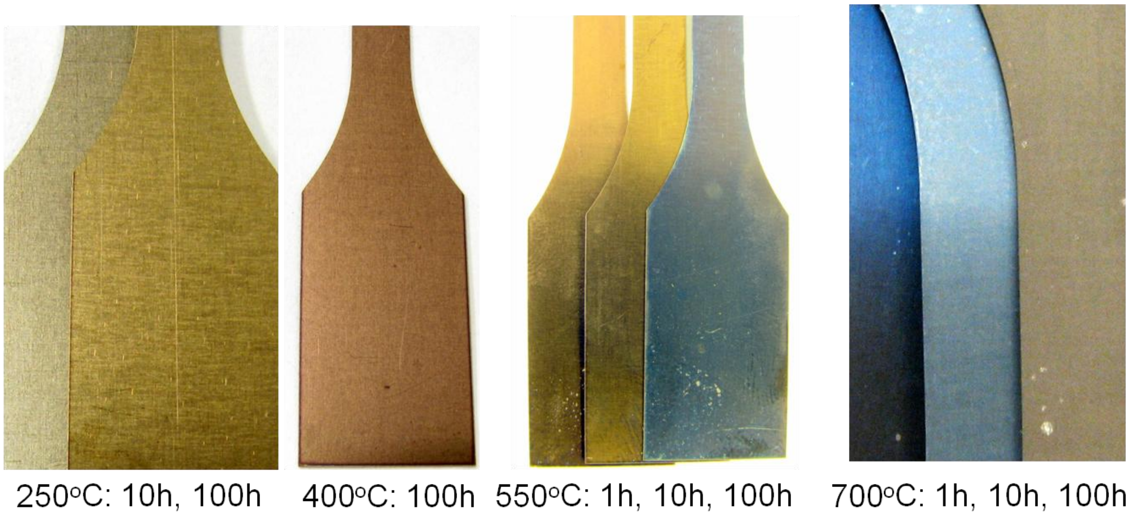

Figure 3.19: Surface appearance of 301 stainless steel after exposure to high temperature.

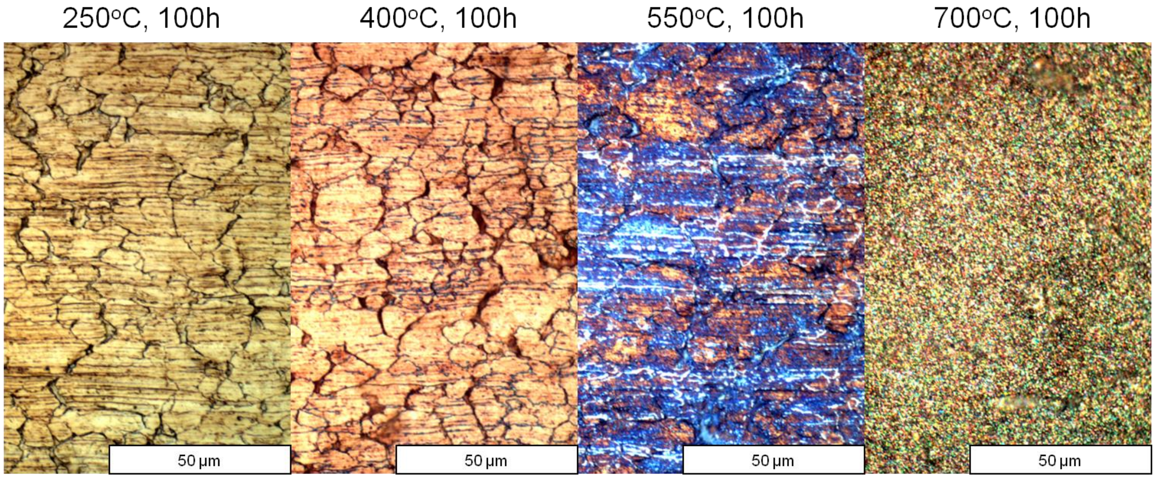

Figure 3.20: Microscopic appearance of 301 stainless steel surface after exposure to high temperature with the rolling direction to the right.

3.3 Fatigue Testing

The fatigue properties of materials subjected to fretting strongly influence the type and extent of damage due to fretting. Fatigue tests were performed on 301 stainless steel to determine the fatigue response as a function of temperature due to the sensitivity of the microstructure to temperature. The results are used during analysis of the fretting results to aid in identification of the causes for changes in the fretting behavior.

3.3.1 Procedure

Plain fatigue tests were performed on specimens of 301 stainless steel in full hard condition at 20^{o}C and 250^{o}C in force control at 10 Hz with a stress ratio R of 0.05. Specimens had the same geometry as the tensile specimens shown in Figure 3.1. Specimens were secured using mechanical grips. A convection oven was placed around the assembly to allow testing at 250^{o}C. A thermocouple was welded near the gage section where the cross-sectional area was larger so that failure did not occur at the thermocouple. The oven was pre-heated before each test so that the specimen reached 250^{o}C in under one minute. Tests were conducted for a maximum of 10^6 cycles, corresponding to a maximum test time of 28 hours. This aging condition was not sufficient to cause significant changes in the room temperature tensile properties when aged with no stress as shown in Figure A1. Failure was defined as separation of the specimen into two pieces. The duration of fatigue crack growth is short for these specimens due to the low cross-sectional area.

3.3.2 Results

The resulting lives are shown in Figure 3.21. The increase in temperature resulted in a decrease in the fatigue limit by approximately 5-10%. The decrease in the fatigue strength was more significant at lower cycles to failure. The larger reduction in fatigue strength at lower cycles to failure is attributed to the decrease in ductility which occurs due to the increase in temperature. This reduction in ductility between 20^{o}C and 250^{o}C was found to be 80% as shown previously. This has a more significant effect for tests with shorter lives because of the larger plastic strain amplitude due to the higher stress amplitude. Fretting of 301 stainless steel at 250°C is expected to cause an increased level of fatigue damage compared to fretting at room temperature based on this result. It is expected that the difference in the level of fatigue damage due to increasing temperature will be greatest for the conditions which result in higher plastic strain, e.g. the cases with higher normal forces.

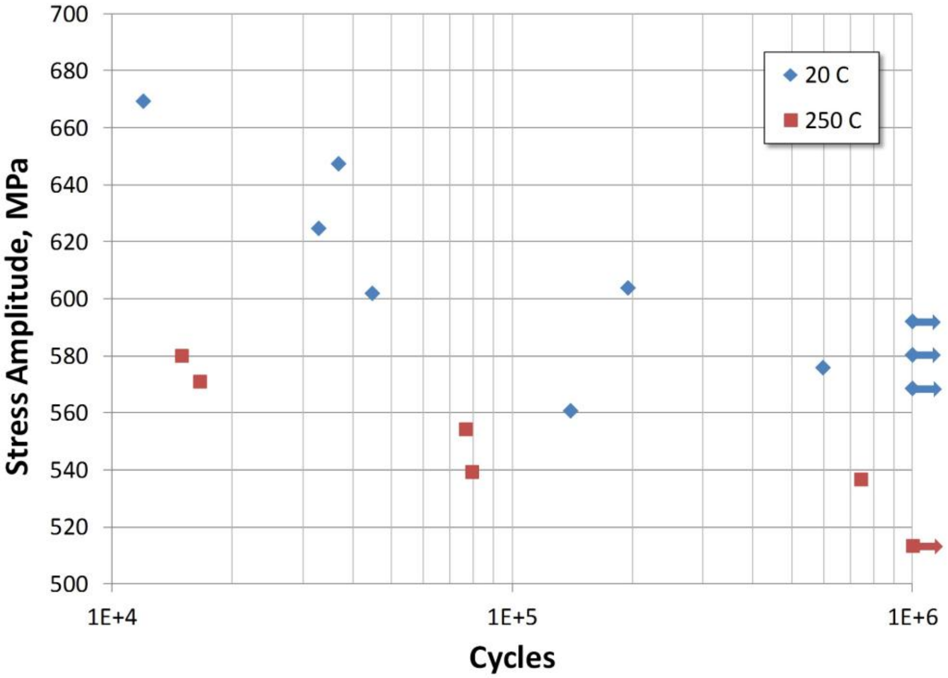

Figure 3.21: S-N curve for 301 stainless steel in the full hard condition at 20°C and 250°C.

CHAPTER 4

EXPERIMENTAL FRETTING INVESTIGATION

Of the fretting studies on 301 stainless steel, none were conducted using material in the full hard condition. The mechanical properties of austenitic stainless steel are very sensitive to cold work due to the metastability of austenite, which will in turn have a significant effect on the fretting behavior as discussed in the previous chapter. A method for performing fretting tests on thin sheets was established in this work since this work was performed using the thinnest specimens used in fretting experiments reported in the literature by a factor of five. The goal of the fretting experiments is to establish a link between contact parameters and the damage response as a function of temperature. This includes determination of the wear behavior and analysis of the interaction of wear and the level of fatigue damage which will be aided by the finite element study presented in the next chapter.

The fretting damage response of 301 stainless steel was analyzed for contact with A356 aluminum at room temperature and 52100 steel at temperatures from 20^{o}C to 550^{o}C with an emphasis on the response at 20^{o}C and 250^{o}C. Fretting damage was generated using a Phoenix Tribology DN55 High Temperature Fretting Machine. The type and extent of damage resulting from fretting was characterized by inspection of the wear profiles, analysis of the fretting debris, and fatigue tests on the samples subjected to fretting.

4.1. Fretting Test Method

4.1.1 Fretting Machine

Fretting tests were conducted using a Phoenix Tribology DN55 Fretting Machine shown schematically in Figure 4.1. A cylindrical moving specimen is clamped into the servohydraulic actuator. The position of the actuator is closed-loop controlled using feedback from a capacitance gage located at the top end of the actuator. The displacement amplitude of the moving specimen can be controlled from 10 µm to 400 µm at frequencies up to 400Hz. The moving specimen can be a sphere which creates a point contact, a cylinder which creates a line contact, or a cylinder rotated 90 degrees to create area contact.

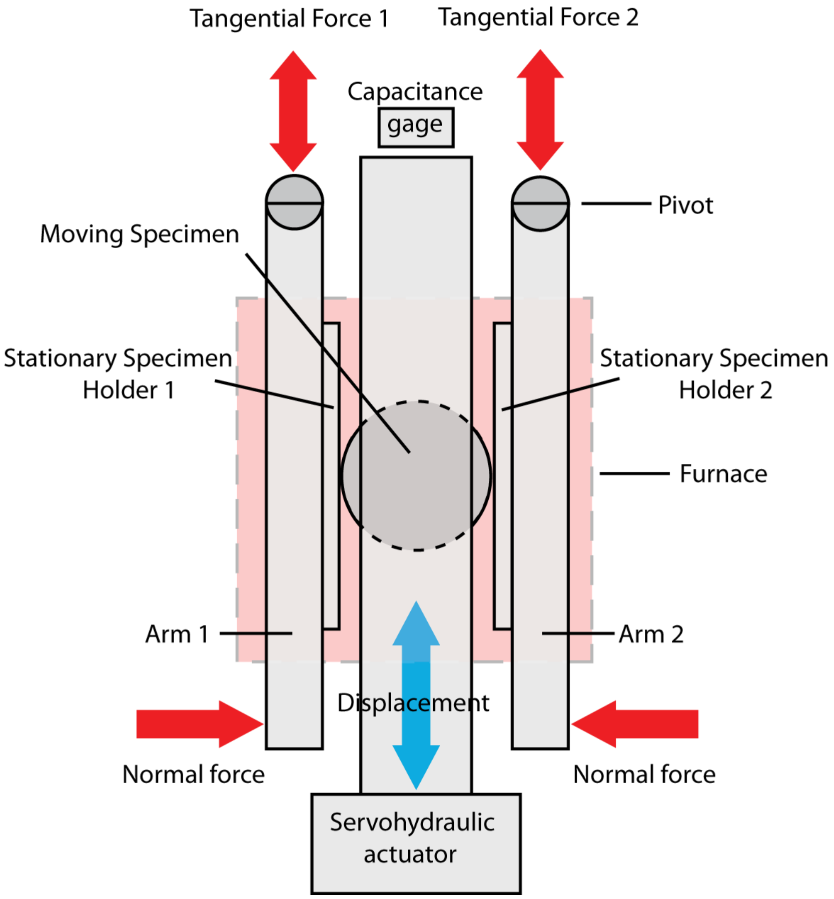

Figure 4.1: Schematic representation of a Phoenix Tribology DN55 Fretting Machine.

A specimen is clamped into each arm, referred to as the stationary specimen. The normal force between the moving specimen and the stationary specimens is developed by applying a force to the ends of the arms by a pneumatic actuator. Tangential force generated from friction at the contact is transmitted by each arm to a piezoelectric force transducer at the top of the arms. The tangential force and the position of the actuator are stored on the host computer at a rate of 1 kHz. Because the displacement is measured remotely, the measurement includes compliance of the system. Therefore, displacement amplitudes reported are considerably larger than the actual displacement at the contact interface which cannot be measured directly.

A furnace can be attached around the region shown in Figure 4.1 allowing tests to be performed at elevated temperature. Heat sensitive components are located away from the specimens so tests can be run at temperatures as high as 800^{o}C. Similarly, a gas chamber can be fitted around the experiment, allowing tests to be performed in a controlled atmosphere.

4.1.2 Specimen Holder Design

The specimen holder used to secure thin specimens in place during testing at up to 250^{o}C is shown in Figure 4.2. The holder is designed to hold the dog-bone specimens shown in Figure 3.1 as well as strip characterization specimens that have the same width as the gage section of the dog-bone specimens but no grip region and a length of 76 mm. The arm adapter shown in Figure 4.2(c) is attached to the backing plate with one M3 screw and is shaped to fit into a recess in the arms of the fretting machine. The whole assembly is then fastened into the arm with one M5 screw to create a stiff interface.

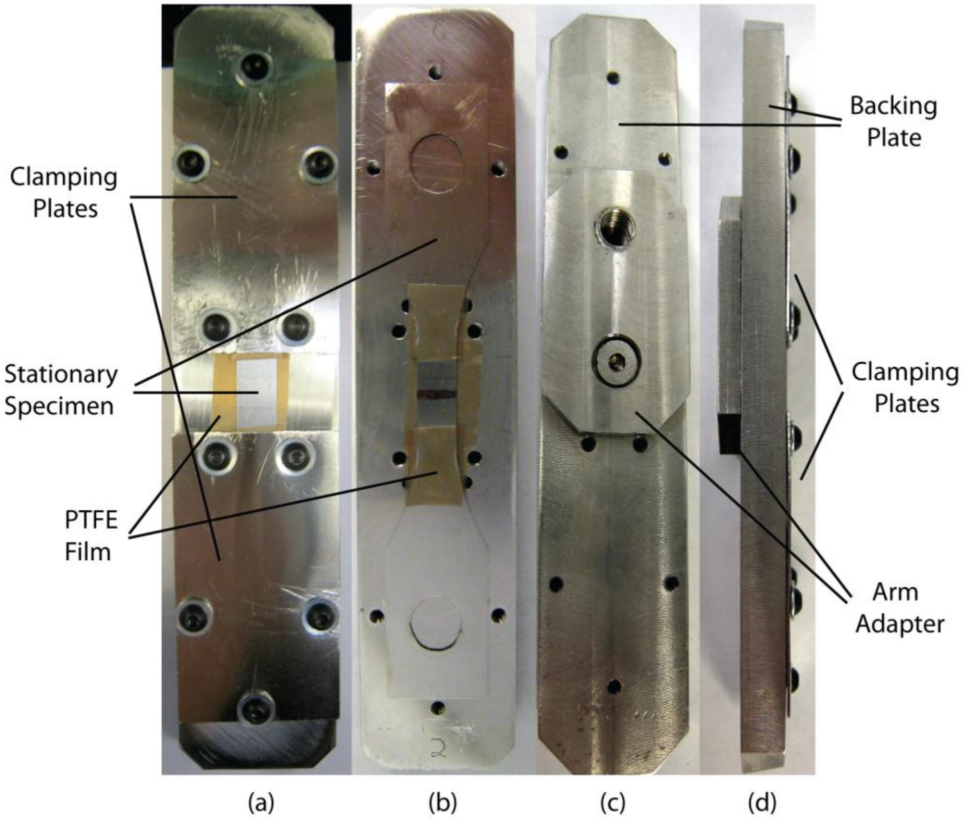

Figure 4.2: Stationary specimen holder showing the (a) top view of unfretted specimen with clamping plates in place, (b) top view of fretted specimen with clamping plates removed, (c) back view, and (d) side view.

The clamping plates secure the specimens in the holder. They are made of steainless steel with a thickness of 0.38 mm, and are attached to the backing plate using five M2 screws. The material of the holder was selected to have the same coefficient of thermal expansion as the specimen so thermal stresses will not be generated in the specimen during heating in elevated temperature tests. An 89 μm thick PTFE tape is adhered to the interface between the edge of the clamping plates and the specimen to prevent unwanted fretting between the specimen and the holder as shown in Figure 4.2 (a) and (b). This area is prone to fretting because of the high contact stress from the square edge of the top plate combined with the small amplitude relative motion from strains in the specimen from the friction force at the main contact. The PTFE tape reduces the COF which lowers the contact stresses, and the compliance of the film helps to distribute the contact pressure. PTFE tape was also used between the back of the specimen and the backing plate directly behind the location of the main contact to alleviate fretting between the back of the specimen and the backing plate. The PTFE layer also promotes self-alignment and hence more uniform pressure distribution across the gage width of the specimen.

PTFE is not able to withstand temperatures above 250^{o}C. A 25 μm thick layer of Boron Nitride (BN) lubricant was applied to the holder and regions of the specimen that contact the holder for tests conducted at temperatures above 250^{o}C as shown in Figure 4.3. The lubricant was applied in two coats with ample drying time between coats to prevent cracking of the coating.

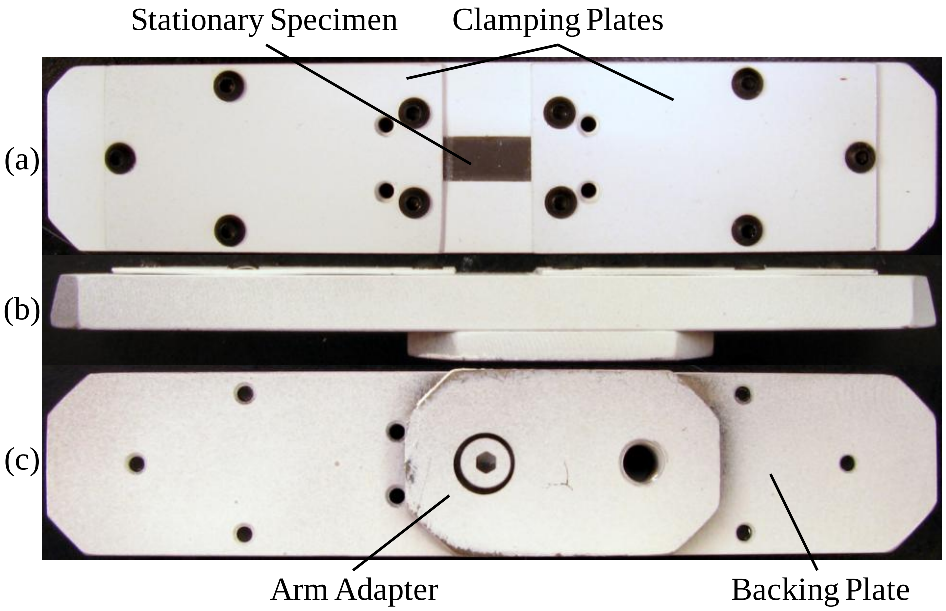

Figure 4.3: Stationary specimen holder coated with Boron Nitride based lubricant showing (a) top view, (b) side view, and (c) back view.

Temperature was controlled using a thermocouple welded to the clamping plate near the contact as shown in Figure 4.4. The thermocouple was not welded to the specimen to avoid damage to the specimen that would affect the subsequent fatigue results. A clamshell furnace was attached around the area labeled "Heated Region" in Figure 4.4. Fittings were attached to the clamshell furnace to allow the heated region to be purged with argon. The oxygen content near the contact was monitored during tests performed in an argon environment. The oxygen content was maintained to 0.3% +/- 0.2% during heating of the setup and during testing.

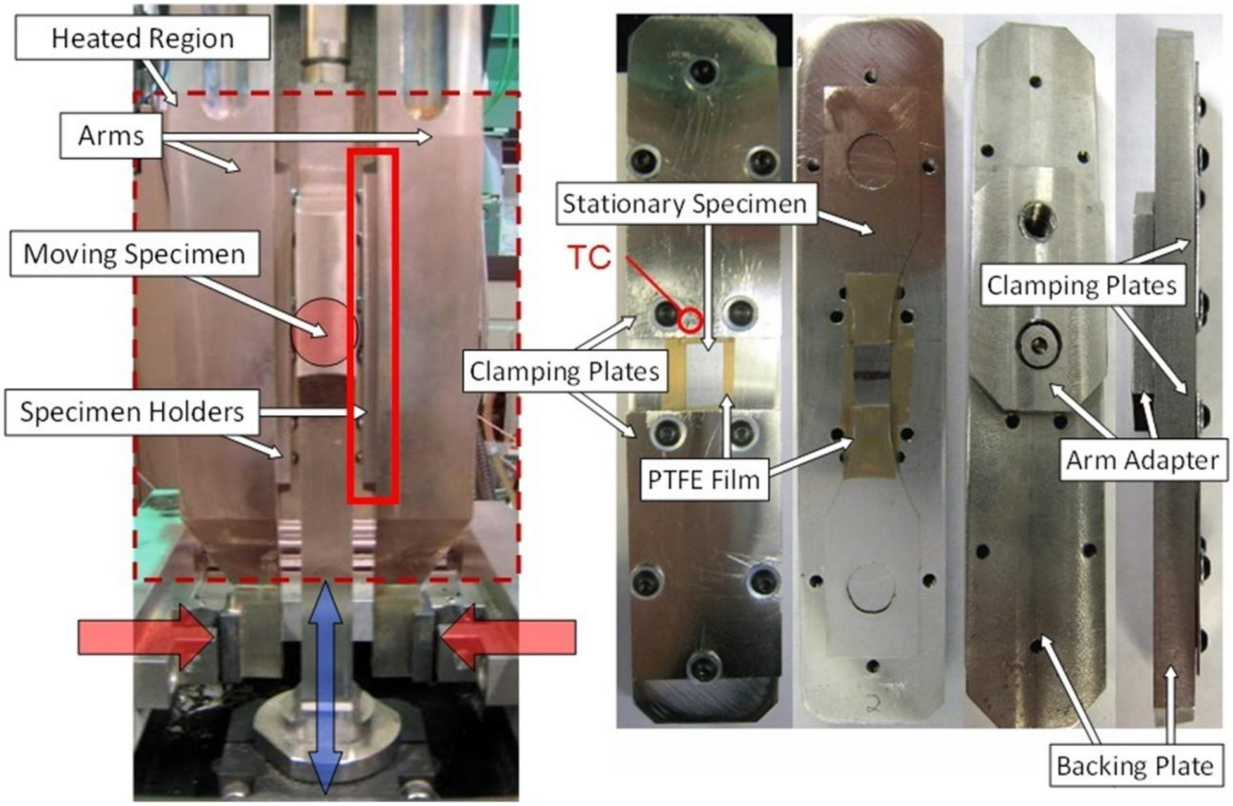

Figure 4.4: Fretting test configuration.

The amount of time required for the specimen to reach the desired temperature varied depending on the target temperature. The time required for the specimen to reach 250^{o}C was approximately 30 minutes. The time required for the specimen to reach 550^{o}C was approximately one hour. The stationary specimen holders were removed after the test completed and were placed on a block of aluminum to cool the specimen by conduction. This allowed for accelerated cooling without the loss of wear debris which would occur for convective cooling. The time required for the specimen to reach room temperature after a test conducted at 250^{o}C and 550^{o}C was 10 minutes and 30 minutes, respectively. At 250^{o}C this duration of exposure is not expected to alter the properties of the 301 stainless steel based on the experiments on the room temperature tensile properties of aged 301 stainless steel. Tests performed at temperatures above 250^{o}C are expected to have altered properties because of the exposure during heating. However, it is expected that the change in properties resulting from performing the test at temperature will have a more significant effect on the fretting response and will out-weigh the effect of aging during heating.

Exposure to 550^{o}C caused observable oxidation of the 52100 moving specimen. The system was heated with the specimens in contact with a normal force of 25 N. The area of the specimens in contact is not expected to oxidize significantly because of the decreased ability of oxygen to reach the material in contact. The contact size increases after the normal force is increased to the test value, which will therefore bring material into contact which was exposed to the environment.

4.1.3 Moving Specimens

Contacting bodies were cylindrical with 20 mm diameter and 15 mm length. Using a cylindrical moving specimen creates line contact, which was chosen to simplify the analysis since the contact configuration can be modeled as 2D plane strain. The two materials used for moving specimens were AISI 52100 steel and ANSI A356 aluminum. These materials were chosen to represent a wide range of strength, stiffness, and oxidation resistance. The compositions of 52100 and A356 are shown in Table 4.1 from ASTM A 295/A 295M – 05 and ASTM B 108-06, respectively.

Table 4.1: Chemical composition of rider materials.

AISI 52100 Steel	
Component	Wt. %
C	0.93-1.05
Mn	0.25-0.45
Cr	1.35-1.60
Si	0.15-0.35
P	0.025 Max
S	0.015 Max
Ni	0.25 Max
Mo	0.10 Max
Cu	0.30 Max
O	0.0015 Max
Al	0.050 Max

ANSI A356 Aluminum	
Component	Wt. %
Al	90.1 - 93.3
Cu	0.25 Max
Fe	0.6 Max
Mg	0.2 - 0.45
Mn	0.35 Max
Si	6.5 - 7.5
Ti	0.25 Max
Zn	0.35 Max

The A356 specimens were machined out of a cast engine block provided by Dr. Charles E. Bates at the University of Alabama at Birmingham. The 52100 specimens were machined from an annealed rod purchased from McMaster-Carr. The surface finish of the rider samples were generated using a five step SiC abrasive paper progression. The rods were mounted on a lathe, and polished progressively using P320, P500, P600, P800, and P1200 Grit SiC abrasive paper. This was done carefully to ensure that there would be no inconsistency in the experiments due to variation in surface finish. After polishing, the rods were cut along the cross section to final dimension. The room temperature hardness of the 52100 and A356 were measured as 21 HRC and 52 HRB, respectively.

4.1.4 Contact Alignment

The alignment of the fretting arms was adjusted to give a uniform pressure distribution along the line of contact between the moving specimen and stationary specimens. This was done by placing a sheet of pressure sensitive film between the stationary specimen and the moving specimen. If the pressure was not uniform, the alignment was adjusted and checked again. This process was repeated until satisfactory alignment was obtained. The pressure sensitive film before and after alignment for each side of the machine is shown in Figure 4.5. After alignment the contact on the right side is slightly more uniform than on the left side.

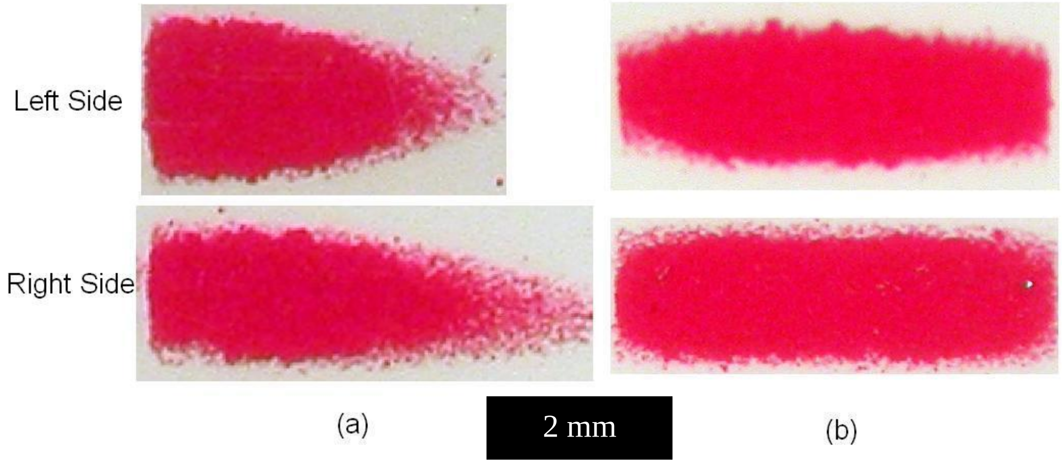

Figure 4.5: Contact pressure distribution (a) before alignment and (b) after alignment.

4.1.5 Test Parameters

Because the severity of fretting damage depends strongly on many parameters, it was necessary to perform many tests to fully characterize the response. Normal force, displacement amplitude, temperature, oxygen content, and contacting material were varied. Fretting experiments were performed over a range of normal forces from 100 N to

375 N and displacement amplitudes from 10 μm to 200 μm which was sufficient to define the fretting map at those normal forces. Tests in contact with A356 were performed in room temperature laboratory air. Tests in contact with 52100 were performed in atmospheres of air and argon (with 0.3% +/- 0.2% O_2), and temperatures from 20^oC to 550^oC. All tests were performed at 10 Hz for 10^4 cycles, which was sufficient to reach a stabilized response for all cases.

4.1.6 Damage Characterization Method

Damage characterization was performed to determine the level of wear and fatigue damage resulting from each condition tested. Wear was measured by stylus profilometry of the wear scars. Three line scans were performed in the direction of fretting motion at locations spaced evenly along the full width of the fretting scar. Wear volumes were calculated by averaging the three wear profiles and multiplying by the scar width. Scars were also inspected using optical microscopy and scanning electron microscopy to determine wear characteristics. The oxide composition as a function of temperature was investigated using X-ray Diffraction (XRD). Specimens were cut so that the fretting scar represented a large portion of the total area scanned.

Fatigue damage due to fretting was characterized by performing uniaxial fatigue tests on samples that were subjected to fretting to determine the subsequent fatigue life. Subsequent fatigue tests were performed at 20 ^oC in force control at 10 Hz using a force ratio of $R = 0.05$. The subsequent fatigue life indicates the extent of fatigue damage that occurred during fretting, with a longer subsequent fatigue life corresponding to less fatigue damage during fretting and vice versa.

4.2 Friction Response

4.2.1 Methods

Characteristics of the friction response were determined by inspection of hysteresis loops (plots of tangential force versus displacement) which were measured during each fretting test. A representative gross slip hysteresis loop is shown in Figure 4.6. The coefficient of friction (COF) was determined by averaging the magnitude of the tangential force near the center of the sliding region in each direction and dividing by the imposed normal force. The max tangential force ratio (TFR) was determined by averaging the maximum measured tangential force magnitude that occurred in each direction and dividing by the normal force. Steady state values are defined here as values determined from the hysteresis loop of cycle 10^4.

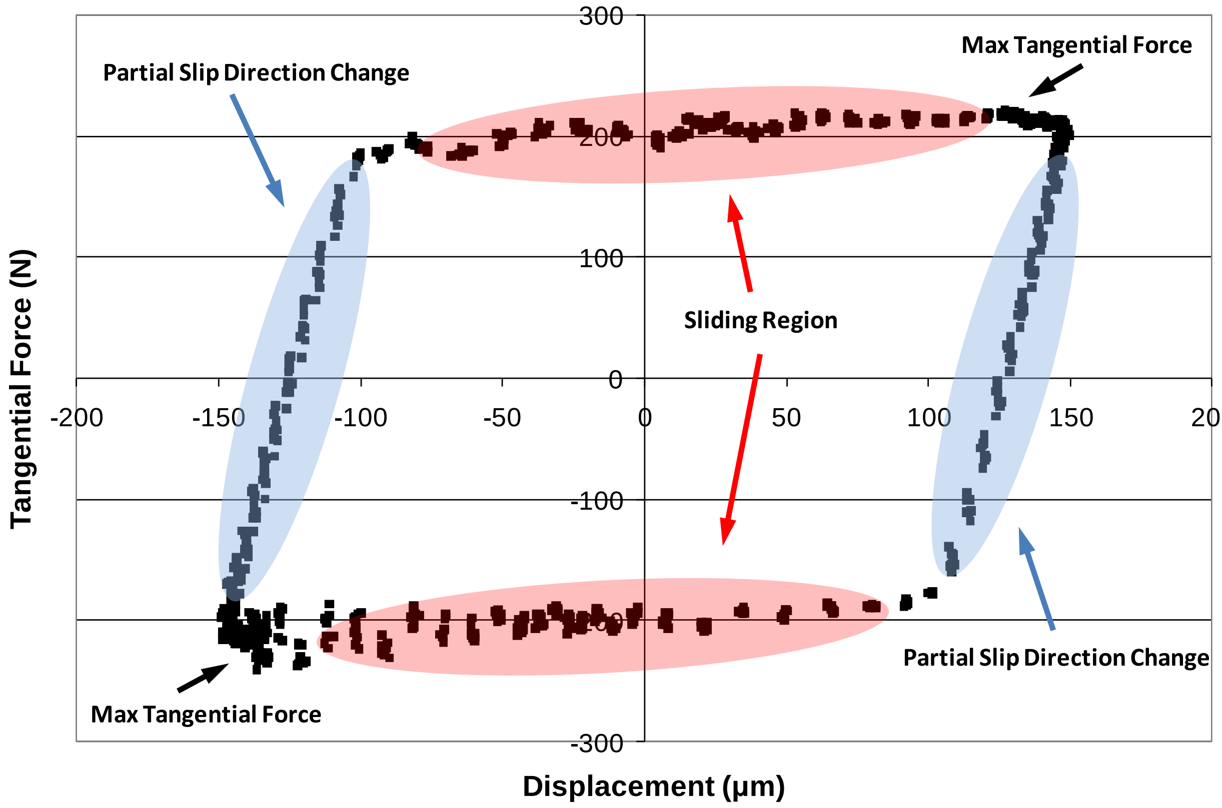

Figure 4.6: Representative gross slip hysteresis loop (contact with 52100 steel with a 150 μm displacement amplitude and 255 N normal force).

It is not possible to determine the COF for cases where the contact condition was partial slip. A representative partial slip hysteresis loop is shown in Figure 4.7. The steady state max TFR is reported for these cases, which serves as a lower bound value of the COF.

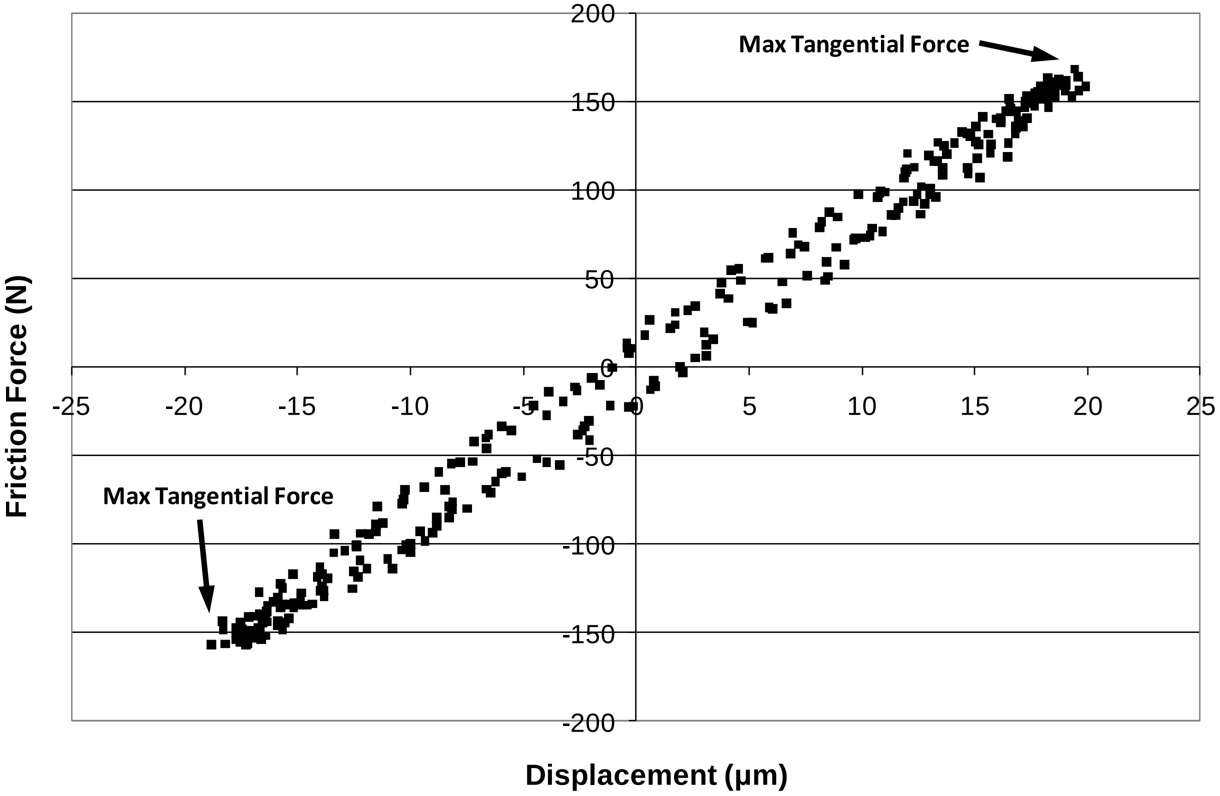

Figure 4.7: Representative partial slip hysteresis loop (contact with A356 aluminum with a 20 μm displacement amplitude and 255 N normal force).

The slip amplitude was calculated by determining the width of the hysteresis at zero tangential force and dividing by two. The amount of energy dissipated per cycle due to friction in gross slip cases was approximated by multiplying the slip range by the COF times the normal force applied. In partial slip cases, the amount of energy dissipated per cycle due to friction is approximated by multiplying the slip range by the TFR times the normal force applied.

The cumulative dissipated energy per contact area was calculated by

$$E_{ADED} = \frac{\sum_{i=1}^{n} 2N\mu_i \left(\delta - \frac{N\mu_i}{s} \right)}{(a+\delta)b} \tag{4.1}$$

where i represents the cycle number, n is the total number of cycles, COF_i is the COF during cycle i, N is the normal force, w is the width of the steady state hysteresis loop at zero tangential force at steady state, a is the contact half-width, δ is the displacement amplitude, and b is the width of the stainless steel specimen, which was 4.762 mm for all cases considered here. The numerator represents the accumulated dissipated energy, and the denominator represents the total area of the stainless steel that was in contact during the test. The most robust method of calculation would use the sum of the area of the hysteresis loop for each cycle as the numerator rather than using stabilized values and approximating the friction loop as a parallelogram, however this would require additional computation for only a small increase in accuracy in the case of contact with 52100. The integral approach would be more beneficial when considering contact with A356 because of the irregular shape of the hysteresis loops, however only a relatively small amount of energy was associated with the spikes in tangential force due to plowing since it was not accompanied by a significant amount of slip, as evidenced by the minimal increase in area of the hysteresis loops. Thus, the relationship used here is an appropriate approximation and enhances the simplicity of the methodology.

Friction logs recorded during fretting tests were used to determine whether the running condition was partial, mixed, or gross slip for each test performed. The partial slip running condition was characterized by hysteresis loops that were initially closed and remained closed for the entire experiment. The mixed slip running condition was distinguished by a hysteresis loop that was open for only a period of the test duration, whereas the gross slip running condition was characterized by an open hysteresis loop for the entire duration of the experiment.

4.2.2 Room Temperature Fretting Results

Examples of friction logs for contact with 52100 and A356 in the mixed slip and gross slip regimes are shown in Figure 4.8.

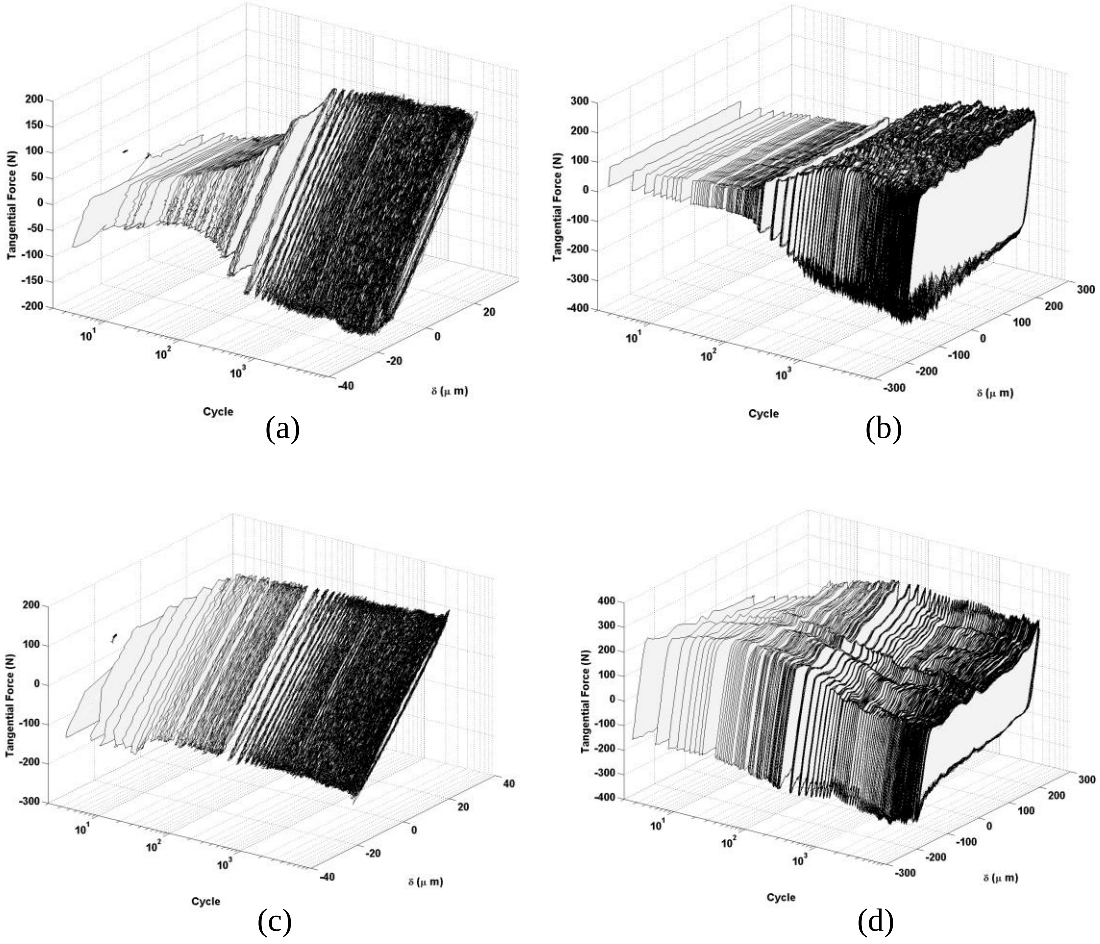

(a) (b)

(c) (d)

Figure 4.8: Friction logs with a normal force of 255 N for contact with and displacement amplitudes of (a) 52100 and 20 μm (MSR), (b) 52100 and a 200 μm (GSR), (c) A356 and a 20 μm (MSR), and (b) A356 and 200 μm (GSR), respectively.

Hysteresis loops for several different cycles during a test with an A356 contacting body, normal force of 255 N, and 100 μm displacement amplitude are shown in Figure 4.9(a). Initially, the tangential force is uniform for the entire sliding portion of the stroke. As the test progresses to 100 cycles, the tangential force increases over the entire displacement range. As the cycle count increases, the tangential force near zero displacement begins to decrease while the tangential force at the ends of the stroke begins to increase. The value of the tangential force ratio (ratio of tangential force to normal force) based on the tangential force near the center of the displacement and the peak tangential force are shown in Figure 4.9(b). The spike in tangential force near the end of the stroke is due to an interaction between aluminum deposited on the 301 specimen and a hemi-cylindrical trough formed on the aluminum contacting body as shown in Figure 4.10. The deposit comes into contact with the edge of the trough at the ends of the stroke that imparts a significant tangential component to the specimen. This causes a rise in the tangential force ratio to as high as 1.4 as the deposit grows compared to the actual sliding value of 0.5. This phenomenon has been observed during other fretting tests involving ductile materials such as aluminum [145, 170-171].

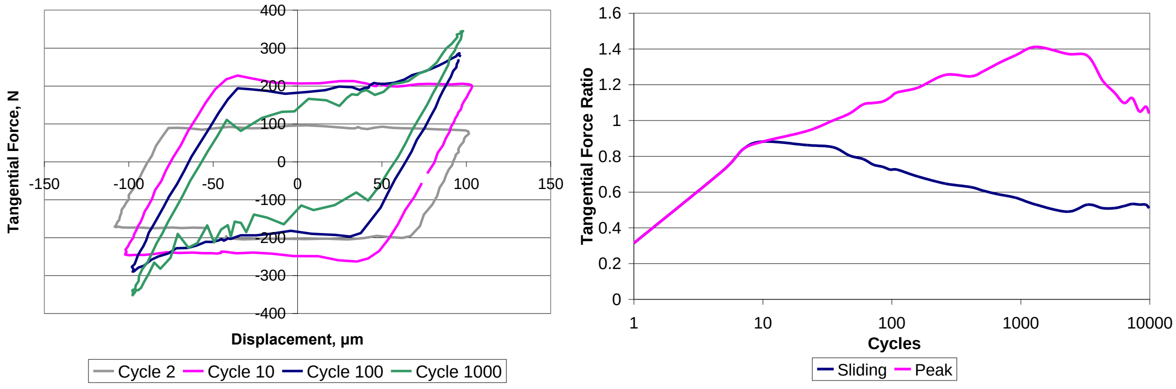

(a) (b)

Figure 4.9: (a) Hysteresis loops for several different cycles for fretting against A356 with a normal force of 255 N and a 100 μm displacement amplitude and (b) a comparison between the TFR and COF as a function of cycles.

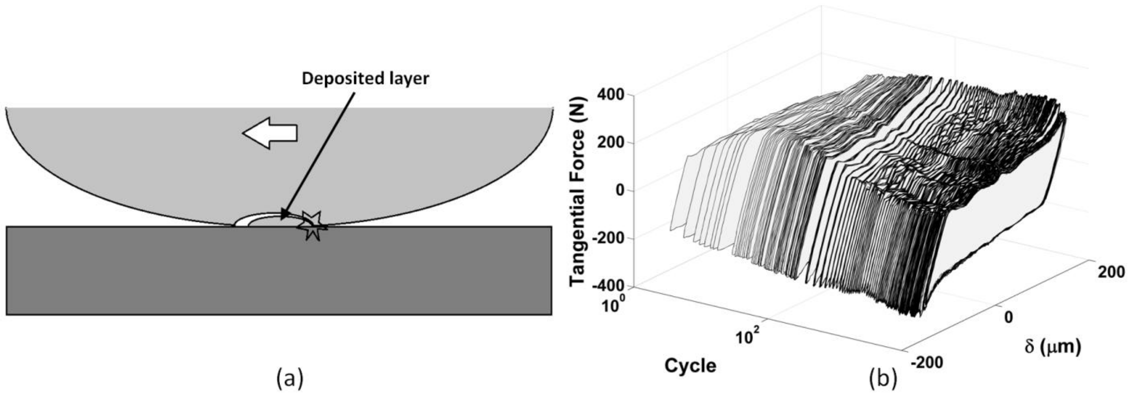

(a) (b)

Figure 4.10: (a) Plowing effect from material transfer and (b) resulting evolution of hysteresis loops.

The evolution of the tangential force ratio for contact with A356 and a normal force of 255 N for various displacement amplitudes is shown in Figure 4.11. Solid lines represent gross slip conditions (open hysteresis loop) and dotted lines represent partial slip conditions (closed hysteresis loop). The test conducted with a 10 μm displacement amplitude was the only test that resulted in a partial slip running condition. The transition from gross slip to partial slip occurs later for higher displacement amplitudes. Tangential force increases until the transition to partial slip and then remains constant for the duration of the test. For tests resulting in a gross slip running condition, the tangential force increases to a maximum value and then decreases to a steady state value after approximately 10^3 cycles. The decrease occurs more rapidly for higher displacement amplitudes.

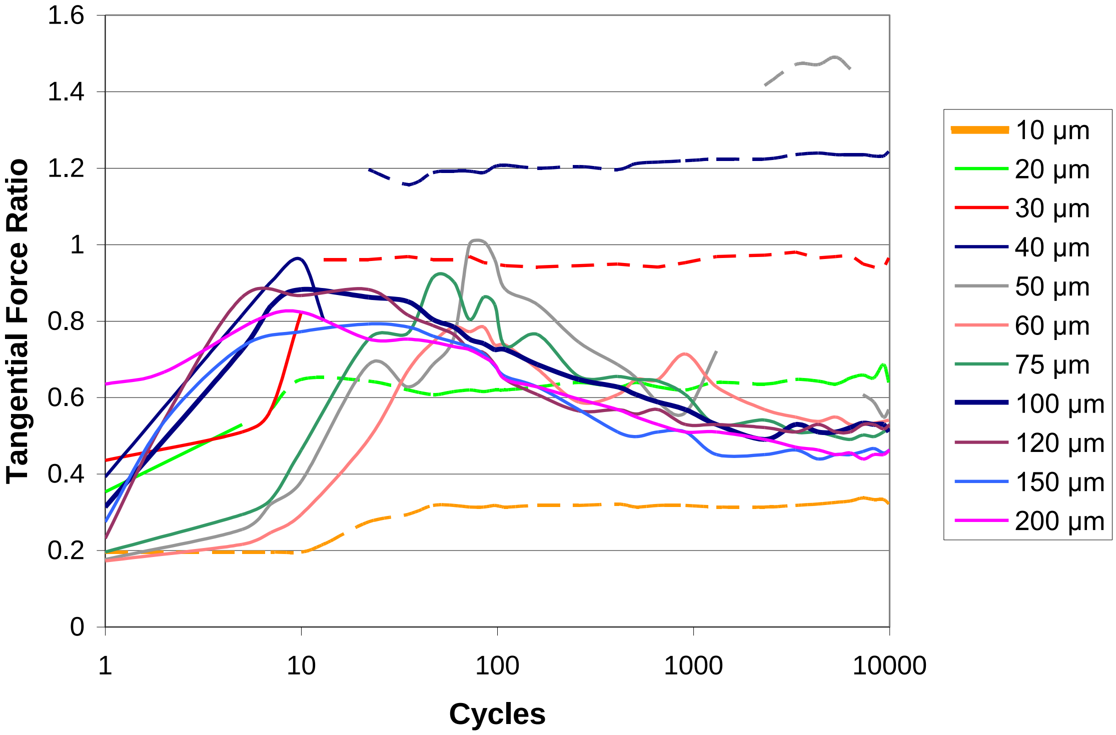

Figure 4.11: Tangential force ratio evolution for contact with 301 with a normal force of 255 N against A356 and various displacement amplitudes where dotted lines identify a partial slip condition and solid lines identify a gross slip condition.

The evolution of the tangential force ratio for contact with 52100 with a 255 N normal force and various displacement amplitudes is shown in Figure 4.12. The test performed with a 10 μm displacement amplitude was the only test with a partial slip running condition, and the 20 μm test was the only mixed slip running condition. The initial value of the tangential force ratio was lower than for contact with A356, and the maximum value was reached after more cycles. This is a consequence of the lower wear rate for contact with 52100 due to its higher hardness. The tangential force value decreases slightly toward the end of the test, however, a test conducted with a displacement amplitude of 100 μm for 10^5 cycles showed that the tangential force does not decrease significantly beyond 10^4 cycles.

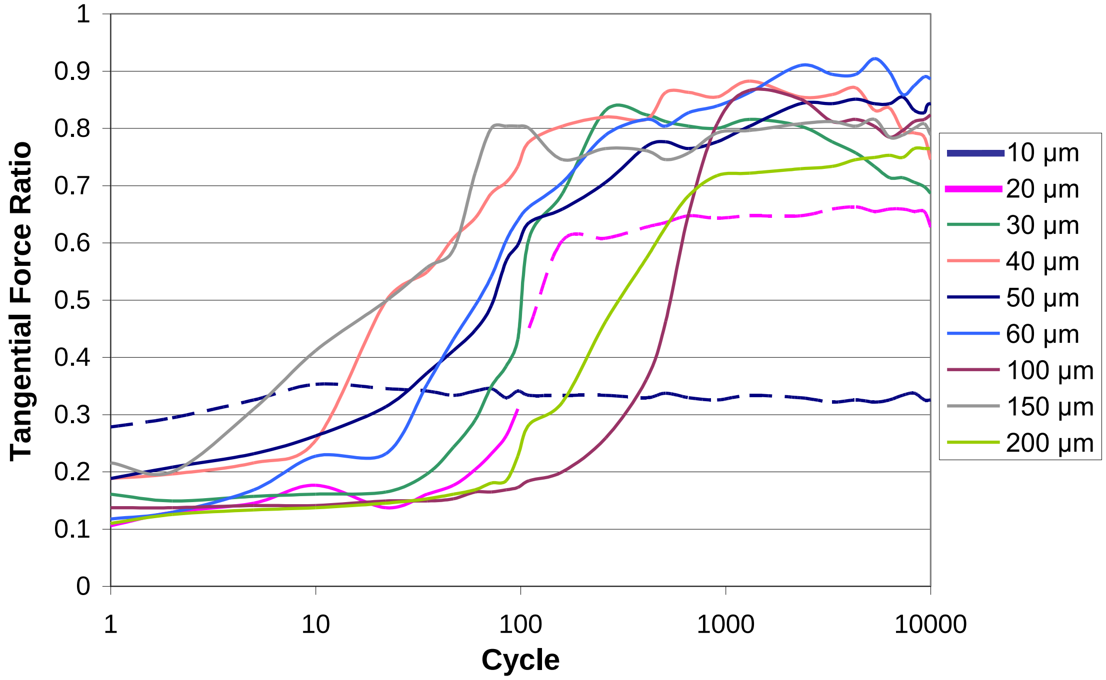

Figure 4.12: Tangential force ratio evolution for contact with 301 with a normal force of 255 N against 52100 and various displacement amplitudes where dotted lines identify a partial slip condition and solid lines identify a gross slip condition.

An example of the repeatability of the friction results for contact with 52100 steel with a displacement amplitude of 60 μm and normal force of 255 N is shown in Figure 4.13. The steady state values COF values for the seven tests for this condition were within the range of 0.81 +/- 0.03.

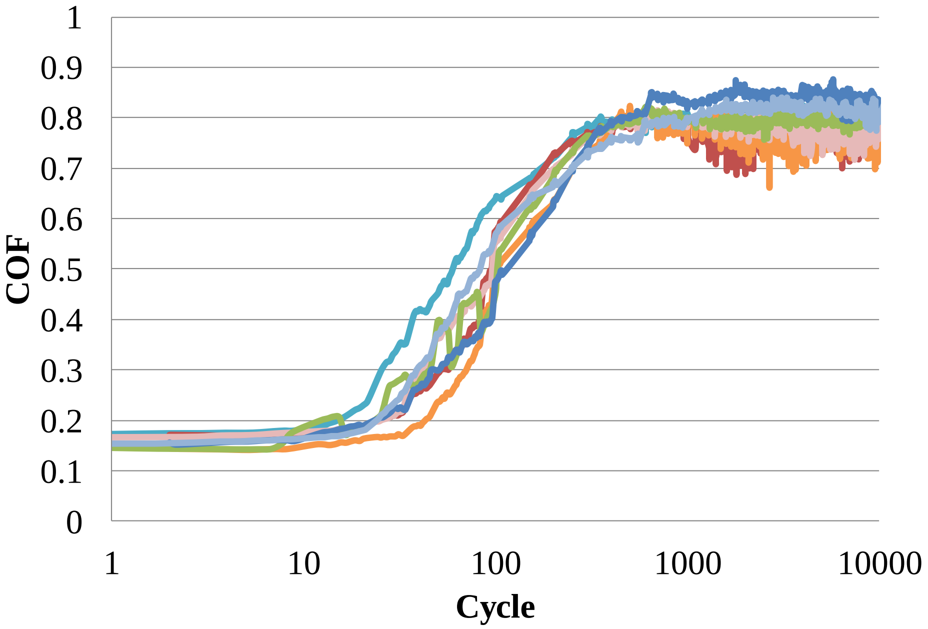

Figure 4.13: Demonstration of friction response repeatability for contact with 52100 steel with a displacement amplitude of 60 μm and a normal force of 255 N.

The steady state values of the tangential force ratio for contact with A356 for a 255 N normal force and various displacement amplitudes are shown in Figure 4.14. The maximum tangential force ratio occurred at the highest displacement amplitude in the mixed slip regime with a value of 1.22. The tangential force ratio decreases with increasing displacement amplitude after the transition to the gross slip regime.

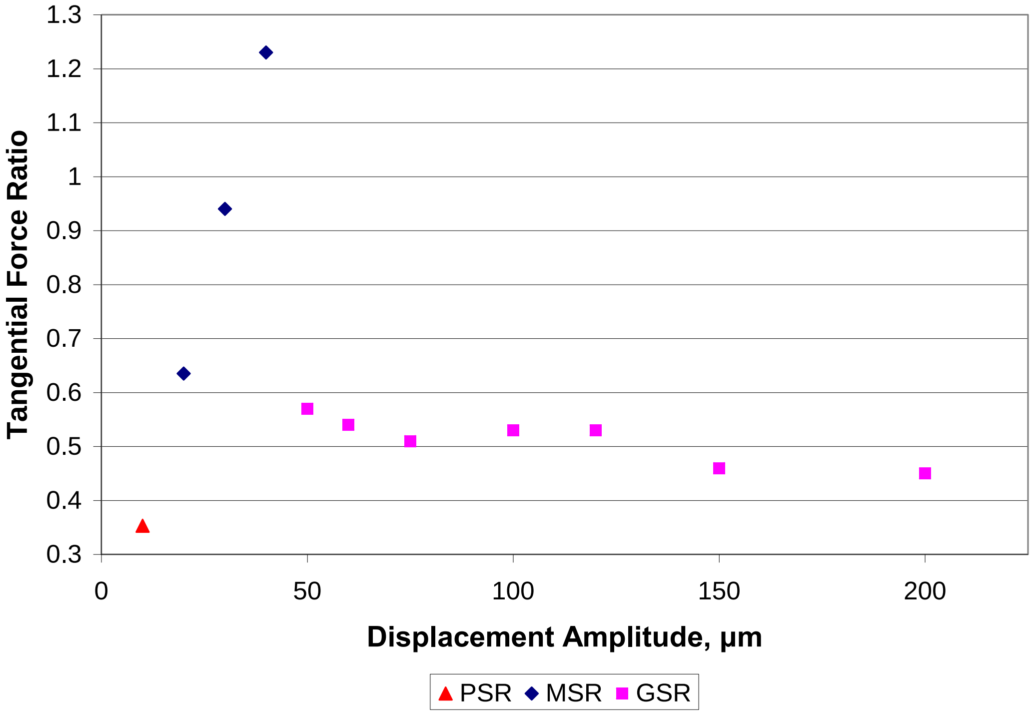

Figure 4.14: Tangential force ratio after 10^4 cycles for contact of 301 against A356 with a normal force of 255 N and various displacement amplitudes showing the corresponding running condition.

The steady state values of the tangential force ratio for 301 in contact with 52100 for a normal force of 255 N and various displacement amplitudes are shown in Figure 4.15. The maximum value of the tangential force does not occur at the upper limit of the MSR as it does for contact with A356. The tangential force continues to increase to a maximum at a displacement amplitude of 60 µm. Similar to contact with A356, the tangential force continues to decrease with increasing amplitude. The average COF after 10^4 cycles for displacement amplitudes that result in a gross slip running condition is 60% higher for contact with 52100 than with A356. However, the maximum value over the first 10^4 cycles is nearly equal.

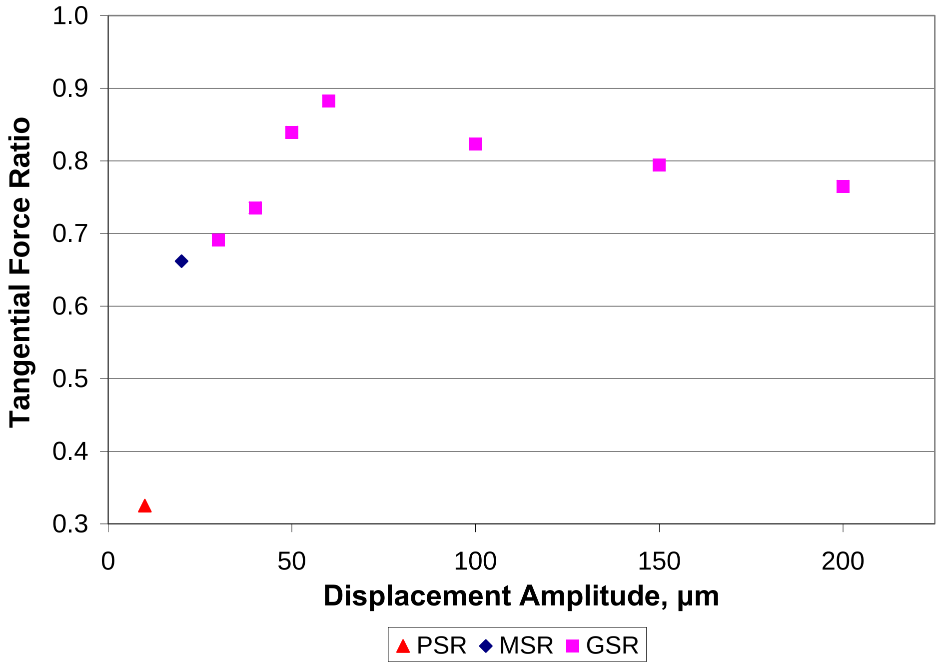

Figure 4.15: Tangential force ratio after 10^4 cycles for contact of 301 against 52100 with a normal force of 255 N and various displacement amplitudes showing the corresponding running condition.

The values of the steady-state COF observed in this study for normal forces of 255 and 375 were similar to values reported by other authors for contact of annealed 304 stainless steel against itself. Raman and Jayaprakash [82] found that steady-state values were reached by 10^4 cycles and were in the range of 0.6 to 1.0 for a grain size of 43 µm and were lower, in the range of 0.45 to 0.85, for a grain size of 277 µm. Kayaba and Iwabuchi [100] also found that steady-state values occur by 10^4 cycles for annealed 304 fretted against itself with a value of 0.65.

A running condition fretting map was created for 301 in contact with A356 at three normal forces, shown in Figure 4.16. The lines drawn represent the expected boundaries between the different regimes. The PSR-MSR transition was found to occur between 20 and 30 µm with a normal force of 375 N, between 10 and 20 µm for a normal force of 255 N, and was below 10 µm for a normal force of 100 N. The MSR-GSR was found to occur between 67 and 75 µm for 375 N, 50 and 60 µm for 255 N, and 15 and 20 µm for 100 N.

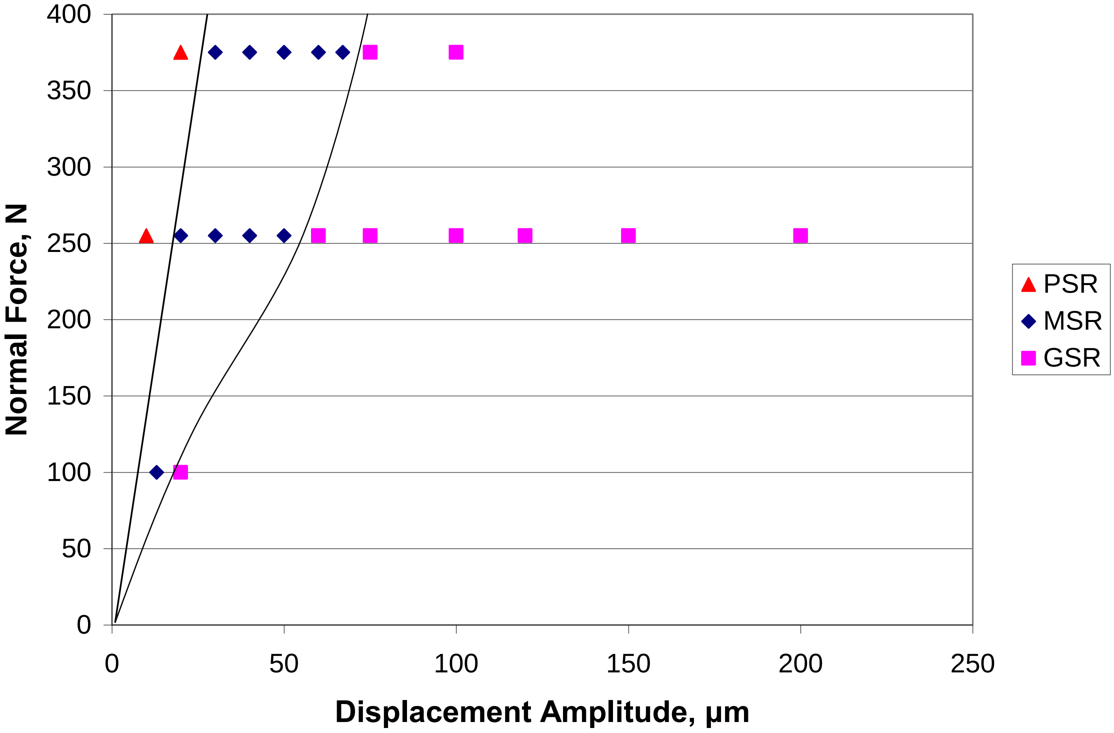

Figure 4.16: Running condition fretting map for contact against A356.

The running condition fretting map for 301 in contact with 52100 at room temperature is shown in Figure 4.17. The PSR-MSR transition occurred between 10 and 20 µm for 255 N, and was below 10 µm for a normal force of 100 N. The MSR-GSR transition was found to occur between 20 and 30 for 255 N, and between 10 and 20 µm for 100 N. These transitions occurred at lower displacement amplitudes than for contact with A356. This is partly due to the higher stiffness of the 52100. Less elastic and plastic deformation takes place in the 52100 moving specimen than the A356 moving specimen, making sliding more likely to occur.

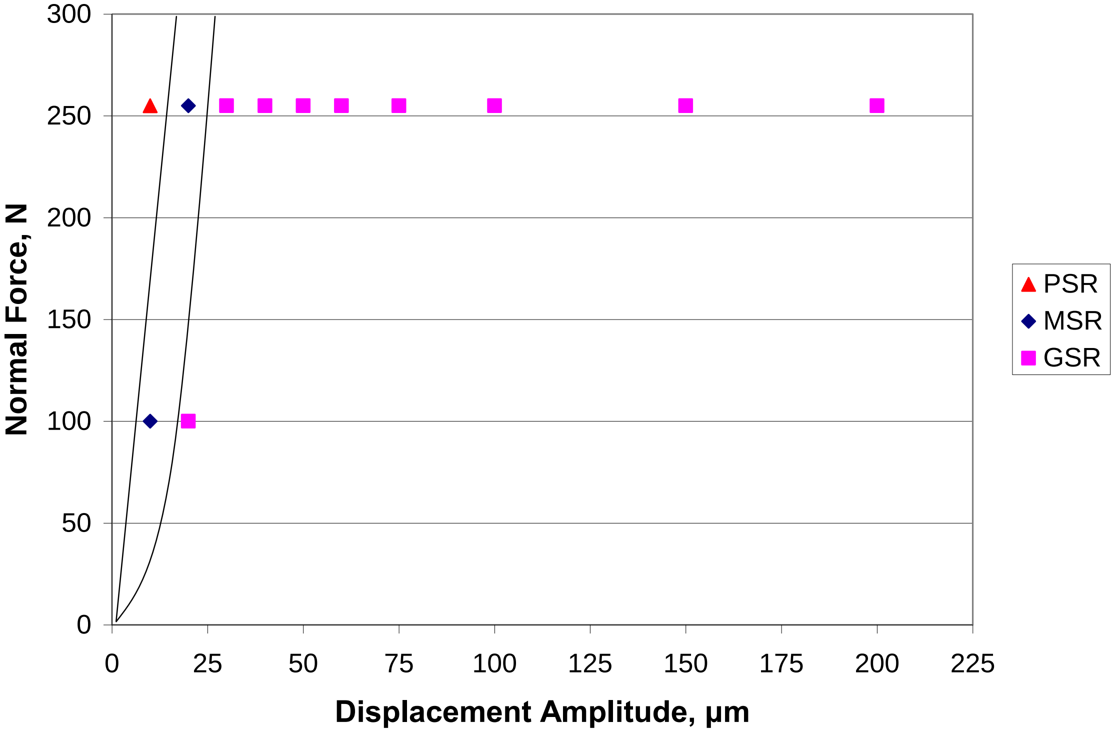

Figure 4.17: Running condition fretting map for contact against 52100 at room temperature.

4.2.3 Fretting at 250°C

Fretting tests were performed in contact with 52100 steel at 250°C. The fretting map for tests conducted at 250°C is shown in Figure 4.18. The transitions between partial slip, mixed slip, and gross slip were identified for each of the normal forces imposed. The transitions in running condition occurred at larger displacement amplitudes with increasing normal force, with an increase of approximately 10 µm per force level.

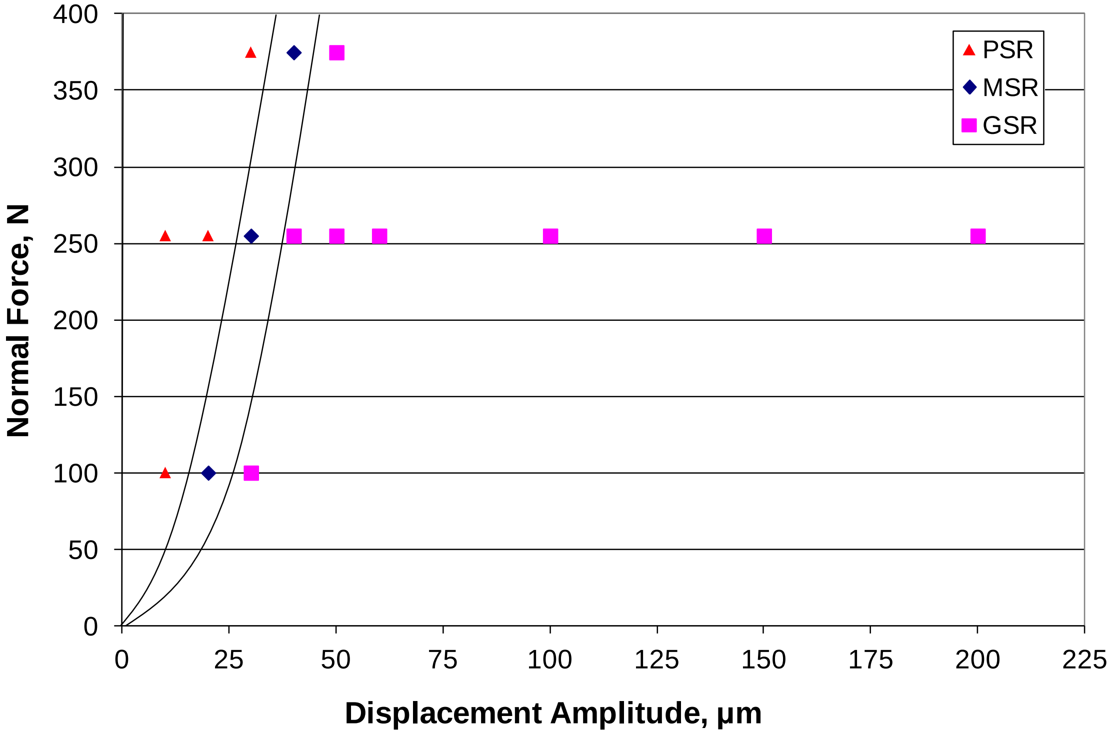

Figure 4.18: Fretting map for contact with 52100 at 250°C.

A comparison between fretting maps determined at room temperature and 250°C is shown in Figure 4.19. The transitions between running conditions occurs at a larger displacement amplitude at 250°C than at room temperature. This could be attributed to the decrease in slip amplitude caused by an increase in compliance of the system caused by elevated temperature due to the lower modulus of the materials at elevated temperature, however the slip amplitude at which the transitions occur is greater for 250°C. The difference is related to the lower COF at 250°C, which is discussed in below.

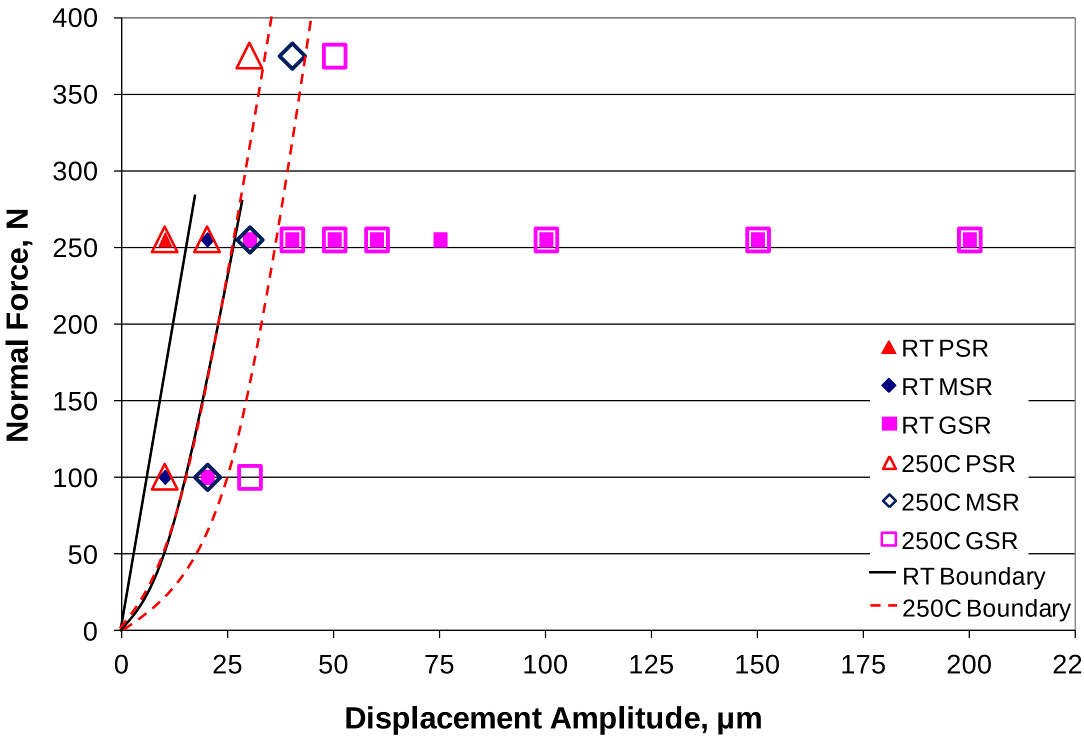

Figure 4.19: Comparison of fretting maps at room temperature and 250°C.

The COF evolution at 20°C and 250°C for gross slip conditions with various displacement amplitudes and normal forces is shown in Figure 4.20. Tests conducted at 20°C had a low initial COF which increased to reach a maximum value after 10^2 to 10^3 cycles and then remained approximately constant for the remaining duration of the test. For tests conducted at 250°C, the COF typically reached a maximum value early in the test, at less than 10 cycles, before decreasing to a stabilized value prior to reaching 10^2 cycles. Tests conducted in the mixed slip regime had different contact condition evolution which is related to this difference in COF evolution. At 20°C, a mixed slip running condition consisted of an initial period of gross slip followed by a transition to stabilized partial slip. Conversely, a mixed slip running condition at 250°C consisted of an initial period of partial slip followed by a transition to stabilized gross slip. The difference in behavior is related to the formation of a glaze oxide on the surface in the tests conducted at elevated temperature. This is discussed in a subsequent section.

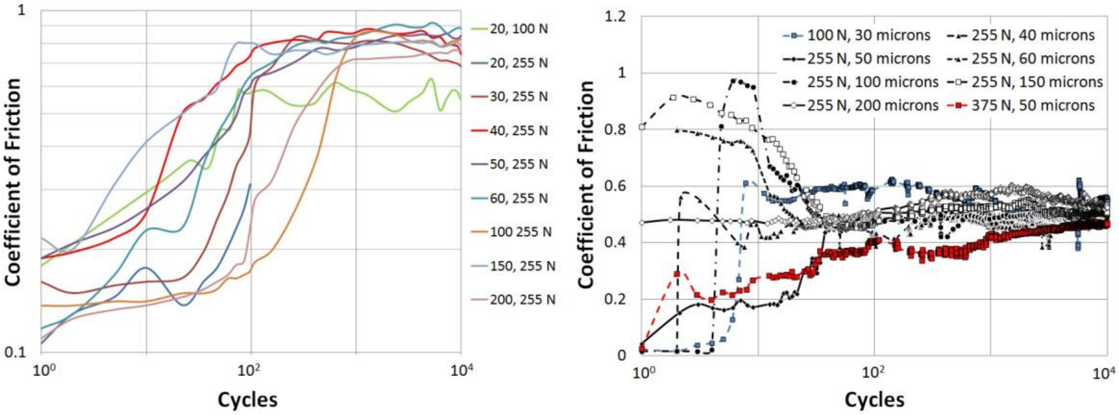

(a) (b)

Figure 4.20: Friction evolution for contact with 52100 at (a) 20°C and (b) 250°C.

The stabilized values of the tangential force ratio (TFR) for each condition at 20°C and 250°C is shown in Figure 4.21. Representation using the steady state slip amplitude helps to remove the effect of test system stiffness change with changing temperature to make a more direct comparison. However, this does not account for the decrease in contact pressure associated with the increase in contact area caused by a decrease in material stiffness with increasing temperature. The stabilized tangential force ratio was higher for tests conducted at 20°C for each test condition.

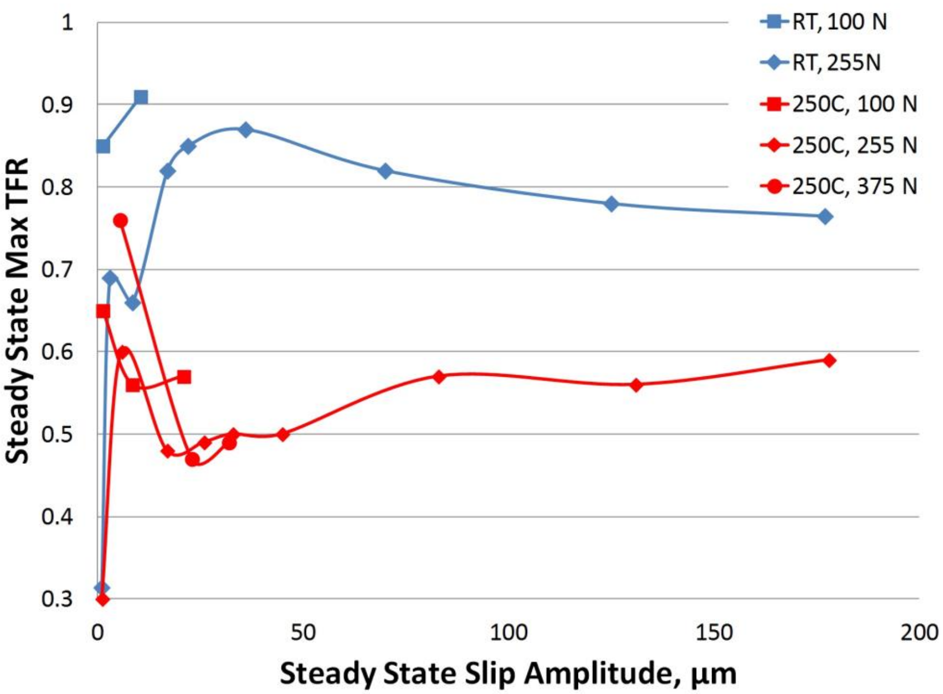

Figure 4.21: Steady state tangential force ratio versus steady state slip amplitude.

A comparison of the steady state COF values at RT and at 250^{o}C are shown for each normal force in Figure 4.22. The COF value was higher at room temperature for all conditions tested. The lower COF at 250^{o}C results in a larger slip amplitude for the same displacement amplitude compared to room temperature. The lower COF at 250^{o}C is due to the formation of a glaze oxide layer which is discussed in more detail in subsequent sections. The glaze oxide layer has a high hardness and low roughness that results in the lower COF. The COF was found to decrease with increasing displacement amplitude within the gross slip regime at room temperature, whereas the COF was found to increase with increasing displacement amplitude at 250^{o}C.

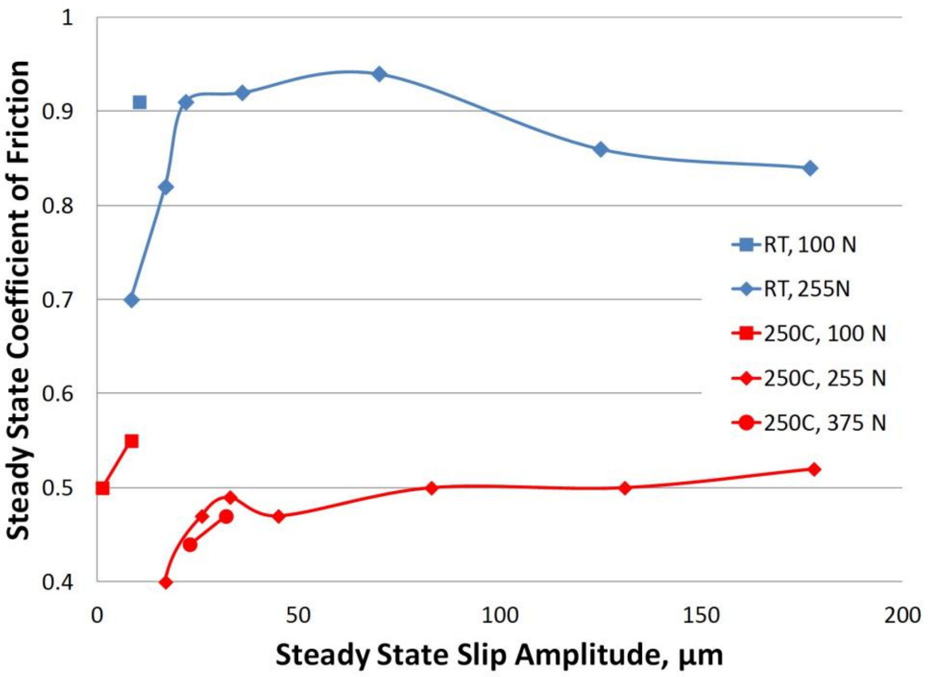

Figure 4.22: Steady state COF values for tests conducted at room temperature and 250^{o}C.

The total energy dissipated during each test conducted at 20^{o}C and 250^{o}C is shown in Figure 4.23. This was calculated based on the area of the stabilized hysteresis loop, which represented at least 90% of the test hysteresis loops for each test. Therefore, this result includes energy dissipated by means other than friction between the moving specimen and stationary specimen (e.g. friction between the stationary specimen and PTFE), necessitating finite element modeling to determine the local frictional energy dissipation. The amount of dissipated energy was higher for tests performed at 20^{o}C. This is a result of the higher tangential force at 20^{o}C. The decrease in COF at elevated temperature decreases the tangential force, but also increases the amount of slip. This tends to offset the difference in dissipated energy.

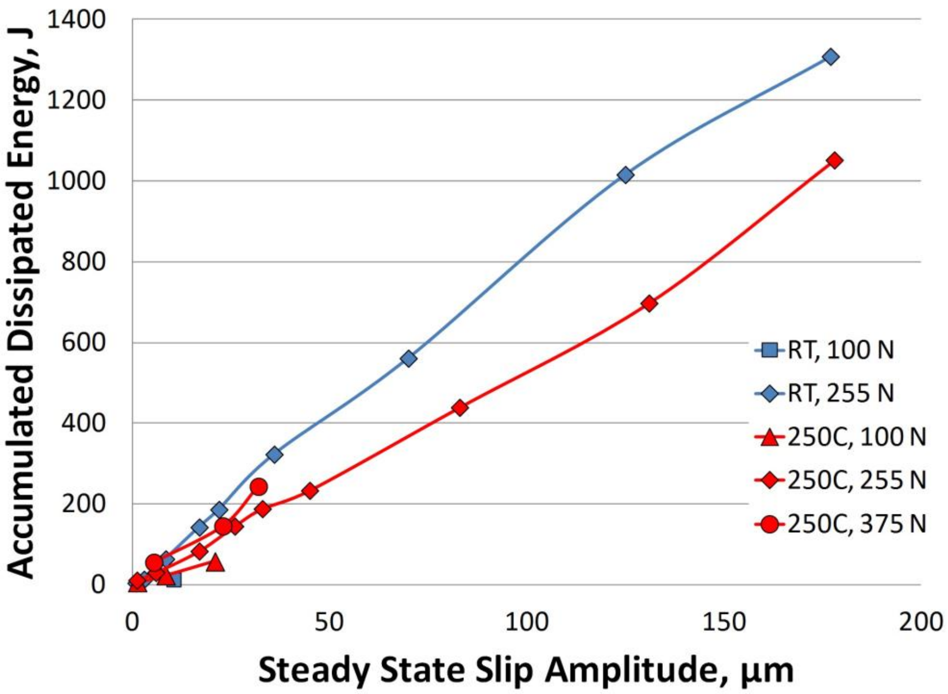

Figure 4.23: Accumulated dissipated energy.

A mixed slip running condition is typically characterized by an initial period of gross slip followed by partial slip which continues for the duration of the test. This is the observed behavior for tests conducted at room temperature for the conditions imposed in this work with both 52100 steel and A356 aluminum contact. However, the tests performed at 250^{o}C displayed the opposite behavior, with an initial period of partial slip followed by gross slip for the remaining duration of the test. This is caused by the formation of the glaze oxide layer which reduced the COF after the initial fretting cycles.

4.2.4 Gross Slip Fretting at High Temperature

Fretting tests were performed in contact with 52100 steel with a 200 µm displacement amplitude and 255 N normal force at temperatures from 20^{o}C to 550^{o}C in laboratory air and in argon. These conditions resulted in a gross slip running condition for all tests. The friction evolution as a function of temperature and atmosphere is shown in Figure 4.24. Tests conducted at room temperature had initially low coefficient of friction (COF) values that steadily increased to reach a stabilized value after approximately 10^3 cycles. Tests at elevated temperature had initial COF values that were more similar to the stabilized values, with the exception of the test conducted in argon at 250^{o}C which had a low initial value that increased rapidly to a high value before decreasing to the stabilized value after approximately 100 cycles. Stabilized values were reached more quickly for tests performed at higher temperatures. Testing in argon had an insignificant effect for the other temperatures investigated.

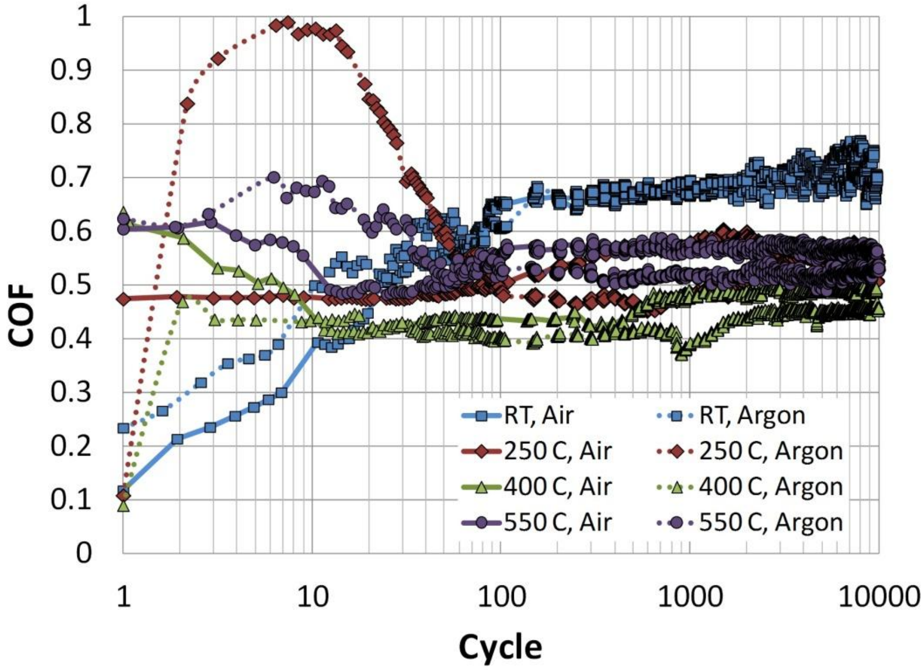

Figure 4.24: COF evolution during fretting at elevated temperature.

The stabilized COF values for each condition are shown in Figure 4.25. The steady state value was highest at room temperature and decreased with increasing temperature, with a slight increase at 550°C. This is consistent with the trend published for contact of annealed 304 stainless steel against itself [100]. Testing in argon had an insignificant effect on the stabilized values of the COF.

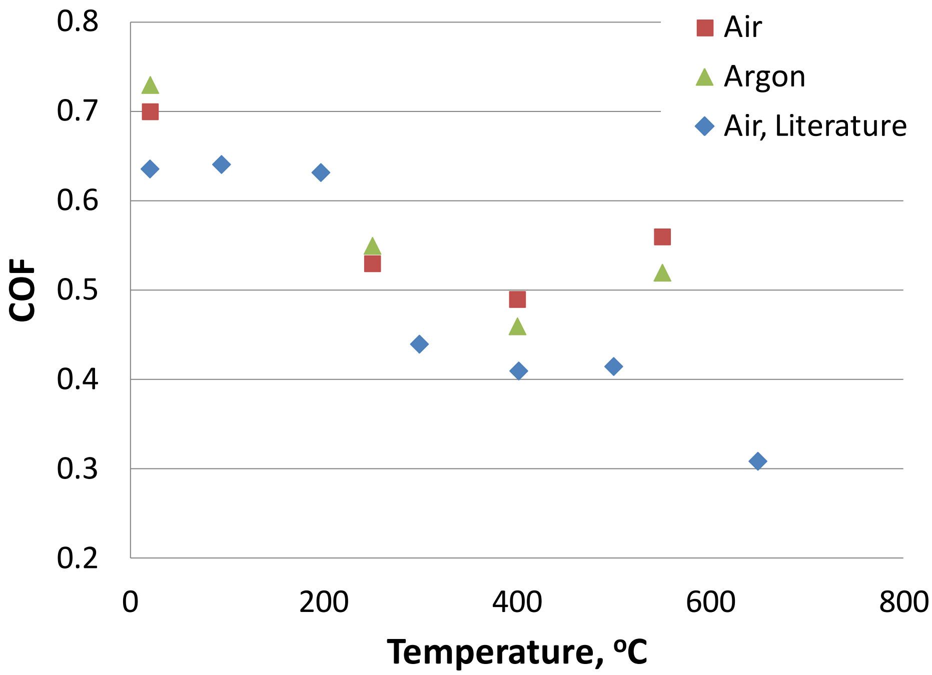

Figure 4.25: Steady state COF as a function of temperature and atmosphere including results reported in the literature [100].

The total energy dissipation over the duration of each test is shown in Figure 4.26. The dissipated energy was determined by summation of the hysteresis loop area measured for each cycle. The total dissipated energy decreased with increasing temperature. This is similar to the trend for the stabilized COF since the majority of the test exhibited the stabilized COF value. The effect of testing in argon was negligible except for the tests performed at 250°C where the test performed in air had a higher total dissipation. This is a consequence of the COF being higher for a longer portion of the test for the test conducted in air despite the stabilized value being similar.

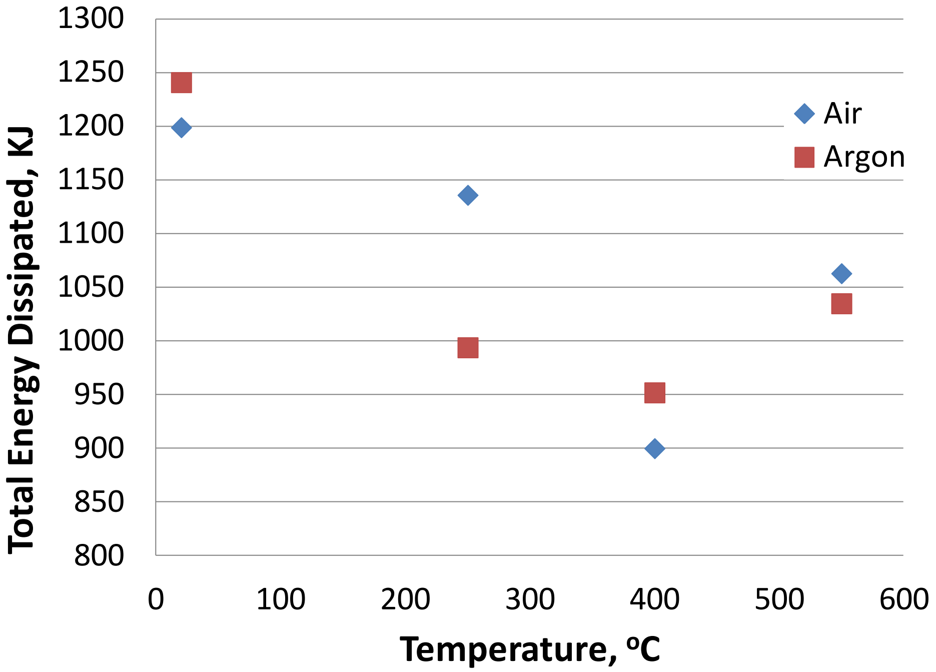

Figure 4.26: Total energy dissipated during the duration of fretting tests as a function of temperature and atmosphere.

4.2.5 Modeling Friction Evolution

Determination of the evolution of friction by using the accumulated dissipated energy makes it possible to assign an evolving COF value at different locations on the surface of a large system where the relative slip amplitude is variable over the contact surface. The COF evolution as a function of cumulative dissipated frictional energy per contact area for contact with 52100 with a 255 N normal force is shown in Figure 4.27. Representation of the COF evolution in terms of the cumulative dissipated energy per area results in a relationship that is less dependent on the displacement amplitude than when represented in terms of cycle count. Results with displacement amplitudes of 100 and 200 μm do not follow the same relationship as the other displacement amplitudes as strongly, however the relationship is generally stronger than when represented in terms of cycles.

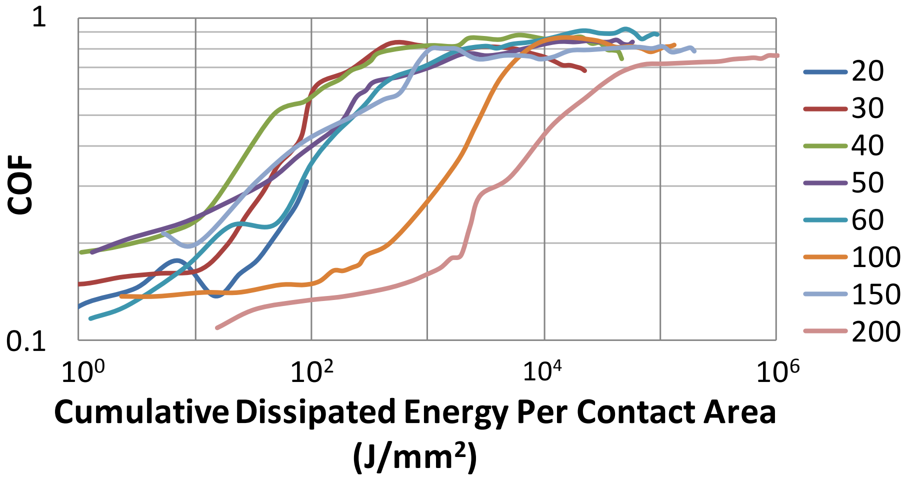

Figure 4.27: COF evolution for contact with 52100 with a 255 N normal force in terms of cumulative dissipated energy per contact area.

The representation of COF in terms of cumulative dissipated energy per contact area can be functionalized by

$$\mu = \mu_0 + \left(\frac{1}{1 + \left(\frac{E_f}{E_{ADED}} \right)^a} \right) \left(\mu_{sat} - \mu_0 \right) \tag{4.2}$$

where μ_0 is the initial COF, μ_{sat} is the stabilized COF, and a and E_f are parameters that control the location and rate of COF increase. A fit was created using the values shown in Table 4.2 and is shown in Figure 4.28.

Table 4.2: Constants used for representation of COF evolution for contact with 52100 steel at room temperature.

a	E_f (mJ/mm^2)	μ_{sat}	μ_0
1	220	0.83	0.14

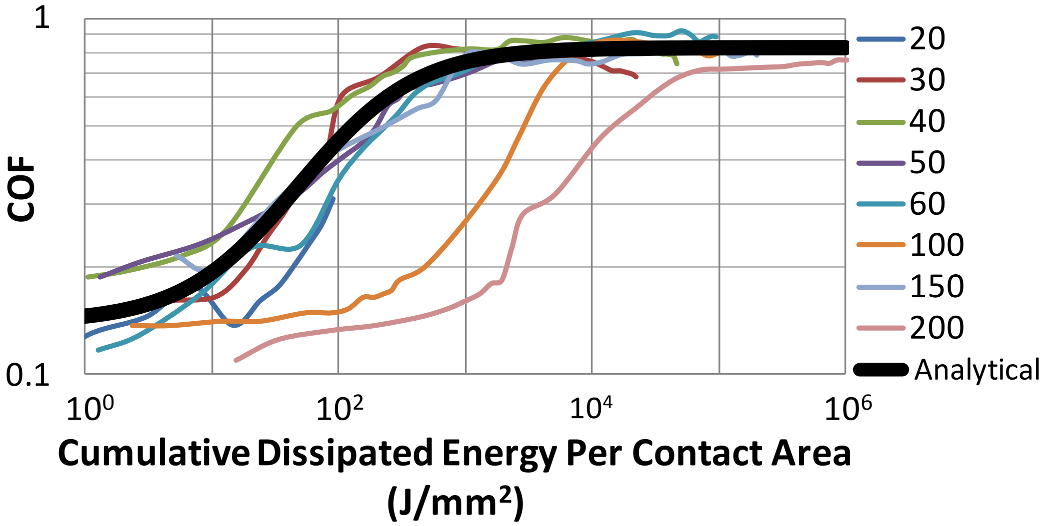

Figure 4.28: COF evolution for contact with 52100 steel with a 255 N normal force shown with an analytical representation.

The COF evolution for contact with A356 aluminum did not demonstrate a trend similar to that of 52100 as shown in Figure 4.29. The COF was found to decrease after reaching a maximum between 10 and 100 cycles. However, the maximum TFR was found to follow a similar trend as the COF evolution for contact with 52100 steel with a 255 N normal force as shown in Figure 4.30.

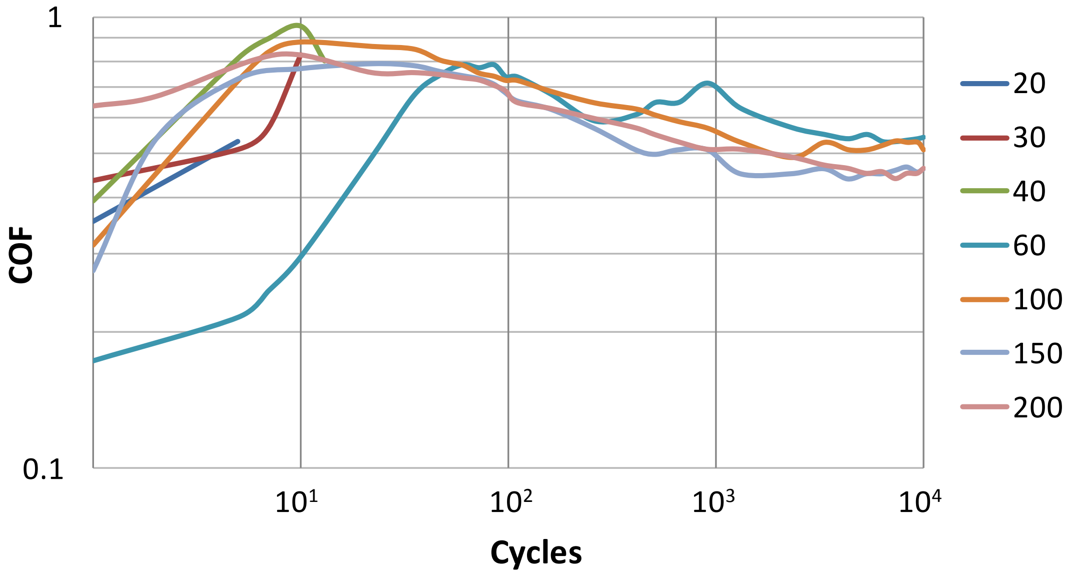

Figure 4.29: COF evolution for contact with A356 aluminum with a 255 N normal force.

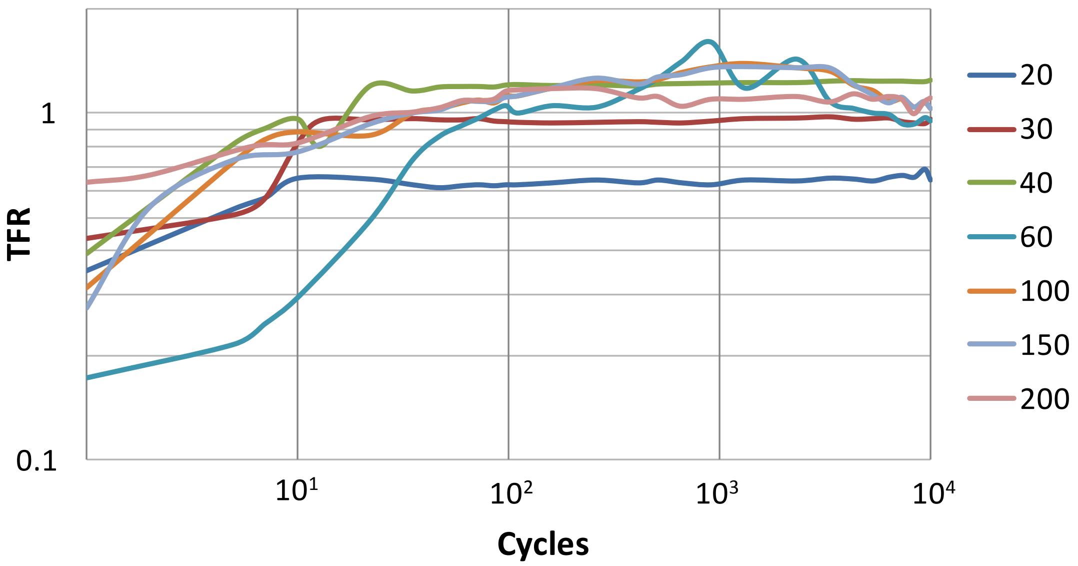

Figure 4.30: Maximum TFR evolution for contact with A356 aluminum with a 255 N normal force.

The maximum TFR evolution for contact with A356 aluminum is driven by adhesive wear resulting in transfer of aluminum to the stainless steel that causes a plowing effect [145, 172]. The extent of material transfer is also related to the energy dissipated by friction. Therefore, representation of the maximum TFR evolution can be represented as a function of cumulative energy dissipation per contact area as shown in Figure 4.31. The cumulative dissipated energy for contact with aluminum was calculated using equation (1). Partial slip hysteresis loops were included toward the accumulation of energy by using the maximum TFR in place of the COF and using the steady state partial slip hysteresis loop width for all partial slip cycles.

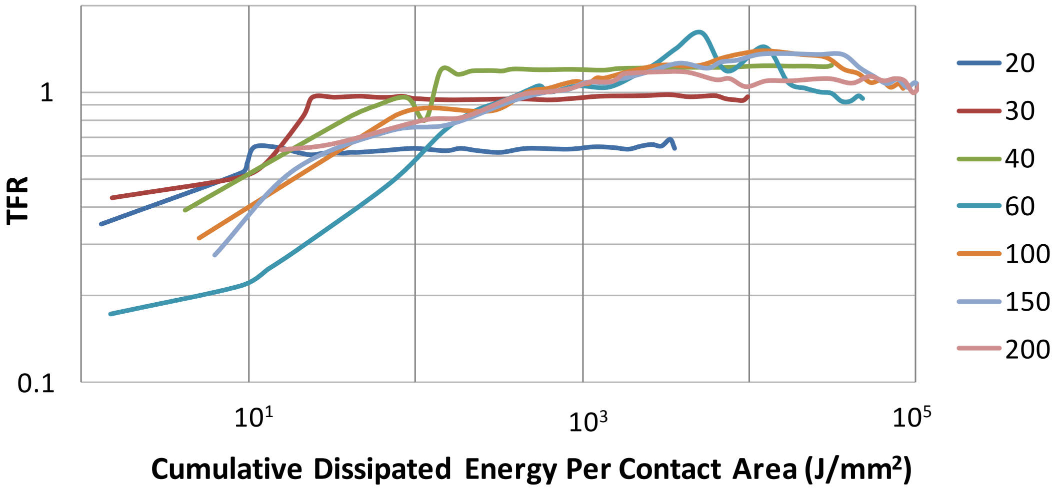

Figure 4.31: Maximum TFR evolution for contact with A356 aluminum with a 255 N normal force represented in terms of cumulative dissipated energy per contact area.

An analytical representation of the maximum TFR evolution for A356 aluminum was created using equation (2) and is shown in Figure 4.32. Values of the constants for this fit are shown in Table 4.3.

Table 4.3: Constants used for representation of maximum TFR evolution for contact with A356 aluminum.

a	E_f (mJ/mm^2)	TFR$_{sat}$	TFR$_0$
1	40	1.14	0.33

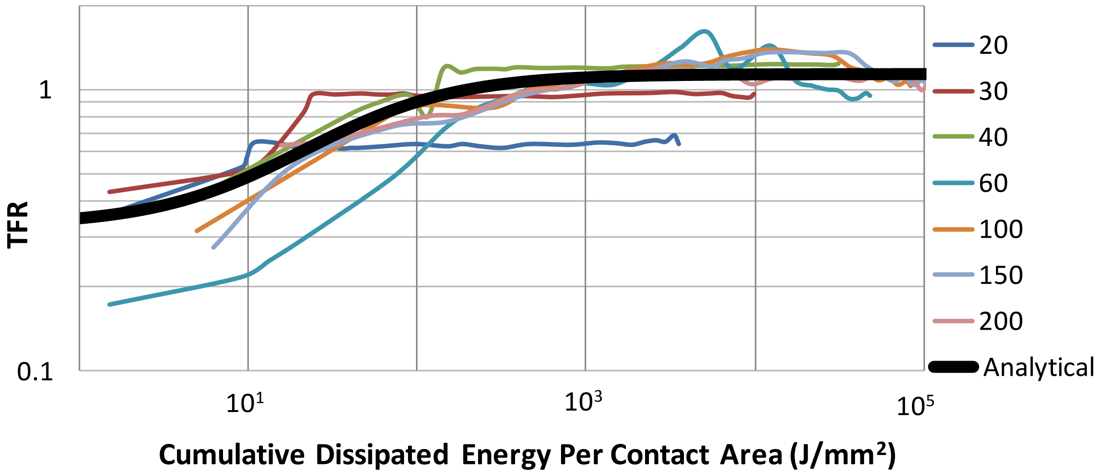

Figure 4.32: Maximum TFR evolution for contact with A356 aluminum with a 255 N normal force with an analytical representation.

The method for implement COF evolution into a finite element model to determine the level of fatigue damage is shown in Figure 4.33. The fatigue damage can be summed at each location using a fatigue damage accumulation rule such the Palmgren-Miner Rule. The method shown requires the use of a user subroutine to change the value of the COF locally based on the contact history. Variation in the COF over the surface of the contact will have a significant effect on the cyclic stress strain behavior and is important to consider when performing a fatigue analysis of a system involving large contact areas. An alternative method is to manually change the COF over the entire surface based on the average dissipated energy density over the whole surface. This method is less accurate, however the implementation difficulty is greatly reduced and may be preferable to using a constant COF.

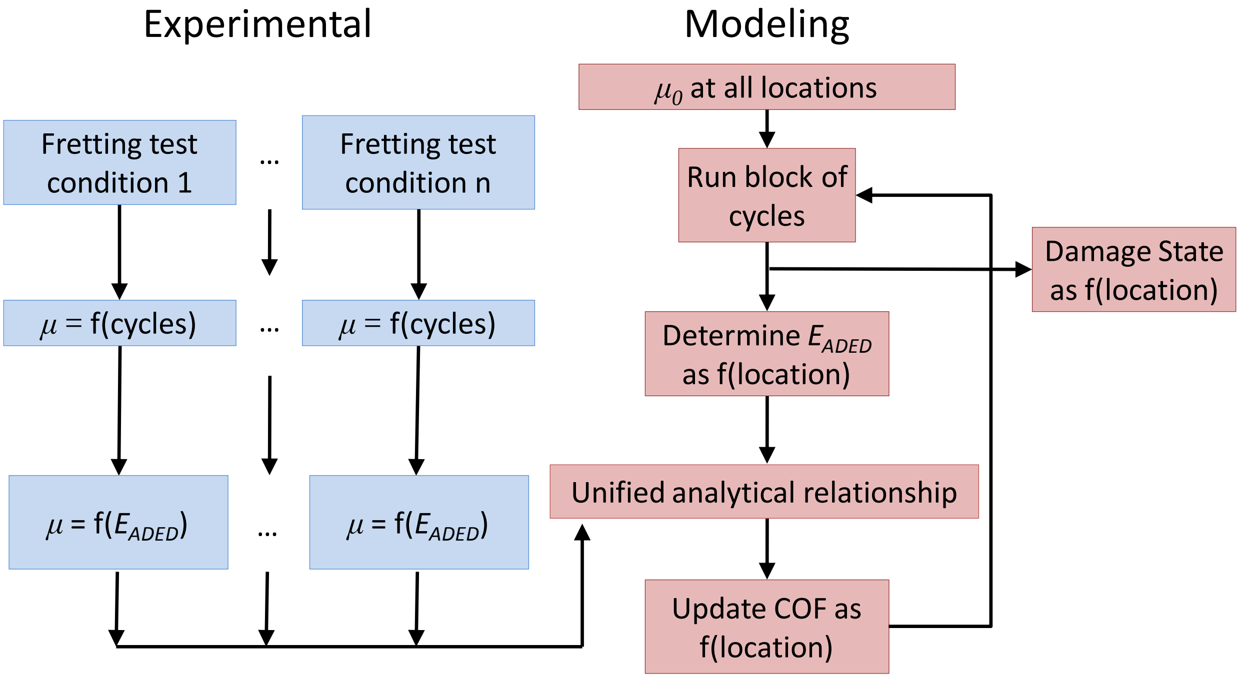

Figure 4.33: Method for utilization of COF evolution relationship.

4.3 Fretting Wear Behavior

The fretting wear behavior was investigated by observation and XRD of the fretting debris to determine the composition and profilometry to determine the wear volume for various conditions tested. This was done to characterize the type and extent of wear which occurred for each test condition to understand the role of wear on the level of fatigue damage resulting from fretting.

4.3.1 Fretting Scar Appearance

The fretting scars resulting from a mixed slip running condition and a gross slip running condition for contact with 52100 with a normal force of 255 N is shown in Figure 4.34. When the displacement amplitude was 20 μm, the scar was light with a typical iron oxide color and almost no visible wear debris. A 200 μm displacement amplitude resulted in large amounts of oxide and wear debris. The composition of the debris was fine with a small amount of larger particles, indicative of abrasive wear. Because the specimens are vertical during testing, it is possible that larger debris was generated but fell from the sample. However, it is believed that the amount of larger debris was insignificant. Clumping of the fine debris may be caused by magnetism in the ferromagnetic α' wear debris.

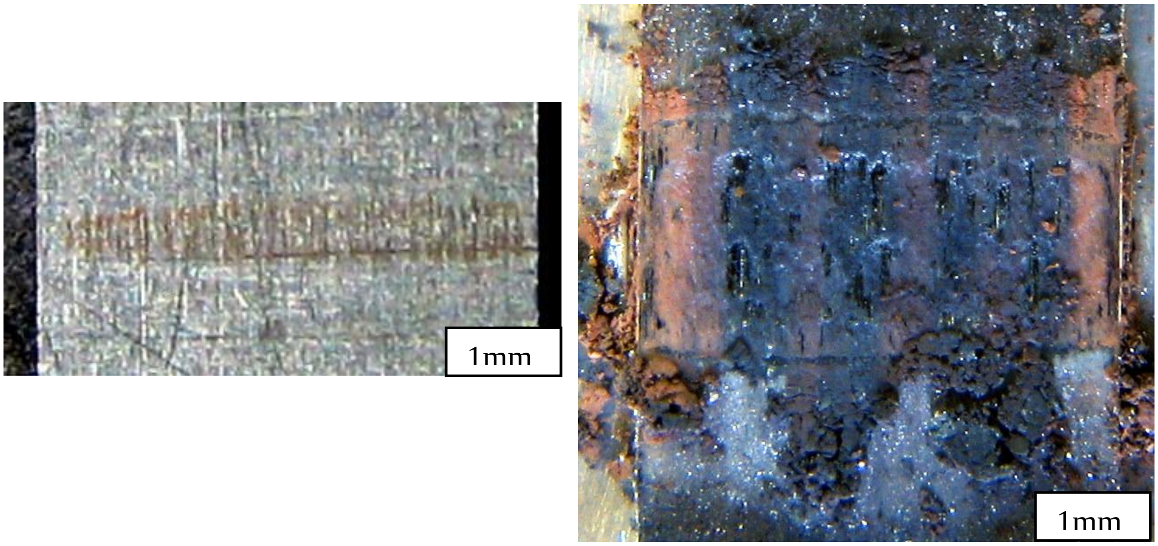

(a) (b)

Figure 4.34: Scars generated on 301 during fretting against 52100 with normal force of 255 N and displacement amplitudes of (a) 20 µm and (b) 200 µm.

Figure 4.35 shows the resulting fretting scars from contact of 301 with A356 with a normal force of 255 N for mixed slip and a gross slip running conditions. In the mixed slip regime the fretting scar is reflective, which indicates a lack of oxidation and transfer of aluminum to the 301 specimen. At larger displacement amplitudes the transfer of aluminum became obvious, and an increasing amount of black wear debris formed. Black cubic alumina (γ-Al_2O_3) has been found to form during fretting in other studies [13, 18, 36]. The moving specimen formed a hemi-cylindrical trough due to the loss of material.

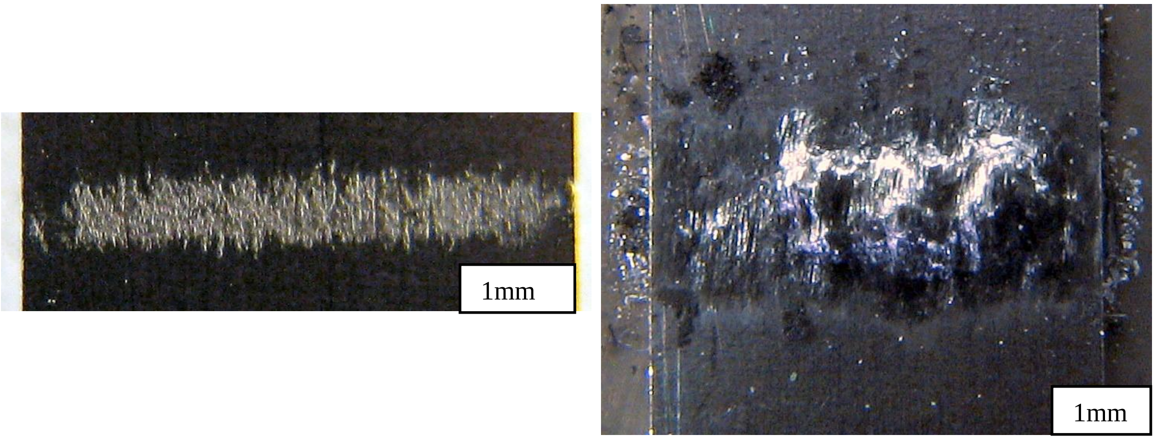

(a) (b)

Figure 4.35: Scars generated on 301 in fretting against A356 with a normal force of 255 N and displacement amplitudes of (a) 20 μm and (b) 200 μm.

Optical microscope images of scars resulting from contact with A356 and 52100 at 20 μm displacement amplitudes are shown in Figure 4.36. Both cases show signs of rough-surface contact. Both scars show portions of intact 301 between bands of contact which are oriented in the fretting direction. For the specimen in contact with A356 the contact resulted in transfer of A356 to the 301 and contact with 52100 caused wear of the 301 and the formation of oxide.

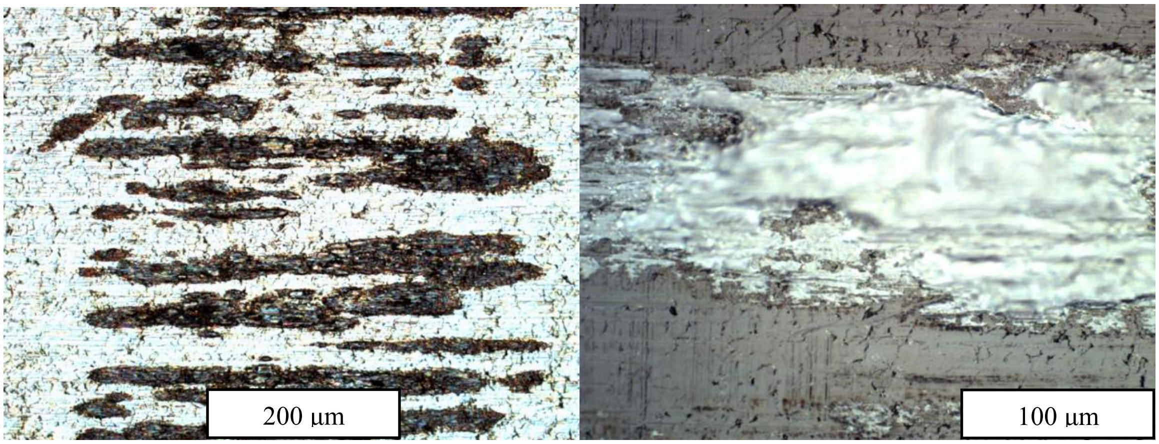

(a) (b)

Figure 4.36: Optical images of fretting scars resulting from a normal force of 375 N and a 20 μm displacement amplitude against (a) 52100 and (b) A356.

The profiles of scars were examined by sectioning. Polished samples were observed with an optical microscope to measure the depth of wear or the thickness of transferred material. The profiles of scars resulting from fretting tests with a normal force of 255 N are shown in Figure 4.37. Contact with A356 resulted in transfer of aluminum for all tests in the mixed slip and gross slip regimes with thicker layers for higher displacement amplitudes. The composition of the layer is mostly metallic with black oxide particles up to 20 μm in diameter distributed throughout.

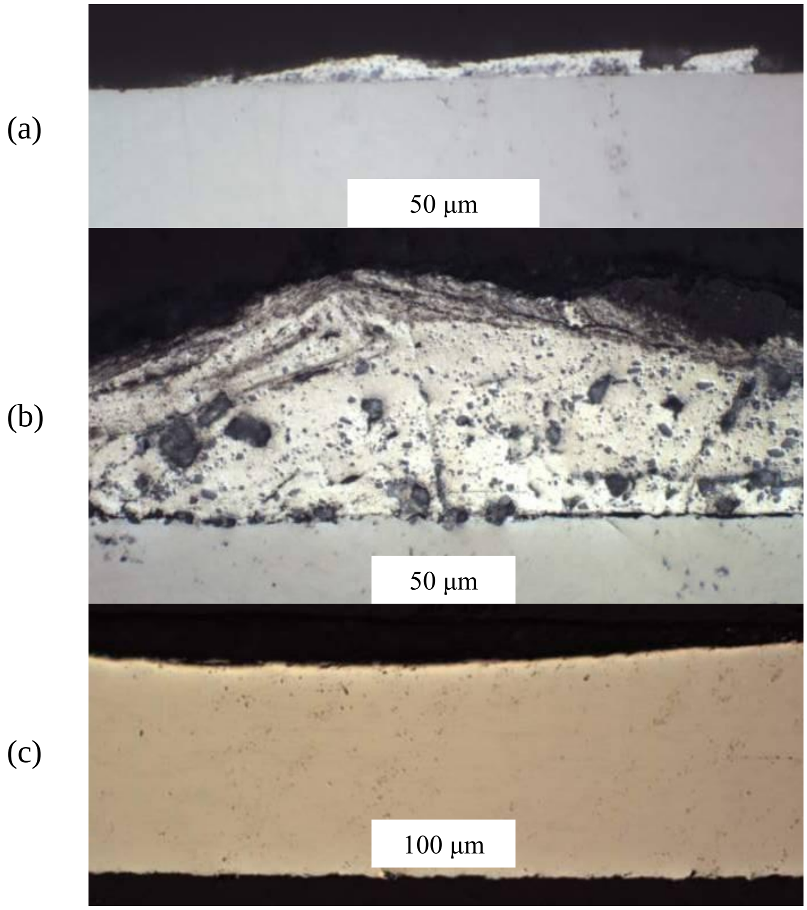

Figure 4.37: Profile of scars generated using a normal force of 255 N for contact with (a) A356 with a 40 μm displacement amplitude, (b) A356 with a 200 μm displacement amplitude, and (c) 52100 with a 200 μm displacement amplitude.

The debris resulting from fretting in air at both room temperature and 400°C are shown in Figure 4.38. The debris resulting from fretting at room temperature demonstrated clumping that was evident when observed using optical microscopy as well as SEM which indicates the presence of magnetic particles of oxide or martensite [90]. Debris generated at 400°C had a finer appearance and did not exhibit clumping in the optical microscope or SEM. The production of finer wear debris with increasing temperature has been related to the extent of transformation of austenite to martensite, with less transformation resulting in finer debris [173]. The color of the debris resulting from tests at room temperature and 250°C varied between shades of orange, typically Fe_2O_3, and black, typically Fe_3O_4, with a heterogonous distribution. The color of the debris transitioned to a homogenous shade of orange as temperature increased. There was no discernible change in the appearance of the oxide caused by testing in argon at any of the temperatures considered. It is likely that the majority of the iron oxide was generated by the 52100 steel due to the low resistance to oxidation.

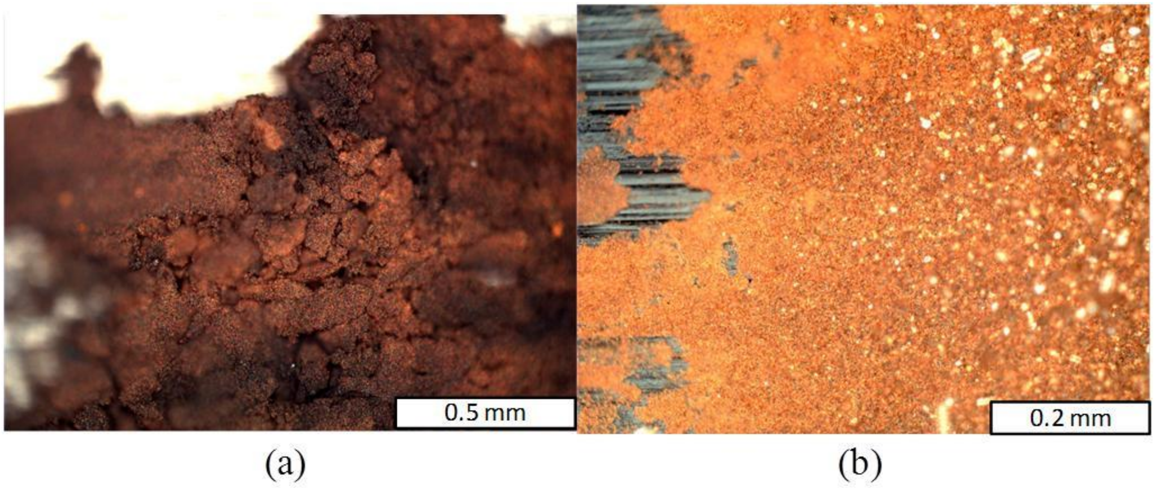

Figure 4.38: Oxide produced from fretting in air at (a) 20°C and (b) 400°C.

An example of the abundance of wear debris present on the sample after fretting is shown in Figure 4.39. Room temperature fretting tests resulted in a significantly higher amount of debris present both in and around the fretting scar than at higher temperatures. Tests performed at elevated temperature showed little oxidation of the material within the scar compared to the surrounding material. Scars at elevated temperature had long, smooth grooves which is typical for glaze oxides [174-175] and has been shown to form for 321 stainless steel at elevated temperature in CO_2 [31].

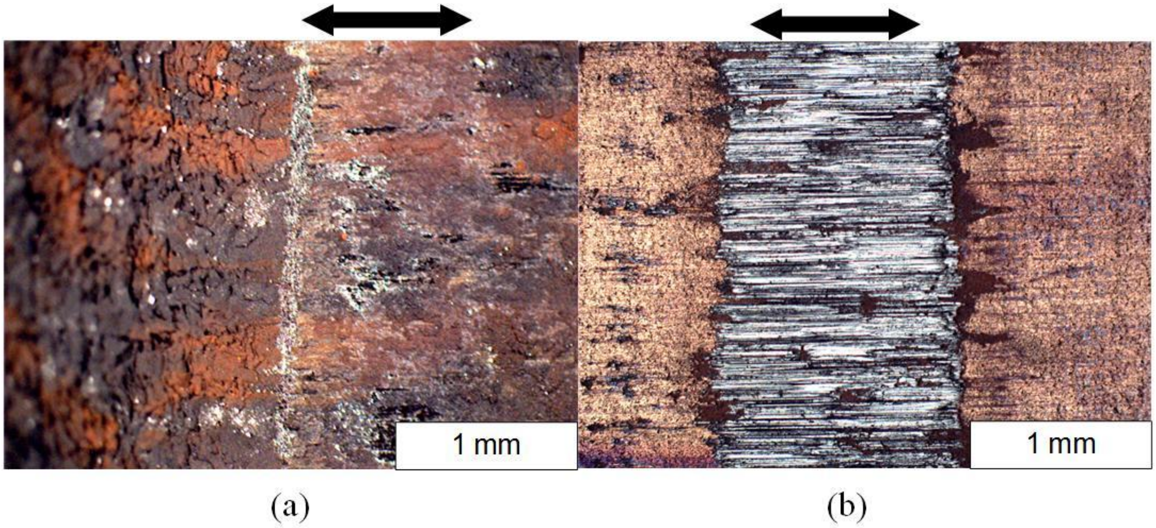

(a) (b)

Figure 4.39: Fretting scars produced from fretting in air at (a) 20^{o}C and (b) 550^{o}C.

The distribution of martensite resulting from fretting at 20^{o}C in air and the subsurface resulting from fretting at 550^{o}C in argon is shown in Figure 4.40. Specimens were etched using Beraha's reagent (100 ml H_2O, 10 ml HCl, 2 g $K_2S_2O_5$ immersed with agitation for 2 minutes) to reveal the austenite and martensite distribution through the depth of the specimen surrounding the fretting scar. Fretting at room temperature was found to cause formation of a layer of martensite on the surface with a depth of approximately 15 µm as shown in Figure 4.40(a). This is expected since room temperature is below M_d and therefore transformation from austenite to martensite is possible. Tests conducted at elevated temperature exceeded the M_d temperature thus eliminating transformation to martensite. Therefore, an increase in martensite near the surface did not occur for elevated temperature tests. A glaze oxide was found to form at elevated temperature as shown in Figure 4.40(b). This layer was not found outside of the contact region. Cracks were found to form near the edge of contact emanating from the interface of the oxide layer and the substrate. The cracks do not appear to propagate into the bulk of the specimen, and therefore may not have resulted in a decrease in residual fatigue life.

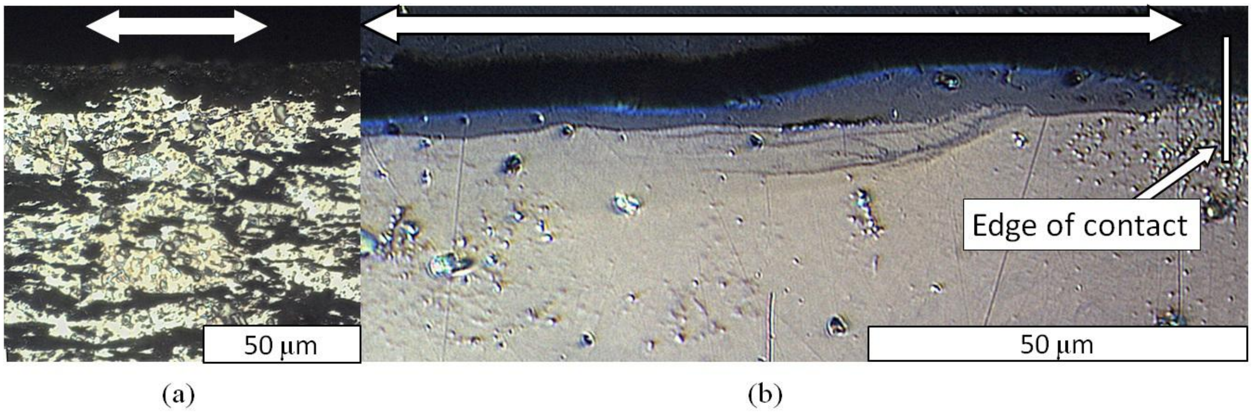

Figure 4.40: Optical images through the depth of 301 stainless steel specimens showing (a) austenite (light) and martensite (dark) phase distribution resulting from fretting at room temperature and (b) glaze oxide resulting from fretting at 550^{o}C.

The oxide composition as a function of temperature was investigated using X-ray Diffraction (XRD). Specimens were cut so that the fretting scar represented a large portion of the total area scanned. The baseline material was scanned for comparison. The results of the XRD analysis showed changes in the chemical composition of the oxide debris with changing temperature. Fe_2O_3 was found to be present at all temperatures. Increasing amounts of Fe_3O_4 was found as temperature increased, however Fe_2O_3 was still the dominant composition at all temperatures investigated. The oxide composition has been shown to transition from Fe_2O_3 to Fe_3O_4 more distinctly over the range of temperatures investigated in published work which used lower contact pressure and longer duration tests [100]. The low fretting debris quantity at elevated temperature may have contributed to the apparent inconsistency since the amount of oxide present from fretting is lower relative to the oxide present on the surrounding material.

An estimate of the expected fretting scar width in the direction of fretting can be made based on the sum of the Hertz contact width (2a) and the displacement range. The experimentally observed widths of the fretting scars are approximately three times the width expected based on this calculation for all displacement amplitudes tested assuming each body is semi-infinite. For example, for a 20 μm displacement amplitude with a normal force of 255 N for contact of 301 with 52100 the expected scar width based on Hertz is 0.20 mm, whereas the average observed width is about 0.60 mm. Similarly, for the 200 μm displacement amplitude case the calculated and actual average scar widths are 0.56 and 2.20 mm respectively. The measured scar widths and the widths calculated based on a Hertz analysis for various displacement amplitudes and a normal force of 255 N for contact of 301 with both A356 and 52100 is shown in Figure 4.41. A test conducted between 301 and 52100 for 100 cycles with a displacement amplitude of 50 μm and a normal force of 255 N generated an average scar width of approximately 0.40 mm compared to a width of 0.95 after 10^4 cycles and an expected width of 0.26 mm. This difference is related to the initial roughness and wear. Another contributor to the increased contact width is the 89 μm thick compliant layer of PTFE between the specimen and the backing plate. The PTFE causes the specimen to conform to the contacting cylinder, thereby causing bending of the specimen. This indicates that it is not appropriate to assume that the specimen is flat in the analysis to determine the cyclic fretting contact stresses and that the PTFE layer needs to be taken into account in the cyclic stress analysis.

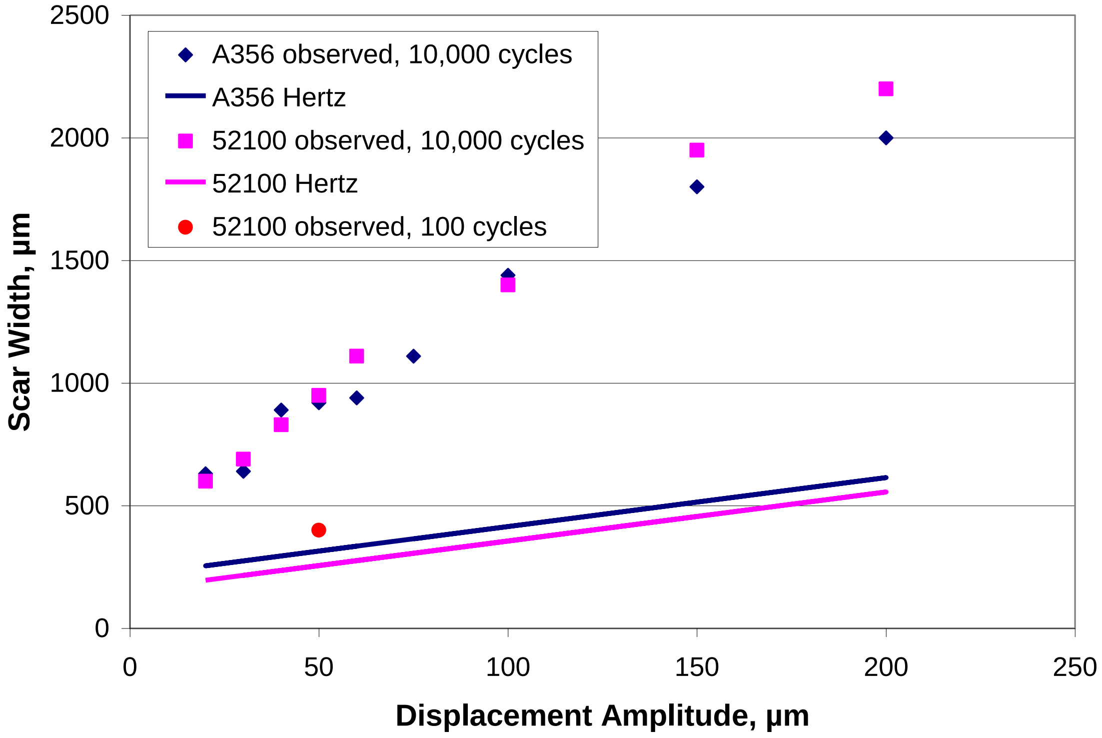

Figure 4.41: Average scar widths for contact of 301 with A356 and 52100 with a normal force of 255 N for various displacement amplitudes where points are experimental results and lines are calculated based on a Hertz analysis.

The Hertz semi-contact-width (*a*) for a normal force of 255 N between 301 and 52100 is 78 µm. Therefore, the onset of reciprocating sliding would occur at a displacement amplitude of 78 µm for the idealized configuration. For A356 against 301 for a normal force of 255 N the Hertz semi-contact-width is 107 μm, and would transition to reciprocating sliding at 107 μm. However, the transition to reciprocating sliding will take place at a higher amplitude due to the increased contact size. The initial transition amplitude is approximately 150 μm for contact with 52100 based on the scar size after 100 cycles with a normal force of 255 N and 50 μm contact force when wear was not significant.

4.3.2 Fretting Wear Volume

The height of aluminum deposited on 301 for contact with A356 and the depth of wear of 301 from contact with 52100 for various displacement amplitudes and a normal force of 255 N determined by inspection of the sectioned samples is shown in Figure 4.42. Both the height of deposit and depth of wear increased with increasing displacement amplitude. The aluminum deposit reached a maximum of 80 μm for a displacement amplitude of 200 μm, and the maximum wear depth was 30 μm.

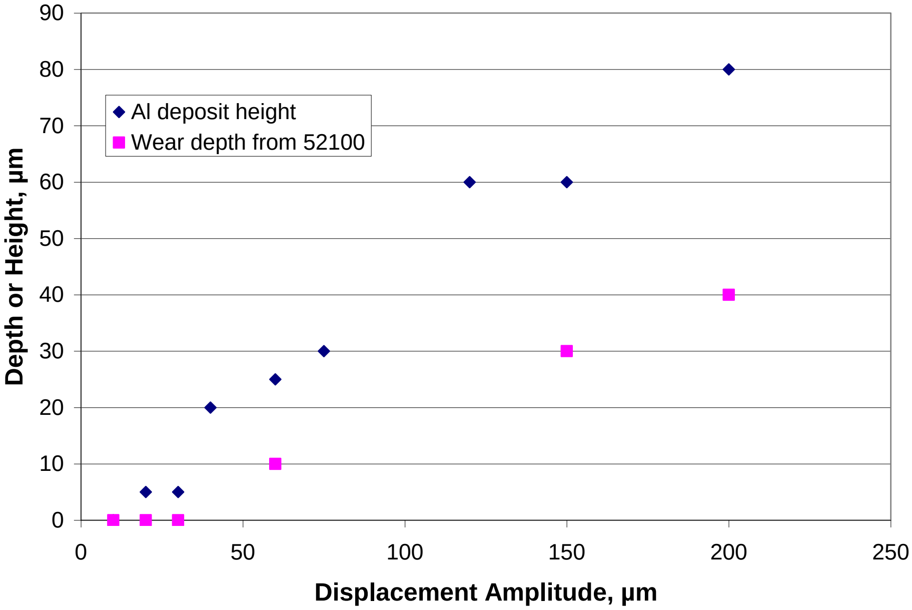

Figure 4.42: The height of aluminum deposited on 301 resulting from contact with A356 and the depth of wear of 301 resulting from contact with 52100 for various displacement amplitudes and a normal force of 255 N.

Wear profiles were measured by stylus profilometry of the wear scars. Three line scans were performed in the direction of fretting motion at locations spaced evenly along the full width of the fretting scar. The reverse side of the sheet specimens were scanned for cases which exhibited plastic deformation to determine the curvature which was subtracted from the scar profile for a more accurate wear measurement. The wear volume on cylindrical specimens was determined by subtraction of the wear profile from the initial cylindrical profile. Wear volumes were calculated by averaging the three wear profiles and multiplying by the scar width. An example of the wear profile measured for a gross slip running condition using 52100 at room temperature is shown in Figure 4.43.

Some height increase was found near the edge of contact, indicating either plastic deformation or embedding of wear debris.

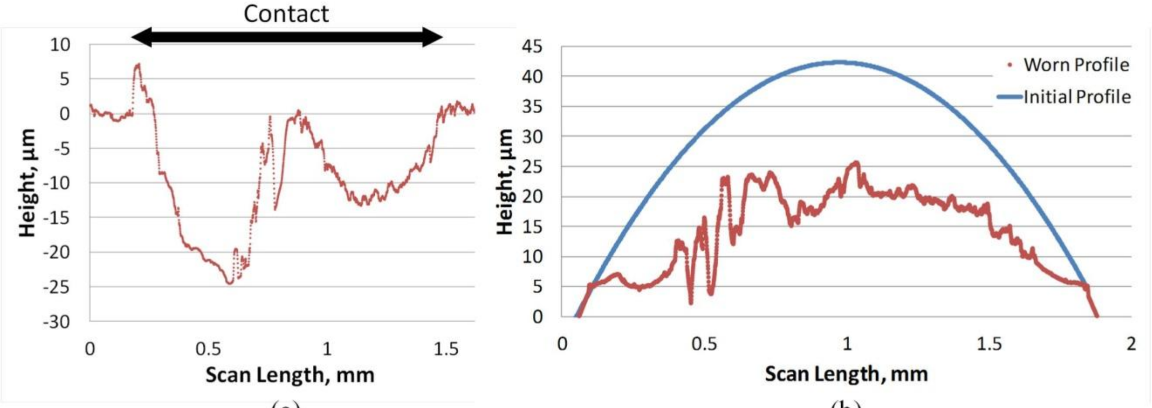

(a) (b)

Figure 4.43: Wear profiles resulting from fretting in air at room temperature for (a) the flat stationary specimen and (b) the cylindrical moving specimen.

The wear volumes measured for contact with 52100 with a 200 μm displacement amplitude and 255 N normal force are shown in Figure 4.44. A large reduction in the wear volume occurred between tests conducted at 20^{o}C and 250^{o}C. The total wear volume was found to be negative for tests conducted at elevated temperature, meaning there was a net gain of volume during fretting. The decrease in wear volume and positive volume change was found in other work for contact of 304 stainless steel against itself [100] as shown in Figure 4.44. The conditions imposed in that study were similar to the conditions here with the exception of the contact pressure, which had an average pressure equal to approximately 13% of the average pressure in this study. The positive volume change was attributed to embedding of oxide debris into the surface since Fe_2O_3 and Fe_3O_4 have volumes that are 2.15 and 2.01 times that of iron, respectively [100]. The positive volume change of 2.87% associated with the transformation from γ to α' [176] is not a contributing factor for the temperatures at which the positive volume change is observed since these temperatures exceed M_d and therefore prohibit transformation.

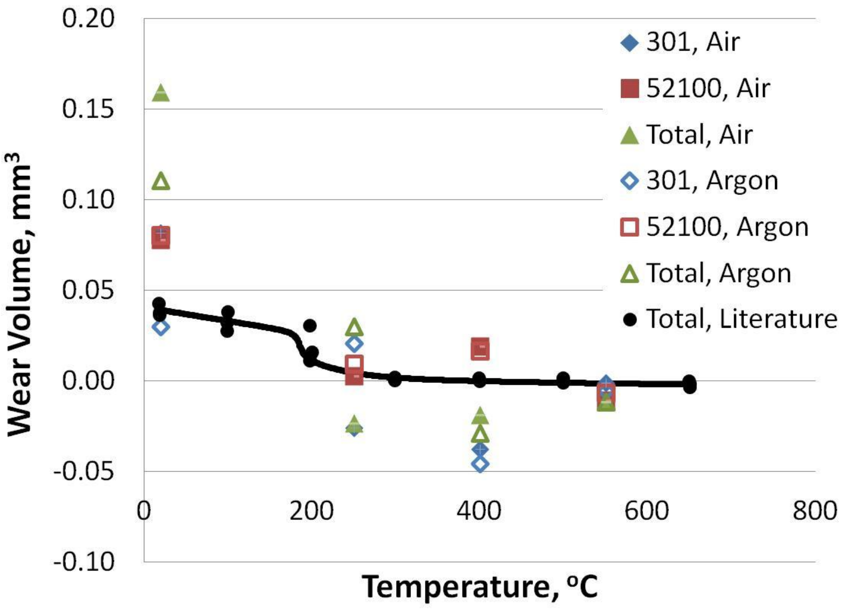

Figure 4.44: Wear volumes measured as a function of temperature for fretting tests in air compared to published data for contact between 304 stainless steel [100].

The wear rate in terms of wear volume per energy dissipated as a function of temperature for the same conditions is shown in Figure 4.45. The wear rate was found to decrease with increasing temperature with a drastic change occurring between 20°C and 250°C corresponding to the decrease in wear volume that occurred over the same temperature range. This shows that the decrease in the wear volume is not purely a result of the decreased energy dissipation that occurs at elevated temperature as a result of the lower COF values.

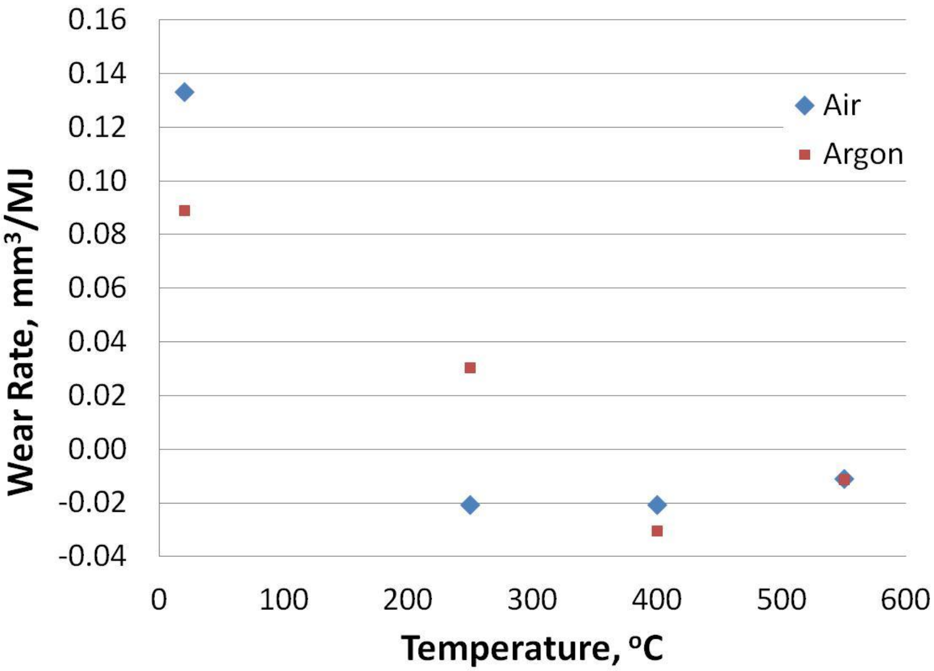

Figure 4.45: Wear rate as a function of temperature.

The total accumulated dissipated energy for each test for both room temperature and 250°C is shown in Figure 4.46. The dissipated energy is lower for tests conducted at 250°C due to the decrease in the slip amplitude resulting from the increased compliance of the test system and the lower COF resulting from the glaze oxide. The decreased amount of energy dissipation is partly responsible for the decreased amount of wear that occurred for tests conducted at 250°C, however the decrease in wear is expected to be much greater than the decreased energy dissipation. This indicates an increase in the wear resistance of the material, which is associated with the oxide composition [100]. A transition in the oxide composition from Fe_2O_3 to Fe_3O_4 occurs between room temperature and 250°C and has been attributed as the cause of a decrease in wear rate at elevated temperature.

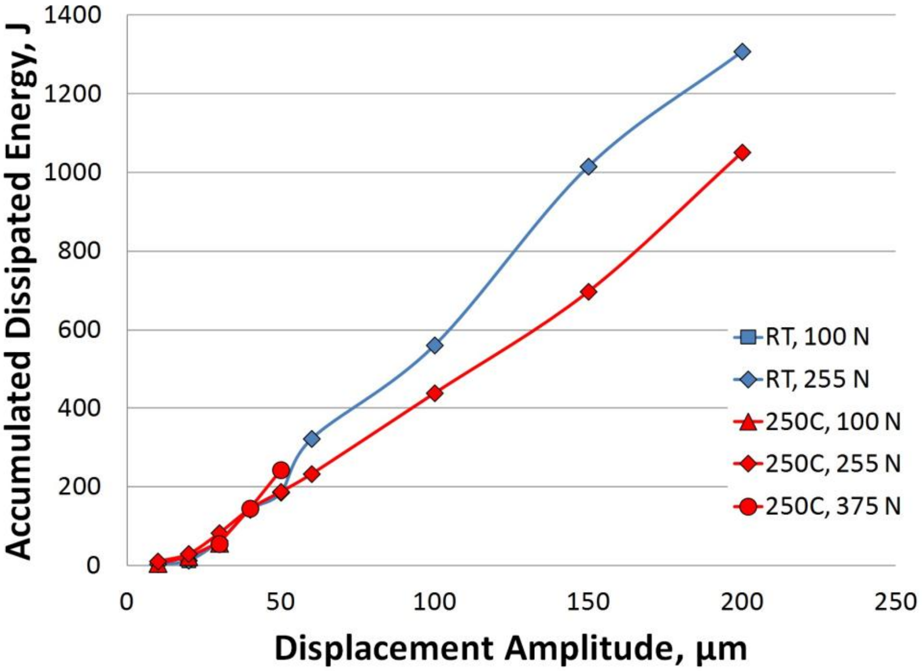

Figure 4.46: Total accumulated dissipated energy versus imposed displacement amplitude.

4.4 Fatigue Damage Due to Fretting

The impact of the fretting damage on the fatigue behavior was determined by performing fatigue tests on dog-bone specimens containing fretting damage using the same method described in Section 3.3.1. Subjecting the damaged specimens to cyclic stress either causes cracks to form and grow in the fretting damaged volume or causes cracks present from fretting to grow. Fretting conditions that are more severe result in a shorter life.

A planar crack in a sample sectioned parallel to the fretting direction in a specimen with fretting damage generated with a displacement amplitude of 60 μm and a normal force of 255 N for contact with 52100 is shown in Figure 4.47. The crack formed near the right edge of contact at an angle of 50 degrees from the surface and is approximately 100 μm in length. Cracks were not found in other samples, including samples tested under the same conditions. Cracks are less likely to form using the test setup in this work because of the bending of the specimens caused by the compliant layer of PTFE. The bending causes compressive normal stress parallel to the contact surface where cracks would form.

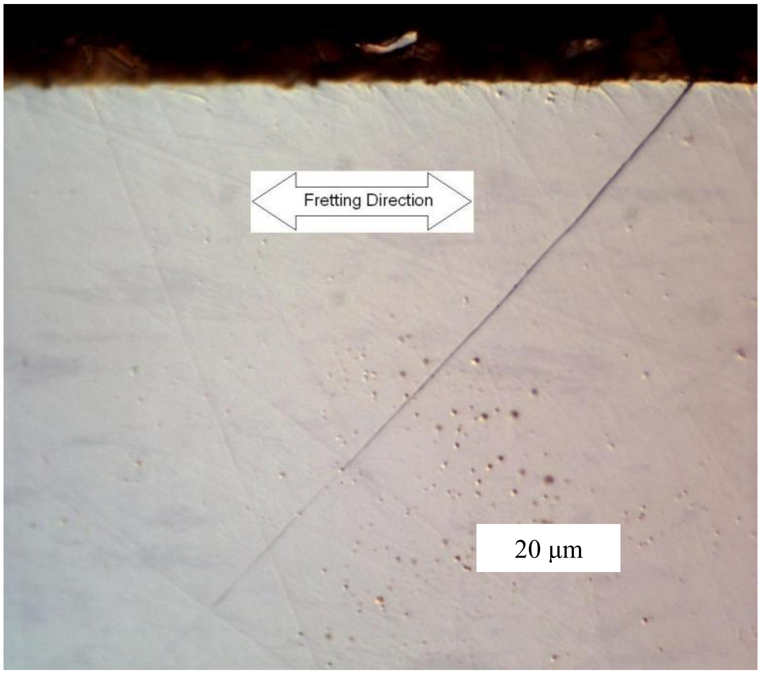

Figure 4.47: A planar crack near the right edge of contact formed after 10^4 cycles of fretting at a normal force of 255 N and displacement amplitude of 60 μm against 52100.

The fatigue response of specimens containing fretting damage generated by contact of 301 with 52100 at a displacement amplitude of 60 μm and normal force of 255 N for 10^4 cycles is compared to the response of the undamaged material in Figure 4.48.

The fatigue limit of the fretting-damaged material is 257 MPa, compared to the undamaged fatigue limit of 468 MPa at R = 0.05. Hence, for this fretting condition there was a 45% knockdown in fatigue strength. This is a more severe knockdown in fatigue strength than the 30% maximum knockdown that has been found using other 300 series stainless steel in the annealed condition in contact with itself [101].

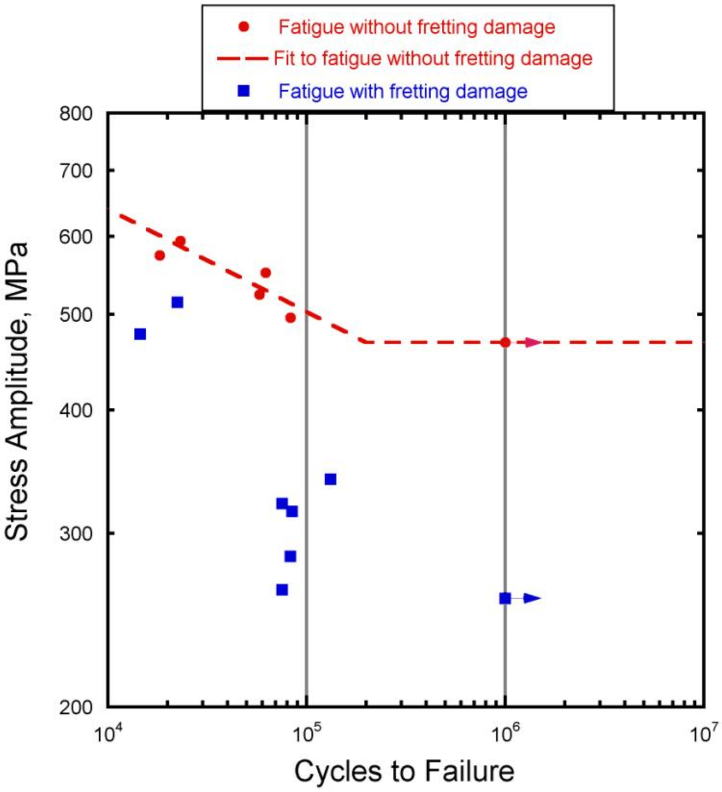

Figure 4.48: Knockdown in fatigue life due to fretting of 301 against 52100 with a normal force of 255 N and displacement amplitude of 60 μm for 10^4 cycles.

The variability of the level of fatigue damage due to fretting is demonstrated by the scatter in the subsequent fatigue life results of specimens subjected to fretting compared to the scatter in the fatigue life results of specimens that were not subjected to fretting. The additional variability in the lives of the samples subjected to fretting is related to the variability of the friction behavior and the material structure. The thickness of the specimens and the contact size are small relative to the grain size, thus the variability of the grain orientation in the area of the highest fatigue damage driver has a larger impact on the resulting fatigue life than would be the case for a finer grain structure or larger contact and specimen sizes.

The front and back of a specimen subjected to fretting against 52100 for 10^4 cycles with a normal force of 255 N and 60 μm displacement amplitude and subsequently cycled to failure at a stress amplitude of 468 MPa and R = 0.05 is shown in Figure 4.49. Examination of the back of the specimen where it is easy to distinguish features because of the lack of a fretting scar shows the presence of multiple initiation sites toward the center of the specimen. Cracks grew outward until the final rupture of the specimen as made evident by the deformation bands on both edges of the specimen. This was a typical result across all conditions tested.

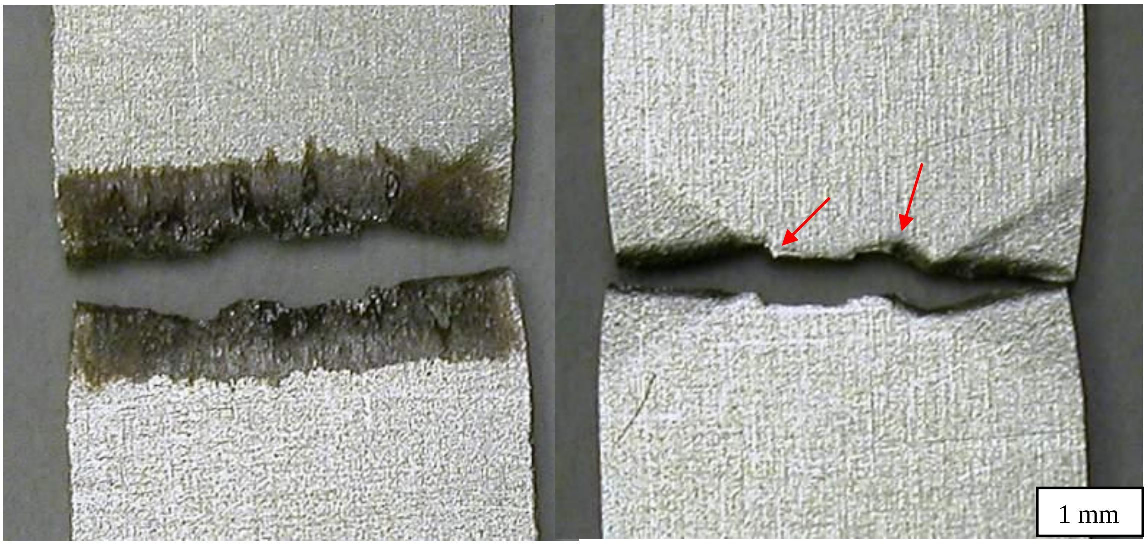

Figure 4.49: Front (left) and back (right) of a 301 specimen subjected to subsequent fatigue after fretting against 52100 for 10^4 cycles with a normal force of 255 N and displacement amplitude of 60 μm showing multiple crack initiation sites in the center of the specimen.

Fatigue tests were conducted with conditions corresponding to the fatigue limit in uniaxial fatigue on the specimens containing different severities of fretting damage. Fretting damage was generated with 52100 at different displacement amplitudes and a normal force of 255 N for 10^4 cycles and subsequent fatigue was performed with a stress amplitude of 468 MPa and a load ratio of R = 0.05. Figure 4.50 shows the resulting lives and failed specimens. Infinite life was found for a 10 μm displacement amplitude, which was the only test resulting in a partial slip running condition. The fatigue life decreases with increasing fretting displacement amplitude beyond the transition from partial to mixed slip. Therefore, there is a transition displacement amplitude below which there is no negative impact on fatigue strength occurring near the transition between partial and mixed slip conditions. At low displacement amplitudes, the catastrophic flaw is located near the center of contact. As the displacement amplitude increases, the critical fretting cracks formed closer to the edges of the contact as observed in the images of the scars and cracks in Figure 4.50. A specimen with fretting damage generated at a displacement amplitude 20 μm failed during fatigue at locations well outside of the primary fretting scar region, and was therefore not shown in this figure. The specimen for this test failed after 52,407 cycles. Therefore, the residual life associated with the fretting damage generated at 20 μm is greater than this value. This life is greater than the life of the specimen with fretting damage generated at a displacement amplitude of 30 μm, which is consistent with the trend of increasing life with decreasing displacement amplitude.

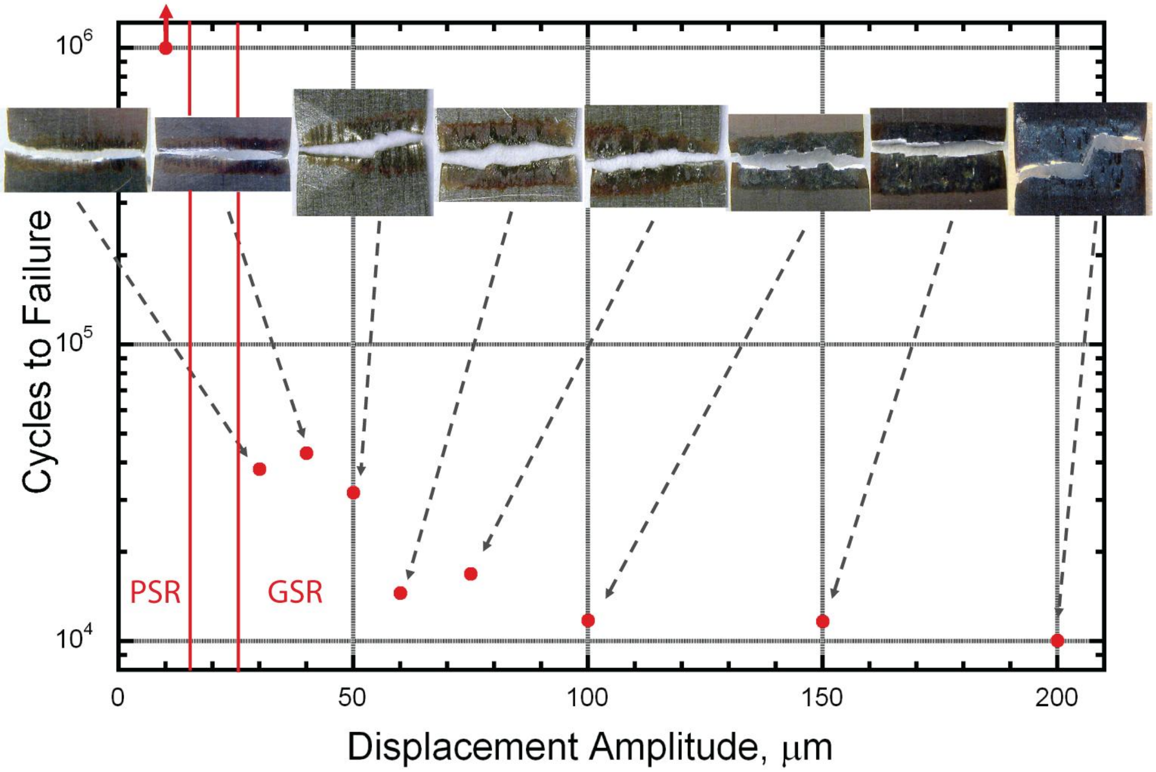

Figure 4.50: Residual fatigue life of specimens containing fretting damage generated by 301 in contact with 52100 at various displacement amplitudes with a normal force of 255 N for 10^4 cycles at room temperature.

The resulting lives and fractured specimens for subsequent fatigue tests performed on 301 specimens contacted with A356 at different displacement amplitudes and a normal force of 255 N for 10^4 cycles are shown in Figure 4.51. No failure occurred for a displacement amplitude of 40 μm. Increasing displacement amplitude caused reduction in life until 100 μm at which point the life increased slightly. Above a threshold displacement amplitude, the cycles to failure is nearly independent of displacement amplitude. This displacement corresponds to a running condition near the transition from mixed slip to gross slip running conditions.

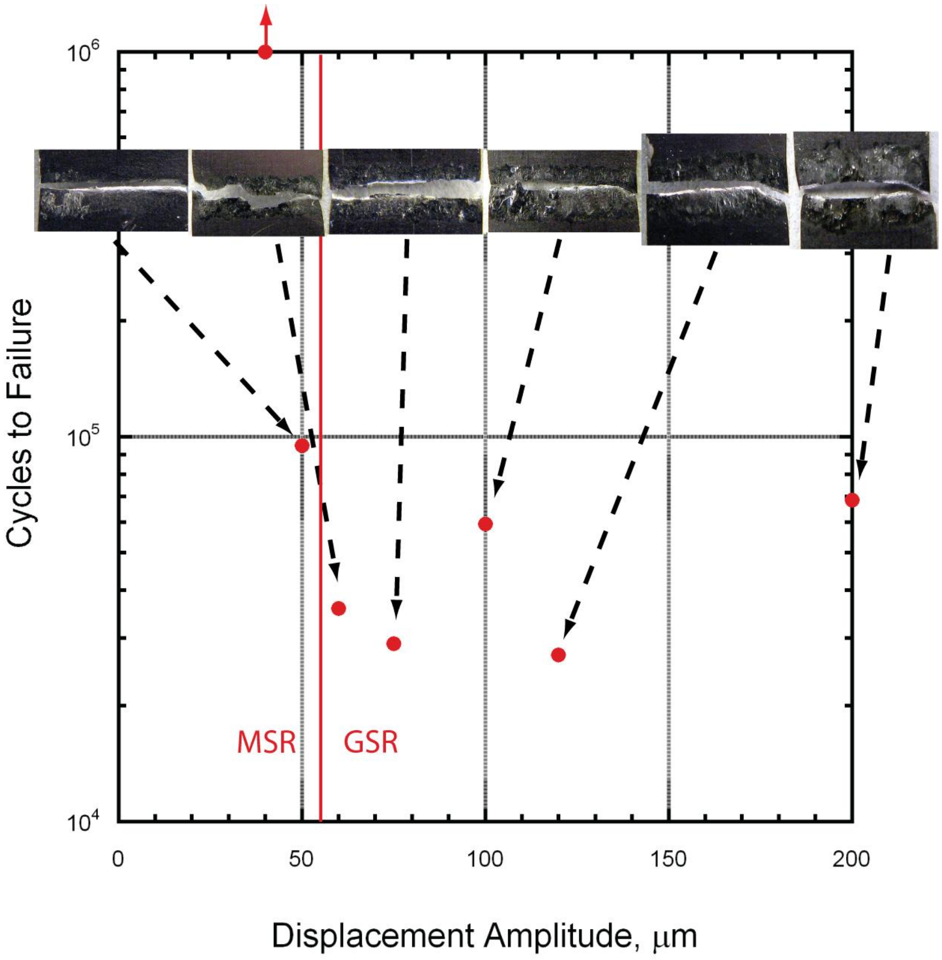

Figure 4.51: Residual fatigue life of specimens containing fretting damage generated by 301 in contact with A356 at various displacement amplitudes with a normal force of 255 N for 10^4 at room temperature.

A comparison between the residual lives obtained when 301 was contacted by A356 and 52100 with a normal force of 255 N and various displacement amplitudes for 10^4 cycles with the running condition indicated is shown in Figure 4.52. The fretting fatigue damage was more severe for 301 in contact with 52100 for all displacement amplitudes.

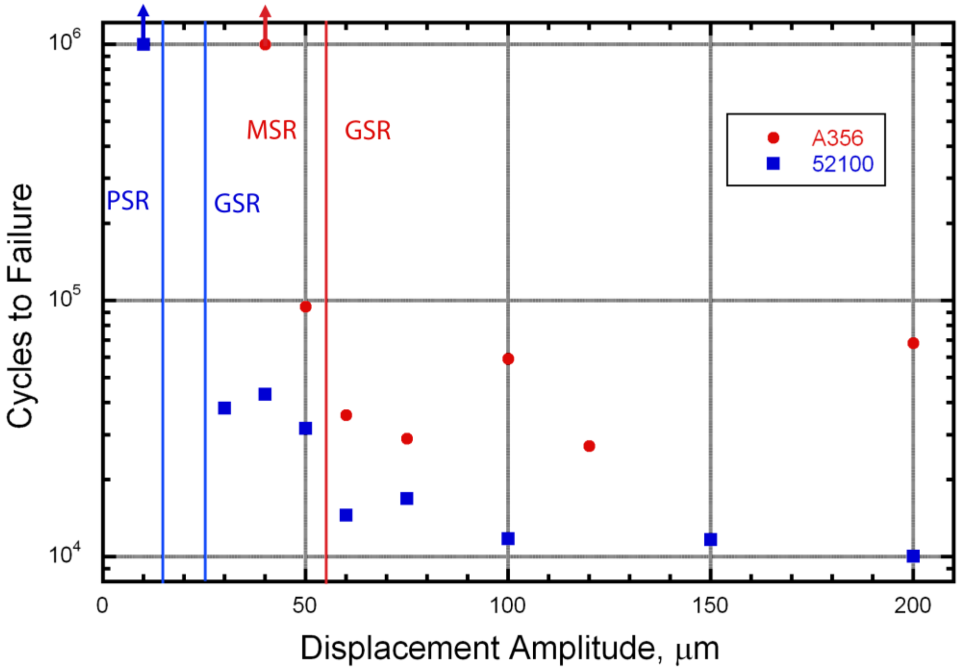

Figure 4.52: Residual fatigue life of specimens containing fretting damage generated by 301 in contact with both A356 and 52100 with a normal force of 255 N for 10^4 cycles at room temperature.

The greatest reduction in fatigue life is expected to occur near the displacement amplitude relating to the transition between mixed and gross slip. However, in this study, the most severe knockdown occurred in the gross slip regime for contact with both A356 and 52100. The threshold displacement amplitude above which fretting affected life occurred just below the observed transition from mixed slip to gross slip for 301 in contact with both A356 and 52100.

At larger displacement amplitudes for thick specimens the fatigue life is expected to increase due to the increased wear rate at larger displacement amplitudes as well as the increased size of contact, causing a reduction in the local pressure [38-39]. At high wear rates, the rate of material removal is larger than the rate of crack propagation. This results in the removal of cracks which therefore increases the life of the component. In this study, life did not increase with displacement amplitude for contact with either material as expected. In contact with A356, there was a slight increase in life for a displacement amplitude of 200 μm, though the increase could be considered to be within experimental scatter. Since wear of the 301 specimen did not take place and cracks were not observed, any increase in life observed would not be due to the removal of cracks. Contact size was increased by wear of the aluminum specimen which may have caused the beneficial reduction in contact pressure. The deposited layer of aluminum may have had a protective effect, since the highest stresses from contact would occur in the deposited layer rather than the 301 specimen.

For contact with 52100, the life continued to decrease with increasing displacement. This is due to the reduction in specimen thickness due to wear. At high displacement amplitudes the wear depth was found to be up to 40 μm. This relates to a 20% decrease in cross-section area for these thin specimens. Calculating the stress amplitude based on the reduced area results in a fatigue life similar to the undamaged condition with the same stress as shown in Figure 4.53. The reduction in thickness would not be significant when testing with thick specimens.

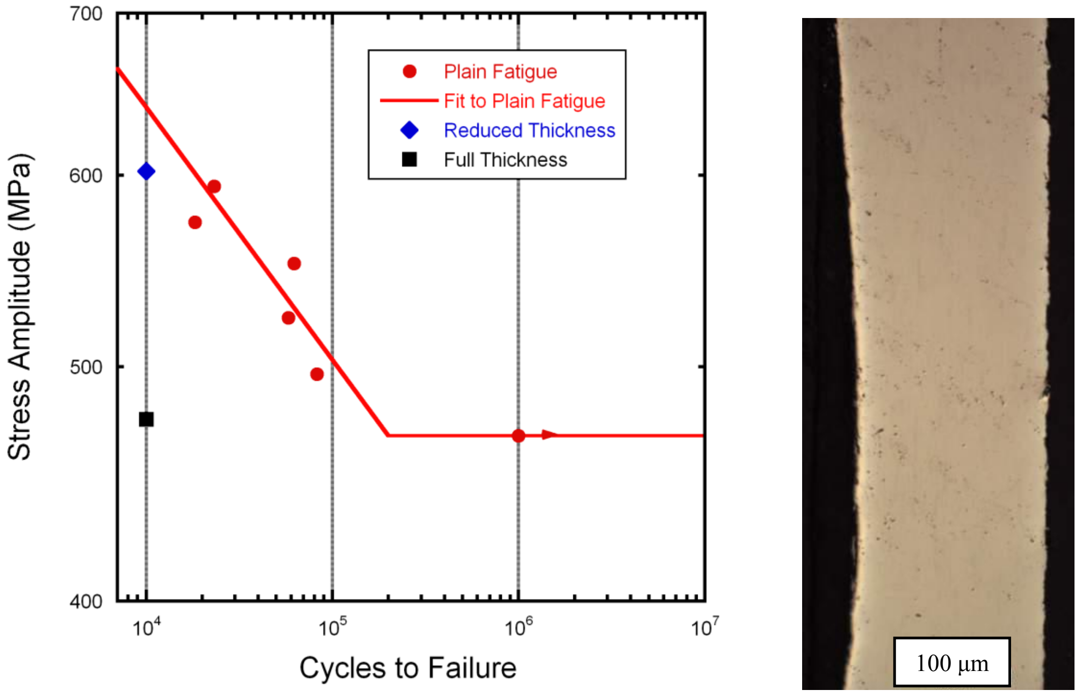

Figure 4.53: Change in actual stress amplitude due to wear of a sample fretted against 52100 with a normal force of 255 N and displacement amplitude of 200 μm for 10^4 cycles.

The subsequent fatigue lives for specimens subjected to fretting using a normal force of 255 N at 20°C and 250°C are shown in Figure 4.54. Fatigue damage due to fretting was found to be more severe at 250°C than at 20 °C for displacement amplitudes below 60 μm. The fatigue damage due to fretting was found to be less severe for tests conducted at 250°C than at 20°C for displacement amplitudes of 60 μm and above. The 20°C results do not demonstrate the beneficial effects associated with high wear at the higher displacement amplitudes as expected. This is due to the significant wear depth for the 20°C tests which causes a reduction in the cross-section of the specimens, which causes a decrease in the subsequent fatigue life [177].

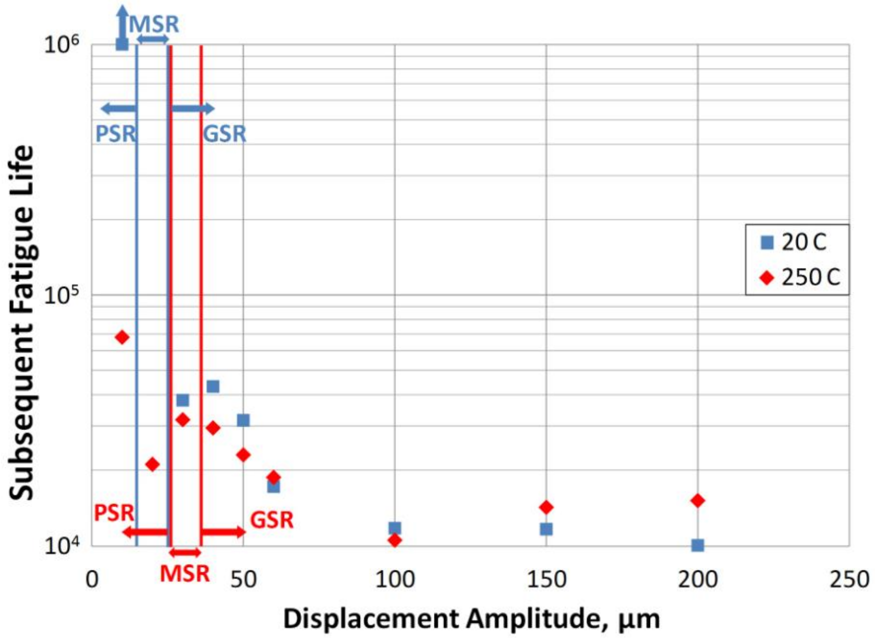

Figure 4.54: Uniaxial fatigue life after fretting with a 255 N normal force.

The subsequent fatigue lives for each fretting condition at 250°C are shown in Figure 4.55. Vertical lines with the same color as a data set indicate transitions in running condition for that data set. All conditions tested exhibited finite subsequent fatigue life. For tests conducted with a normal force of 100 N, the partial slip (PS) case demonstrated a shorter life than the mixed slip (MS) case and the gross slip (GS) case demonstrated the shortest life. For tests conducted with a normal force of 255 N, the lowest displacement amplitude resulted in the longest subsequent fatigue life, with a decrease in life as displacement amplitude increased within the partial slip regime (PSR). Life increased as the displacement amplitude increased into the mixed slip regime (MSR) and decreased steadily until reaching 100 μm. Life increased with further increase in displacement amplitude in the gross slip regime (GSR). Thus both the 100 N and 255 N cases demonstrated a longer life in the MSR than the PSR and had a minimum in the GSR. The 375 N case also demonstrated minimum life from fretting in the GSR, however fretting in the PSR caused less fatigue damage than the MSR.

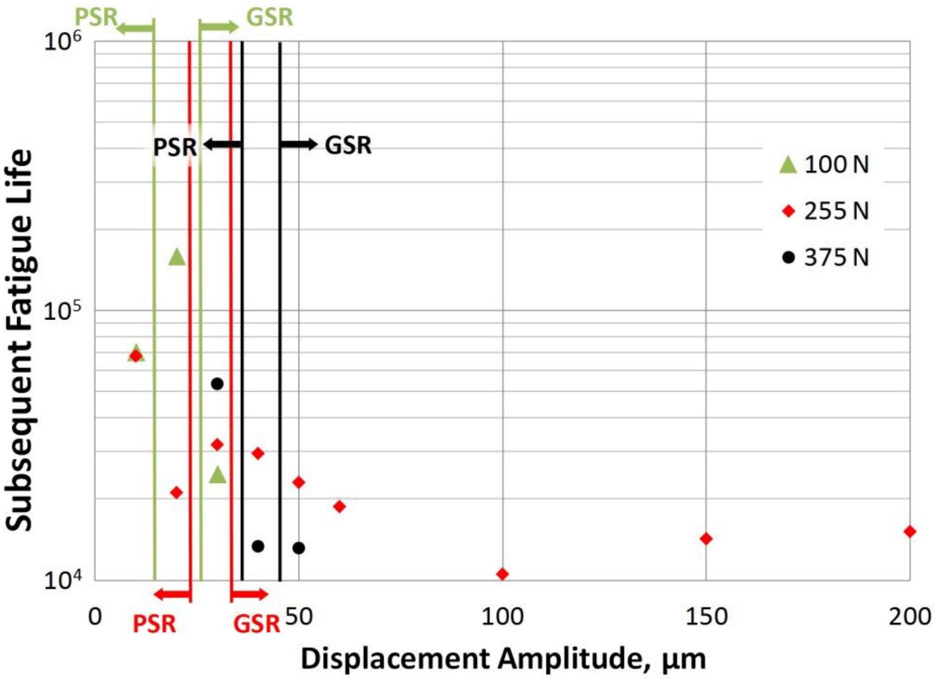

Figure 4.55: Subsequent fatigue lives for tests conducted at 250°C.

A comparison of the subsequent fatigue lives resulting from fretting at room temperature and 250°C is shown in Figure 4.56. Tests performed with a normal force of 255 N demonstrated shorter subsequent fatigue lives for fretting tests performed at 250°C than for tests performed at 20°C for displacement amplitudes of 50 μm and below. Subsequent fatigue lives were higher for the tests performed with a normal force of 255 N at 250°C than for tests performed 20°C for higher displacement amplitudes.

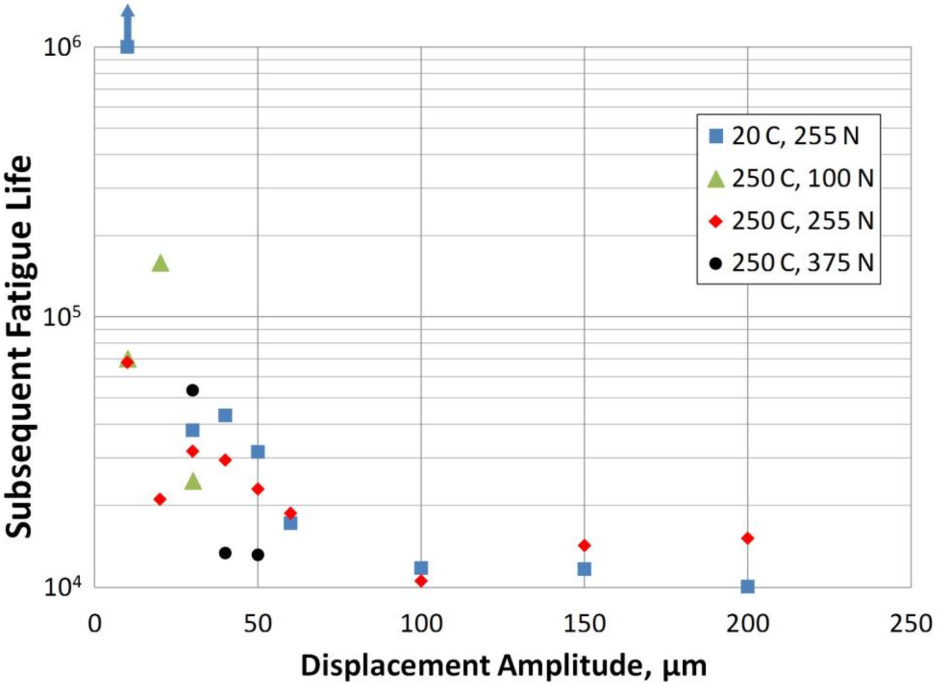

Figure 4.56: Comparison of subsequent fatigue lives for tests conducted at RT and 250^{o}C.

Previous work has identified a strong correlation between the steady state tangential force and the fatigue damage due to fretting. The subsequent fatigue life as a function of the steady state max tangential force including room temperature results is shown in Figure 4.57. There is no significant correlation between the steady state maximum tangential force and the subsequent fatigue life for the tests conducted at elevated temperature. The lack of correlation between the response at different temperatures and normal forces indicates that wear has a substantial effect on the subsequent fatigue life.

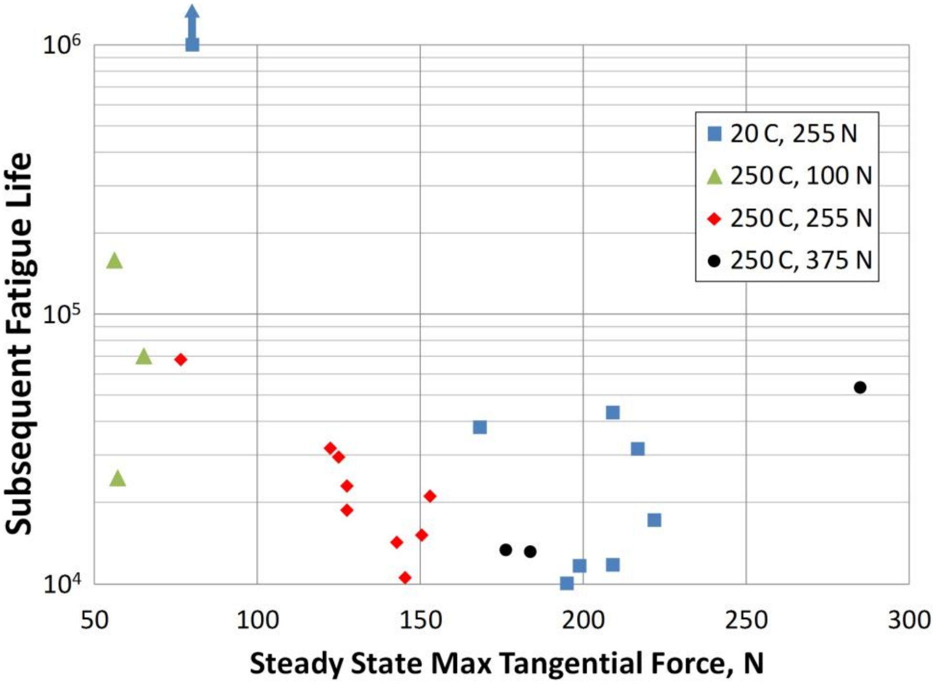

Figure 4.57: Subsequent fatigue life as a function of steady state maximum tangential force.

The subsequent fatigue life for each test in terms of the accumulated dissipated energy (ADE) is shown in Figure 4.58. The correlation between the subsequent fatigue life and ADE suggests that the dissipated energy is a driver for fatigue damage. The ADE consists of energy dissipation associated with wear processes as well as cyclic plastic deformation, which each influence the subsequent fatigue lives. Tests performed with a normal force of 255 N demonstrated shorter subsequent fatigue lives for fretting tests performed at 250^{o}C than for tests performed at 20^{o}C for dissipated energies below 450 J. Subsequent fatigue lives were higher for the tests performed with a normal force of 255 N at 250^{o}C than for tests performed 20^{o}C for higher dissipated energies. This transition may be a result of the difference in the wear resistance of the material at these two temperatures or the increased susceptibility of fatigue damage at higher temperature due to the loss of ductility. The wear rate has been shown to be significantly lower at 250^{o}C than at 20^{o}C. The lower life at low dissipated energy at higher temperature may indicate that the more significant wear at room temperature is beneficial through the redistribution of stresses and removal of fatigue damaged material. More significant amounts of wear at higher levels of dissipated energy may result in a decrease in life at room temperature due to thinning, whereas wear at the higher dissipated energies at elevated temperature does not result in a significant reduction of thickness. This could be verified by determination of the wear profile in future work. The higher fatigue damage at elevated temperature for cases in which wear is insignificant at both temperatures could be due to the reduced ductility of 301 stainless steel at elevated temperature due to the increased stability of austenite. The reduced ductility is expected to increase the level of fatigue damage based on the concept of ductility exhaustion.

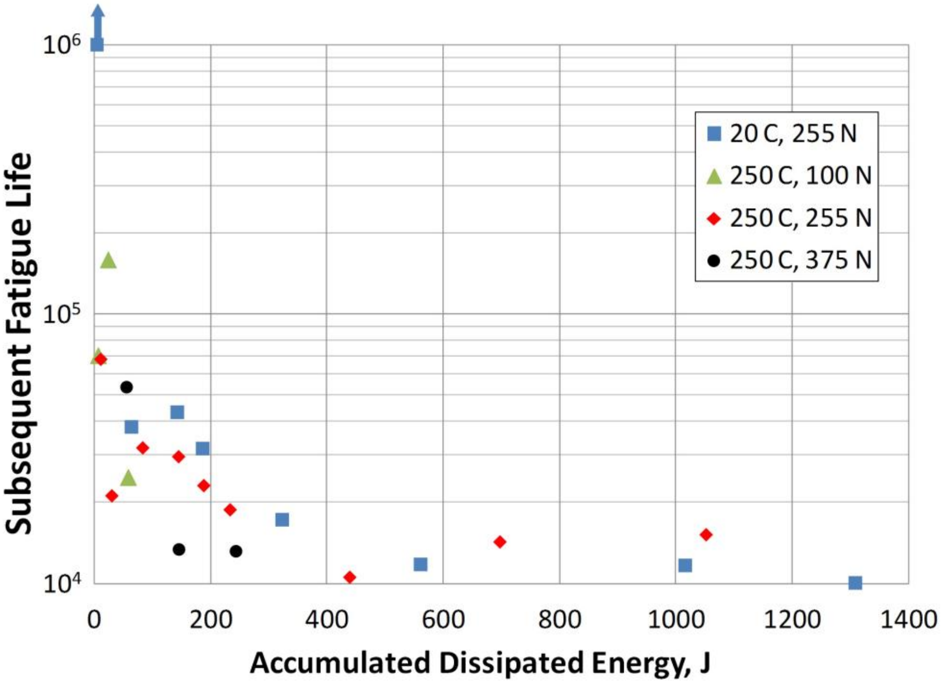

Figure 4.58: Subsequent fatigue life in terms of ADE.

The failure locations resulting from subsequent fatigue of specimens subjected to fretting in contact with 52100 steel at 250^{o}C are shown in Figure 4.59. The location of crack formation is influenced by the wear behavior. the location of maximum wear for gross slip conditions occurs at the center of contact, and the location of maximum cyclic stress and strain occurs near the edge of contact. This suggests that specimens with a subsequent fatigue life which is limited by thinning should fail at the center of the specimen at the location of maximum wear, whereas specimens with a subsequent fatigue life which is limited by fatigue damage should fail near the edge of contact. Tests performed at room temperature in contact with 52100 with a relatively high wear rate demonstrated a crack formation location farther from the center of contact for increasing displacement amplitudes. This suggests that the increase in the cyclic stress state in the center of the specimen during subsequent fatigue due to wear was less significant than the effect of the cyclic stresses toward the edge of contact during fretting. Tests performed at elevated temperature with a lower wear rate compared to room temperature demonstrated a crack formation location which did not have a clear trend. The crack formation location for tests conducted at the lowest normal force moved farther from the center of contact with increasing amplitude, whereas the crack formation location for tests conducted at the highest normal force moved closer to the center of contact with increasing amplitude. Specimens tested using the intermediate normal force demonstrated crack formation locations near the edge of contact with the exception of the MS condition. These results show that the wear behavior is still influential on the location of the fatigue damage. Calculation of fatigue damage parameters will aid in determination of the extent of damage interaction.

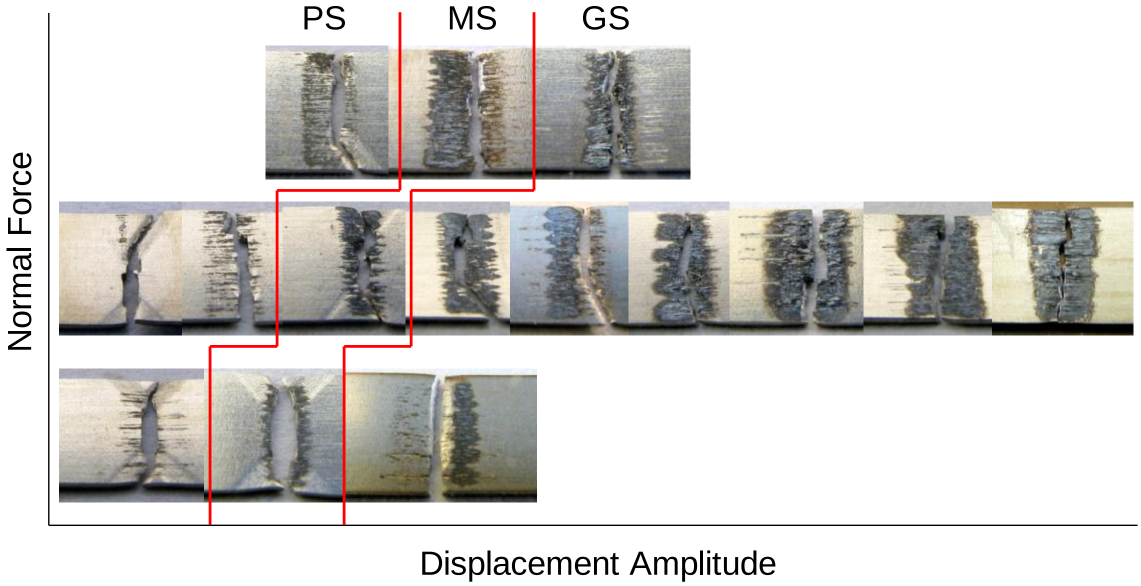

Figure 4.59: Specimens subjected to fretting in contact with 52100 at 250^{o}C after subsequent fatigue testing.

The fatigue lives of specimens after being subjected to fretting against 52100 steel with 255 N normal force and 200 μm displacement amplitude are shown in Figure 4.60. Failure during subsequent fatigue occurred within the fretting scar for all specimens tested. Subsequent fatigue lives tended to increase as the fretting test temperature increased to 400^{o}C, indicating that less fatigue damage occurred during fretting as temperature increased. Tests conducted in argon at temperatures at 400^{o}C and below had lower subsequent fatigue lives than the analogous test in air. Tests conducted at 550^{o}C demonstrated the lowest subsequent fatigue life of all conditions tested. Room temperature tensile tests were performed on samples exposed to elevated temperature to determine the effects of exposure to high temperature during the fretting. Exposure to 550^{o}C in air for 1 hour was found to decrease the yield strength by approximately 200 MPa, whereas exposure to 400^{o}C did not decrease the room temperature yield strength. Therefore, the fatigue load imposed on the samples exposed to 550^{o}C was a higher fraction of the yield strength. Other factors that contributed to the trend in fatigue lives with changing temperature are discussed later.

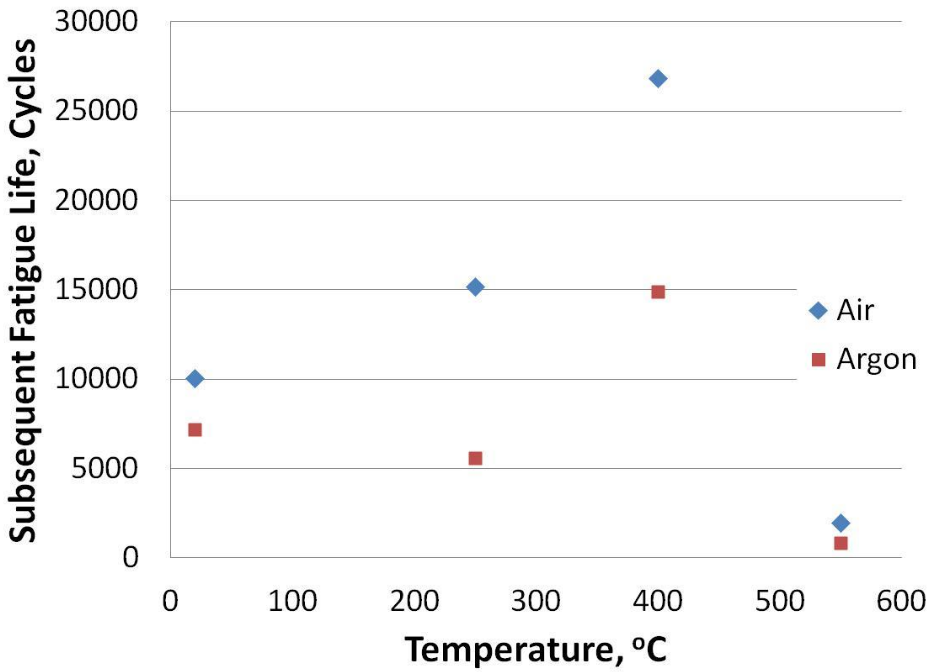

Figure 4.60: Subsequent fatigue lives for contact with 52100.

4.5 Discussion of Experimental Results

The evolution of the COF during fretting is due to modification of the surface and entrapment of debris. Austenitic stainless steel forms a chromium oxide passivation layer that protects the substrate from further oxidation. The passivation layer for 301 stainless steel is composed of as much as 90% Cr_2O_3 [14], which has a thickness typically between 1 and 10 nm in air at room temperature [64-65]. This layer is removed easily by fretting and becomes trapped in the contact, which causes a high wear rate due to its high hardness [31]. Reformation of the protective oxide eventually results in depletion of Cr in the near surface region. This results in formation of chromium spinel oxide ($FeCr_2O_4$), which is not suitable for wear prevention [99]. Further sensitization results in increased formation of iron oxides. The process stabilizes and thus the COF also stabilizes. This process is accelerated in oxidizing environments such as elevated temperature, hence the observation of a more quickly stabilized COF value for tests performed at higher temperature.

The COF and wear rate are strongly influenced by the composition of the wear debris. Kayaba and Iwabuchi [100] found that fretting between annealed 304 stainless steel and itself results in formation of Fe_2O_3 at room temperature which transitions to Fe_3O_4 at 300^oC and then to FeO at temperatures above 650^oC. The decrease in wear rate with increasing temperature was attributed to the change in the oxide composition. Experiments conducted here show the formation of a glaze oxide at elevated temperature, which is associated with a low wear rate and decreased COF [179], both of which were observed in this study. The experiments performed by Kayaba and Iwabuchi utilized an average contact pressure of approximately 41 MPa whereas the average pressure used in this study was 320 MPa. The higher contact pressure used in this study promotes formation of the glaze oxide and explains why a glaze oxide layer was not observed with the lower contact pressure.

The phase of the metallic wear debris also influences the COF and wear behavior. The study by Kayaba and Iwabuchi utilized annealed 304 stainless steel which is composed exclusively of austenite. Therefore, metallic wear debris generated at temperatures above M_d did not contain martensite. The 301 stainless steel used in this study had an initial martensite content of approximately 60% due to cold rolling. Therefore, metallic wear debris generated at temperatures above M_d consisted of both austenite and martensite phases. This difference may increase the wear rate at elevated temperature since martensite is harder than austenite, thus decreasing the severity of the reduction in wear rate with increasing temperature. However, the role of the metallic wear debris appears insignificant relative to the oxide characteristics since the wear rate observed here also decreased drastically despite the difference in metallic wear debris composition.

The oxidation rate and oxide composition is influenced by the phase composition. Grain boundaries between austenite and martensite grains have high diffusion rates of Cr and therefore result in increased oxidation resistance due to increased availability of Cr for formation of a passivation layer [91]. This could result in an increase in the amount of hard Cr_2O_3 and $FeCr_2O_4$ and therefore increase the wear rate. The lower austenite stability of 301 results in increased martensite formation at the surface of the fretting contact which can lead to fracture and an increased wear rate [90]. It is unclear from this study whether these factors were significant due to the large difference in the contact pressure between the tests conducted here and the tests of Kayaba and Iwabuchi.

The amount of fatigue damage caused by fretting is affected by many factors. A high wear rate typically results in a low level of fatigue damage [34] since surface material that accumulates fatigue damage is removed by wear [38-41] and the contact stresses are reduced as the geometry changes due to wear cause an increase in contact conformity [40, 43, 143]. In this study, fretting at room temperature resulted in the highest wear rate but a low subsequent fatigue life. This is largely due to the reduction in area of the specimen due to wear. The maximum wear depth for the room temperature case was 24 μm, which reduced the cross-sectional area by 12% compared to the nominal area used for selection of the forces used for subsequent fatigue loading. This corresponds to an increase in the actual stress amplitude imposed during subsequent fatigue in the fretting scar from 470 MPa to 530 MPa, ignoring notch effects. The plain fatigue life of this material when loaded with a 530 MPa amplitude and load ratio of 0.05 is approximately 62000 cycles [180]. Therefore, the subsequent fatigue life is lower partly due to the reduction in area caused by wear. This effect would be negligible for fretting of thick specimens since the wear depth would be insignificant compared to the sample thickness. The higher COF observed during room temperature fretting also contributed to the lower subsequent fatigue life due to the increase of tangential stresses during fretting.

The decreasing level of fatigue damage due to fretting in both atmospheres as temperature was increased from 20^{o}C to 400^{o}C is partially due to the decrease in COF which was caused by the change in oxidation characteristics. There was no reduction in the specimen thickness due to wear to cause an apparent increase in fatigue damage, as was the case for fretting at room temperature. The decrease in strength and large decrease in ductility during fretting at 250^{o}C and 400^{o}C appears to be a less significant factor than the changes in wear behavior and COF since these cases demonstrated the least amount of fatigue damage due to fretting. The low subsequent fatigue lives of the tests performed at 550^{o}C is due to a combination of the decrease in strength during fretting at high temperature, and the decrease in room temperature strength due to exposure to high temperature. The cracking observed beneath the glaze oxide appears to propagate parallel to the surface and therefore may not have been a cause of the low subsequent fatigue life. The increase in fatigue damage caused by fretting in argon compared to fretting in air, which was most pronounced at 250^{o}C and 400^{o}C, may be caused by differences in the glaze oxide characteristics that were not apparent from inspection by optical microscopy.

Therefore, subsequent fatigue testing provides more sensitive characterization of the level of fatigue damage caused during fretting than inspection of the oxidation and wear behavior.

CHAPTER 5

MODELING FRETTING DAMAGE

A finite element model of the fretting configuration was created to determine the cyclic stress-strain behavior and local frictional energy dissipation for various contact parameters. The finite element model is necessary due to the lack of available analytical solutions for the special case of a thin specimen geometry. The results of the simulations help to explain the local behavior which cannot be measured experimentally and are needed to evaluate damage metrics. The results demonstrate the sensitivity of the response to conditions of the interaction such as the COF, thus aiding in the identification of the changes in damage drivers with changing conditions. A new fatigue damage metric is developed to account for differences in the wear behavior between the bodies in contact based on the dominant wear mechanism.

5.1 Model Geometry

The compliance of the test system has a large effect on the fretting behavior since deformation in the system causes the local displacements to be significantly lower than the remotely measured values. A finite element model needs to incorporate the machine compliance to accurately capture the response. However, modeling the entire test system is impractical. The finite element model consists of the region surrounding the contact with compliant layers to represent the machine compliance as shown in Figure 5.1. The model consists of three parts: the moving specimen with a rigid layer at the top, the stationary specimen with a compliant layer at each end, and the bottom body which includes a PTFE layer, backing plate, and a compliant layer at each side of the backing plate. A point force is applied to a reference node in the rigid layer which distributes the force across the top of the moving specimen. Horizontal displacements are applied at the same reference node. Rotation of the rigid layer is constrained to prevent rolling due to the friction force. The moving specimen has a radius of 10 mm, the stationary specimen has a thickness of 205 µm, and the PTFE layer has a thickness of 89 µm. A plane strain analysis is performed since the thickness of the specimen is less than five percent of the out-of-plane dimension. The bodies are partitioned so that separate material properties can be prescribed. All materials are modeled as linear-elastic. The stress levels determined in preliminary results have shown that an elastic analysis is sufficient for the loading conditions considered [177].

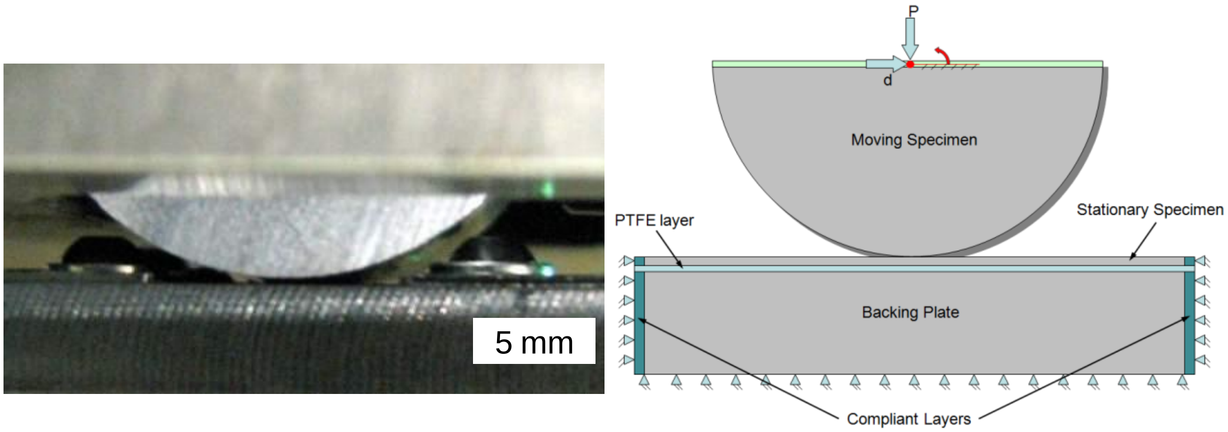

(a) (b)

Figure 5.1: (a) Region to be modeled by FEM and (b) schematic representation of the model.

5.1.1 Verification model

A simple model was created using ABAQUS/CAE to represent the case of a cylinder sliding on a half-space for which a well established analytical solution exists in order to verify the contact formulation. The solution for the surface tractions for a cylinder sliding on a half-space is given by [30]:

For x < |a|,

$$S_{11} = -p_0\left(\sqrt{1-\frac{x^2}{a^2}} + \frac{2\mu x}{a}\right) \tag{5.1}$$

$$S_{22} = -p_0\sqrt{1-\frac{x^2}{a^2}} \tag{5.2}$$

$$S_{12} = -\mu \cdot p_0\sqrt{1-\frac{x^2}{a^2}} \tag{5.3}$$

for x < -a,

$$S_{11} = -2\mu p_0\left(\sqrt{\frac{x^2}{a^2}-1} + \frac{x}{a}\right) \tag{5.4}$$

$$S_{22} = 0 \tag{5.5}$$

$$S_{12} = 0 \tag{5.6}$$

for x > a,

$$S_{11} = 2\mu p_0\left(\sqrt{\frac{x^2}{a^2}-1} - \frac{x}{a}\right) \tag{5.7}$$

$$S_{22} = 0 \tag{5.8}$$

$$S_{12} = 0 \tag{5.9}$$

where

$$p_0 = \sqrt{\frac{PE^*}{\pi R}} \tag{5.10}$$

$$E^* = \left(\frac{1-\upsilon_1^2}{E_1} + \frac{1-\upsilon_2^2}{E_2} \right)^{-1} \tag{5.11}$$

$$a = \sqrt{\frac{4PR}{\pi E^*}} \tag{5.12}$$

where x is the distance along contact from the center and the direction in which the cylinder is sliding, a is the contact half width, μ is the coefficient of friction, P is the force per unit length of contact, E_1 and E_2 are the elastic moduli of each material, υ_1 and υ_2 are the Poisson's ratios of each material, R is the radius of the cylindrical body, the 1 direction is horizontal, and the 2 direction is downward.

A schematic of the verification model with boundary conditions is shown in Figure 5.2. The moving specimen was modeled as a half-cylinder due to symmetry. The vertical force P and horizontal displacement d are prescribed at a reference point on a rigid layer at the top of the moving specimen. The rigid layer distributes the point force along the top of the moving specimen and allows for the rotation to be fixed so that the friction at contact causes only translation.

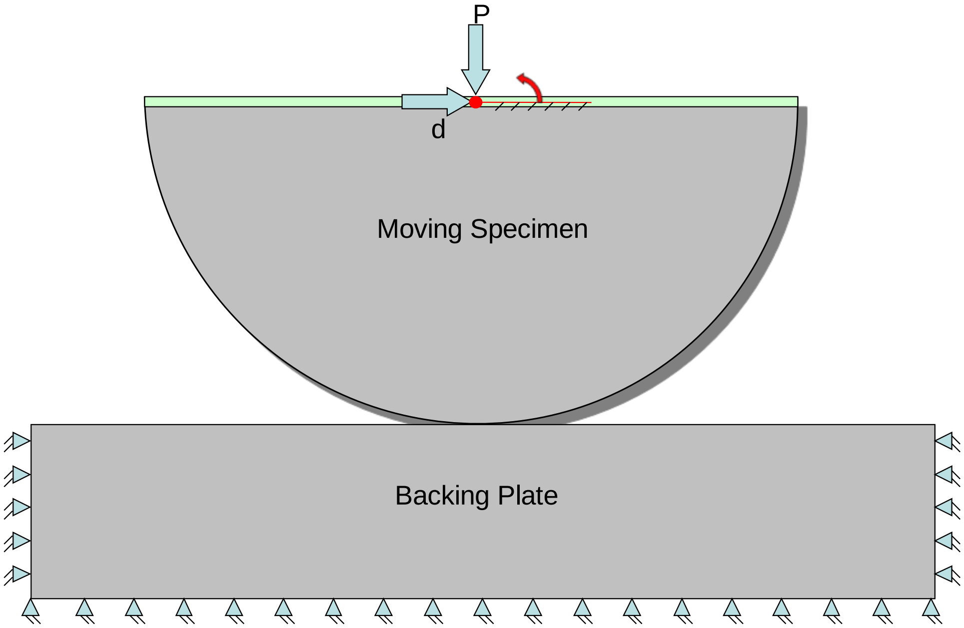

Figure 5.2: Schematic of verification model.

The verification simulation was performed using Abaqus/Standard and was broken into the three steps shown in Figure 5.3. The indentation of the cylinder was divided into two steps. First, a downward displacement of 1 µm was imposed at the reference point at the top center of the moving specimen to initiate contact. The second step removed the downward displacement constraint, and imposed a downward force at the reference point. During indentation, displacement of the rigid layer in the lateral direction was not allowed. This two-step method of applying the normal force greatly increased stability compared to a direct force-controlled indentation. The third step imposed a displacement at the reference point at the top center of the moving specimen in the horizontal direction to result in sliding between the bodies.

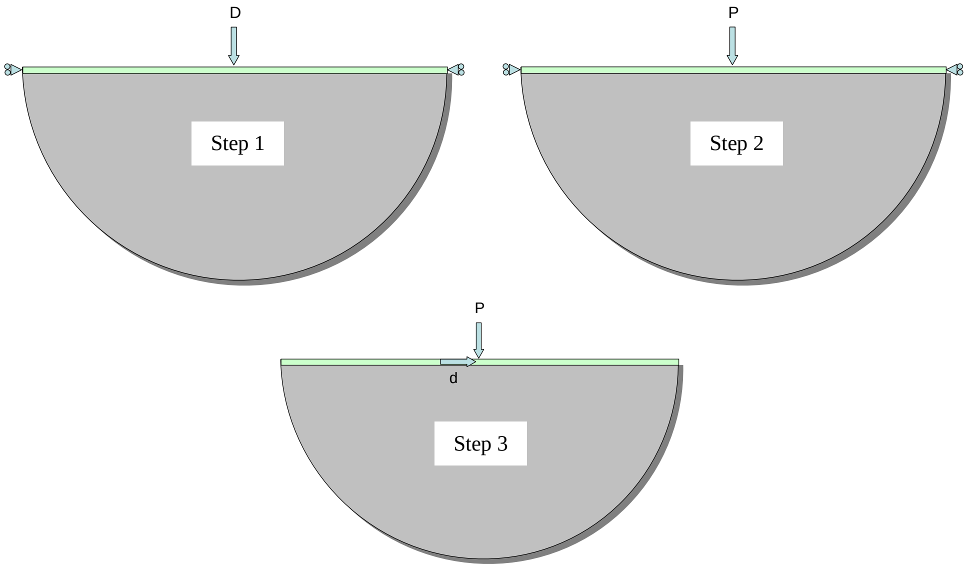

Figure 5.3: Steps used for the verification simulation.

There are several calculation methods for both the normal and tangential contact behavior with varying levels of complexity, computation time and stability. Surface-to-surface contact was used with a finite sliding formulation and hard contact pressure-overclosure behavior. Hard contact enforces no penetration of the bodies, that there is no force between the bodies if they are not in contact (no adhesion effects), and allows an infinite pressure to be transferred between the master and slave surfaces. The backing plate was chosen as the master surface and the moving specimen was chosen as the slave surface.

A Lagrange Multiplier friction formulation was used for the tangential contact behavior. The Lagrange Multiplier friction formulation enforces the sticking constraints at an interface between two surfaces so there is no relative motion unless $\tau = \tau_{\text{critical}}$. The Lagrange Multiplier formulation was used because of its ability to enforce exact stick unlike penalty friction that permits relative motion of the surfaces (an "elastic slip") when they should be sticking (i.e., $\tau < \tau_{critical}$). However, using Lagrange Multiplier contact formulation decreases stability and increases computation time. Isotropic friction was used for the verification analysis, with no dependence on pressure, velocity, or temperature. The constant COF was chosen to be 0.55 based on experimental data. The Penalty constraint enforcement method was used for the normal contact behavior to reduce the computation difficulty. It was determined that this did not compromise accuracy since the tangential contact behavior was the primary focus.

Simulations were performed to represent experiments performed at 20^{o}C and at 250^{o}C. Simulations of experiments at 20^{o}C were performed using isotropic elastic material models. An elastic approximation was found to be appropriate by analysis of the maximum Von Mises stresses determined from the simulations. Simulations of experiments performed at 250^{o}C were performed using isotropic elastic models for the materials other than the 301 stainless steel moving specimen, which was modeled using isotropic hardening to fit the experimental stress-strain response from a tensile test. The choice of hardening law was not critical because the stress-strain behavior was nearly elastic-perfectly plastic. The elastic constants used for each material at each temperature are shown in Table 5.1. The measured values of the elastic moduli were used for materials other than PTFE. The values used for PTFE were in agreement with the literature [181]. The modulus of the compliant layers was determined by comparison of the hysteresis loops calculated from the model to the hysteresis loops measured in the corresponding fretting test, and iteration of the compliant layer modulus until correspondence was achieved.

Table 5.1: Elastic constants used for material models.

	E, GPa		**υ**	
	$20^{o}C$	**$250^{o}C$**	**$20^{o}C$**	**$250^{o}C$**
Stationary Specimen	167	142	0.30	0.30
Backing Plate	195	182	0.30	0.30
52100 Moving Specimen	210	200	0.30	0.30
A356 Moving Specimen	70	-	0.33	-
PTFE Layer	0.5	0.03	0.46	0.46

The COF for the contact between the moving specimen and the stationary specimen was uniform over the surface and was specified as the value measured during the fretting test of the corresponding conditions. The COF for contact between the stationary specimen and the PTFE used was 0.04 for $20^{o}C$ and 0.03 for $250^{o}C$, which was in agreement with the literature [182].

Simulations were performed for three cycles, which was found to be sufficient to stabilize the model response. This was indicated by a negligible difference in plastic strain between cycles three and four for the most highly loaded test condition. Model results for the third cycle were used for analysis.

The mesh of the verification model is shown in Figure 5.4. The mesh density is higher in the region of contact where there is a large stress gradient during sliding. In that area, elements are 2D plane strain linear quadrilateral reduced integration (CPE4R) meshed using a structured technique. Linear elements were used because of convergence issues that arise with using quadratic elements for contact simulations. Reduced integration elements were used since strains and stresses are calculated at the locations that provide optimal accuracy (Barlow points) while simultaneously reducing computation time and storage requirements. In the contact area the mesh is progressive so that the elements are smaller near contact. Areas other than the region near contact were meshed using a quadrilateral dominated meshing scheme. By allowing triangular elements (CPE3) to be used in areas where the solution was less critical, fewer elements had poor aspect ratios because of the added freedom. These regions were not meshed using the structured meshing routine, but rather free meshing to aid in mesh transition between the densely meshed area and the coarsely meshed area. The size of the mesh in the dense-mesh region was decreased until there was acceptable correspondence between the analytical solution and the computational solution along a path on the contact surface of the pseudo-half-space. The results for a 5 μm, 2 μm, and 1 μm mesh size compared to the analytical solution are shown in Figure 5.5.

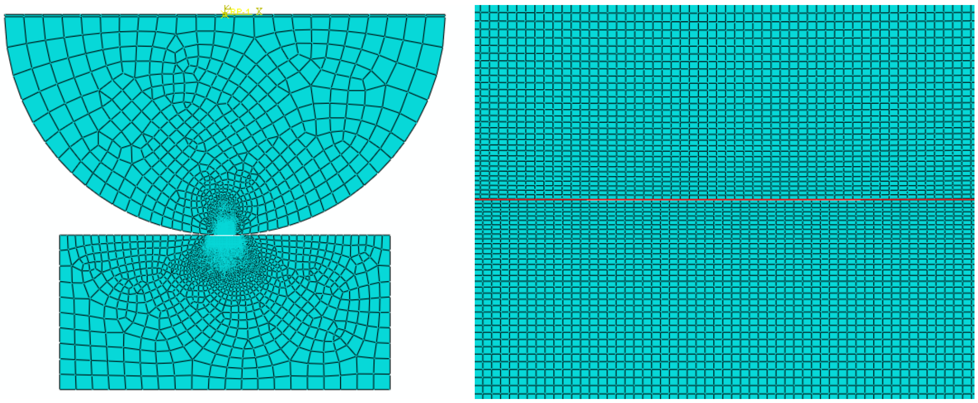

Figure 5.4: Mesh of the verification model with both zoomed-out and zoomed-in views where the red line shows the boundary between the top and bottom bodies.

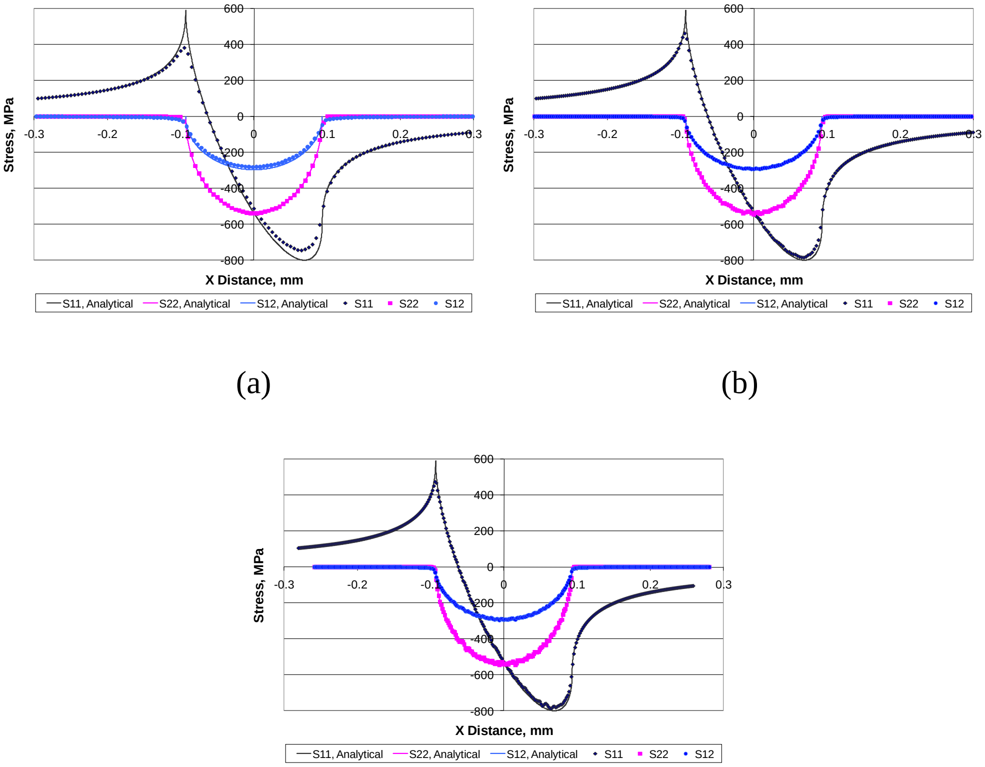

(a) (b)

(c)

Figure 5.5: Comparison of analytical solution to computational solution of the stresses along the surface of the stationary specimen while the moving specimen translates to the right using three different mesh sizes in the dense mesh region: (a) 5 µm, (b) 2 µm, and (c) 1 µm.

The mesh needed to be very fine in order to capture the sharp gradient in the S_{11} stress component at the trailing edge of contact (left side in Figure 5.5). Based on the analytical solution, the value of S_{11} at that location is 590 MPa. The 5 µm mesh size case shows a peak stress of 380 MPa at that location. Using a 2 µm mesh size, a value of 461 MPa was calculated. The 1 µm mesh size case showed a value of 473 MPa. Because the 1 µm case still did not capture the extent of the stress concentration and was only marginally closer than the 2 μm case with a large computation cost penalty, the mesh size for the final model was chosen to be 2 μm. Using an element size of 2 μm resulted in 35,300 CPE4R elements in the contact region on the half-cylinder and 55,800 CPE4R elements in the contact region on the pseudo-half-space. A total of 106,350 elements were used: 105,718 CPE4R and 632 CPE3. Although the peak S_{11} stress captured by the FEA was significantly lower than the analytical model (22% lower), volume averaging was used for calculation of fatigue damage metrics thus it is not critical to accurately capture the peak stress since it occurs over such a small volume.

5.1.2 Model of the Experimental Configuration

The model of the experimental configuration was based on the region immediately surrounding the contact since it would be impractical to model the entire test system. However, the stiffness of the test system has a large effect on the contact condition, and therefore the material response. Therefore, layers of compliant material were added to the sides of the model to account for the machine compliance.

The complete model is shown schematically in Figure 5.6. The model is an assembly of three parts: the moving specimen with the rigid layer, the stationary specimen with a compliant layer at each end, and the bottom body which includes a PTFE layer, backing plate, and a compliant layer at each side of the backing plate. The moving specimen has a radius of 10 mm, the stationary specimen has a thickness of 205 μm, and the PTFE layer has a thickness of 89 μm. The bodies were partitioned so that the separate material properties could be prescribed. There are two contact interactions. The contact interaction between the moving specimen and the stationary specimen was Lagrange Multiplier for the tangential contact behavior and Penalty constraint enforcement was used for the normal contact behavior. The stationary specimen was chosen as the master surface for this contact interaction because it experiences more deformation than the moving specimen. For the interaction between the stationary specimen and the PTFE layer, a Penalty constraint enforcement method was used for the normal behavior and a Penalty friction formulation was used for the tangential behavior since it was not critical to enforce exact stick at that location at the expense of stability. The PTFE layer was chosen as the master surface since it experiences more deformation than the moving specimen. The first three steps used were the same as for the verification model. Two additional steps were added where the displacement direction was reversed so that the moving specimen translated to the left and then reversed again to complete one full fretting cycle.

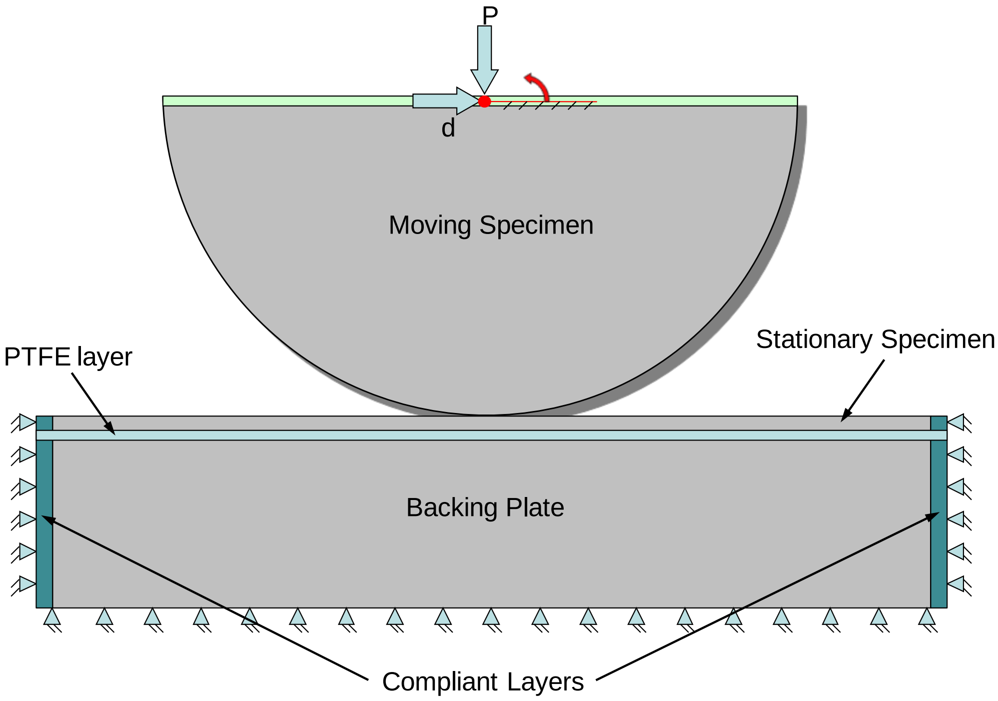

Figure 5.6: Schematic of the experimental configuration model.

The mesh of the final model was created similarly to that of the verification model and is shown in Figure 5.7. There was a total of 40,219 CPE4R elements and 466 CPE3 elements in the moving specimen, 41,955 CPE4R and 64 CPE3 in the stationary specimen (41,200 of which were in the contact region), 468 CPE4R in the PTFE layer, and 4,996 CPE4R and 92 CPE3 elements in the backing plate. Plane strain elements were used because of the in-plane symmetry and relatively large out-of-plane dimension of the configuration compared to the thickness of the specimen.

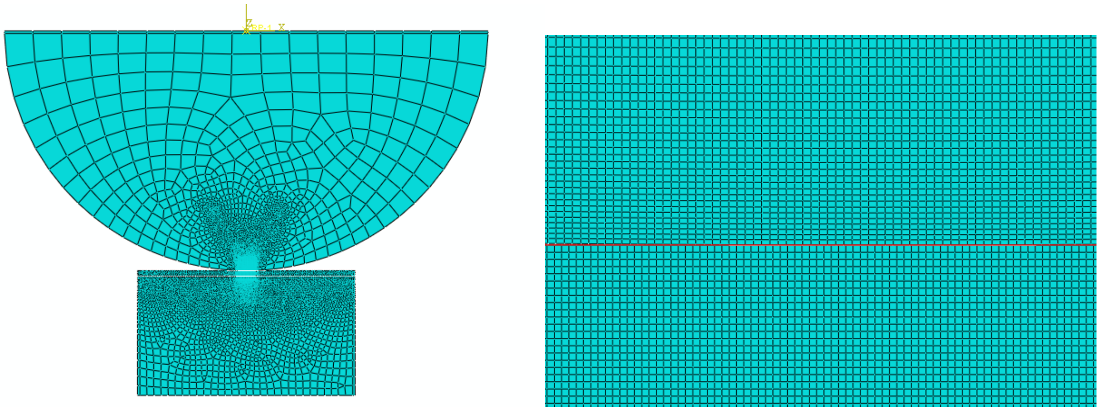

Figure 5.7: Mesh of the experimental configuration model.

The stiffness of the compliant layers that is representative of the test configuration was determined by comparing the slope of the hysteresis loops generated from the model to the slope of the hysteresis loops measured in experiments. Hysteresis loops were determined from the model by plotting the horizontal reaction force at the reference node where the displacement was applied versus the displacement at the same point. Adjustments were made to the stiffness of the compliant layers iteratively until correspondence was achieved.

The COF specified at the interaction between the PTFE layer and the stationary specimen was also determined iteratively by comparison of model and experimental hysteresis loops. The value used affects the hysteresis loop width, since it is representative of the amount of energy dissipated due to friction. The COF at that interface also affected the slope of the hysteresis loop since a higher COF results in higher stiffness. The COF at the contact between the moving and stationary specimens was specified as the value measured experimentally for the certain combination of normal force and displacement amplitude.

An example of a hysteresis loop generated from a model with an incorrect PTFE-stationary specimen COF and compliant layer stiffness is shown in Figure 5.8. In this example, the average slope of the model hysteresis loop (the slope of a straight line connecting the minimum value to the maximum value) is lower than the average slope of the measured hysteresis loop. This indicates that the stiffness of the compliant layers is too low.

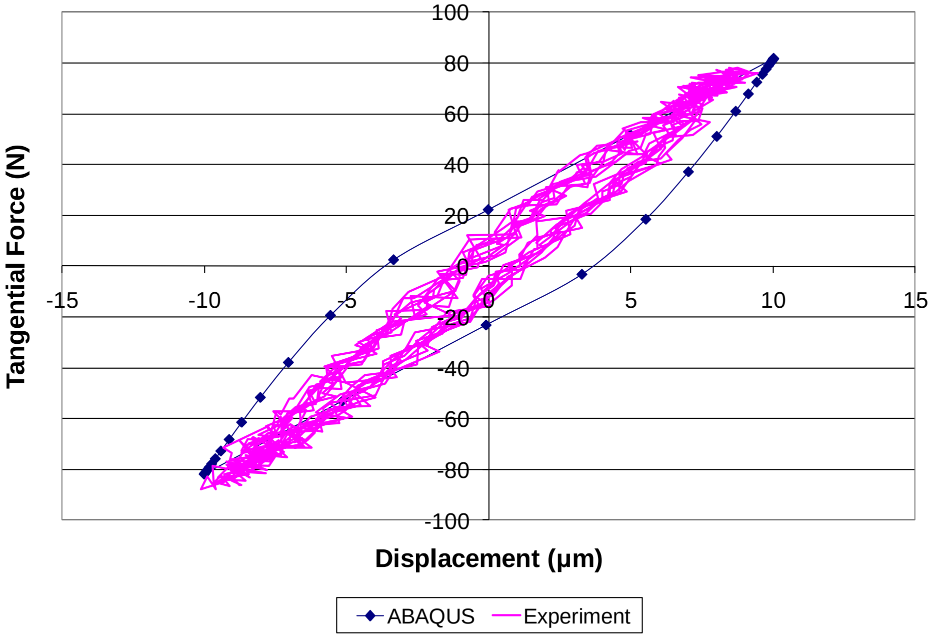

Figure 5.8: Example of hysteresis response with poorly tuned model properties.

5.2 Damage Parameter Evaluation Method

The Fatemi-Socie (FS) [120] and Smith-Watson-Topper (SWT) [121] parameters were evaluated using the cyclic stress strain response determined from the finite element model. The FS parameter is based on the principle that fatigue damage, both the nucleation and propagation of fatigue cracks, is driven by the combination of the shear strain range ($\Delta\gamma$) and the maximum normal stress (σ_n^{max}) on the same plane during a cycle so that the fatigue life is related to the maximum value of that combination for all planes,

$$\left(\frac{\Delta\gamma}{2}\left[1 + k\frac{\sigma_n^{max}}{\sigma_y}\right]\right)_{max} = F(N) \tag{5.13}$$

where σ_y is the yield strength, *k* is a constant that approaches unity for long lives [122], and *F(N)* is a function that relates to the fatigue life. Thus, the parameter serves as a relative measure of the severity of fatigue damage and indicates the orientation of the plane on which crack formation and growth is most likely to occur. The value of *k* was set to unity for all conditions, which is the value to which *k* approaches for long lives [122].

The SWT parameter was evaluated similarly, but is based on fatigue damage being driven by the normal strain amplitude ($\Delta\varepsilon/2$) and maximum stress (σ_{max}) on the same plane over a cycle so that the fatigue life is related to the maximum value of the product for all orientations,

$$\left(\frac{\Delta\epsilon}{2}\sigma_{max}\right)_{max} = F(N) \tag{5.14}$$

where *F(N)* is a function that relates to fatigue life, which is inversely related to the magnitude of the FS and SWT parameters. Since the exact functional form of *F(N)* has not been established for this material, these parameters give a relative indication of fretting fatigue damage. Both parameters were evaluated by computing values on planes in increments of five degrees and finding the maximum value and corresponding plane.

The FS and SWT values were averaged over a 15 μm radius, approximately equal to the grain size, to account strain gradient sensitivity [106]. The value of the FS parameter was averaged rather than the stresses, however the two approaches have been shown to yield similar results [116].

The energy dissipated due to fretting is the integral over a cycle of the product of the local shear stress and local infinitesimal slip, therefore being a path-dependent local measure [155]. The dissipated energy was calculated numerically using equation 5.3,

$$\left(\sum_{i=1}^{n}\tau_i\delta_i\right)_{\max} = f\left(N_f\right) \tag{5.15}$$

where τ_i is the average shear stress on a node during increment i, and δ_i is the slip magnitude at the same node during the same increment. Shear stress at nodes was determined using the CSTRESS output in Abaqus, and slip at nodes was determined using the CSLIP output.

5.3 Results

The agreement between model and experimental hysteresis loops after tuning the stiffness and PTFE-stationary specimen COF is shown in Figure 5.9. Experimental hysteresis loops were plotted for three consecutive cycles to show the typical variation. The optimal value of the COF against the PTFE layer was found to be 0.04, which is a physically realistic value for contact between steel and PTFE. The optimal stiffness of the compliant layers was determined to be 375 MPa. These values were determined by comparison with results using 52100 steel as the moving specimen, and were found to be appropriate for use with an A356 aluminum moving specimen as well, shown in Figure 5.9(b). Intuitively this should be the case, since the machine compliance should be independent of the choice of the moving specimen material.

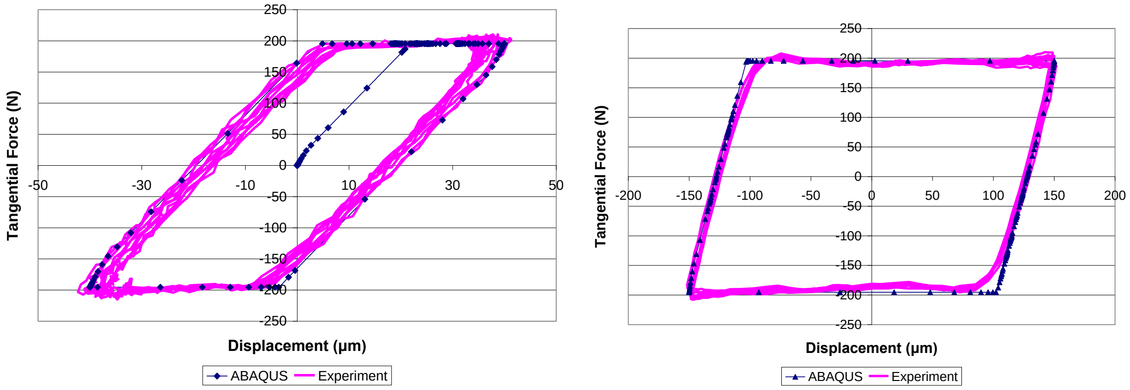

(a) (b)

Figure 5.9: Comparison of model and experimental hysteresis loops for contact with (a) 52100 steel and (b) A356 aluminum.

The model is able to accurately represent both partial slip and gross slip conditions. The model also demonstrates the transition from partial slip to gross slip conditions at the correct displacement amplitude. The agreement between the hysteresis loops for partial slip and gross slip conditions is shown in Figure 5.10 where the only difference in the contact parameters is a 10 μm increase in displacement amplitude and a decrease in the COF at the contact between the moving and stationary specimens from 1.22 to 0.78, which are equal to the experimentally measured values. The ability of the model to demonstrate this behavior is a critical aspect in the analysis of the fretting behavior and shows that the model is a good representation of the mechanics of the interaction.

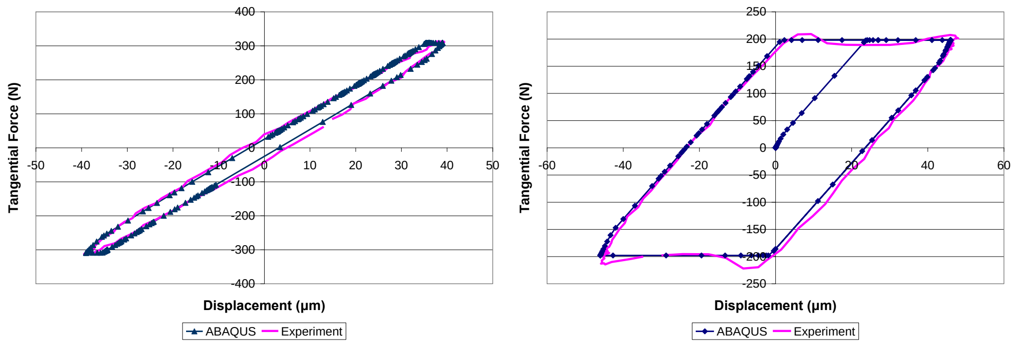

(a)

(b)

Figure 5.10: Model results for modeling of (a) partial slip conditions and (b) gross slip conditions.

The Lagrange Multiplier tangential friction formulation required 15% more computation time than the Penalty method. The computation time for the simulation with a Lagrange Multiplier formulation ranged from 0.5 hours when using a 10 μm displacement amplitude to 1.5 hours for a 200 μm displacement amplitude using a single 3.2 GHz Pentium 4 processor.

The model response was determined to be stabilized by comparison of the change in plastic strain between cycles for a case with a 375 N normal force at 250^{o}C . The difference in the horizontal plastic strain component between the end of the cycle used as the stabilized response and the following cycle is shown in Figure 5.11. The maximum change in this plastic strain component in the near surface region is approximately 0.002%, relative to a total plastic strain value at that location of 0.028%.

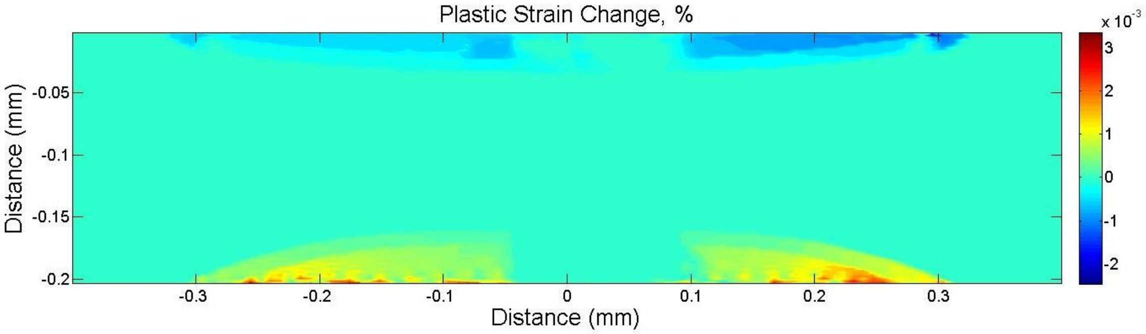

Figure 5.11: Change in horizontal plastic strain between the end states of the final two cycles.

The Von Mises stress field resulting from the moving specimen sliding to the right is shown in Figure 5.12(a). The maximum value occurs at the bottom of the stationary specimen at the interface with the PTFE layer, which was not the expected result. Inspection of the horizontal normal stress as shown in Figure 5.12(b) shows that there is a compressive stress at the top surface of the stationary specimen and a tensile stress at the bottom surface. This shows that the specimen is subjected to bending. The PTFE layer that supports the thin stationary specimen easily deforms beneath the contact location, allowing the specimen to bend. The additional tensile horizontal stress at the bottom of the specimen due to bending causes an increase in the Von Mises stress at that location.

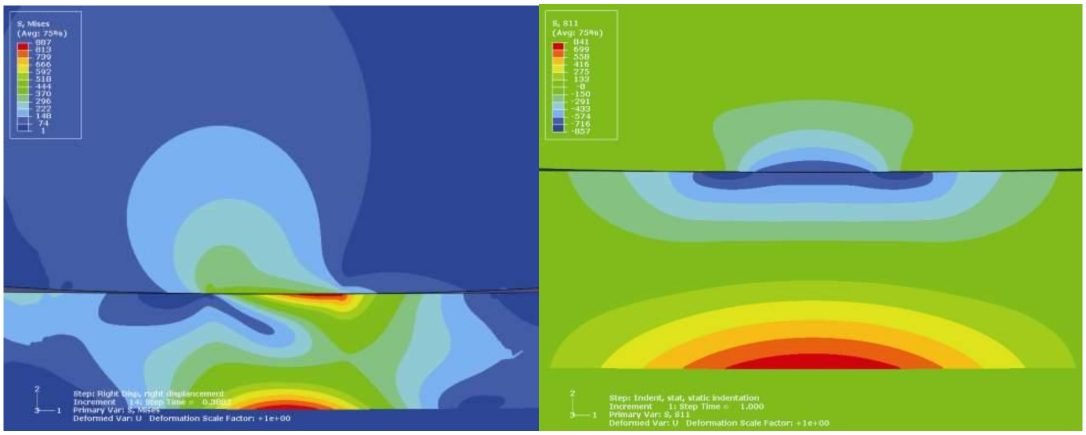

(a) (b)

Figure 5.12: (a) Von Mises stress while the moving specimen is sliding to the right and (b) horizontal normal stress during indentation.

A comparison of the analytical solution for the stresses on the surface of a half-space in contact with a cylinder that is sliding to the right [30] and the stresses on the surface of the stationary specimen calculated from the finite element model with the PTFE layer represent using a 375 N normal force and COF of 0.55 is shown in Figure 5.13. The radius of curvature related to the observed bending stress is 31 mm. This increases the conformity of the contact, which increases the contact area by 24% and therefore decreases the contact pressure. The superposition of the bending stresses shifts the tangential (1- direction) stress component so that it is entirely compressive for values of COF less than approximately 0.55, which reduces the tendency for crack formation at the contact interface. Therefore, it is expected that the decrease in fatigue life due to fretting would be larger in the absence of the additional bending component.

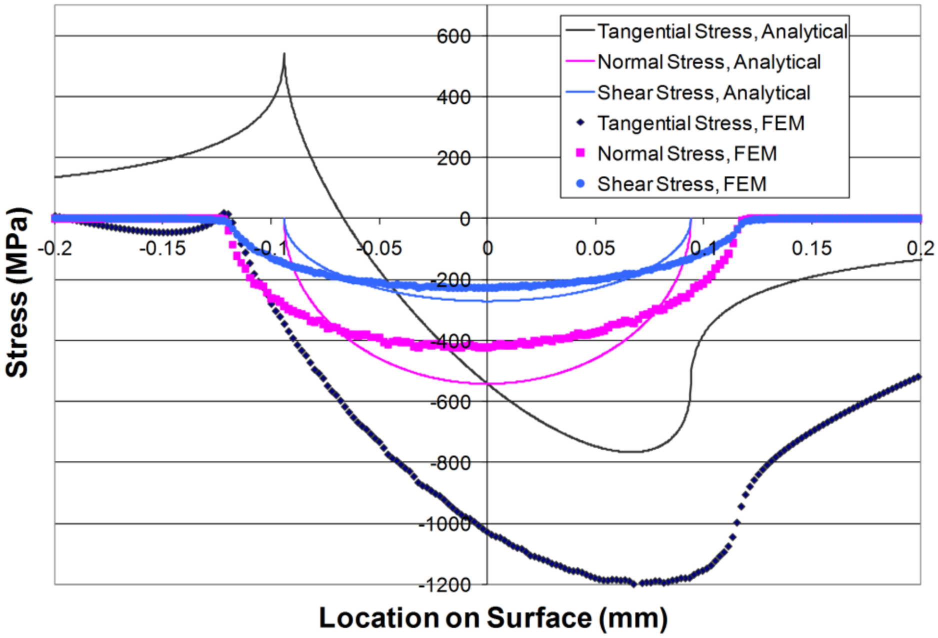

Figure 5.13: Comparison of the surfaces stresses due to sliding contact with and without a PTFE layer.

Analysis of the through-the-thickness deformation of the specimen shows that a minimal amount of buckling of the specimen occurs. The maximum deflection of the specimen in a direction normal to the holder at a location away from contact is 4 µm, with a maximum range of motion of approximately 7 µm, thus showing that the holders are effective at minimizing buckling.

An example of the output of the accumulation of frictional energy dissipation at the surface of the stationary specimen throughout a cycle is shown in Figure 5.14. The total energy dissipated per cycle is equal to the area under the curve at the end of the cycle. The dissipated energy distribution has a maximum value in the center of the contact for the gross slip case. This is expected and is the reason for the typical "U" shaped wear profile for gross slip conditions. The dissipated energy distribution for the partial slip condition is maximum near the edges of contact, which is the only portion of the contact that undergoes slip. This distribution leads to the typical "W" shaped wear profile.

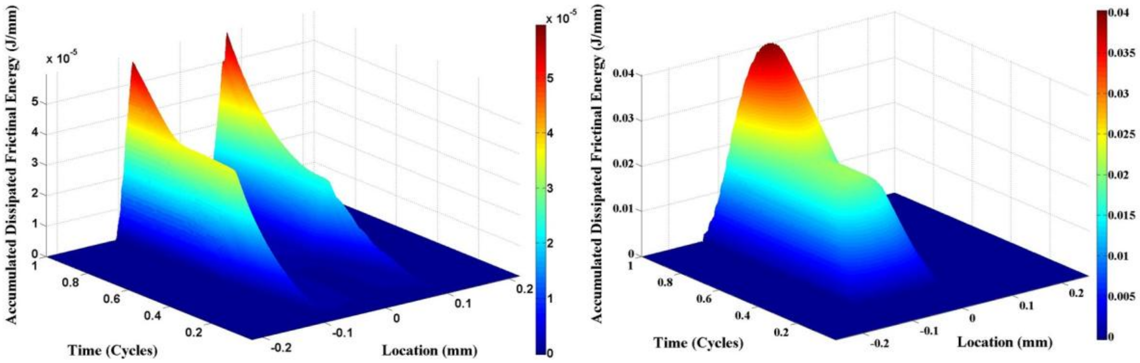

(a) (b)

Figure 5.14: Frictional energy dissipation accumulation for a (a) gross slip condition and (b) partial slip condition.

The total energy dissipation on the surface of the stationary specimen determined from the model for a normal force of 255 N is shown in Figure 5.15. The total energy dissipation is higher for the tests conducted at 20°C for displacement amplitudes above 40 μm. The difference in the total energy dissipation is similar to the amount measured experimentally. Representation in terms of the energy dissipated per area of material over which the energy was dissipated (contact width plus displacement range) shows a larger difference between the results at 20°C and 250°C. This is due to the larger contact area at 250°C resulting from a decrease in the modulus of the materials. Having a similar total dissipated energy would suggest a similar total wear volume if the material resistance to wear were unchanged. The greater difference in the dissipated energy density suggests that the difference in the wear depth would be greater than the difference in the total wear volume, since the similar total amount of energy is concentrated on a smaller area. This would lead to a more significant decrease in the subsequent fatigue lives for high wear cases due to the increased reduction in thickness, and would lead to an increase in subsequent fatigue lives for lower wear cases where the additional wear could increases the beneficial effects.

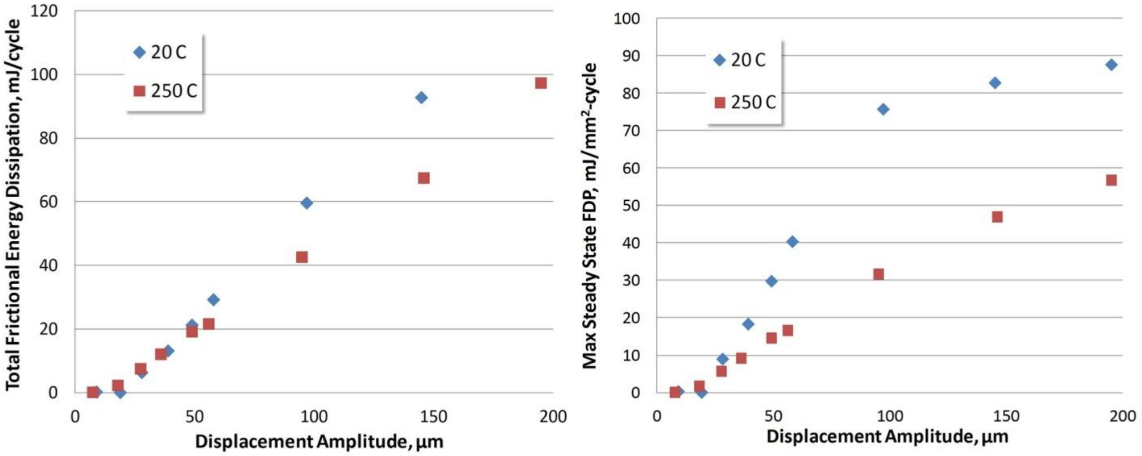

(a)

(b)

Figure 5.15: Frictional energy dissipation per cycle on the surface of the stationary specimen in terms of (a) the total dissipation and (b) dissipation per unit contact area.

Contour plots of the FS and SWT parameters calculated in the contact region on the stationary specimen for a 52100 moving specimen using a 255 N normal force and a 100 µm displacement amplitude are shown in Figure 5.16. FS values are highest on the surface surrounding the contact region because of the cyclic shear strain induced by friction, whereas the SWT values are highest at the bottom surface of the specimen because of the tensile stresses caused by bending. Evaluation of the fracture surfaces of specimens that underwent subsequent fatigue testing has shown that fatigue cracks formed in the fretting scar. Therefore, the FS parameter more accurately predicts the location of failure and is used exclusively for further analysis.

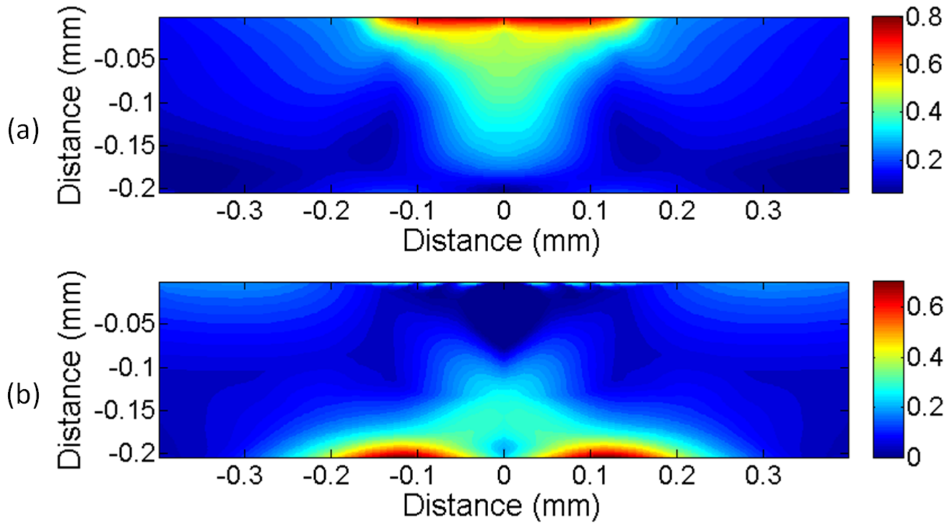

Figure 5.16: Values of (a) FS in percent and (b) SWT in MPa for a displacement amplitude of 100 μm.

The locations of the maximum values of the FS and SWT parameters for a 255 N normal force and various displacement amplitudes are shown in Figure 5.17. The maximum values of FS and SWT tend to move farther from the center of contact as the displacement amplitude increases for contact with both 52100 and A356. This trend is consistent with the experimentally observed failure locations from subsequent fatigue tests [180]. The scatter of the values may indicate the need to incorporate a higher degree of volume averaging when performing the FS calculation. Currently FS values are calculated at integration points and therefore are based on average values over the size of an element.

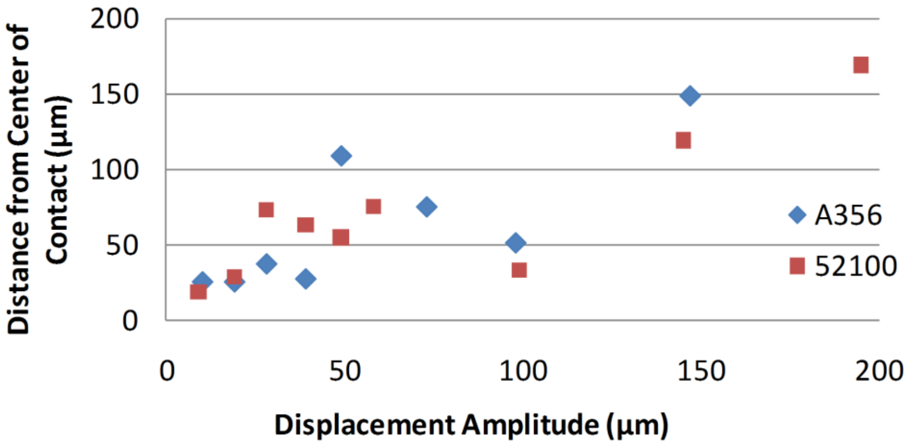

Figure 5.17: Location of the maximum values of the FS parameter.

A comparison of the maximum FS values to the COF values used in the simulations for a 255 N normal force and various displacement amplitudes is shown in Figure 5.18. There is a strong correlation between the COF and FS values, especially for contact with A356. This is expected since, as the COF increases for the same normal force, the shear applied to the surface increases which increases fatigue damage. This supports the claim that the COF is the most important parameter affecting the fretting fatigue behavior [1].

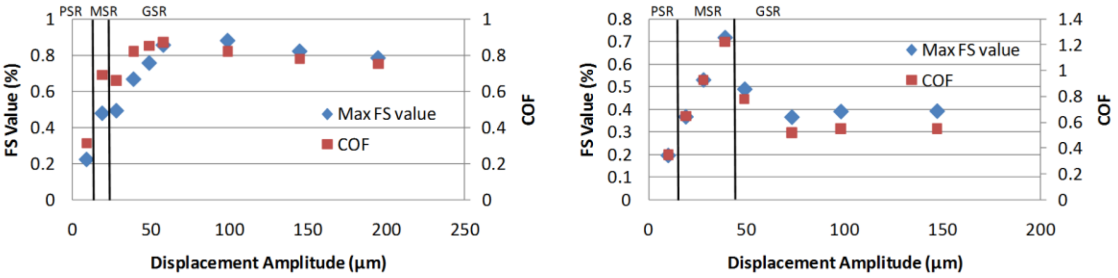

(a) (b)

Figure 5.18: Comparison of maximum FS values to the values of COF for contact with (a) 52100 steel and (b) A356 aluminum.

A comparison of the maximum FS values to the experimentally observed reduction in fatigue life due to fretting with a 255 N normal force and various displacement amplitudes as determined by subsequent fatigue tests is shown in Figure 5.19. Subsequent fatigue tests were performed using conditions corresponding to infinite life of the unfretted specimens, defined as 10^6 cycles. The trend of increasing fatigue damage with increasing displacement amplitude found experimentally is also demonstrated by the FS parameter for contact with 52100 steel. The values of the FS parameter are similar in magnitude to values reported elsewhere for fretting [52]. The value of the FS parameter for the uniaxial fatigue limit is 0.39%, thus fretting conditions that resulted in FS values of less than that value should result in infinite life. For specimens with fretting damage, this FS threshold value seems to capture the transition from no decrease in life to finite life for contact with 52100 steel. There is some departure between the FS values and the observed life as the displacement amplitude grows larger. This is likely due to the large amount of wear that occurred at these higher displacement amplitudes. The area of the specimen was reduced by 20% when the displacement amplitude was 200 µm. This causes the stress amplitude during subsequent fatigue to be greater than the plain fatigue limit thus reducing the fatigue life. Therefore, the model suggests that the fatigue damage due to fretting would marginally decrease as the displacement amplitude increases in the absence of wear or for thick specimens where the wear depth is not significant compared to the thickness.

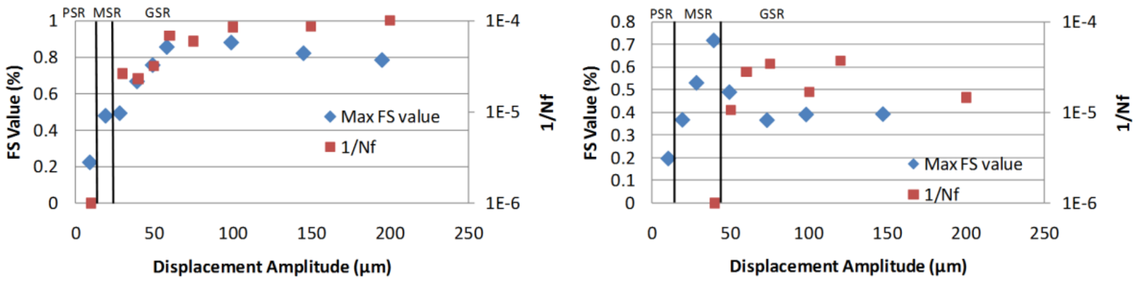

(a) (b)

Figure 5.19: Comparison of maximum FS values to the experimentally observed reduction in fatigue life due to fretting for contact with (a) 52100 and (b) A356.

The values of FS for contact with A356 aluminum do not agree as well with the observed life as for contact with 52100 steel. This discrepancy is due to material transfer from the aluminum moving specimen to the stainless steel specimen. In the mixed slip regime (MSR), the initial GS contact condition deposited a layer of aluminum on the surface as shown in Figure 5.20. The thickness of the aluminum layer is large compared to the depth of FS values that are above the fatigue damage threshold value. Therefore, the layer of aluminum accumulated during GS would effectively protect the specimen from further fatigue damage after the contact condition transitions to PS where the tangential force is high. The FS value is based on the high COF PS contact since it is the steady state response, and so the value of FS calculated by the model is correspondingly high.

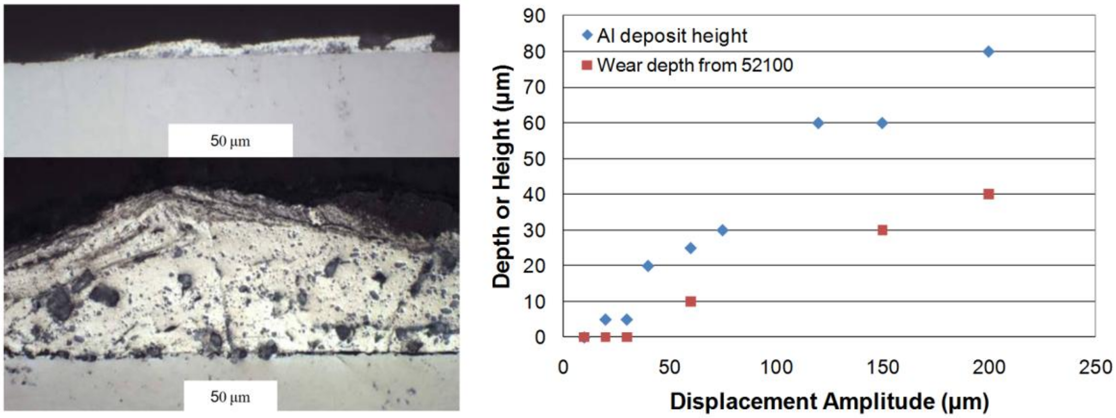

(a) (b)

Figure 5.20: (a) Aluminum layer transferred to stainless steel specimen for 40 µm mixed slip condition and a 150 µm gross slip condition and (b) measured thickness of the deposited A356 layer and approximate wear depth into the stationary specimen from contact with 52100.

The values for FS are below the threshold FS value for contact with aluminum in the GS regime despite the experiments exhibiting finite life. For GS conditions with aluminum, the large deposit of aluminum accumulated on the stationary specimen resulted in a plowing effect at the ends of the travel as discussed previously [145]. The deposit interference causes large increases in the tangential force at the ends of the stroke that are not captured by the finite element model. This increase in tangential force likely contributed to reducing the fatigue life of the specimens despite the FS value for an equivalent condition without plowing being below the FS threshold value.

The maximum FS values calculated from the model for each simulation are shown in Figure 5.21. The max FS values for a normal force of 255 N are higher for the 20 ^{o}C cases than for the 250 ^{o}C cases for displacement amplitudes up to 150 μm. This is due partly to the increased contact area at elevated temperature due to the decrease in modulus and partly due to the difference in the COF values, which are the closest in value at the highest displacement amplitudes. The max FS values at 250 ^{o}C calculated for a 100 N normal force were higher than or similar to the values the 255 N normal force. This was not expected since the tangential force was higher for the 255 N case. Similarly, the max FS values for the 255 N normal force were similar to or higher than the values for the 375 N normal force. The increased contact area resulting from the higher normal force causes a reduction in the pressure, which is enhanced by the presence of the compliant PTFE layer, helps explain this result.

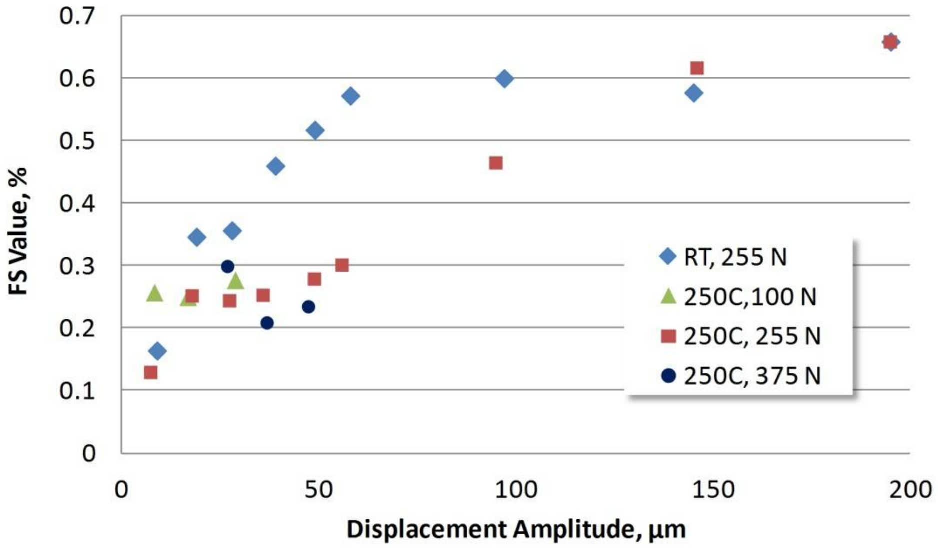

Figure 5.21: Maximum Fatmi-Socie values for contact with 52100.

A comparison of the model prediction for fatigue damage and the experimental subsequent fatigue lives is shown in Figure 5.22. The subsequent fatigue results are presented as the inverse of life so that both sets are proportional to fatigue damage and the comparison is more clear. The prediction for the level of fatigue damage was fairly consistent for the tests conducted at 20 ^{o}C for all displacements. It was expected that the actual fatigue damage would be more severe than the prediction at high amplitudes because of the reduction in thickness, rather than the expected result for a thick specimen which would have a higher level of fatigue damage than predicted due to the beneficial effects of wear. This suggests that the detrimental effect of thickness and the beneficial effects of material removal nearly offset one another.

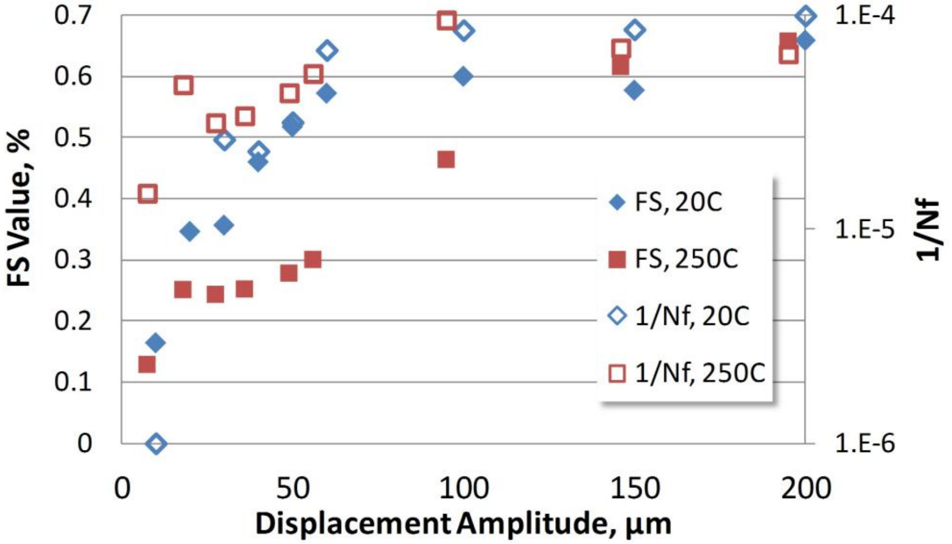

Figure 5.22: Maximum FS values and experimental subsequent fatigue results.

The actual level of fatigue damage at 250^{o}C was higher than predicted by the model, especially at the lower displacement amplitudes. This is due to the reduction in fatigue strength of the material at elevated temperature. At higher displacements, the predicted level of fatigue damage increases because the COF values increase with increasing amplitude. However, the actual level of fatigue damage did not continue to increase with increasing displacement. The glaze oxide layer which is more prominent at higher displacements may have provided a protective effect.

5.4 A New Fretting Damage Metric

5.4.1 Model Formulation

Prediction of the extent of fatigue damage due to fretting via FEM is complex due to the interaction of fatigue and wear. The typical interaction between wear and fatigue for abrasive material removal and a constant normal force is shown in Figure 5.23. Wear is low at low displacement amplitudes and has an insignificant effect on the fatigue life. The fatigue life is minimum at moderate displacement amplitudes due to the acceleration of fatigue damage caused by asperity interaction resulting in localized plasticity and crack formation. The wear rate increases with displacement amplitude, which tends to cause a reduction in the level of fatigue damage. This is caused by an increase in contact conformity due to wear which lowers contact stresses because of the increased contact area [40, 42-43] and by the removal of surface material which was subjected to the highest level of fatigue damage [38-41]. The overall effect of wear on the fatigue life is dependent on the competition of the beneficial and detrimental effects of wear which are active at different levels of energy dissipation.

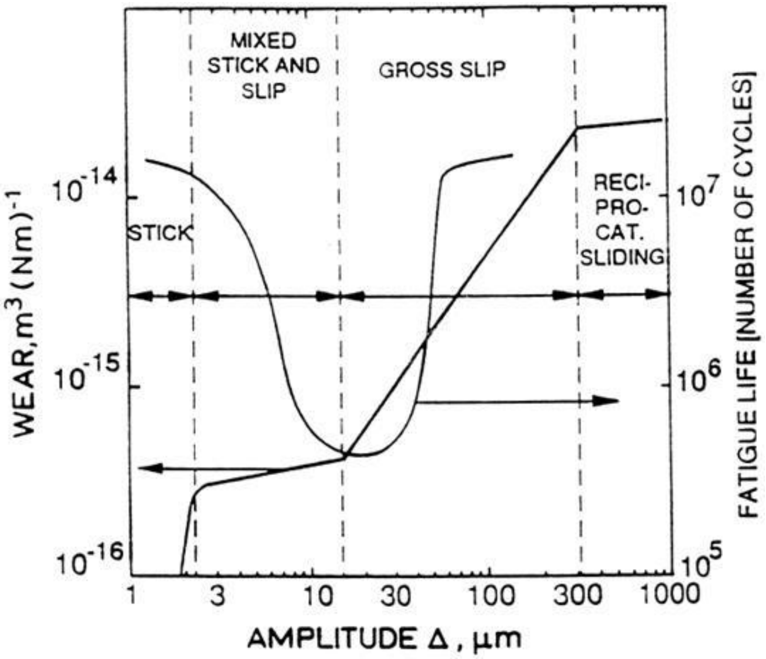

Figure 5.23: Vingsbo-Soderberg diagram [34].

Critical plane fatigue damage metrics do not account for the effects of wear on the extent of fatigue damage and are only sufficient for fatigue damage prediction for cases where the extent of wear is insignificant. However, critical plane fatigue damage metrics have been successfully used to predict fatigue damage in cases where wear is significant when combined with explicit wear modeling [183]. In this method, fretting cycles are simulated with calculation of the critical plane parameter over the body and alteration of the geometry based on the frictional energy dissipation after each cycle [184]. The accumulated level of fatigue damage throughout the volume is determined after each cycle by incorporating the fatigue damage from previous cycles using a fatigue damage summation rule. This method is able to capture the decrease in fatigue damage due to the reduction of stress from the increase in contact size as well as the removal of material which has accumulated fatigue damage. However, it is not able to capture the increase in fatigue damage at moderate slip amplitudes due to asperity interaction, and is computationally expensive due to the need to simulate multiple cycles and adjust the model geometry. A simpler method which accounts for the effects of wear with reduced computational expense is desired for practical application.

Ding et al. [110, 157] recently proposed a modified SWT parameter (mSWT) that considers the combined effects of frictional energy dissipation and the cyclic stress state to determine the level of fatigue damage using only the stress state and slip response for the stabilized fretting cycle. The mSWT parameter accounts for the cyclic stress using the SWT critical plane based multiaxial fatigue damage parameter with an expression based on the frictional dissipated energy to account for the influence of slip on the extent of fatigue damage predicted. The modified SWT parameter is given by

$$\left(\sigma_{\max}\varepsilon_a D_{fret2}\right)_{\max} = f\left(N_f\right) \quad \text{for} \quad \tau\delta \le \left(\tau\delta\right)_{th} \tag{5.16}$$

where $\sigma_{\max}$ is the maximum normal stress on a plane, ε_a is the strain amplitude normal to the same plane, τ is the shear stress from friction, δ is the slip amplitude, $\tau\delta$ is the frictional dissipated energy, $(\tau\delta)_{th}$ is the empirical threshold dissipated energy, and D_{fret2} is given by

$$D_{fret2} = \left(1 + C\tau\delta\right)\left\langle 1 - \frac{\tau\delta}{\left(\tau\delta\right)_{th}} \right\rangle^n \tag{5.17}$$

where C and n are empirical constants that are dependent on the wear properties of the material. The first factor within parenthesis describes the observed result of the trend of an increase in the level of fatigue damage in slip regions where energy is dissipated at the surface. C must be a positive value based on this definition, thus the first factor is a linearly increasing function of the frictional work which acts to increase the predicted level of fatigue damage at locations with higher levels of energy dissipated by friction. The rest of the factor is descriptive of the beneficial effects associated with wear such as reduction of the stresses by the increase in the contact area and the removal of material which had undergone accumulation of fatigue damage.

A plot of D_{fret2} which represents a typical fretting response is shown in Figure 5.24. In the absence of contact, $\tau\delta$ is equal to zero and D_{fret2} is unity, thus the mSWT parameter becomes equivalent to the SWT parameter outside of the contact region. The linear factor of D_{fret2} is dominant at low levels of energy dissipation to describe the negative effects of slip, and the power law factor becomes dominant at higher levels of energy dissipation to describe the beneficial effects of wear. For values of dissipated energy greater than or equal to the threshold value, D_{fret2} is equal to zero and the mSWT parameter indicates zero fatigue damage, which is the observed result for abrasive material removal.

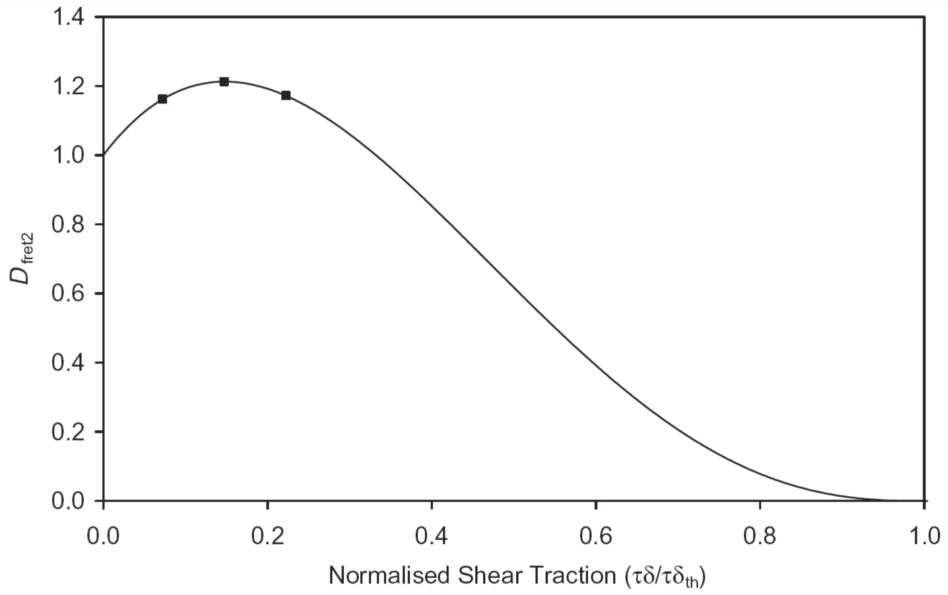

Figure 5.24: D_{fret2} for a typical fretting response for abrasive material removal [157].

The modified SWT parameter has been used for analysis of three sets of experiments, and was found to be successful in each: a CrMoV spline coupling [110, 158], a Ti-6Al-4V half cylinder on flat fretting fatigue arrangement [159], and a Al4%Cu (HE15-TF) half cylinder on flat fretting fatigue arrangement [116]. The three empirical constants in the modified SWT enhance the ability of the modified SWT to provide accurate predictions in a variety of conditions, and the modified SWT parameter is more accurate than any other parameter reported in the literature when considering all running conditions. However, the modified SWT parameter is only well suited to represent the typical fretting result where wear results in the removal of material from the body of interest. For contact between a cylinder of A356 aluminum and a sheet of 301 stainless steel, aluminum transfers to the stainless steel and results in a response which does not follow the classic result described by Vingsbo and Soderberg. D_{fret2} is largely empirical and can be adjusted to fit a wide range of conditions, however it was not developed with regard to many situations, such as adhesive material transfer.

The form of D_{fret2} required to provide an accurate fatigue damage prediction is related to the fatigue damage parameter and energy dissipation fields over the surface of the contact. D_{fret2} must be tuned to amplify or attenuate the fatigue damage parameter based on the dissipated energy behavior such that the maximum value corresponds to the location of observed failures with consideration to a wide range of conditions. An example of the dissipated energy and FS values for contact with 52100 with a 255 N normal force and 200 μm displacement amplitude is shown in Figure 5.25. The observed location of failure after being subjected to uniaxial fatigue was at the center of contact, whereas the FS parameter indicates a failure location near the edge of contact. Therefore, a form of D_{fret2} is needed which will reduce the level of fatigue damage at the lower energy levels, which is not realistic for abrasive material removal, or increase the level of fatigue damage at high energy levels while still being applicable to the results of other test conditions.

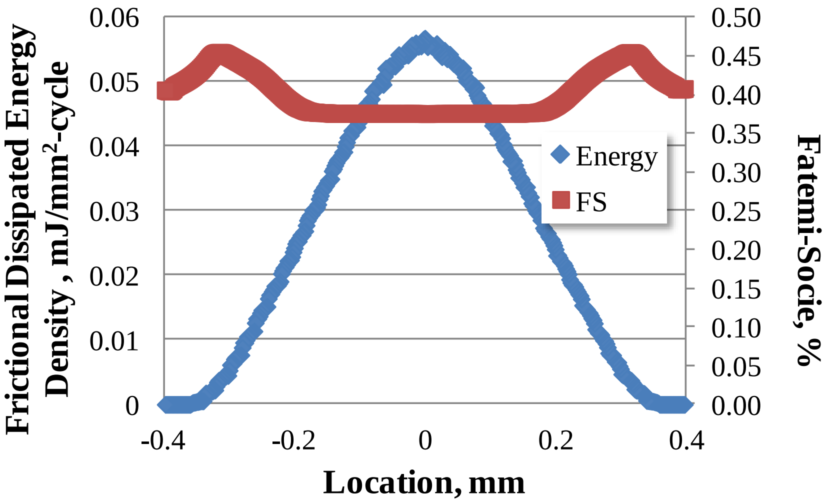

Figure 5.25: Energy dissipation density and Fatemi-Socie profiles.

The form of D_{fret2} required to describe the behavior of 301 stainless steel in contact with A356 aluminum is shown in Figure 5.26. As discussed in the previous chapter, a small amount of transferred aluminum was found to provide a protective effect, thus the value of D_{fret2} is below unity for low levels of energy dissipation. The extent of transfer of aluminum continues to increase as the level of dissipated energy continues increases, causing an increase in the level of fatigue damage due to the increase of the plowing effect. The energy threshold description used in the mSWT parameter no longer accurately describes the behavior in this case and the expression for D_{fret2} is not able to describe the effect on the level of fatigue damage.

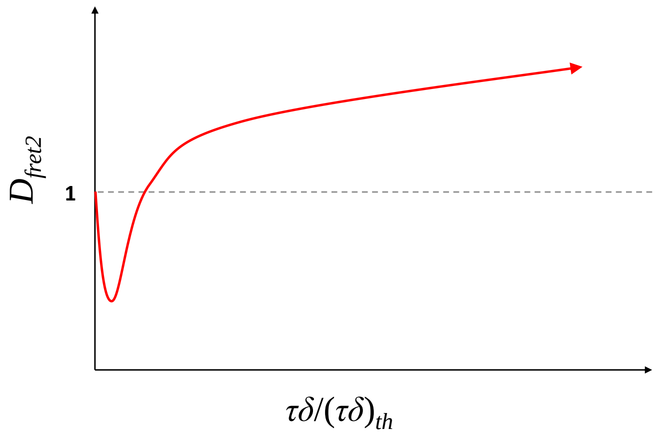

Figure 5.26: Approximate shape of Dfret2 required to capture response for contact between aluminum and stainless steel.

A new fretting fatigue damage metric is proposed which is based on the influence of wear processes on the level of fatigue damage and the competition between the beneficial and detrimental effects of slip. The new parameter is given by

$$FS \cdot D = f\left(N_f\right) \tag{5.18}$$

where

$$D = \left[\left(1-a\right)e^{bRW_{eff}} + a\right]\left[\left(1-c\right)e^{dRW_{eff}} + c\right] \tag{5.19}$$

and

$$W_{eff} = \frac{k_{dam}}{1+\alpha_{cp}}\left(\tau\delta\right) \tag{5.20}$$

where a, b, c, and d are constants, FS is the Fatemi-Socie parameter, R is the wear rate for the body of interest, and W_{eff} is the effective work as described by Vidner and Leidich [111] in terms of the dissipated energy density (energy per surface area), where k_{dam} is the fraction of the total frictional energy that goes toward fatigue damage, α_{cp} is the ratio of the frictional energy that goes toward the contacting body to the frictional energy that goes toward the body of interest, and ($\tau\delta$) is the frictional work. The FS parameter is used for this study because it was shown to provide a more accurate prediction of the location of maximum fatigue damage due to fretting than the SWT parameter for the conditions examined in this work. Other fatigue damage metrics can be substituted in place of the FS parameter as appropriate. The factor which modifies the FS value (*D*) describes the extent of acceleration or retardation of fatigue damage caused by processes related to slip.

The first term in square brackets describes the effects of slip which are detrimental to the fatigue life and the second factor in square brackets describes the effects of slip which are beneficial. The extent of the effect is governed by the empirical constants and the wear rate. An example of the form of each of the factors of *D* are shown in Figure 5.27. Each factor has the form of exponential saturation, with the beneficial factor decaying to a value below unity and the detrimental factor saturating to a value above unity. The value of *D* is unity for zero energy dissipation, thus the prediction of the level of fatigue damage is equal to that of the FS parameter. A net value of *D* which is above unity results in an amplification of the fatigue damage predicted by the FS parameter, and a net value below unity results in the reduction of the level of fatigue damage predicted by the FS parameter.

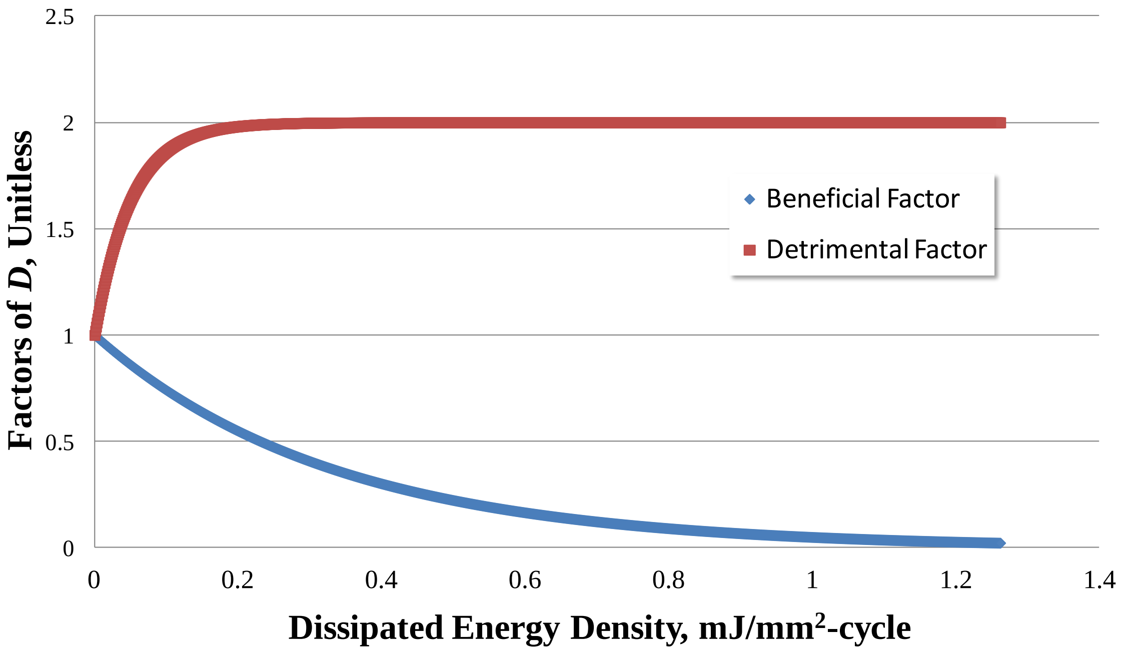

Figure 5.27: Example of the beneficial and detrimental factors which comprise *D*.

The constants *a* and *c* are the saturation values of the detrimental and beneficial factors, respectively, and dictate the maximum influence of slip on the level of fatigue damage for high energy dissipation levels. The constants *b* and *d* influence the rate at which the value of the factor approaches *a* and *c*, respectively. The wear rate also influences the rate of approach to *a* and *c*, with a higher magnitude wear rate resulting in an increase in the rate of approach to stabilized value. This is expected since an increase in wear rate results in a reduction of the extent of dissipated energy which results in an equal amount of wear.

Several processes affecting wear are exponential in nature. The accumulation of debris in the contact displays exponential growth and saturation with increasing levels of dissipated energy since the rate of generation becomes higher relative the rate of ejection [185-187]. This can be beneficial or detrimental depending on the composition of the debris. The beneficial effect of contact stress reduction with geometry change also saturates at high levels of energy dissipation since the geometry approaches a conforming contact. Thus the exponential form of the factors of *D* can be appropriate to describe the effects of slip on the severity of fatigue damage. Other forms of *D* were investigated but were not able to describe the behavior.

A threshold energy is not used in this model since it is not appropriate when applied to the case of adhesive material transfer to the body of interest. For the case of abrasive wear removal, *c* becomes zero and the predicted level of fatigue damage approaches zero as the energy level increases, thus retaining the ability to predict the classic result in a similar manner to the mSWT parameter.

The effective frictional work described by Vidner and Leidich is used rather than the total frictional work to further enhance the physical basis of the model. This description of the effective work allows for adjustment of the influence of energy dissipation on the level of fatigue damage by dividing the measured energy dissipation into categories based on the method of dissipation [160]: a mechanical component (deformation and wear), a thermal component (heat), a chemical component (tribo-oxidation [161]), and other tribo-physical components (e.g. sound [162]). Therefore, only a portion of the total frictional energy causes fretting damage to the specimen. The dissipated frictional energy is also divided between the two bodies in contact since only a portion of the dissipated energy results in damage to the body of interest.

5.4.2 Application to Fretting of 301 Stainless Steel

The model was calibrated to the results for fretting of 301 stainless steel against A356 aluminum at room temperature to demonstrate the ability to predict fretting fatigue damage in the case of adhesive material transfer and 52100 steel at 250°C to demonstrate the ability to predict fretting fatigue damage for the case of abrasive material removal. As discussed previously, the apparent increase in the level of fatigue damage inflicted during fretting of 301 stainless steel specimens in contact with 52100 steel at room temperature was affected by the increase in the subsequent fatigue stresses as a resulting of the significant thinning of the sample during fretting due to the high wear rate. This effect is only significant because of the thickness of the specimens and thus is not an effect which should be described by a fretting damage fatigue metric. Therefore the model was not calibrated to results for fretting in contact with 52100 steel at room temperature.

The frictional dissipated energy density was calculated in ABAQUS using the shear stress interpolated to surface nodes using the CSTRESS output and the slip displacement at nodes using the CSLIP output. FS values were calculated at integration points. FS values were assigned to the surface nodes to allow calculation of the new parameter by using an average of the FS values at integration points within a 15 μm radius, which corresponds to the approximate grain size of the 301 stainless steel used in this study. The wear rate for contact with 52100 steel was determined for a displacement amplitude of 200 μm and normal force of 255 N. This case had the most significant level of wear for tests conducted at 250°C with a 255 N normal force and resulted in the most accurate wear measurement. The wear rate was determined as the total measured wear volume divided by the total frictional energy dissipated on the surface of the specimen as determined by FEA. The energy dissipation profile is highest in the center of contact and decreases toward the edge of contact for gross slip cases, thus various locations on the surface undergo wear over a range of local energy dissipation levels. Using the total volume and energy to calculate the wear rate therefore represents the average wear rate for a range of energy levels which spans the range of energy levels resulting from the fretting tests performed in this work. R for contact with aluminum was determined in the same way using the results from fretting with aluminum at room temperature with a displacement amplitude of 150 μm and a normal force of 255 N. The 200 μm case was not used because the height of the deposited layer was higher than could be measured with the profilometer used.

The value W_{eff} was taken as the value of the frictional energy density dissipated on the surface of the specimen as determined by FEA. It was not possible to determine the portions of the energy which were dissipated by methods which did not result in fatigue damage to the surface using the experiments conducted, thus it was assumed that all of the energy resulted in fatigue damage. Using a different values for k_{dam} and α_{cp} would change the values of b and d determined during calibration.

Calibration was performed by identifying the locations of failure after subsequent fatigue testing for each fretting condition considered. The FS parameter was calculated over the surface of the specimen and was compared to the distribution of frictional energy dissipation. The relationship between the energy and the FS values at the actual location of failure was used to determine the necessary value of D at that energy level. This was done with consideration for all conditions tested, since the value of D which caused a desired effect on the response a particular energy level for one case could cause an undesired effect for another condition. An example of this is shown in Figure 5.28. The actual location of failure was at the center of contact, so the FS parameter needed to be modified such that the value in the center was greater than near the edge of contact where the value of energy is low. A form *D* which results in lower value at low energy levels causes a decrease in the fatigue damage prediction at the center of contact for lower amplitude conditions where energy levels are lower.

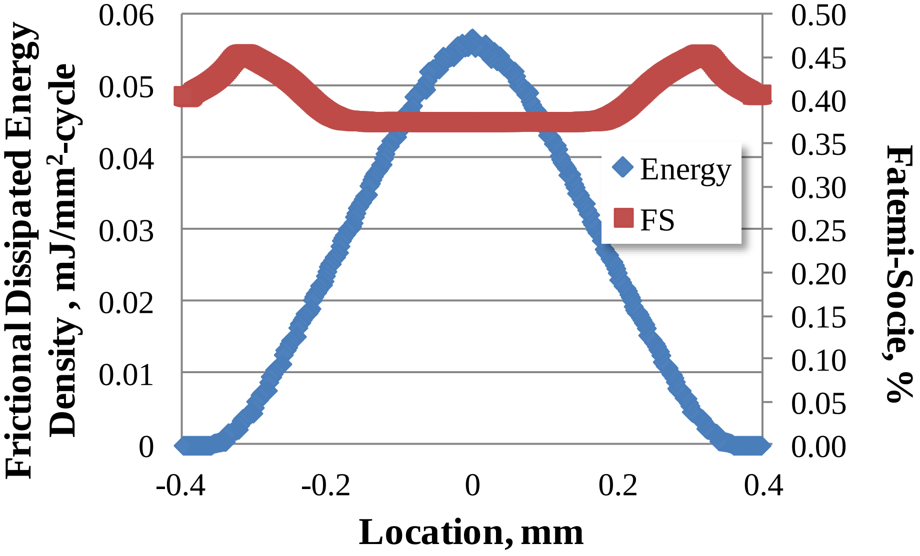

Figure 5.28: Energy dissipation and FS parameter value over the contact surface for contact with 52100 at 250°C with a displacement amplitude of 200 μm.

The forms of the beneficial and detrimental factors describing the influence of slip are shown in Figure 5.29. The constants used are shown in Table 5.2. The detrimental factor describing the effects of asperity plasticity increases to a saturated value at low levels of energy dissipation while the beneficial effects of stress redistribution and fatigue damaged material removal saturates at a lower rate. The resulting form of *D* for contact with 52100 steel at 250°C is shown in Figure 5.30. This form is similar to that of the classical result for abrasive material removal, however this form spans a large range of energy levels because of the high wear resistance at elevated temperature. Energy levels for tests performed in contact with 52100 at 250°C were all in the lower energy range where wear caused an increase in predicted level of fatigue damage since the beneficial effects of wear were not experienced for the low levels of wear.

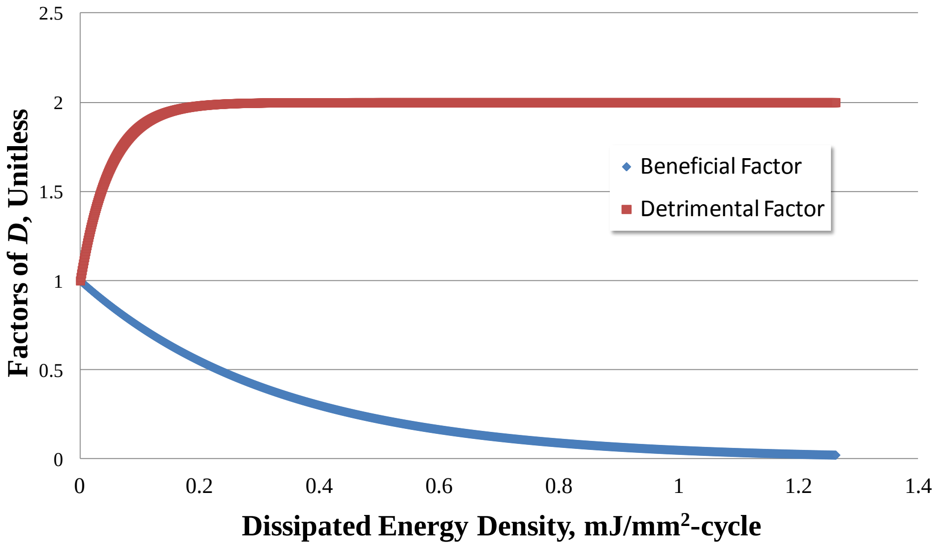

Figure 5.29: Form of beneficial and detrimental factors of *D* for contact with 52100 at 250°C.

Table 5.2: Constants used for calibration of the new parameter for contact with 52100 steel at 250°C.

a	*b*	*c*	*d*	*R*
1.8	-930×10^{3} cycle/μm	0	-140×10^{3} cycle/μm	21.5×10^{-6} mm^3/J

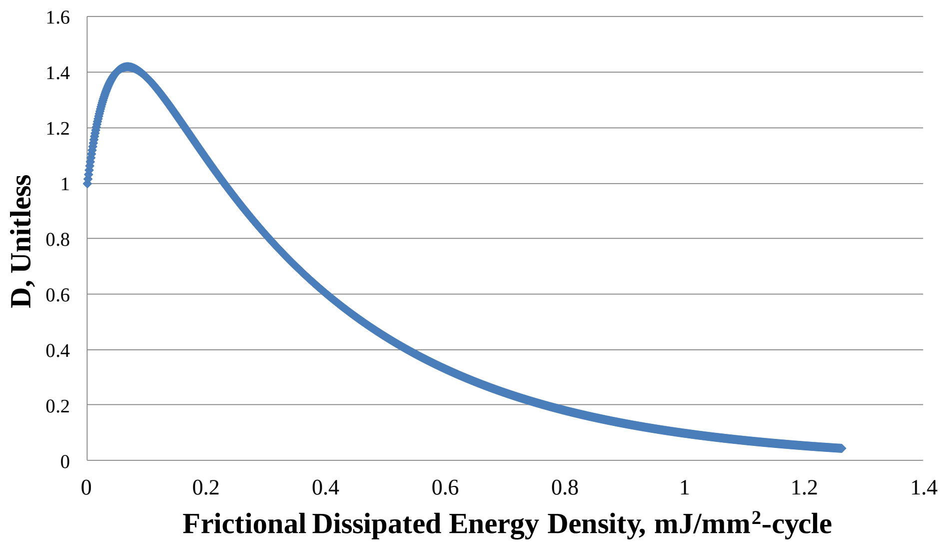

Figure 5.30: Form *D* for contact with 52100 at 250°C.

The resulting prediction of the location of failure from the new parameter compared to the FS prediction and the experimentally observed location for contact with 52100 steel at 250°C is shown in Figure 5.31. The prediction of the new parameter is consistent with the FS prediction at low displacement amplitudes where the level of energy dissipation is low. The prediction of the new parameter was more consistent with the experimentally observed failure locations at higher energy levels. A closer match could not be made without affecting the failure location at other conditions or the fatigue damage level prediction.

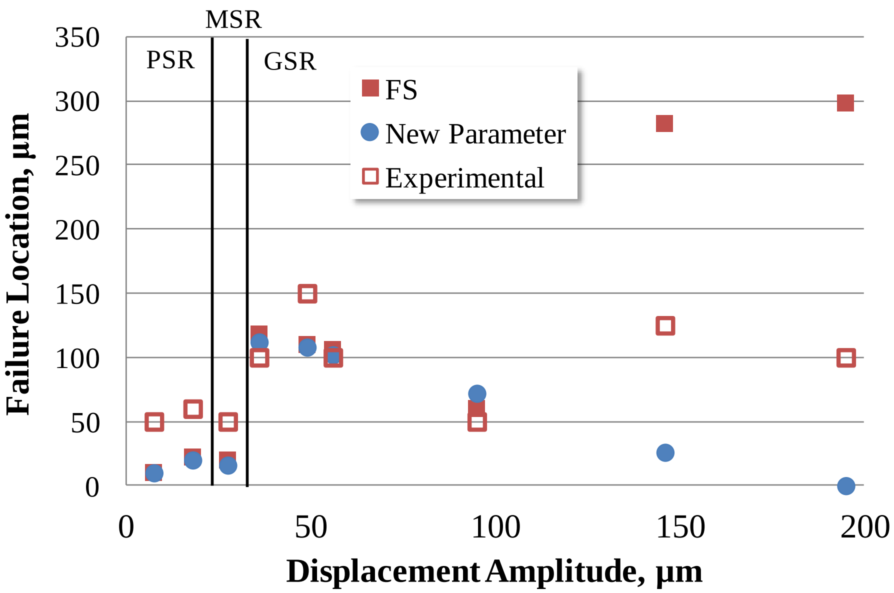

Figure 5.31: Failure location predictions compared to experimental results for contact with 52100 steel at 250°C.

A comparison between the values of the new parameter and FS parameter over the contact surface for contact with 52100 at 250°C with a displacement amplitude of 200 μm is shown in Figure 5.32. The location of the maximum value was shifted from near the edge of contact to the center of contact. The failure location predicted by the new parameter is closer to the actual observed location than the FS value, however it was not possible to make a more accurate prediction without affecting the level of fatigue damage predicted at other conditions.

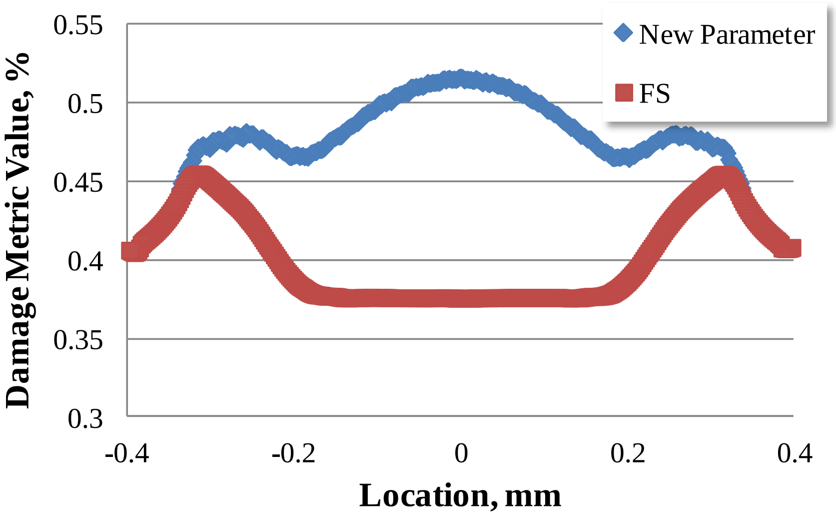

Figure 5.32: New parameter and FS parameter over the contact surface for contact with 52100 at 250°C with a displacement amplitude of 250 μm.

A comparison of the level of fatigue damage predicted by the new parameter, the FS parameter, and the experimental results for contact with 52100 steel at 250°C is shown in Figure 5.33. The level of fatigue damage predicted by the new parameter was similar to the level predicted by the FS parameter at lower energy levels. A small benefit was achieved for the 50 μm and 60 μm conditions where the new parameter correctly predicted a higher level of fatigue damage for the 60 μm condition which was not the case for the FS parameter. The prediction was also improved for higher displacements.

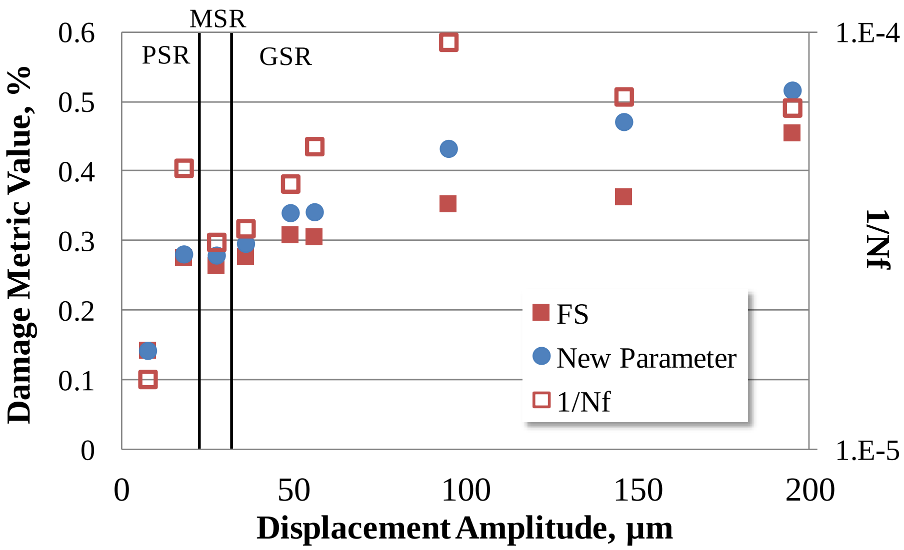

Figure 5.33: Fatigue damage level predictions and experimental results for contact with 52100 steel at 250^{o}C.

The forms of the beneficial and detrimental factors describing the influence of slip on the level of fatigue damage are shown in Figure 5.34. The constants used are shown in Table 5.3. The beneficial effect of the deposited layer of aluminum has a strong influence at low levels of energy dissipation and reaches a saturated value at a high rate. The detrimental effect of plowing becomes influential at a lower rate, and has a strong effect at high levels of energy dissipation. The resulting form of D for contact with A356 aluminum is shown in Figure 5.35. This form is significantly different than of the classical result for abrasive material removal. D_{fret2} is not able to achieve the same form.

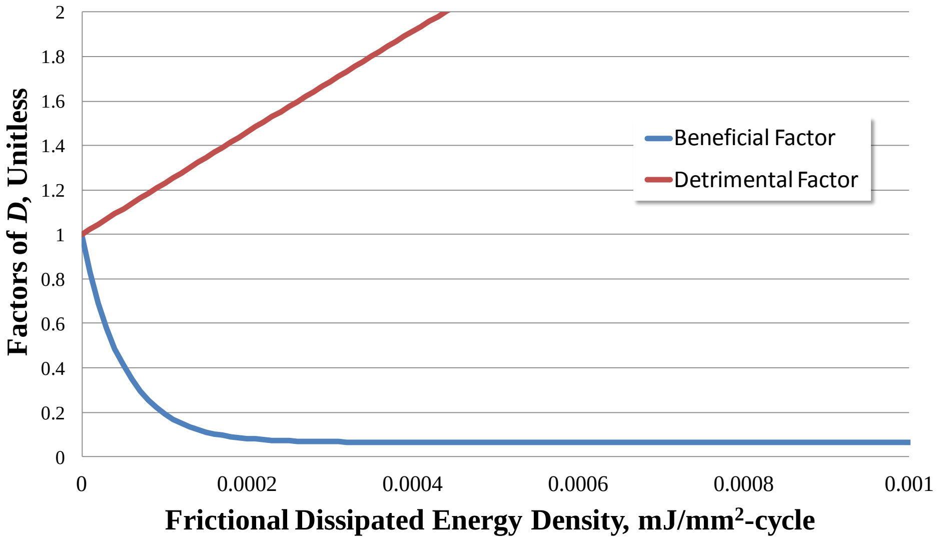

Figure 5.34: Form of beneficial and detrimental factors of *D* for contact with A356 aluminum at 20°C.

Table 5.3: Constants used for calibration of the new parameter for contact with A356 aluminum.

a	*b*	*c*	*d*	*R*
0.065	$51.4\text{x}10^{6}$ cycle/µm	30	$206\text{x}10^{3}$ cycle/µm	$-389\text{x}10^{-6}$ mm^{3}/J

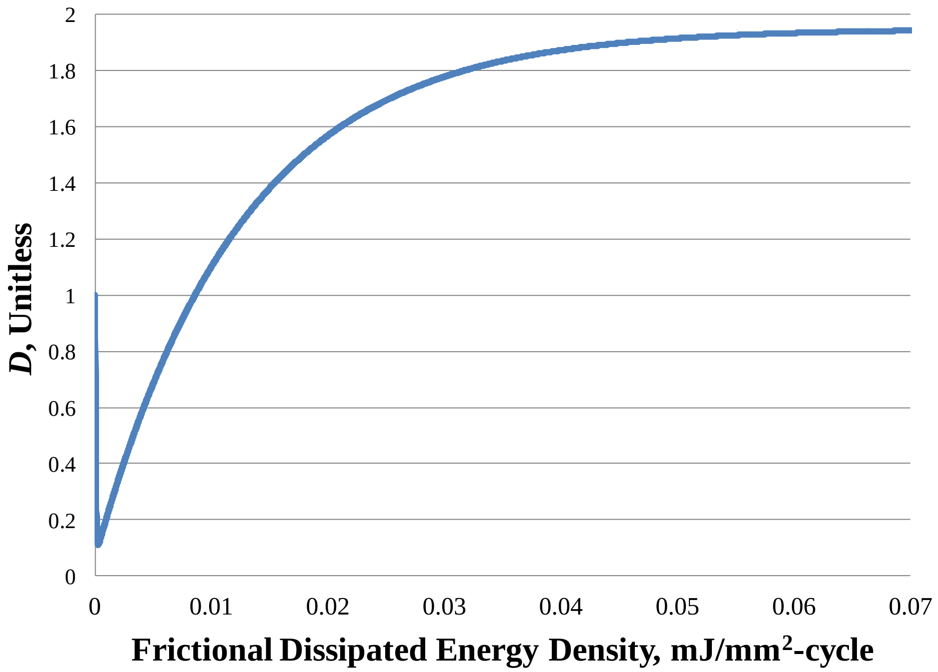

Figure 5.35: Form of *D* for contact with A356 aluminum.

The resulting prediction of the location of failure from the new parameter compared to the FS prediction and the experimentally observed location for contact with a356 aluminum is shown in Figure 5.36. The prediction of the new parameter is inconsistent with the FS prediction at displacement amplitudes of 30 μm and 40 μm where the level of energy dissipation is low, however it is unknown which is the better prediction since the specimens for those conditions did not fail during subsequent fatigue. The failure location prediction for the FS parameter was closer than for the new parameter at displacement amplitudes of 50 μm and 60 μm. The new parameter was inconsistent for these cases due to the large reduction in fatigue damage at low energy levels needed to predict the lives of the low amplitude tests. The prediction of the new parameter was more consistent with the experimentally observed failure locations at displacement amplitudes above 100 μm.

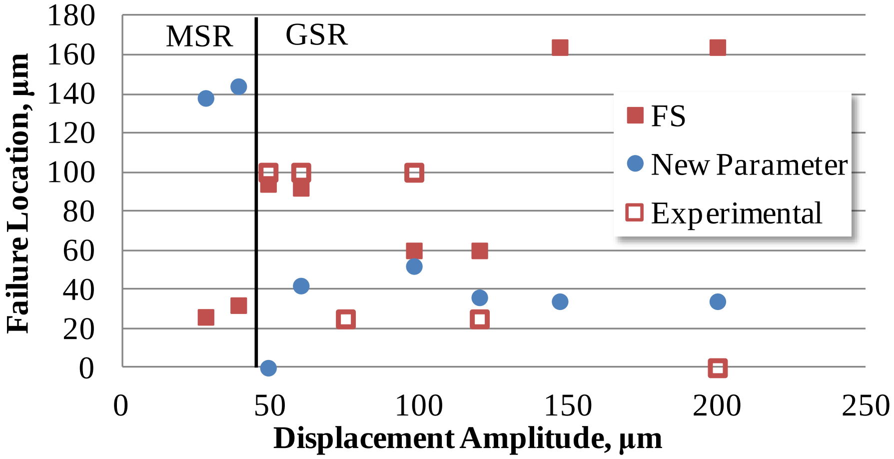

Figure 5.36: Failure location predictions compared to experimental results for contact with A356 aluminum.

A comparison of the level of fatigue damage predicted by the new parameter, the FS parameter, and the experimental results for contact with aluminum is shown in Figure 5.37. The level of fatigue damage predicted by the new parameter is a large improvement over the prediction the FS parameter at the lowest displacement amplitudes. The values of the new parameter at 30 µm and 40 µm displacement amplitudes are lower than the 0.4% threshold which corresponds to the FS value of the uniaxial fatigue limit of the virgin material at room temperature, thus the parameter predicts the lack failure observed experimentally. The new parameter was also much more successful at predicting fatigue damage than the FS parameter for all other conditions.

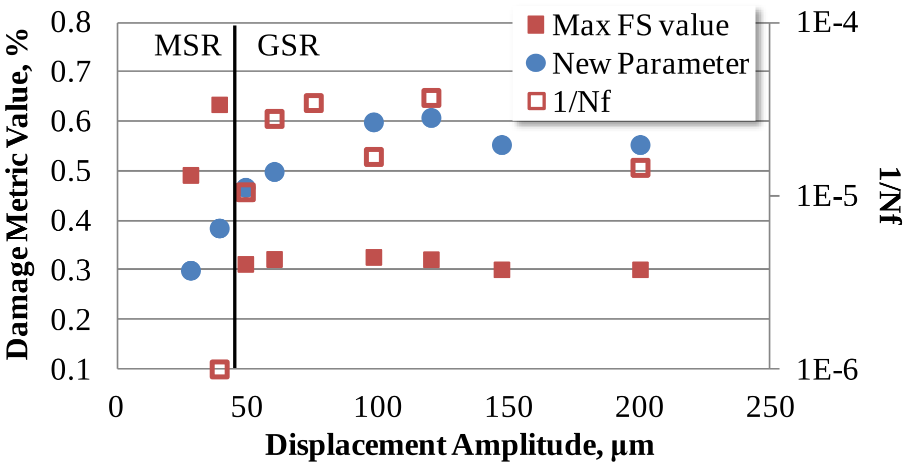

Figure 5.37: Fatigue damage level predictions and experimental results for contact with A356 aluminum.

The new parameter demonstrates an enhanced overall ability to predict the location and extent of fatigue damage compared to the FS parameter for contact with both materials. The quality of the predictions for contact with 52100 steel are similar to that of using D_{fret2}, however the new parameter provides superior predictions for contact with A356 aluminum. The addition of the wear rate into the parameter helps to enhance predictions in cases where the wear rate is dissimilar from the rates observed here, however it was not possible to validate this without data at additional wear rates.

CHAPTER 6

CONCLUSIONS AND RECOMMENDATIONS

6.1 Significance and Conclusions

- A new experimental fretting test method was developed which allows tests to be performed on thin sheets at temperatures up to 800°C in various atmospheres with independent control of displacement amplitude and normal force. The use of subsequent fatigue tests allows for the characterization of the level of fatigue damage imposed to determine the relative influence of the various contact parameters which is not as readily determined using standard fretting fatigue test methods.
- Fretting tests were performed on the thinnest specimens used in studies reported in the literature. The thinnest specimens tested in studies in the open literature are thicker than the specimens used in this study by a factor of five. This identified the importance of considering the reduction in thickness of the specimen due to wear as a contributor to apparent reduction in fatigue life which would not occur for standard thick specimens.
- This work includes the first experimental fretting investigation of 301 stainless steel in the full hard condition available in the literature. Material response fretting maps were generated for 301 stainless steel in the full hard condition for various contacting materials and temperatures. Determination of the wear rates and debris compositions for fretting of 301 stainless steel in the full hard condition as a function of temperature identified that the presence of martensite in the wear debris at room temperature was not the primary cause of the greater wear rate at room temperature

relative to elevated temperature. The primary cause of the decrease in wear rate was the transition in the oxide debris composition which lead to the formation of a glaze oxide layer.

- The stabilized coefficient of friction (COF) was found to decrease with increasing temperature for contact with 52100 caused by the formation of the glaze oxide layer. This causes a decrease in the cyclic stress-strain response and acts to decrease the level of fatigue damage caused by fretting.
- The fatigue damage due to fretting was found to decrease with increasing temperature up to 400^{o}C for contact with 52100 steel in the gross slip regime. Reduction in the cross-sectional area due to wear resulted in a reduction in fatigue life for fretting at room temperature. The decrease in COF, which directly relates to the cyclic stress state, and decrease in wear with increasing temperature caused a decrease in fatigue damage. Subsequent fatigue lives for fretting tests performed at 550^{o}C indicated a high level of fatigue damage due to fretting. The decrease in strength associated with exposure to high temperature is likely the cause of the apparent reduction in fatigue resistance.
- Testing in an inert atmosphere did not have a significant effect on the friction or wear behavior for the conditions investigated. The materials and environment studied did not have a high oxidation rate at the imposed test frequency, and therefore were not sensitive to a decreased O_2 content.
- An investigation of the tensile and fatigue properties of 301 stainless steel in the full hard condition allowed the establishment of a link between material properties and sensitivity to fretting degradation. Tensile and fatigue properties of 301 stainless steel

in the full hard condition as a function of temperature were not available in the literature. Identification of the reduction in ductility due to the stabilization of austenite which prohibits the transformation to martensite, relatively low loss of strength, and the reduction in the fatigue damage resistance at elevated temperature coupled with the results of the fatigue damage metric evaluation made it possible to determine the protective nature of the glaze oxide layer which formed at 250^{o}C.

- Fretting tests performed on 301 stainless steel in contact with 52100 steel and A356 aluminum provided a means for a direct comparison of the effects of abrasive material removal and adhesive material deposition on the fatigue damage response due to fretting. This comparison demonstrated the positive effect of the deposition of aluminum to the surface of the stainless steel, as well as the negative effects of thinning due to material removal and the increase in tangential force due to plowing.
- A simple model for the evolution of friction which is suitable for incorporation in finite element studies was developed based on the accumulated frictional energy dissipation density. This model makes it possible to assign an evolving COF field in a finite element simulation on the surface of a complex system where the contact pressure and relative slip amplitude are variable over the interface. This can have important implications on the system response and is critical to consider when performing fretting simulations where the number of cycles required to reach a stabilized COF is a significant portion of the number of cycles considered.
- Finite element modeling was used to determine the local cyclic stress-strain and energy dissipation behavior by calibration of hysteresis loops determined by the model to the experimental hysteresis loops using a layer of elastic elements to

represent the compliance of the entire test system. Finite element modeling identified bending of the specimen occurs due to the compliance of the PTFE layer which was necessary to prevent fretting damage between the specimen and specimen holder. The bending has the effect of reducing the tensile tangential stress at the fretting location. The bending also increases the contact conformity and therefore lowers the contact pressure and shear stress. Both effects of bending tend to reduce the severity of the fretting damage at the interface. The finite element model at room temperature and 250^{o}C identified the reduction in contact stresses due to the decreased modulus of the system.

- The Fatmi-Socie (FS) and Smith-Watson-Topper (SWT) parameters were evaluated using the finite element model. The FS parameter was found to provide a more accurate prediction of the location of maximum fatigue damage due to fretting for the conditions tested in this work. The maximum value of the FS parameter was strongly related to the COF, and was found to correspond well with the fatigue damage incurred due to fretting that was observed experimentally for contact with 52100 steel for partial slip (PS) and mixed slip (MS) conditions in which wear was not significant. Increasing disagreement at higher displacement amplitudes was found due to the thickness reduction of the sample due to wear which was not captured in the model. The correspondence of the FS parameter and experimental results was poor for contact with A356 aluminum. This is attributed to the transfer of aluminum from the moving specimen to the surface of the stainless steel. For MS conditions, the highest cyclic stresses were contained within the layer of aluminum that was transferred to the specimen reducing the fatigue damage accumulated in the stainless steel specimen after the transition to the PS condition. In gross slip (GS) conditions, a plowing effect from the high level of material transfer caused large spikes in the tangential force that are not captured by the model, resulting in low lives compared to those indicated by the calculated FS values.

- A new fretting fatigue damage parameter was developed that accounts for the competitive interaction between the beneficial effects and the detrimental effects of slip on the level of fatigue damage. The parameter was calibrated to provide a prediction of the location of failure and level of fatigue damage due to fretting using the understanding of the fretting behavior gained from the fretting friction response, fatigue damage characterization, wear characterization, and material property determination. This parameter improves current methods by expanding the range of applicability from only cases of abrasive material removal to include cases in which adhesive wear results in material transfer.
- A methodology for evaluation of the type and extent of damage due to fretting of thin sheets was developed. This method serves as a protocol which can be used for the determination of fretting damage response and calibration of a fretting fatigue damage metric for other materials and conditions of interest which can be used to design components for reduced fatigue damage due to fretting.

6.2 Recommendations

This work was performed using 301 stainless steel in the full hard condition, which has an initial martensite content of approximately 60% from cold rolling. All other studies of fretting of stainless steel reported in the literature have been performed using the annealed condition which consists of only austenite. Since the microstructure of 301 stainless steel has a significant effect on the fretting response, further analysis of the damage and microstructural evolution during fretting should be performed to better understand the effect of the microstructure and its evolution on the fretting response. This can be accomplished by performing tests with various durations and examining the phase distribution after each of the different durations. Specimens of 301 stainless steel could be annealed to result in a fully austenitic structure prior to testing. Comparison of the fretting response of annealed specimens and full hard specimens could help to identify the role of the structure on the fretting behavior, including the influence of strength, ductility, and oxidation behavior on the COF, wear, and fatigue response.

The effect of the contact geometry on the fretting behavior may be significant and was not addressed in this work. The wear behavior is strongly influenced by the debris generated during fretting. The level of debris entrapment is related to the contact geometry. The composition of the debris can also be related to the contact geometry due to the difference in the accessibility of oxygen to the metallic debris, which result in a change in the rate sensitivity. Experiments can be performed using contacting bodies with varying radius to change the level of debris entrapment, with the normal force adjusted to result in similar contact pressure. Using larger contact sizes would be beneficial to avoid the influence of gradient effects.

The COF evolution was assumed to have a negligible effect on the material response in this work since the portion of the test over which the COF was transient was typically only approximately 10%. The effect of the friction evolution will be important for tests which exhibit friction evolution for a more significant portion of the total test duration. The effect of the COF evolution can be studied using the modeling method described in Chapter 4, where a user subroutine is used to vary the COF over the surface of a system using the cumulative frictional energy dissipation as the internal state variable. This method can be used to study the effect of a non-uniformly evolving friction behavior on the cyclic stress-strain behavior and thus the fatigue damage response. Fretting experiments can be performed with shorter durations to determine the level of fatigue damage when the COF evolution is significant and compared to the model for validation.

The COF evolution relationship is based on the average COF and energy dissipation over the surface of the entire contact in experiments. The actual COF distribution over the surface of a contact is unknown. The COF distribution could be investigated using digital image correlation to determine the deformation of the contacting bodies. A finite element model can be created in which the COF distribution is adjusted until the deformation field in the model corresponds to the deformation field measured using digital image correlation. This could help to identify a more accurate COF evolution relationship.

The fretting fatigue damage parameter developed in this work has been calibrated to a relatively small range of materials and conditions. Application of the parameter to additional material combinations and model geometry will help to identify aspects of the parameter which could be developed further to enhance the predictive capability. This can be performed using the same protocol used in this study. Application of the fatigue damage metric to the fretting behavior of complex geometries will determine the viability of the parameter and identify aspects of the parameter which could be improved.

Further enhancement of the physical basis of the newly developed fretting fatigue damage parameter can improve the predictive capability for a wider range of conditions. The effects of wear could be better captured by incorporating material properties related to the wear behavior, e.g. fatigue and fracture properties (critical stress intensity, threshold stress intensity range) to better describe wear by delamination or the oxidation behavior to identify the transition between adhesive and abrasive wear. Further enhancement of the physical basis could incorporate rate sensitivity of the mechanical properties (significant for 301 stainless steel) and oxidation behavior by inclusion of the temperature, cycle time, activation energy, and the effectiveness of oxygen transport related to geometry and environment [188]. Fretting experiments performed using a wide range of frequencies can be conducted to determine the rate dependence of the friction, wear, and fatigue damage behavior. Further development of the model can be performed to incorporate the rate dependence through the use of an Arrhenius relationship to describe the oxidation behavior. Incorporation of the oxidation behavior in the model can be beneficial for increasing the ability of the parameter to capture the changes that occur with changes in temperature and test frequency.

The mechanical properties of 301 stainless steel in the full hard condition are likely to be orthotropic due to the high level of rolling. This work focused on the behavior only in the rolling direction and approximated the behavior as isotropic for modeling. The study could be repeated for other orientations to determine the sensitivity of the fretting response to the material texture. It has been shown that the formation of martensite demonstrates tension-compression asymmetry [189-190]. A constitutive model for 301 stainless steel which incorporates phase transformation as a function of temperature could be developed using the results from this work with additional experiments to determine the behavior for additional orientations and loading conditions. This could be used to help identify the role of phase transformation on the fretting response.

Appendix A: Aged Specimen Tensile Behavior

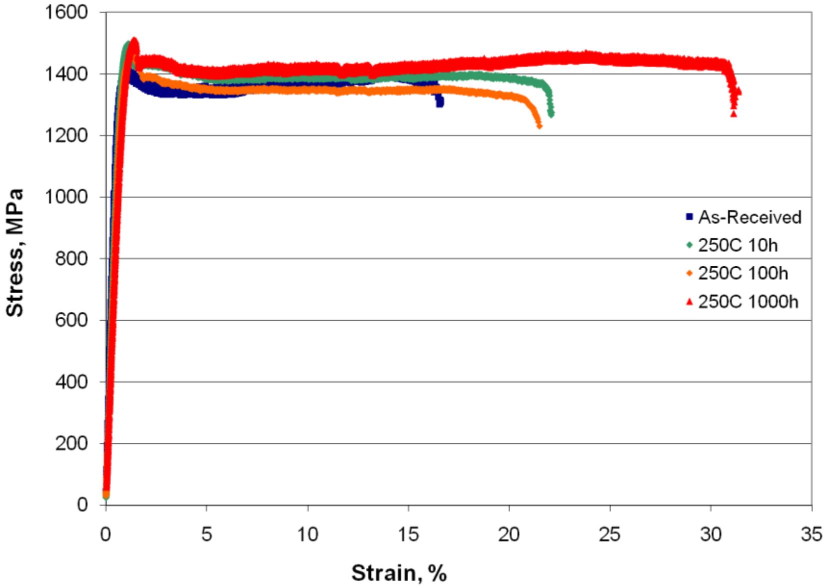

Figure A1: Room temperature stress-strain response for 301 stainless steel aged at 250^{o}C for 10, 100, and 1000 h.

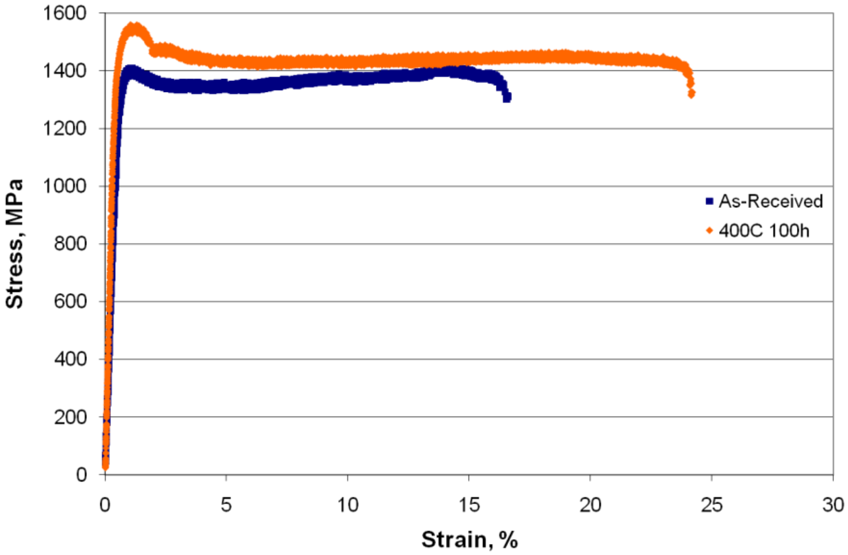

Figure A2: Room temperature stress-strain response for 301 stainless steel aged at 400^{o}C for 100 h.

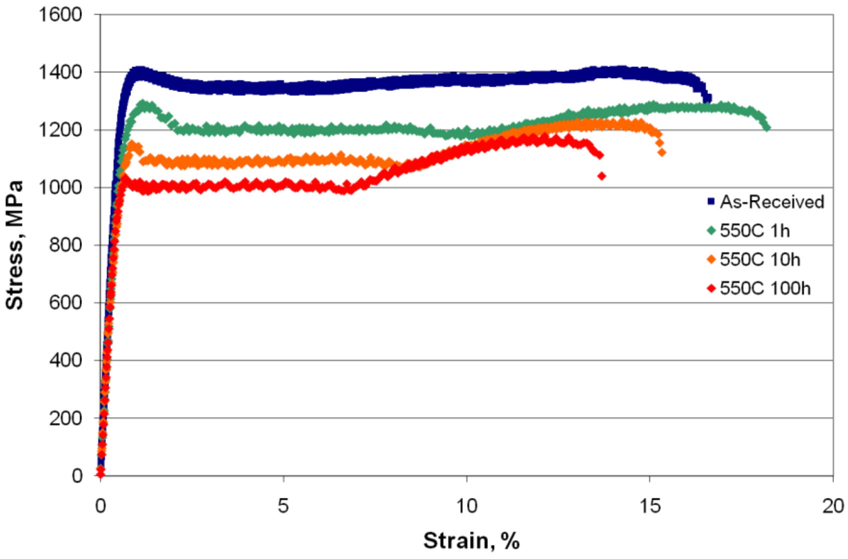

Figure A3: Room temperature stress-strain response for 301 stainless steel aged at 550^{o}C for 1, 10, and 100 h.

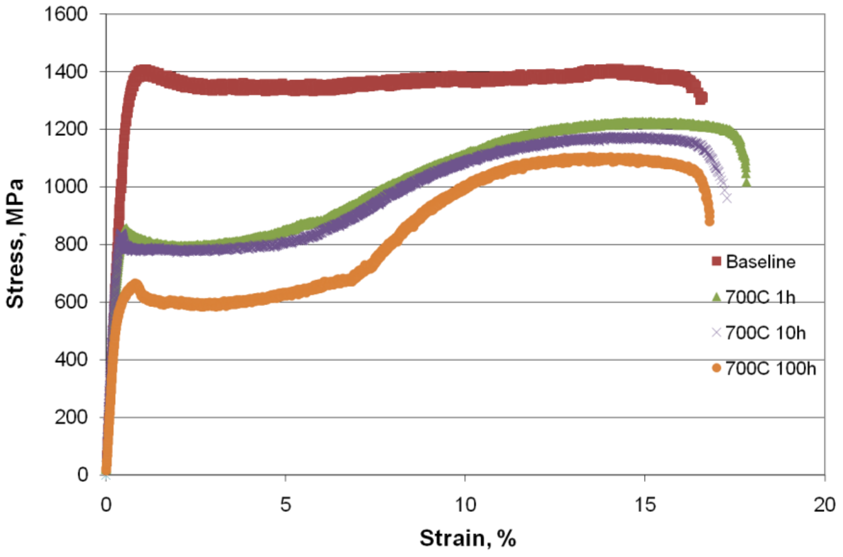

Figure A4: Room temperature stress-strain response for 301 stainless steel aged at 700^{o}C for 1, 10, and 100 h.

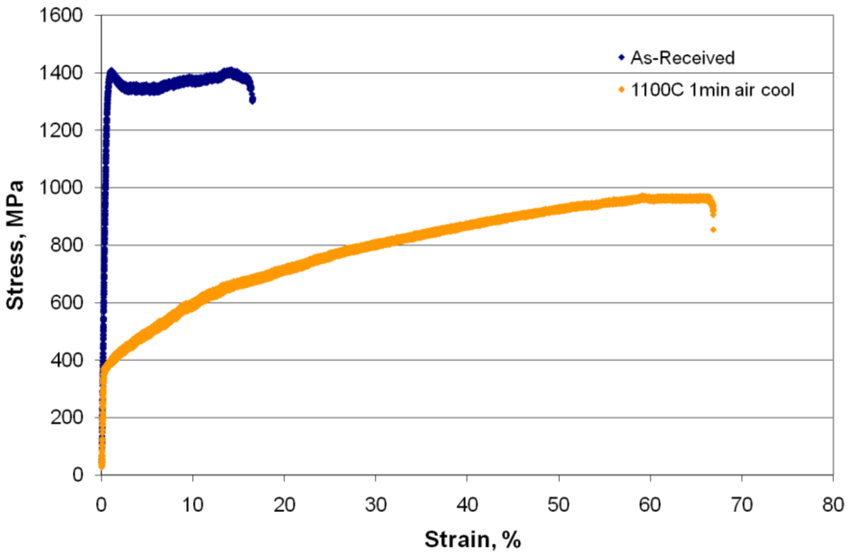

Figure A5: Room temperature stress-strain response for 301 stainless steel aged at 250^{o}C for 1, 10, and 100 h.

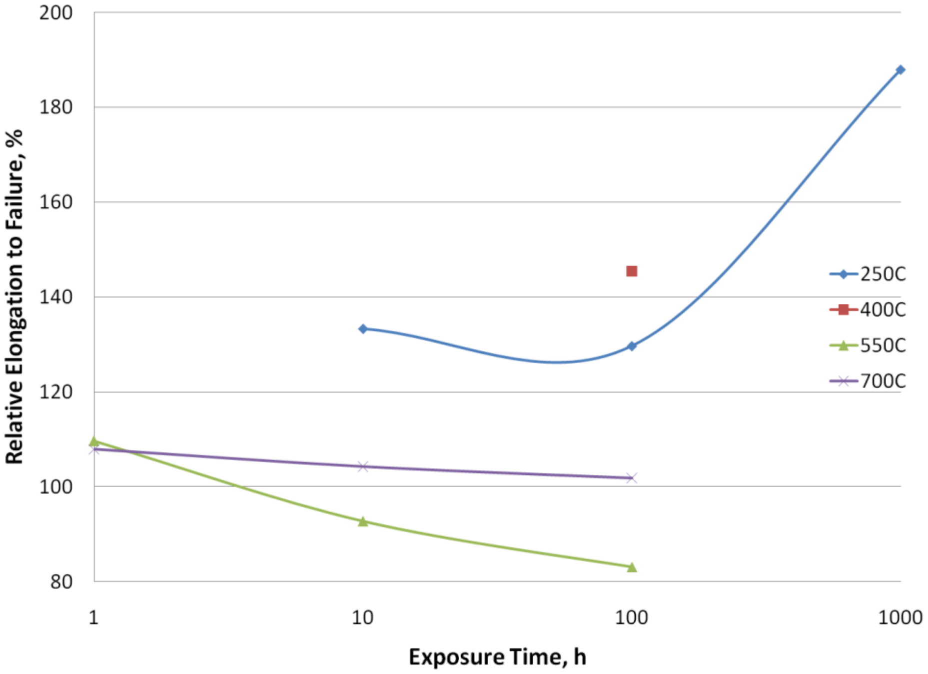

Figure A6: Elongation to failure of aged 301 stainless steel relative to room temperature.

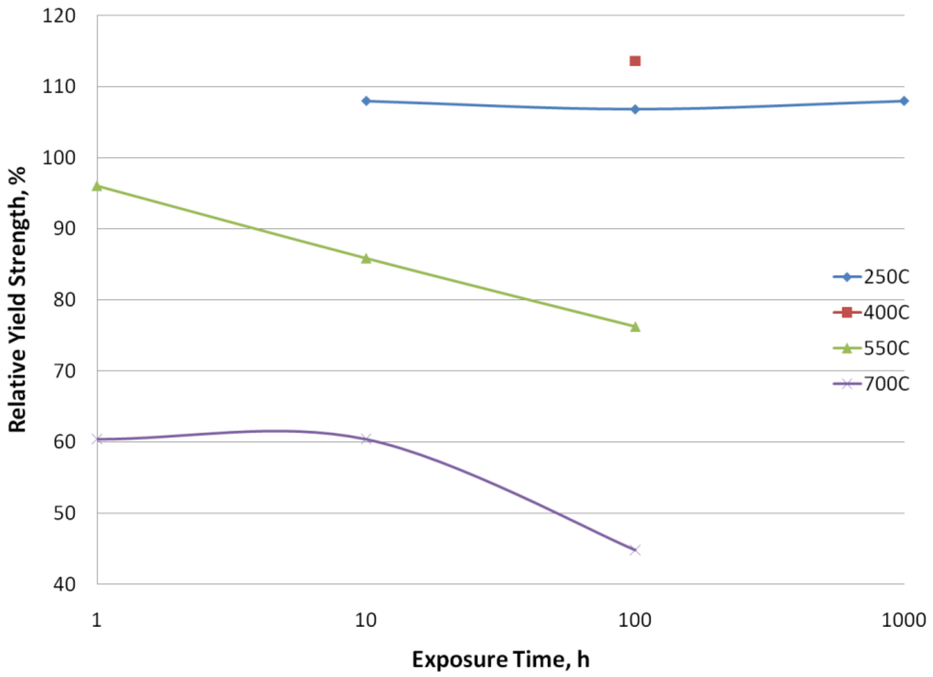

Figure A7: Yield strength of aged 301 stainless steel relative to room temperature.

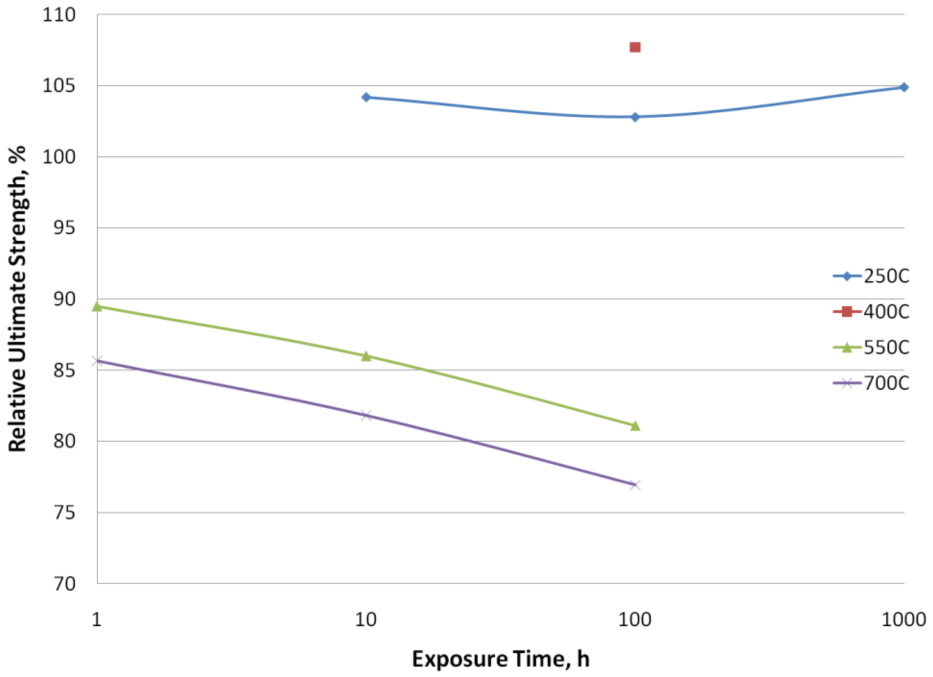

Figure A8: Ultimate strength of aged 301 stainless steel relative to room temperature.

REFERENCES

1. Dobromirski, J.M., *Variables of Fretting Process: Are There 50 of Them?*, in *Standardization of Fretting Fatigue Test Methods and Equipment, ASTM STP 1159*, H.M. Attia and R.B. Waterhouse, Editors. 1992, American Society for Testing and Materials: Philadelphia. p. 60-66.

2. Waterhouse, R.B., *Fretting fatigue.* International Materials Reviews, 1992. **37**(2): p. 77-97.

3. Fellows, L.J., D. Nowell, and D.A. Hills, *Contact stresses in a moderately thin strip (with particular reference to fretting experiments).* Wear, 1995. **185**(1-2): p. 235-8.

4. Keer, L.M. and T.N. Farris, *Effects of Finite Thickness and Tangential Loading on Development of Zones of Microslip in Fretting.* ASLE transactions, 1987. **30**(2): p. 203-210.

5. Bentall, R.H. and K.L. Johnson, *An elastic strip in plane rolling contact.* International Journal of Mechanical Sciences, 1968. **10**(Copyright 1969, IEE): p. 637-64.

6. Bartha, B.B., T. Nicholas, and T.N. Farris, *Modeling of geometry effects in fretting fatigue.* Tribology International, 2006. **39**(10): p. 1131-1141.

7. Ahmad, J. and U. Santhosh. *Small Scale Yielding In Fretting Fatigue*. in *Proceedings of the 9th National Turbine Engine High Cycle Fatigue Conference*. 2003. Monterey, CA: Universal Technology Corp., Dayton, OH.

8. Hutson, A.L., et al., *Effect of sample thickness on local contact behavior in a flat-on-flat fretting fatigue apparatus.* International Journal of Fatigue, 2001. **23**(SUPPL 1): p. 445-453.

9. Waterhouse, R.B., *Fretting Fatigue.* Applied Science Publishers, 1981.

10. Lindley, T.C. and K.J. Nix, *The Role of Fretting in the Initiation and Early Growth of Fatigue Cracks in Turbo-Generator Materials.* ASTM STP 853, 1982: p. 340.

11. Hoeppner, D.W., *Mechanisms of fretting fatigue and their impact on test methods development.* ASTM STP 1159, 1992: p. 23-32.

12. Tomlinson, G.A., *The rusting of steel surfaces in contact.* Proc. R. Sot . London, Ser. A, 1927(115): p. 472-483.

13. Waterhouse, R.B., *Fretting Corrosion* Pergamon Press, Oxford, 1972.

14. Shreir, L.L., *Corrosion*. 1963: John Wiley & Son, Inc., New York.

15. Sato, H., *Recent Trend in Studies of Fretting Wear.* Transactions JSLE, 1985. **30**: p. 853-858.

16. Shaffer, S.J. and W.A. Glaeser, *Fretting Fatigue.* Metals Handbook. **19**: p. 321-329.

17. Waterhouse, R.B., *The role of adhesion and delamination in the fretting wear of metallic materials.* Wear, 1977. **45**(3): p. 355-64.

18. Doeser, B.A. and R.B. Waterhouse, *METALLOGRAPHIC FEATURES OF FRETTING CORROSION DAMAGE.* Microstructural Science, 1979. **7**: p. 205-215.

19. Suh, N.P., *The delamination theory of wear.* Wear, 1973. **25**: p. 111-124.

20. Suh, N.P., *An overview of the delamination theory of wear.* Wear, 1977. **44**(1): p. 1-16.

21. Fleming, J.R. and N.P. Suh, *Mechanics of crack propagation in delamination wear.* Wear, 1977. **44**(1): p. 39-56.

22. Glaeser, W.A. and B.H. Lawless, *Behavior of alloy Ti-6Al-4V under pre-fretting and subsequent fatigue conditions.* Wear, 2001. **250-251**(PART 1): p. 621-630.

23. Conner, B.P., et al., *Application of a fracture mechanics based life prediction method for contact fatigue.* International Journal of Fatigue, 2004. **26**(5): p. 511-520.

24. Golden, P.J. and J.R. Calcaterra, *A fracture mechanics life prediction methodology applied to dovetail fretting.* Tribology International, 2006. **39**(10): p. 1172-1180.

25. Nowell, D., D. Dini, and D.A. Hills, *Recent developments in the understanding of fretting fatigue.* Engineering Fracture Mechanics, 2006. **73**(2): p. 207-22.

26. Fellows, L.J., D. Nowell, and D.A. Hills, *Analysis of crack initiation and propagation in fretting fatigue: the effective initial flaw size methodology.* Fatigue and Fracture of Engineering Materials & Structures, 1997. **20**(1): p. 61-70.

27. Hills, D.A., *Mechanics of fretting fatigue.* Wear, 1994. **175**(1-2): p. 107-113.

28. Wharton, M.H., D.E. Taylor, and R.B. Waterhouse, *Metallurgical Factors in the Fretting Fatigue Behavior of 70/30 Brass and 0.7% Carbon Steel by Fretting*. Wear, 1973. **17**: p. 139-147.

29. Nicholas, T., *Critical issues in high cycle fatigue.* International Journal of Fatigue, 1999. **21**(SUPPL): p. 221-231.

30. Johnson, K.L., *Contact Mechanics*. 1985, Cambridge, New York: Cambridge University Press.

31. Waterhouse, R.B., *Fretting at High Temperatures.* Tribology International, 1981. **14**(4): p. 203-207.

32. Amargier, R., et al., *Stress gradient effect on crack initiation in fretting using a multiaxial fatigue framework.* International Journal of Fatigue, 2010. **32**(12): p. 1904-1912.

33. Colombie, C., et al., *FRETTING: LOAD CARRYING CAPACITY OF WEAR DEBRIS.* Journal of Tribology, Transactions of the ASME, 1984. **106**(2): p. 194-201.

34. Vingsbo, O. and S. Soderberg, *On fretting maps.* Wear, 1988. **126**(2): p. 131-47.

35. Fouvry, S., et al., *Palliatives in fretting: A dynamical approach.* Tribology International, 2006. **39**(10): p. 1005-1015.

36. Blanchard, P., et al., *Material effects in fretting wear: application to iron, titanium and aluminum alloys.* Metallurgical Transactions A (Physical Metallurgy and Materials Science), 1991. **22A**(7): p. 1535-44.

37. Waterhouse, R.B., *Fretting Wear.* Wear, 1984. **100**(1-3): p. 107-118.

38. Gordelier, S.C. and T.C. Chivers, *A literature review of palliatives for fretting fatigue.* Wear, 1979. **56**(1): p. 177-190.

39. Nishioka, K. and K. Hirakawa, *Fundamental investigations of fretting fatigue. IV. The effect of mean stress.* Bulletin of the Japan Society of Mechanical Engineers, 1969. **12**(51): p. 408-14.

40. Malkin, S., D.P. Majors, and T.H. Courtney, *Surface Effects During Fretting Fatigue of Ti-6Al-4V.* Wear, 1972. **22**(2): p. 235-244.

41. Magaziner, R., O. Jin, and S. Mall, *Slip regime explanation of observed size effects in fretting.* Wear, 2004. **257**(1-2): p. 190-197.

42. Madge, J.J., et al., *Contact-evolution based prediction of fretting fatigue life: Effect of slip amplitude.* Wear, 2007. **262**(9-10): p. 1159-70.

43. Jin, O. and S. Mall, *Influence of contact configuration on fretting fatigue behavior of Ti-6Al-4V under independent pad displacement condition.* International Journal of Fatigue, 2002. **24**(12): p. 1243-1253.

44. Mindlin, R.D., *Compliance of elastic bodies in contact.* American Society of Mechanical Engineers -- Transactions -- Journal of Applied Mechanics, 1949. **16**(3): p. 259-268.

45. Cattaneo, C., *Sul contatto di due corpi elastici: distribuzione locale degli sforzi.* Rendiconti dell' Accademia nazionale dei Lincei, 1938. **27**(6).

46. Hills, D.A. and D. Nowell, *Mechanics of Fretting Fatigue*. 1994, Dordrecht, The Netherlands: Kluwer Academic Publishers.

47. Nowell, D. and D.A. Hills, *MECHANICS OF FRETTING FATIGUE TESTS.* International Journal of Mechanical Sciences, 1987. **29**(5): p. 355-365.

48. Nowell, D. and D.A. Hills, *Crack initiation criteria in fretting fatigue.* Wear, 1990. **136**(2): p. 329-43.

49. Kuno, M., et al., *Initiation and growth of fretting fatigue cracks in the partial slip regime.* Fatigue & Fracture of Engineering Materials & Structures, 1989. **12**(5): p. 387-98.

50. Ruiz, C., P. Boddington, and K. Chen, *An investigation of fatigue and fretting in a dovetail joint.* Experimental Mechanics, 1984. **24**(3): p. 208-217.

51. Ruiz, C. and K.C. Chen. *Life Assessment of Dovetail Joints Between Blades and Discs in Aero-Engines*. 1986. Sheffield, Engl: Mechanical Engineering Publ Ltd, London, Engl.

52. Neu, R.W., J.A. Pape, and D.R. Swalla, *Methodologies for linking nucleation and propagation approaches for predicting life under fretting fatigue.* ASTM Special Technical Publication, 2000(1367): p. 369-388.

53. Camp, J.M. and C.B. Francis, *Making, Shaping and Treating of Steel*. 6th Edition ed. 1951: United States Steel Co.

54. Lamb, S., *Casti Handbook of Stainless Steel and Nickel Alloys*. 2001, Edmonton, Canada: CASTI Publishing Inc./ASM International.

55. Garud, C., et al. *Microhardness Testing as a Method of Evaluating Bauschinger Phenomena in Cold Formed 301 Austenitic Stainless Steel Sheet Used in Automotive Head Gaskets*. in *TMS Annual Meeting*. 2004. Charlotte, NC, United States: Minerals, Metals and Materials Society, Warrendale, PA 15086, United States.

56. Maxwell, P., A. Goldberg, and J. Shyne, *Influence of martensite formed during deformation on the mechanical behavior of Fe-Ni-C Alloys.* Metallurgical and Materials Transactions B, 1974. **5**(6): p. 1319-1324.

57. Sessler, J. and V. Weiss, *Materials Data Handbook Type 301 Stainless Steel*, N.A.a.S. Administration and G.C.M.S.F. Center, Editors. 1966: Huntsville, Alabama. p. 152.

58. Greenwood, G.W. and R.H. Johnson, *Deformation of metals under small stresses during phase transformations.* Royal Society -- Proceedings Transactions Series A, 1965. **283**(1394): p. 403-422.

59. Fischer, F.D., et al., *A new view on transformation induced plasticity (TRIP).* International Journal of Plasticity, 2000. **16**(7-8): p. 723-748.

60. Nosova, L.V., V.G. Serebryakov, and E.L. Estrin, *Dependence of the plasticity of dual-phase austenite-martensite steels on phase composition.* Physics of Metals and Metallography (English translation of Fizika Metallov i Metallovedenie), 1991. **71**(5): p. 191-194.

61. Estrin, E.I., *Martensite transformations in metals and alloys.* Steel in Translation, 1994. **24**(9): p. 3.

62. Fischer, F.D., Q.P. Sun, and K. Tanaka, *Transformation-induced plasticity (TRIP).* Applied Mechanics Reviews, 1996. **49**(6): p. 317-364.

63. Stringfellow, R.G., D.M. Parks, and G.B. Olson, *A constitutive model for transformation plasticity accompanying strain-induced martensitic transformations in metastable austenitic steels.* Acta Metallurgica et Materialia, 1992. **40**(7): p. 1703-16.

64. Haupt, S. and H.H. Strehblow, *Combined surface analytical and electrochemical study of the formation of passive layers on Fe/Cr alloys in 0.5 M H2SO4.* Corrosion Science, 1995. **37**(1): p. 43-54.

65. Sugimoto, K. *Passivity of Fe-Cr and Fe-Cr-Ni Alloys in High-Temperature Aqueous Solutions*. 1985. Goteborg, Swed: Inst of Metals (Book n 320), London, Engl.

66. Marshall, P., *Austenitic stainless steels - microstructure and mechanical properties*. 1984, London; New York: Elsevier Applied Science.

67. Pineau, A. and R. Pelloux, *Influence of strain-induced martensitic transformations on fatigue crack growth rates in stainless steels.* Metallurgical and Materials Transactions B, 1974. **5**(5): p. 1103-1112.

68. Voort, G.F.V., G.M. Lucas, and E.P. Manilova, eds. *Metallography and Microstructures of Stainless Steels and Maraging Steels*. ASM Handbook. Vol. 9: Metallography and Microstructures. 2004, ASM.

69. Narutani, T., *Effect of deformation-induced martensitic transformation on the plastic behavior of metastable austenitic stainless steel.* Materials Transactions, JIM, 1989. **30**(1): p. 33-45.

70. Tanaka, T., K. Ito, and K. Hoshino, *Effect of Alloying Elements, Cold-Rolling Reduction and Deformation-Induced Martensite on Mechanical Properties of Low Carbon Type 301 Hard Stainless Steel. (Development of Low Carbon High Strength Stainless Steels - II).* Transactions of the Iron and Steel Institute of Japan, 1982. **23**(4): p. 140.

71. Schuster, G. and C. Altstetter, *Fatigue of annealed and cold worked stable and unstable stainless steels.* Metallurgical Transactions A (Physical Metallurgy and Materials Science), 1983. **14A**(10): p. 2077-84.

72. Kalkhof, D., et al., *Monitoring fatigue degradation in austenitic stainless steels.* Fatigue and Fracture of Engineering Material and Structures, 2004. **27**(7): p. 595-607.

73. Miller, A., Y. Estrin, and X.Z. Hu, *Magnetic force microscopy of fatigue crack tip region in a 316L austenitic stainless steel.* Scripta Materialia, 2002. **47**(7): p. 441-446.

74. Bressanelli, J.P. and A. Moskowitz, *Effects of strain rate, temperature, and composition on tensile properties of metastable austenitic stainless steels.* ASM -- Transactions, 1966. **59**(2): p. 223-239.

75. Tourki, Z., H. Bargui, and H. Sidhom, *The kinetic of induced martensitic formation and its effect on forming limit curves in the AISI 304 stainless steel.* Journal of Materials Processing Technology, 2005. **166**(3): p. 330-336.

76. Livitsanos, C.P. and P.F. Thomson, *The effect of temperature and deformation rate on transformation-dependent ductility of a metastable austenitic stainless steel.* Materials Science and Engineering, 1977. **30**(2): p. 93-98.

77. Luksza, J., et al., *Texture evolution and variations of α-phase volume fraction in cold-rolled AISI 301 steel strip.* Journal of Materials Processing and Technology, 2006. **177**: p. 555-560.

78. Talyan, V., R.H. Wagoner, and J.K. Lee, *Formability of stainless steel.* Metallurgical and Materials Transactions A (Physical Metallurgy and Materials Science), 1998. **29A**(8): p. 2161-72.

79. Pineau, A.G., L.F. Van Swam, and R.M. Pelloux, *CYCLIC STRESS-STRAIN CURVES OF A STAINLESS AUSTENITIC STEEL IN THE M//S-M//D RANGE.* Scripta Metallurgica, 1973. **7**(6): p. 657-660.

80. Barclay, W.F. and Publ, *"Mechanisms of deformation and work hardening in AISI type 301 stainless steel"*. 1965, American Society for Testing and Materials (ASTM), Philadelphia, PA, United States. p. 26-29.

81. Mughrabi, H. and H.-J. Christ, *Cyclic Deformation and Fatigue of Selected Feritic and Austenitic Steels: Specific Aspects*. ISIJ International. Vol. 37. 1997. 1154-1169.

82. Raman, S.G.S. and M. Jayaprakash, *Plain fatigue and fretting fatigue behaviour of AISI 304 austenitic stainless steel.* Materials Science and Technology, 2007. **23**(1): p. 45-54.

83. Khan, Z. and M. Ahmed, *Stress-induced martensitic transformation in metastable austenitic stainless steels: effect on fatigue crack growth rate.* European Journal of Radiology, 1996. **21**(3): p. 201-208.

84. Baudry, G. and A. Pineau, *Influence of strain-induced martensitic transformation on the low-cycle fatigue behavior of a stainless steel.* Materials Science and Engineering, 1977. **28**(2): p. 229-242.

85. Maier, H.J., et al., *Low-temperature fatigue-induced martensitic transformation of a metastable austenitic stainless steel: optimization of strength and fatigue properties.* Zeitschrift fur Metallkunde, 1993. **84**(12): p. 820-6.

86. Socie, D. *Critical plane approaches for multiaxial fatigue damage assessment*. 1993. San Diego, CA, USA: Publ by ASTM, Philadelphia, PA, USA.

87. Plumbridge, W.J., *Review: fatigue-crack propagation in metallic and polymeric materials.* Journal of Materials Science, 1972. **7**(8): p. 939-62.

88. Wright, R.N., *The High Cycle Fatigue Strength of Commercial Stainless Steel Strip.* Materials Science and Engineering, 1976. **22**: p. 223-230.

89. Suh, N.P. and N. Saka, *The stacking fault energy and delamination wear of single-phase f.c.c. metals.* Wear, 1977. **44**(1): p. 135-143.

90. Hsu, K.L., T.M. Ahn, and D.A. Rigney, *Friction, wear and microstructure of unlubricated austenitic stainless steels.* Wear, 1980. **60**(1): p. 13-37.

91. Pednekar, S. and S. Smialowska, *The effect of prior cold work on the degree of sensitization in Type 304 stainless steel.* Corrosion, 1980. **36**(10): p. 565-77.

92. Kubota, M., et al., *Fretting fatigue in hydrogen gas.* Tribology International, 2006. **39**(10): p. 1241-1247.

93. Kato, K., et al., *Fretting Damage of SUS 304 in a Vacuum.* JSME International Journal, 1987. **30**(260): p. 330-336.

94. Iwabuchi, A., et al., *Fretting Damage of SUS304 in a Vacuum (Discussion of the Condition of Crack Generation.* JSME International Journal, 1987. **30**(266): p. 1319-1325.

95. Nakazawa, K., M. Sumita, and N. Maruyama, *Fatigue and fretting fatigue of austenitic and ferritic stainless steels in pseudo-body fluid.* Journal of the Japan Institute of Metals, 1999. **63**(12): p. 1600-8.

96. Brown, S.A. and K. Merritt, *Fretting Corrosion in Saline and Serum.* Journal of Biomedical Materials Research, 1981. **15**(4): p. 479-488.

97. Geringer, J., B. Forest, and P. Combrade, *Wear analysis of materials used as orthopaedic implants.* Wear, 2006. **261**(9): p. 971-979.

98. Bateni, M.R., et al., *Wear and Corrosion Wear of Medium Carbon Steel and 304 Stainless Steel.* Wear, 2006. **260**: p. 116-122.

99. Taylor, D.E., et al., *The fretting wear of an austenitic stainless steel in air and in carbon dioxide at elevated temperatures.* Wear, 1979. **56**(1): p. 9-18.

100. Kayaba, T. and A. Iwabuchi, *The fretting wear of 0.45% C steel and austenitic stainless steel from 20 to 650 C in air.* Wear, 1981. **74**(2): p. 229-45.

101. Nakazawa, K., N. Maruyama, and T. Hanawa, *Effect of contact pressure on fretting fatigue of austenitic stainless steel.* Tribology International, 2003. **36**(2): p. 79-85.

102. Leheup, E.R. and R.E. Pendlebury, *Unlubricated reciprocating wear of stainless steel with an interfacial air flow.* Wear, 1991. **142**(2): p. 351-372.

103. You, B.-R. and S.-B. Lee, *A critical review on multiaxial fatigue assessments of metals.* International Journal of Fatigue, 1996. **18**(4): p. 235-244.

104. Das, J. and S.M. Sivakumar, *An evaluation of multiaxial fatigue life assessment methods for engineering components.* International Journal of Pressure Vessels and Piping, 1999. **76**(10): p. 741-746.

105. Garud, Y.S., *Multiaxial Fatigue: A Survey of the State of the Art.* Journal of Testing and Evaluation, 1981. **9**(3): p. 165-178.

106. Araujo, J.A., D. Nowell, and R.C. Vivacqua, *The use of multiaxial fatigue models to predict fretting fatigue life of components subjected to different contact stress fields.* Fatigue and Fracture of Engineering Materials and Structures, 2004. **27**(10): p. 967-978.

107. Swalla, D.R. and R.W. Neu, *Influence of coefficient of friction on fretting fatigue crack nucleation prediction.* Tribology International, 2001. **34**(7): p. 493-503.

108. Fridrici, V., et al., *Prediction of cracking in Ti-6Al-4V alloy under fretting-wear: use of the SWT criterion.* Wear, 2005. **259**(1-6): p. 300-8.

109. Sum, W.S., E.J. Williams, and S.B. Leen, *Finite element, critical-plane, fatigue life prediction of simple and complex contact configurations.* International Journal of Fatigue, 2005. **27**(4): p. 403-416.

110. Ding, J., et al., *Fretting fatigue predictions in a complex coupling.* International Journal of Fatigue, 2007. **29**(7): p. 1229-44.

111. Vidner, J. and E. Leidich, *Enhanced Ruiz criterion for the evaluation of crack initiation in contact subjected to fretting fatigue.* International Journal of Fatigue, 2007. **29**(9-11): p. 2040-2049.

112. Lykins, C.D., S. Mall, and V. Jain, *Evaluation of parameters for predicting fretting fatigue crack initiation.* International Journal of Fatigue, 2000. **22**(8): p. 703-716.

113. Navarro, C., S. Munoz, and J. Dominguez, *On the use of multiaxial fatigue criteria for fretting fatigue life assessment.* International Journal of Fatigue, 2008. **30**(1): p. 32-44.

114. Mohd Tobi, A.L., et al., *A study on the interaction between fretting wear and cyclic plasticity for Ti-6Al-4V.* Wear, 2009. **267**(1-4): p. 270-282.

115. Dubourg, M.-C. and V. Lamacq, *Stage II crack propagation direction determination under fretting fatigue loading: A new approach in accordance with experimental observations.* ASTM Special Technical Publication, 2000(1367): p. 436-450.

116. Araujo, J.A. and D. Nowell, *The effect of rapidly varying contact stress fields on fretting fatigue.* International Journal of Fatigue, 2002. **24**(7): p. 763-75.

117. Fouvry, S., et al., *Identification of the characteristic length scale for fatigue cracking in fretting contacts.* Journal De Physique. IV : JP, 1998. **8**(8): p. 159-166.

118. Fouvry, S., P. Kapsa, and L. Vincent, *A multiaxial fatigue analysis of fretting contact taking account of the size effect. Fretting Fatigue: Current Technology and Practices, ASTM STP 1367(Eds D. Hoeppner, V Chandrasekaran and C. B. Elliot), 2000, 167-182(American Society of Testing and Materials, West Conshohocken, Pennsylvania).*

119. Fouvry, S., K. Elleuch, and G. Simeon, *Prediction of crack nucleation under partial slip fretting conditions.* Journal of Strain Analysis for Engineering Design (Professional Engineering Publishing), 2002. **37**(6): p. 549-564.

120. Fatemi, A. and D.F. Socie, *A critical plane approach to multiaxial fatigue damage including out-of-phase loading.* Fatigue & Fracture of Engineering Materials & Structures, 1988. **11**(3): p. 149-65.

121. Smith, K.N., P. Watson, and T.H. Topper, *A stress-strain function for the fatigue of metals.* Journal of Materials, 1970. **5**(4): p. 767-78.

122. Fatemi, A. and P. Kurath, *Multiaxial fatigue life predictions under the influence of mean-stresses.* Journal of Engineering Materials and Technology, Transactions of the ASME, 1988. **110**(Compendex): p. 380-388.

123. Zhang, R. and S. Mahadevan. *Probabilistic prediction of fretting fatigue crack nucleation life of riveted lap joints*. 2000. Atlanta, GA, USA: American Inst. Aeronautics and Astronautics Inc., Reston, VA, USA.

124. Lee, H., O. Jin, and S. Mall, *Fretting fatigue behavior of Ti-6Al-4V with dissimilar mating materials.* International Journal of Fatigue, 2004. **26**(4): p. 393-402.

125. Szolwinski, M.P. and T.N. Farris, *Observation, analysis and prediction of fretting fatigue in 2024-T351 aluminum alloy*. Wear, 1998. **221**(1): p. 24-36.

126. McDiarmid, D.L., *A Shear Stress Based Critical-Plane Criterion of Multiaxial Fatigue Failure for Design and Life Prediction.* Fatigue & Fracture of Engineering Materials & Structures, 1994. **17**(12): p. 1475-1484.

127. Papadopoulos, I.V., et al., *Comparative study of multiaxial high-cycle fatigue criteria for metals.* International Journal of Fatigue, 1997. **19**(3): p. 219-235.

128. Gallagher, J., et al., *Advanced High Cycle Fatigue (HCF) Life Assurance Methodologies*, A.F.R. Laboratory, Editor. 2005: Wright-Patterson Air Force Base, Dayton, OH.

129. McDiarmid, D.L., *A General Criterion for High Cycle Multiaxial Fatigue Failure.* Fatigue & Fracture of Engineering Materials & Structures, 1991. **14**(4): p. 429-453.

130. Kallmeyer, A.R., A. Krgo, and P. Kurath, *Evaluation of multiaxial fatigue life prediction methodologies for Ti-6Al-4V.* Journal of Engineering Materials and Technology, Transactions of the ASME, 2002. **124**(2): p. 229-237.

131. Findley, W.N., *Fatigue of Metals Under Combinations of Stresses.* Trans. ASME, 1957. **79**: p. 429-453.

132. Dang Van, K., *Sur la résistance à la fatigue des métaux.* Sciences et techniques de l'armement, Mémorial de l'artillerie française, 3ème fascicule, 1973.

133. Dang Van, K. and B. Griveau, *Message, O.(1989) On a new multiaxial fatigue limit criterion: theory and application.* Biaxial and Multiaxial Fatigue: p. 479-496.

134. Papadopoulos, I.V., *A new criterion of fatigue strength for out-of-phase bending and torsion of hard metals.* International Journal of Fatigue, 1994. **16**(6): p. 377-384.

135. Papadopoulos, I.V., *A High-Cycle Fatigue Criterion Applied in Biaxial and Triaxial Out-of-Phase Stress Conditions.* Fatigue & Fracture of Engineering Materials & Structures, 1995. **18**(1): p. 79-91.

136. Papadopoulos, I.V., *Exploring the High-Cycle Fatigue Behaviour of Metals from the Mesoscopic Scale.* Journal of the Mechanical Behavior of Materials, 1996. **6**(2): p. 93-118.

137. Dick, T., et al., *Experimental and numerical analysis of local and global plastic behaviour in fretting wear.* Tribology International, 2006. **39**(10): p. 1036-1044.

138. Dick, T. and G. Cailletaud, *Fretting modelling with a crystal plasticity model of Ti6Al4V.* Computational Materials Science, 2006. **38**(1): p. 113-125.

139. Fouvry, S., et al., *Theoretical analysis of fatigue cracking under dry friction for fretting loading conditions.* Wear, 1996. **195**(1-2): p. 21-34.

140. Crossland, B. *Effect of Large Hydrostatic Pressures on the Torsional Fatigue Strength of an Alloy Steel*. in *Proceeding of the International Conference on Fatigue of Metals, Institute of Mechanical Engineers*. 1956. London

141. Fouvry, S. and K. Kubiak, *Introduction of a fretting-fatigue mapping concept: Development of a dual crack nucleation - crack propagation approach to formalize fretting-fatigue damage.* International Journal of Fatigue, 2009. **31**(2): p. 250-262.

142. Fouvry, S. and K. Kubiak, *Development of a fretting-fatigue mapping concept: The effect of material properties and surface treatments.* Wear, 2009. **267**(12): p. 2186-2199.

143. Madge, J.J., S.B. Leen, and P.H. Shipway, *The critical role of fretting wear in the analysis of fretting fatigue.* Wear, 2007. **263**(1-6 SPEC. ISS.): p. 542-551.

144. Ding, J., S.B. Leen, and I.R. McColl, *The effect of slip regime on fretting wear-induced stress evolution.* International Journal of Fatigue, 2004. **26**(5): p. 521-31.

145. Fouvry, S., P. Duo, and P. Perruchaut, *A quantitative approach of Ti-6Al-4V fretting damage: friction, wear and crack nucleation.* Wear, 2004. **257**(9-10): p. 916-29.

146. Archard, J.F., *Contact and rubbing of flat surfaces.* Journal of Applied Physics, 1953. **24**(8): p. 981-988.

147. Ding, J., et al., *Experimental characterisation and numerical simulation of contact evolution effect on fretting crack nucleation for Ti-6Al-4V.* Tribology International, 2009. **42**(11-12): p. 1651-1662.

148. Leis, B.N., *An Energy-Based Fatigue and Creep-Fatigue Damage Parameter.* Journal of Pressure Vessel Technology, 1977. **99**(4).

149. Ellyin, F. and K. Golos, *Multiaxial Fatigue Damage Criterion.* Journal of Engineering Materials and Technology, 1988. **110**(1).

150. Liu, K.C., *A Method Based on Virtual Strain-Energy Parameters for Multiaxial Fatigue Life Prediction*, in *Advances in Multiaxial Fatigue, ASTM STP 1191*, D.L. McDowell and R. Ellis, Editors. 1993, American Society for Testing and Materials: Philadelphia, PA. p. 67-84.

151. Liu, K.C. and J.A. Wang, *An energy method for predicting fatigue life, crack orientation, and crack growth under multiaxial loading conditions.* International Journal of Fatigue, 2001. **23**(Supplement 1): p. 129-134.

152. Varvani-Farahani, A., *A new energy-critical plane parameter for fatigue life assessment of various metallic materials subjected to in-phase and out-of-phase multiaxial fatigue loading conditions.* International Journal of Fatigue, 2000. **22**(4): p. 295-305.

153. Glinka, G., G. Shen, and A. Plumtree, *A Multiaxial Fatigue Strain Energy Density Parameter Relsated to the Critical Fracture Plane.* Fatigue & Fracture of Engineering Materials & Structures, 1995. **18**(1): p. 37-46.

154. Chu, C.C., F.A. Conle, and J.F. Bonnen, *Multiaxial Stress-Strain Modeling and Fatigue Life Prediction of SAE Axle Shafts*, in *Advances in Multiaxial Fatigue, ASTM STOP 1191*, D.L. McDowell and R. Ellis, Editors. 1993, American Society for Testing and Materials: Philadelphia, PA. p. 37-46.

155. Ziaei, M., *Analytical Study of Noncircular Profile Families and Numerical Optimization of Standardised Polygon Profiles for Shaft-Hub Connections*. 2002, Chemnitz University of Technology.

156. Son, J.H., et al., *Fretting damage prediction of connecting rod of marine diesel engine.* Journal of Mechanical Science and Technology, 2011. **25**(2): p. 441-447.

157. Ding, J., et al., *Simple parameters to predict effect of surface damage on fretting fatigue.* International Journal of Fatigue, 2011. **33**(3): p. 332-342.

158. Wavish, P.M., et al., *A multiaxial fretting fatigue test for spline coupling contact.* Fatigue & Fracture of Engineering Materials & Structures, 2009. **32**(4): p. 325-345.

159. Jin, O. and S. Mall, *Effects of slip on fretting behavior: experiments and analyses.* Wear, 2004. **256**(7-8): p. 671-684.

160. Abdel-Aal, H.A., *On the interdependence between kinetics of friction-released thermal energy and the transition in wear mechanisms during sliding of metallic pairs.* Wear, 2003. **254**(9): p. 884-900.

161. Santner, E., *Friction and Wear of Materials, Components and Constructions.* Renningen: Expert Verlag [in German], 2004.

162. Nakayama, K. and J.-M. Martin, *Tribochemical reactions at and in the vicinity of a sliding contact.* Wear, 2006. **261**(3-4): p. 235-240.

163. Kupkovits, R.A., *Thermomechanical Fatigue Behavior of the Directionally-Solidified Nickel-Base Superalloy CM247 LC*, in *Woodruff School of Mechanical Engineering*. 2009, Georgia Institute of Technology: Atlanta, GA. p. 279.

164. Hecker, S., et al., *Effects of Strain State and Strain Rate on Deformation-Induced Transformation in 304 Stainless Steel: Part I. Magnetic Measurements and Mechanical Behavior.* Metallurgical and Materials Transactions A, 1982. **13**(4): p. 619-626.

165. Olson, G. and M. Azrin, *Transformation behavior of TRIP steels.* Metallurgical and Materials Transactions A, 1978. **9**(5): p. 713-721.

166. Rice, R.C., Jackson, J. L., Bakuckas, J., and Thompson, S. (2003). "Metallic Materials Properties Development and Standardization (MMPDS)." DOT/FAA/AR-MMPDS-01, U.S. Department of Transportation, Federal Aviation Administration.

167. Muraca, R.F. and J.S. Whittick, *Stainless Steel Type 301*, in *Materials Data Handbook.* 1972, Western Applied Research & Development, Inc.: San Carlos, CA. p. 105.

168. Kim, J.W. and T.S. Byun, *Analysis of tensile deformation and failure in austenitic stainless steels: Part I – Temperature dependence.* Journal of Nuclear Materials, 2010. **396**(1): p. 1-9.

169. Ahmad, Z., *Principles of Corrosion Engineering and Corrosion Control*. Materials & Mechanical. 2006: Butterworth-Heinemann. 1-672.

170. Zhou, Z.R., et al., *Investigation of fretting behaviour of several metallic materials under grease lubrication.* Tribology International, 2000. **33**(2): p. 69-74.

171. Zhou, Z.R., S. Fayeulle, and L. Vincent, *Cracking behaviour of various aluminium alloys during fretting wear.* Wear, 1992. **155**(2): p. 317-330.

172. Hirsch, M.R. and R.W. Neu, *Fretting damage in thin sheets: Analysis of an experimental configuration.* Tribology International. **In Press, Corrected Proof**.

173. Yang, Z.Y., M.G.S. Naylor, and D.A. Rigney, *Sliding wear of 304 and 310 stainless steels.* Wear, 1985. **105**(1): p. 73-86.

174. Waterhouse, R.B., *Fretting Wear.* Wear of Materials: International Conference on Wear of Materials, 1981: p. 17-22.

175. Stott, F.H., D.S. Lin, and G.C. Wood, *The structure and mechanism of formation of the 'glaze' oxide layers produced on nickel*-*based alloys during wear at high temperatures.* Corrosion Science, 1973. **13**(6): p. 449-469.

176. Mészáros, I. and J. Prohászka, *Magnetic investigation of the effect of α'-martensite on the properties of austenitic stainless steel.* Journal of Materials Processing Technology, 2005. **161**(1–2): p. 162-168.

177. Hirsch, M.R. and R.W. Neu, *Fretting damage in thin sheets: Analysis of an experimental configuration.* Tribology International, 2011. **44**(11): p. 1503-1510.

178. Hirsch, M.R. and R.W. Neu, *Influence of temperature on the fretting response between AISI 301 stainless steel and AISI 52100 steel.* Tribology International, (0).

179. Iwabuchi, A., *Fretting wear of inconel 625 at high temperature and in high vacuum.* Wear, 1985. **106**(1-3): p. 163-175.

180. Hirsch, M.R. and R.W. Neu, *Fretting behaviour of AISI 301 stainless steel sheet in full hard condition in contact with AISI 52100 steel.* Tribology - Materials, Surfaces and Interfaces, 2008. **2**(1): p. 3-9.

181. Zhang, Z., X. Chen, and Y. Wang, *Uniaxial ratcheting behavior of polytetrafluoroethylene at elevated temperature.* Polymer Testing, 2010. **29**(3): p. 352-357.

182. Briscoe, B.J., Y. Lin Heng, and T.A. Stolarski, *The friction and wear of poly(tetrafluoroethylene)-poly (etheretherketone) composites: An initial appraisal of the optimum composition.* Wear, 1986. **108**(4): p. 357-374.

183. Ding, J., et al., *A multi-scale model for fretting wear with oxidation-debris effects.* Proceedings of the Institution of Mechanical Engineers, Part J (Journal of Engineering Tribology), 2009. **223**(Copyright 2010, The Institution of Engineering and Technology): p. 1019-31.

184. McColl, I.R., J. Ding, and S.B. Leen, *Finite element simulation and experimental validation of fretting wear.* Wear, 2004. **256**(11-12): p. 1114-27.

185. Berthier, Y., L. Vincent, and M. Godet, *Velocity accommodation in fretting.* Wear, 1988. **125**(1-2): p. 25-38.

186. Godet, M., *The third-body approach: A mechanical view of wear.* Wear, 1984. **100**(1-3): p. 437-452.

187. Fouvry, S., et al., *An energy description of wear mechanisms and its applications to oscillating sliding contacts.* Wear, 2003. **255**(1-6): p. 287-298.

188. Warmuth, A.R., et al., *The effect of contact geometry on fretting wear rates and mechanisms for a high strengthsteel.* Wear, 2013. **301**(1–2): p. 491-500.

189. Iwamoto, T., T. Tsuta, and Y. Tomita, *Investigation on deformation mode dependence of strain-induced martensitic transformation in trip steels and modelling of transformation kinetics.* International Journal of Mechanical Sciences, 1998. **40**(2–3): p. 173-182.

190. Lebedev, A.A. and V.V. Kosarchuk, *Influence of phase transformations on the mechanical properties of austenitic stainless steels.* International Journal of Plasticity, 2000. **16**(7-8): p. 749-767.